

# Classical ghost imaging with opto-electronic light sources: novel and highly incoherent concepts

Dissertation approved by the Department of Physics of the Technische Universität Darmstadt in fulfillment of the requirements for the academic degree of Doctor rerum naturalium (Dr. rer. nat.) by M. Sc. Sébastien Adrian Blumenstein (name of birth: Hartmann)  
Day of submission: 07.02.2017, Day of examination: 19.04.2017  
Darmstadt 2017 – D17

First referee: Prof. Dr. Wolfgang Elsäßer  
Second referee: Prof. Dr. Reinhold Walser



TECHNISCHE  
UNIVERSITÄT  
DARMSTADT



---

# **Classical ghost imaging with opto- electronic light sources: novel and highly incoherent concepts**

## **Klassisches Ghost Imaging mit opto- elektronischen Lichtquellen: neue und hoch inkohärente Konzepte**

Vom Fachbereich Physik der Technischen Universität Darmstadt

zur Erlangung des Grades eines Doktors der  
Naturwissenschaften (Dr. rer. nat.)

genehmigte Dissertation von M. Sc. Sébastien Adrian  
Blumenstein (geb. Hartmann) aus Frankfurt am Main

Referent: Prof. Dr. Wolfgang Elsäßer  
Korreferent: Prof. Dr. Reinhold Walser

Tag der Einreichung: 7. 2. 2017

Tag der Prüfung: 19. 4. 2017

Darmstadt 2017

D17

---



---

## Table of Content

<b>LIST OF ABBREVIATIONS .....</b>	<b>1</b>
<b>1. INTRODUCTION .....</b>	<b>2</b>
<b>2. FUNDAMENTALS .....</b>	<b>5</b>
<b>2.1. Correlations of light .....</b>	<b>5</b>
2.1.1. First-order correlations .....	5
2.1.2. Second-order temporal auto-correlations .....	8
2.1.3. Higher-order temporal auto-correlations .....	12
<b>2.2. Ghost Imaging .....</b>	<b>15</b>
<b>3. EXPERIMENTAL METHODS.....</b>	<b>24</b>
3.1. Determining photon statistics by one single-photon-counting detector.....	24
3.2. Determining intensity correlations by two-photon-absorption interferometry.....	30
<b>4. TAILORING FIRST- AND SECOND-ORDER COHERENCE PROPERTIES OF LIGHT EMITTED BY SLDS.....</b>	<b>40</b>
4.1. Superluminescent diodes (SLDs) .....	40
4.2. Coherence control via broadband optical feedback .....	48
4.3. Coherence control by mixing incoherent SLD light with coherent laser light.....	53
<b>5. GHOST IMAGING (GI) WITH OPTO-ELECTRONIC EMITTERS .....</b>	<b>61</b>
<b>5.1. Photon statistics-based GI with pseudo-thermal light.....</b>	<b>63</b>
5.1.1. GI scheme .....	63
5.1.2. Model.....	68
5.1.3. Experimental results .....	76
5.1.4. Numerical 2D ghost images .....	81
<b>5.2. Spectrally ultra-broadband GI with hybrid pseudo-thermal-SLD light .....</b>	<b>85</b>
5.2.1. GI scheme .....	85
5.2.2. Point-to-point correspondence .....	87
5.2.3. GI experiment .....	88
<b>5.3. Spectrally ultra-broadband GI with a broad-area SLD .....</b>	<b>91</b>
5.3.1. The broad-area SLD.....	91
5.3.2. Temporal correlations.....	92
5.3.3. Spatial correlations .....	94
5.3.4. GI experiment .....	98
<b>6. SUMMARY .....</b>	<b>101</b>
6.1. Key findings .....	101

---

---

---

6.2.	Summary, conclusions and outlook .....	102
<b>7.</b>	<b>ZUSAMMENFASSUNG .....</b>	<b>106</b>
7.1.	Schlüsselergebnisse.....	106
7.2.	Zusammenfassung, Schlussfolgerungen und Ausblick .....	107
<b>8.</b>	<b>APPENDIX .....</b>	<b>111</b>
8.1.	Towards ultra-broadband GI in 2D .....	111
	<b>BIBLIOGRAPHY .....</b>	<b>113</b>
	<b>LIST OF FIGURES.....</b>	<b>127</b>
	<b>ACKNOWLEDGEMENT .....</b>	<b>133</b>
	<b>CURRICULUM VITAE.....</b>	<b>134</b>
	<b>PUBLICATIONS AND PROCEEDINGS .....</b>	<b>135</b>
	<b>SUPERVISED THESES .....</b>	<b>138</b>
	<b>ERKLÄRUNGEN .....</b>	<b>139</b>

---

---

---

## List of abbreviations

---

AR	anti-reflection
BE	Bose-Einstein
CCD	charge-coupled device
DFB	distributed feedback
DLS	dynamic light scattering
DM	discrete mode
DMD	digital micromirror device
DWELL	dot-in-well
ECDL	external-cavity diode laser
EM	electro-magnetic
FCS	fluorescence correlation spectroscopy
FP	Fabry-Pérot
FTIR	Fourier-transform infrared
FWHM	full width at half maximum
GI	ghost imaging
HBT	Hanbury Brown – Twiss or Hanbury Brown and Twiss
HR	high-reflection
MM	multimode
NIR	near infra-red
OCT	optical coherence tomography
OFB	optical feedback
OSA	optical spectrum analyzer
PS-GI	photon statistics-based ghost imaging
PT	pseudo-thermal
QD	quantum dot
RGG	rotating ground glass
RIN	relative intensity noise
RGB	red green blue
SLD	superluminescent diode
SLM	spatial light modulator
SM	single-mode
SOA	semiconductor optical amplifier
TCSPC	time-correlated single-photon-counting
UBB-GI	ultra-broadband ghost imaging
VCZ	Van-Cittert-Zernike

---

## 1. Introduction

---

Since the invention of the laser in the 1960s, higher-order correlations of optical fields have been a central aspect of fundamental research on the coherence of light. The first-order coherence of light is described by correlation functions of the electric field, closely connected to its spectral properties, which were already studied and applied in the 19<sup>th</sup> century [1, 2]. The simplest manifestation of electric field correlations is the well-known interference effect that occurs when two light beams from the same source are superposed [3]. Second- and higher-order correlations of light relate to the statistical properties of light. The basic difference between the statistical properties of thermal light and laser light can only be understood by considering at least the correlation order of two. In this case, one refers to *intensity correlations* of an optical field.

Within their famous experiment, Hanbury Brown and Twiss (HBT) discovered enhanced intensity correlations of light originating from a mercury arc lamp by studying correlations between the photoelectrons of two detectors [4]. For the first time, enhanced correlations between photons of two different beams were detected providing evidence for the well-known photon-bunching effect of thermal light. The engendered controversy about its appropriate theoretical interpretation, especially in terms of light quanta, was closed by the formalism of the quantum theory of optical coherence by R. J. Glauber [5], for which he was awarded the Nobel prize of physics.

From the early days of the laser until today's high-tech developments, intensity correlation measurements of light have been carried out for determining the onset of lasing. i.e. for differing between spontaneous and stimulated emission regimes [6, 7]. In this context, the photon statistics of emitted light are the footprint of the photon generation process inside a light source. Furthermore, intensity correlations are an established measure in the field of quantum optics for verifying the presence of photon entanglement or the quality of single-photon emitters. So-called *anti-bunching* measurements are mostly performed exploiting HBT configurations with sophisticated photon-counting modules. However still today, new detection schemes are developed to access new regions of interest regarding the electro-magnetic spectrum [8] and to improve the correlation time resolution for addressing several types of light sources [9, 10, 11].

Moreover, second- and higher-order correlations of light are not solely objects of fundamental research. The stellar intensity interferometer for determining the angular diameter of stars was the immediate application [12]. In the field of dynamic light scattering and diffusing wave spectroscopy, intensity correlation signals are exploited to extract size distributions and dynamic properties of particles in suspensions [13]. By fluorescence correlations spectroscopy and related techniques, the fields of microbiology and life-sciences exploit the fact that biochemical parameters such as the concentration and the shape of molecules as well as the viscosity of their environment are reflected in the temporal fluctuations of the fluorescence intensity [14]. And most importantly to this thesis, intensity correlations are the basis of the *ghost imaging* phenomenon.

More precisely, a *ghost image* is obtained by correlating the total intensity of the transmitted or reflected light of an illuminated object with the spatially resolved intensity of a position-correlated reference beam which itself has never interacted with the object. Intriguingly, the spatial resolution of the image is provided by the non-interacting reference beam which has led to the terminology of *ghost imaging* (GI). The first experimental realization of GI goes back to 1995 where intensity correlations between entangled photon pairs from a parametric down-conversion source were exploited [15]. Due to the use of non-classical light, the GI phenomenon was initially interpreted as a quantum effect. However, it has been extensively proven, starting with first experimental demonstrations on *GI with thermal light* in 2002, that an exclusive quantum foundation is no longer sustainable [16, 17, 18]. In such *classical* GI experiments, usually a pseudo-thermal light source is utilized consisting of coherent laser light which is

---

focused onto a rotating diffuser. The generated *speckle patterns* are sent through a beam splitter generating mutually (statistically) correlated light beams. Whereas one light beam interacts with the object with subsequent *spatially integrating detection*, the other beam is guided onto another, *spatially resolving detector*. By correlating the two detector signals, i.e. by determining the *intensity cross-correlations* between the light fields in both optical paths, an image of the object can be retrieved. In the following years, an intense time of predominantly fundamental research on GI took place leading to a profound gain of knowledge in the field regarding comprehensive theoretical descriptions and experimental investigations on the imaging properties such as contrast and resolution. Within the present decade, GI research has moved to more application-oriented studies [19] to explore its promising potential for imaging in turbid media [20], for offering simplified image acquisition techniques such as single-pixel cameras [21] and for proposing new image encryption protocols [22].

This thesis pursues a rather unorthodox strategy to contribute to the development of GI towards its applicability in future work. In first place, fundamental investigations on the second-order correlations of light emitted by a special type of broadband opto-electronic emitter are carried out. The so-called *quantum dot superluminescent diode* (QD SLD) yields spectrally broadband *amplified spontaneous emission* (ASE), a photon generation process holding spontaneous as well as stimulated emission events with a substantial number of modes. Motivated by recent studies on novel QD SLD light states [23], the temporal second-order coherence of these light sources is further investigated. In particular, a simultaneous tailoring of their first- and second-order coherence properties is achieved within two different experiments, which shall provide new insights into the physics of semiconductor light generation at the edge to stimulated emission. In a second step, these comprehensively characterized QD SLDs are exploited for proposing new light source concepts to GI. In contrast to the straightforward approach building on conventional GI schemes, these opto-electronic light sources are incorporated into novel detection concepts. From a fundamental point of view, it is aimed to exceed the *degree of classicality* of state-of-the-art GI by developing GI concepts with highly incoherent light. Specifically, three GI experiments are realized which follow the thesis guideline: *from novel to highly incoherent concepts*. First, a classical GI detection scheme based on the determination of photon number probability distributions is developed. Within a second scheme, two-photon-absorption interferometry is exploited, which allows introducing compact, spectrally broadband opto-electronic emitters to GI. By setting a two-fold research objective, namely new detection concepts *and* new light sources, it is expected to provide a broader platform together with already established GI technologies for enabling GI applications in future work.

In more detail, this thesis is structured as follows.

Chapter 2 gives a short introduction to the fundamentals on correlations of light as well as to the ghost imaging phenomenon. Important definitions of first- and higher-order correlation functions are reviewed by keeping the focus on auto-correlations. Various measures of the coherence of light of different orders are specified (Section 2.1) where mostly the formalism of Mandel and Wolf is adopted [3]. In Section 2.2, the image formation of ghost imaging is briefly discussed in terms of classical physics. An overview of basic GI research and developments are given emphasizing established GI detection methods and state-of-the-art GI light sources.

Chapter 3 presents two experimental methods which are employed for determining second- and higher-order correlations of light. In Section 3.1, a direct measurement technique with moderate correlation time resolution is presented based on one single-photon-counting detector for determining photon number probability distributions with subsequent evaluation of higher-order correlations of optical fields. Then, the two-photon-absorption (TPA) method is introduced for measuring second-order correlation functions of light on ultra-short correlation timescales (Section 3.2). The accomplishments of the thesis are set out in two main chapters.

---

---

Chapter 4 covers the fundamental temporal coherence investigations of quantum dot superluminescent diodes. Firstly, the special diode structure as well as the quantum dot gain medium are introduced. A brief review on preceding coherence studies of QD SLDs is given followed by the presentation of a theoretical model for the state of light of SLD ASE (Section 4.1). In a first experiment (Section 4.2), broadband optical feedback is applied onto a QD SLD for controlling the number of emitted modes and for enabling a direct comparison to the predictions by the model. In Section 4.3, a second experiment is presented in which coherent light is superimposed with QD SLD light, again compared to model calculations.

Chapter 5 contains all ghost imaging findings. In Section 5.1, a novel classical GI detection concept based on the photon statistics determination of Section 3.1 is proposed. One-dimensional proof-of-principle experiments with a laser diode based pseudo-thermal light source are presented. A simple model is developed supporting first experimental results and predicting imaging performances for two-dimensional objects. Section 5.2 deals with a second, novel GI detection scheme based on TPA interferometry where a QD SLD is utilized in combination with a rotating diffuser. One-dimensional proof-of-principle GI scenarios are demonstrated. Finally, Section 5.3 presents the most incoherent GI experiment by incorporating a broad-area SLD as the GI light source. A comprehensive analysis of the high *incoherence* of the broad-area SLD is carried out in the temporal as well as the spatial domain.

Chapter 6 summarizes the thesis and discusses perspectives for future developments and applications of the demonstrated proof-of-concepts.

---

## 2. Fundamentals

---

This chapter sets out the most important basics of the thesis. Section 2.1. deals with the description and various definitions of the coherence and the correlation functions of the electromagnetic (EM) field. Section 2.2. introduces the ghost imaging phenomenon and shall also serve as an overview of the research status of the field.

### 2.1. Correlations of light

The introductory section (Chapter 0) has already indicated that ghost imaging relies on correlations of light. More precisely, the ghost image signal is a cross-correlation function of intensity distributions detected in two different planes originating from a suitable light source. It is therefore necessary to review some basic definitions on the correlations of light which will be used throughout the thesis. It involves the temporal as well as the spatial domain of different correlation orders with special focus on auto-correlation functions because of their direct relation to the coherence degree of light. Most of the following definitions are based on a classical description of the EM field since the here utilized sources yield classical light with a considerable amount of optical power. However, single-photon-counting detection will be an important part of the experimental methodologies. In this context, it is appropriate to clarify the connection between correlation functions and photon statistics by quantized light fields.

The  $j$ -th order normalized auto-correlation function of the electric field  $\vec{E}(\vec{r}, t)$  of a classical EM wave is defined by [3]<sup>1</sup>

$$g^{(j)}(\vec{r}_1, t_1; \dots, \vec{r}_j, t_j; \vec{r}_{j+1}, t_{j+1}; \dots, \vec{r}_{2j}, t_{2j}) = \frac{\langle \vec{E}^*(\vec{r}_1, t_1) \dots \vec{E}^*(\vec{r}_j, t_j) \vec{E}(\vec{r}_{j+1}, t_{j+1}) \dots \vec{E}(\vec{r}_{2j}, t_{2j}) \rangle}{\sqrt{\langle \vec{E}^*(\vec{r}_1, t_1) \vec{E}(\vec{r}_1, t_1) \rangle \dots \langle \vec{E}^*(\vec{r}_{2j}, t_{2j}) \vec{E}(\vec{r}_{2j}, t_{2j}) \rangle}} \quad (1)$$

with the space coordinate  $\vec{r}_j$  and time  $t_j$ .  $\langle \dots \rangle$  denotes ensemble averaging. The notation of Eq. (1) already suggests a correlation function definition of one single field  $\vec{E}(\vec{r}, t)$ , i.e. auto-correlations. However, one could consider different fields  $\vec{E}_i(\vec{r}, t)$  for Eq. (1) which then would become the  $j$ -th order cross-correlation function.

#### 2.1.1. First-order correlations

The most basic type of temporal correlations is described by the first-order auto-correlation function

$$\begin{aligned} g^{(1)}(\vec{r}, t; \vec{r} + \Delta\vec{r}, t + \tau) &= \frac{\langle \vec{E}^*(\vec{r}, t) \vec{E}(\vec{r} + \Delta\vec{r}, t + \tau) \rangle}{\sqrt{\langle \vec{E}^*(\vec{r}, t) \vec{E}(\vec{r}, t) \rangle \langle \vec{E}^*(\vec{r} + \Delta\vec{r}, t + \tau) \vec{E}(\vec{r} + \Delta\vec{r}, t + \tau) \rangle}} \\ &= \frac{G^{(1)}(\vec{r}, t; \vec{r} + \Delta\vec{r}, t + \tau)}{\sqrt{G^{(1)}(\vec{r}, t) G^{(1)}(\vec{r} + \Delta\vec{r}, t + \tau)}} \end{aligned} \quad (2)$$

---

<sup>1</sup> Within the framework of the classical theory of fluctuating wavefields, higher-order correlation functions were introduced by Wolf and Mandel [261, 265].

comprising a time delay  $\tau$  and a displacement  $\Delta\vec{r}$  as the function variables. The absolute value of Eq. (2) is typically referred to as the first-order coherence degree, sometimes as the mutual degree of self-coherence [3]. Light fields are classified as

- coherent for  $|g^{(1)}(\vec{r}, t; \vec{r} + \Delta\vec{r}, t + \tau)| = 1$
- incoherent for  $|g^{(1)}(\vec{r}, t; \vec{r} + \Delta\vec{r}, t + \tau)| = 0$
- partially coherent for  $0 < |g^{(1)}(\vec{r}, t; \vec{r} + \Delta\vec{r}, t + \tau)| < 1$

**First-order temporal auto-correlations.** For considering the temporal domain exclusively, a fixed space variable  $\vec{r}$  is considered such that  $\Delta\vec{r} = \mathbf{0}$ .

$$g^{(1)}(\tau) = \frac{\langle \vec{E}^*(t) \vec{E}(t + \tau) \rangle}{\sqrt{\langle \vec{E}^*(t) \vec{E}(t) \rangle \langle \vec{E}^*(t + \tau) \vec{E}(t + \tau) \rangle}} \quad (3)$$

represents the normalized first-order temporal auto-correlation function<sup>2</sup>. A conventional Michelson interferometer experiment can assess the real part of  $g^{(1)}(\tau)$ . It is directly linked to the optical spectrum of the light field by the well-known Wiener-Khintchine theorem [24]:

$$s(\nu) = \int_{-\infty}^{\infty} d\tau e^{i 2\pi\nu \tau} g^{(1)}(\tau). \quad (4)$$

$s(\nu)$  denotes the normalized spectral distribution of optical frequencies  $\nu$  with

$$\int_0^{\infty} s(\nu) d\nu = 1. \quad (5)$$

**Coherence time and bandwidth.** In the context of the coherence degree, one can realize that ideal first-order coherence is only valid for perfectly monochromatic light, i.e. a single optical frequency with vanishing linewidth. On the other hand, ideal first-order incoherence is only given for an infinitely large spectral bandwidth. Of course, nature does neither provide such light sources with an infinite amount of energy nor does it allow vanishing linewidths due to the limit of the natural linewidth founded in the uncertainty principle of quantum mechanics. Real light sources are thus inherently (temporally) partially coherent. A more convenient measure for the first-order temporal coherence is given by the coherence time [3]

$$\tau_c = \int_{-\infty}^{\infty} |g^{(1)}(\tau)|^2 d\tau. \quad (6)$$

It reflects the timescale on which the values of  $|g^{(1)}(\tau)|$  vanish. Via the Wiener-Khintchine theorem, the coherence time is connected to the spectral bandwidth by

$$\tau_c = \frac{1}{\Delta\nu} \quad (7)$$

<sup>2</sup> It is assumed that the light field fluctuations are conform with a stationary random process and ergodic. This makes correlation functions  $g^{(j)}(\tau)$  independent of the specific time  $t$  and it allows for utilizing time averaging instead of ensemble averaging without constraints.

with the spectral width  $\Delta\nu$  in terms of frequency. The coherence time is connected to the longitudinal coherence length  $l_c$  by

$$l_c = c \tau_c \quad (8)$$

with the speed of light in vacuum  $c$ . Quoting from the coherence theory of Mandel and Wolf, Eq. (8) in combination with Eq. (6) represents *the extent of a unit cell of photon phase space* [3]. Note that the coherence time, the coherence length and the spectral width are merely characteristic measures, and thus different definitions can have their most significant justification. In practice, it is common to use a 10dB or 3dB spectral width criterion, the latter also known as the full-width-at-half-maximum (FWHM). Eq. (6), introduced here, results in a spectral width of [3]

$$\Delta\nu_s = \frac{1}{\int_0^\infty s^2(\nu) d\nu} , \quad (9)$$

known as the Suessmann measure [25]. Its integrative form characterizes more appropriately highly multimode (MM) and irregularly shaped spectral distributions as appearing frequently during this thesis.

**First-order spatial auto-correlations.** Just as first-order correlations can be exclusively considered in the time domain for understanding the basic temporal coherence properties, Eq. (2) is regarded in the following solely in the spatial domain for explaining basic spatial coherence measures:

$$g^{(1)}(\vec{r}, \Delta\vec{r}) = \frac{\langle \vec{E}^*(\vec{r}) \vec{E}(\vec{r} + \Delta\vec{r}) \rangle}{\sqrt{\langle \vec{E}^*(\vec{r}) \vec{E}(\vec{r}) \rangle \langle \vec{E}^*(\vec{r} + \Delta\vec{r}) \vec{E}(\vec{r} + \Delta\vec{r}) \rangle}} . \quad (10)$$

Whereas the longitudinal coherence is described by the time-domain of correlation functions, spatial correlation functions such as Eq. (10) address the transverse coherence properties of a light field. The displacement  $\Delta\vec{r} > 0$  after which the absolute square value of  $g^{(1)}(\Delta\vec{r})$  vanishes, is related to the extent of a transverse coherence area  $A_c$ . Spatially coherent light yields a constant behavior of  $|g^{(1)}(\Delta\vec{r})|^2 = 1$  for any displacement  $\Delta\vec{r}$  consistent with a single transverse mode. On the other hand, a spatially partially coherent light source exhibits multiple transverse modes. The precise number, the shape and the alignment of transverse modes of a specific light source as well as the value of the coherence area at a defined plane (near- or far-field) are strongly dependent on the structure, on the functionality and on the operation conditions of the light source itself and beyond, on the propagation of the emission.

A commonly used approximation of the transverse coherence is one of the central theorems of the fundamental theory of partial coherence which was formulated by Van-Cittert (VC) and Zernike (Z) [26, 27]. The VCZ theorem expresses the first-order spatial correlations between two points in the light field generated by a spatially incoherent, quasi monochromatic, planar source. Applying Zernike's propagation laws,  $g^{(1)}(\Delta\vec{r})$  takes a first-order Bessel function in the far-field. Assuming a 12% amplitude drop of  $g^{(1)}$ , the coherence area  $A_c$  in the far-field - close to the direction normal and parallel to the source plane of a uniform, circular source of radius  $a$  - is approximately [3]

$$A_c = \frac{0.063 L^2 \lambda^2}{\pi a^2} . \quad (11)$$

$L$  stands for the distance from the source to the plane and  $\lambda$  for the wavelength.

In general, the transverse coherence length  $\sigma_c \sim \sqrt{A_c}$  within the intensity distribution of a light field at a specific plane can be determined by a Young's double slit interference experiment with a variable slit separation. The mutual degree of spatial self-coherence  $|g^{(1)}(\Delta\vec{r})|$  can be deduced from the visibility of interference patterns for increasing slit separation on a screen located behind the double slit aperture.

Alternatively, interferometric approaches using e.g. reverse wave-front Michelson interferometers [28] are applied. For the sake of completeness, note that for identifying solely  $\sigma_c$ , also higher-order spatial correlation measurements - presented in the following two sections - are applicable such as spatial HBT experiments or time-resolved charge-coupled device (CCD) measurements [29] with subsequent spatial intensity correlation computation.

It is worth noticing that first-order correlations are not restricted to the description of the basic coherence properties of a light field. Many light interferometry applications are based on evaluating  $g^{(1)}(\vec{r}_1, t_1; \dots, \vec{r}_j, t_j)$  in complex optical systems. Fourier-Transform Infra-Red (FTIR) spectroscopy [30], white-light interference microscopy [31] and optical coherence tomography (OCT) [32] are just three examples out of numerous well-established applications.

Next, second-order auto-correlation functions are discussed for understanding the most relevant physical quantity of the thesis. In order not to go beyond the scope of a fundamental introduction, the rest of this chapter is limited to a time-domain discussion of higher-order correlations.

### 2.1.2. Second-order temporal auto-correlations

Second-order auto-correlations characterize the first level of higher-order coherence of a light field. Compared to first-order correlations, it is not the field but the intensity appearing in the auto-correlation function. The classical definition of the normalized temporal intensity auto-correlation function [33, 34]

$$g^{(2)}(\tau) = \frac{\langle I(t)I(t+\tau) \rangle}{\langle I(t) \rangle^2} = \frac{G^{(2)}(\tau)}{G^{(1)}(t, t)G^{(1)}(t, t)} \quad (12)$$

is often referred to as *the second-order coherence degree of a light field*<sup>3</sup>. Eq. (12) is a symmetric function, i.e.  $g^{(2)}(\tau) = g^{(2)}(-\tau)$ . Because the intensity can assume positive values only, it can principally take any positive value  $g^{(2)}(\tau) \geq 0$  [35].

Figure 1 (left) shows possible  $g^{(2)}(\tau)$  trajectories for four different types of light fields. At first, one should note that the intensity correlation timescales are dictated by the first-order coherence which is also true for any higher-order correlation function. For time delays  $\pm\tau$  exceeding the coherence time  $\pm\tau_c$ , Eq. (12) reduces to a value of 1 reflecting vanished correlations. The value of  $g^{(2)}$  at a time delay of zero, i.e.  $\tau = 0$ , is connected to the photon statistics of a light field. One way to understand this connection is considering the quantum optical definition of Eq. (12) given by

$$g^{(2)}(\tau = 0) = \frac{\langle :\hat{n}(t)\hat{n}(t): \rangle}{\langle \hat{n}(t) \rangle^2} = \frac{\langle \hat{n}^2(t) \rangle - \langle \hat{n}(t) \rangle^2}{\langle \hat{n}(t) \rangle^2}. \quad (13)$$

Here, the intensity is replaced by the photon number operator  $\hat{n} = \hat{a}^\dagger \hat{a}$  constituted by the field creation- and annihilation operators,  $\hat{a}^\dagger$  and  $\hat{a}$ , respectively. The photon number operators in the correlation term are put in normal order ( $: : \rangle$ ) following the Wick ordering rule. Applying commutation relations, one can write down the right-hand side of Eq. (13) which comprises exclusively the first and the second statistical momentum of the photon number probability distribution  $P(n)$ , expressed by [3]

$$\langle \hat{n}^m \rangle = \sum_n P(n) n^m \quad (14)$$

<sup>3</sup> Note that  $g^{(2)}(\tau)$  does not comprise a specific time dependence  $t$ . This case holds for stationary light which is valid for all considerations and experimental investigations in this thesis.

with the  $m$ -th statistical moment and the photon number  $n$ . The latter is also referred to as the eigenvalue of the eigenstates of the photon number operator  $\hat{n}$ , known as number states or *Fock* states. Using more common statistical parameters, namely the variance  $\Delta n^2 = \langle (\hat{n}(t) - \langle \hat{n}(t) \rangle)^2 \rangle$  and the mean  $\bar{n} = \langle \hat{n}(t) \rangle$ , one can easily deduce

$$g^{(2)}(0) = 1 + \frac{\Delta n^2 - \bar{n}}{\bar{n}^2}. \quad (15)$$

with the typical abbreviation  $g^{(2)}(\tau = 0) \equiv g^{(2)}(0)$ . Eq. (15) illustrates best how temporal second-order correlations are connected to photon statistics. In particular,  $g^{(2)}(0)$  comprises the most basic descriptive characteristics of a photon number distribution, namely where  $P(n)$  is centred (at  $\bar{n}$ ) and how wide  $P(n)$  is (by  $\Delta n^2$ ). Furthermore, the variance relates to the photon number fluctuation characterizing how regular photons are arriving over time. On this account,  $g^{(2)}(0)$  serves as a measure for the level of the so-called *photon-bunching effect* which was experimentally discovered by Hanbury Brown and Twiss in 1956 [4]. Whereas coherent light yields a constant  $g^{(2)}(\tau) = 1$  function attributed to totally random photon arrivals without any correlations (see Figure 1) [34], thermal light shows enhanced second-order correlations for  $\tau < \tau_c$  associated with photons tending to form bunches on the time axis (see Figure 1, right) [36]. These two examples emphasize that the photon number distribution of a light field depends fundamentally on the nature of light generation or in other words, on the photon emission process at the light source. Whereas ideal laser light is based on stimulated photon emission, ideal thermal light generates photons by spontaneous emission processes. Both light sources are prominent examples for fundamentally differing types of coherence with completely different photon statistics. While photons from coherent light obey a Poisson distribution (Figure 2, blue)

$$P_{poi}(n) = \frac{\bar{n}^n e^{-\bar{n}}}{n!}, \quad (16)$$

thermal light exhibits a Bose-Einstein (BE) distribution (Figure 2, red), here expressed in terms of photon numbers<sup>4</sup>:

$$P_{BE}(n) = \frac{\bar{n}^n}{(1 + \bar{n})^{n+1}}. \quad (17)$$

Both are parametrized by the mean photon number  $\bar{n}$ . The variance  $\Delta n^2$  amounts to  $\bar{n}$  and  $\bar{n}^2 + \bar{n}$  for the Poisson and the BE distribution, respectively, resulting in  $g_{poi}^{(2)}(0) = 1$  and  $g_{BE}^{(2)}(0) = 2$ . As  $g^{(2)}(0)$  is a unit-free quantity describing the photon number distribution at first level (by comprising  $\Delta n^2$ ), it is sometimes referred to as the *central second-order coherence degree*. It can be interpreted as a probability measure for the simultaneous occurrence of two photons. In particular, the probability is twice as high for thermal light as for coherent light. Furthermore, the specific value for the central second-order coherence degree of an arbitrary light field can be affected by polarization, transverse mode properties and attenuation [37]. Also, there are other types of light fields showing  $g^{(2)}(0) > 2$  as already mentioned at the beginning of this section and as indicated in Figure 1. This is often entitled as photon *super-bunching* or as *extra-bunching*, which is observed for nonlinearly generated light [38] and for interfering thermal light [39]. On the other hand, it is also possible to reduce the photon-bunching effect below the classical limit of coherent light. That is, the randomness of stimulated photon emission processes can be regularized when considering non-classical light sources or single-photon emitters. Such sources can yield central second-order coherence degrees less than 1. The absolute boundary value is  $g^{(2)}(0) = 0$  for equidistant photons over time reflecting a probability of 0 for two photons to occur simultaneously.

<sup>4</sup> More precisely, Eq. (17) is the probability distribution of photons in one cell of phase space when the optical field is in thermal equilibrium [3].

Therefore,  $g^{(2)}(0)$ - and  $g^{(2)}(\tau)$ -measurements serve typically as the quality criterion for single-photon emission and entanglement (see [40] and reference therein).

For the sake of completeness, it must be noted that other temporal second-order coherence measures exist. Whilst  $g^{(2)}(0)$  was introduced by Glauber within his coherence theory of radiation fields [34], the Fano-factor  $F$  emerged in a mathematical signal context [41] expressed by

$$F = \frac{\Delta n^2}{\bar{n}^2} = g^{(2)}(0) - 1 + \bar{n} \quad (18)$$

and the Mandel  $Q$ -factor in the context of sub-Poissonian states of light [42]:

$$Q = \frac{\Delta n^2 - \bar{n}}{\bar{n}} = \bar{n}(g^{(2)}(0) - 1). \quad (19)$$

Both,  $F$  and  $Q$  are equivalent to the Glauber central second-order coherence degree whose relations are shown on the right-hand side of Eq. (18) and (19). However, in this thesis,  $g^{(2)}(0)$  will be utilized exclusively for reasons of clarity.

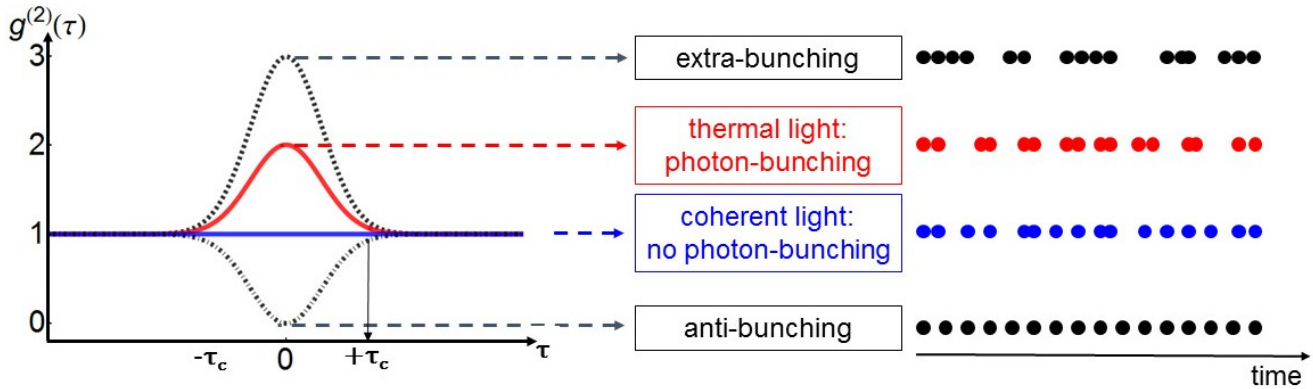


Figure 1. **Illustration of second-order temporal correlations.** Left: Illustrative intensity auto-correlation functions originating from coherent light (blue), from thermal light (red), from non-classical light (dash-dotted) and from light showing extra-bunching (dotted). Right: Visualization of photon streams for the four different levels of photon-bunching.

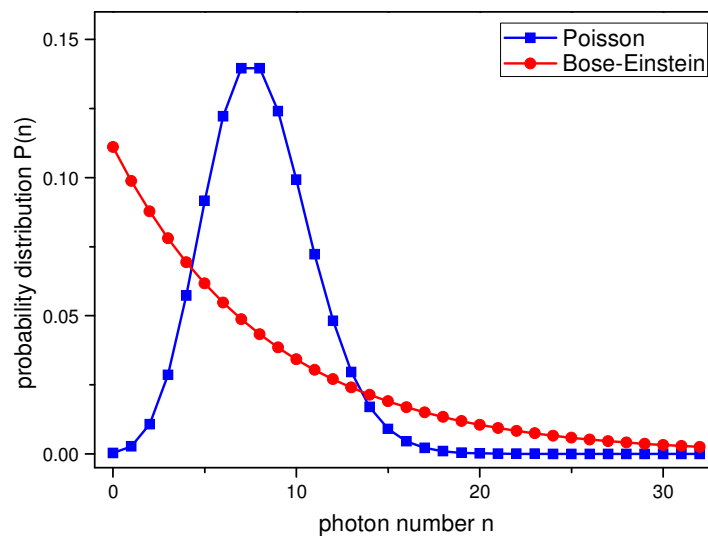


Figure 2. **Exemplary photon number probability distributions  $P(n)$ :** a Bose-Einstein distribution (red) and a Poissonian distribution (blue) with a mean photon number of  $\bar{n} = 8$ .

**Detection methods.**

The most common experimental method for determining the second-order temporal correlation function  $g^{(2)}(\tau)$  is the coincidence count technique based on a two-detector intensity interferometer. Hanbury Brown and Twiss were the first to introduce this technique for radio sources [43], which nowadays is well-known under the same name. Later, they applied this technique to a mercury arc lamp discovering the famous photon-bunching effect (or HBT effect) for thermal light sources [4]. It can be argued that the HBT experiment stimulated the creation of the modern field of quantum optics [40].

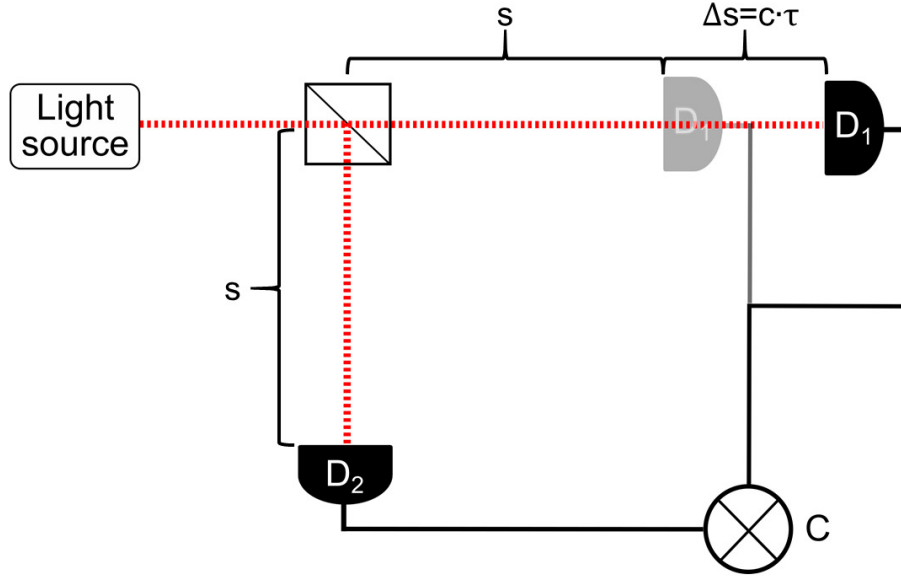


Figure 3. **Schematic drawing of a coincidence measurement based on the HBT configuration** for determining the second-order correlation function  $g^{(2)}(\tau)$ . Here, the time delay  $\tau$  is introduced by varying the optical path delay  $s$  by  $s + \Delta s$  between the two detectors  $D_1$  and  $D_2$  connected to a correlator  $C$ .

Figure 3 shows a generic scheme of the HBT configuration. The light emitted by a source is split by a beamsplitter and each beam is guided towards one of the two photon-counting detectors  $D_1$  and  $D_2$ . A correlator  $C$  evaluates the coincidences of photon counts registered by both detectors. Implementing a variable optical path delay or using a variable electronic delay and applying an appropriate normalization, the full function  $g^{(2)}(\tau)$  can be experimentally reconstructed. Nowadays, sophisticated time-tagging modules offer the possibility to acquire photon count time traces in both detectors individually with good time resolution (integration time gates  $T_k = t_k - t_{k-1}$ ) and excellent timing (between both detector channels) for calculating the intensity correlations after the signal acquisition. In case one doesn't rely on photon counting, synchronous signal acquisition of two detectors is feasible, while intensity-correlations are subsequently evaluated by

$$G^{(2)}(\tau) = \frac{1}{M} \sum_{k=1}^M I_1(t_k) I_2(t_k + \tau) \quad (20)$$

with the total number of measurements  $M$  indexed by  $k$ .

One important criterion for choosing an appropriate  $g^{(2)}$ -detection system is the time resolution which must be adapted to the coherence time of the investigated light [40]. A specific challenge of the thesis is that spectrally broadband light sources, i.e. sources of very short coherence time, are investigated (Chapter 4) and exploited (Chapter 5.2 and 5.3) in the context of  $g^{(2)}$ -detection. Thus, there is a considerably high-resolution demand of the detection system. Two different methods for  $g^{(2)}$ -detection

are applied in the course of this work: a photon statistics measurement method based on one single-photon-counting detector as a simple scheme with moderate time resolution and nonlinear interferometry featuring a very high correlation time resolution (see Chapter 3).

Besides being an indispensable tool in quantum optics for coincidence correlation and anti-bunching analysis, there are some applications related to  $g^{(2)}(\tau)$ -measurements. In life science microscopy, time-correlated single-photon-counting (TCSPC) techniques are widely used, e.g. for fluorescence correlation spectroscopy (FCS) as an analysis tool for the characteristic fluorescence intensity fluctuations, diffusion and concentration of detected fluorescent molecules. The strength and the duration of temporal auto-correlation signals are linked to the average number, the average volume and the average diffusion time through a volume. Also, biochemical parameters such as the concentration, the size and the shape of particles can be determined [14]. Further related applications are fluorescence lifetime correlation spectroscopy and fluorescence cross-correlation spectroscopy [44]. Apart from fluorescence application, intensity correlation measurements are generally carried out by light scattering techniques such as dynamic light scattering (DLS) [45] and diffusing wave spectroscopy (DWS) [46]. The size, the weight, the shape, the diffusion and the charge of nanoparticles, polymers and proteins can be addressed within the context of micro-rheology but also for emulsions, solutions, gels, colloidal or foaming environments [47]. Moreover, intensity correlations and intensity-noise properties of light sources are complementary [48] and therefore quantum noise can be assessed by  $g^{(2)}(\tau)$  measurements [49]. Also, a second-order OCT system has been proposed for improved OCT performances based on the detection of intensity instead of field cross-correlations [50]. Needless to say, ghost imaging is a straight application of intensity correlations as those form the image signal, as will be presented in detail in Section 2.2.

A brief discussion about higher-order temporal correlations and their detection is presented hereinafter due to its relevance for higher-order ghost imaging in Chapter 5.1.

### 2.1.3. Higher-order temporal auto-correlations

Deduced from Eq. (1), pure temporal auto-correlations are given by

$$g^{(j)}(t, \tau_1, \dots, \tau_{j-1}) = \frac{\langle \vec{E}^*(t) \vec{E}^*(t + \tau_1) \dots \vec{E}^*(t + \tau_{j-1}) \vec{E}(t) \vec{E}(t + \tau_1) \dots \vec{E}(t + \tau_{j-1}) \rangle}{\langle \vec{E}^*(t) \vec{E}(t) \rangle \langle \vec{E}^*(t + \tau_1) \vec{E}(t + \tau_1) \rangle \dots \langle \vec{E}^*(t + \tau_{j-1}) \vec{E}(t + \tau_{j-1}) \rangle} \quad (21)$$

$$= \frac{\langle I(t) I(t + \tau_1) \dots I(t + \tau_{j-1}) \rangle}{\langle I(t) \rangle \langle I(t + \tau_1) \rangle \dots \langle I(t + \tau_j) \rangle}.$$

In general, the  $j$ -th order temporal auto-correlation function refers to higher *intensity* correlation orders involving an amount of  $j$  intensities within the auto-correlation term (nominator) and exhibiting  $j - 1$  time delays among each other. Therefore, Eq. (21) is sometimes called the  *$j$ -time intensity auto-correlation function*. For a correct radiometric definition, an appropriate factor relates the electric field and the intensity of a light field by [24, 51]

$$I(t) = 2\varepsilon_0 c |\vec{E}(t)|^2 \quad (22)$$

with the vacuum permittivity  $\varepsilon_0$ . Due to the normalization (see denominator of Eq. (21)), these proportionality factors cancel out. If additionally, stationarity for the intensity signals as well as equal intensity values are valid, Eq. (21) reduces to

$$g^{(j)}(\tau_1, \dots, \tau_{j-1}) = \frac{\langle I(t) I(t + \tau_1) \dots I(t + \tau_{j-1}) \rangle}{\langle I(t) \rangle^j}. \quad (23)$$

For the two special cases of classical light, already discussed in the previous section, the central higher-order coherence degrees are [34]

$$g_{coh}^{(j)}(\tau_1, \dots, \tau_{j-1} = 0) = 1 \quad (24)$$

for coherent light and [52]

$$g_{th}^{(j)}(\tau_1, \dots, \tau_{j-1} = 0) = j! \quad (25)$$

for fully polarized, single-mode thermal light. By extending the intensity interferometer (Figure 3) to  $j$  optical paths with an equivalent number of detectors and correlator input channels,  $g^{(j)}(\tau_1, \dots, \tau_{j-1})$  is experimentally accessible. While a schematic diagram of such an interferometer is shown in Figure 4 (left), an alternative measurement scheme is depicted on the right-hand side of Figure 4. It represents a two-detector intensity interferometer only, however, the detector signals  $I_1(t)$  and  $I_2(t)$  measured by  $D_1$  and  $D_2$  are registered individually and synchronously. This could be implemented either by time-tagging modules acquiring photon count time traces or by a synchronized detector read-out. This means that two-time higher-order auto-correlations can be calculated by

$$G^{(l,m)}(t, t + \tau) = \langle I_1^l(t) I_2^m(t + \tau) \rangle \quad (26)$$

with arbitrary order  $(l, m)$ <sup>5</sup>. Care must be taken, when comparing this definition to the more common higher-order correlation expressions of Eq. (21) and (23). In particular,  $g^{(j)} \equiv g^{(l=j/2, m=j/2)}$  with an exclusively valid correspondence for even correlation orders  $j$  [53].

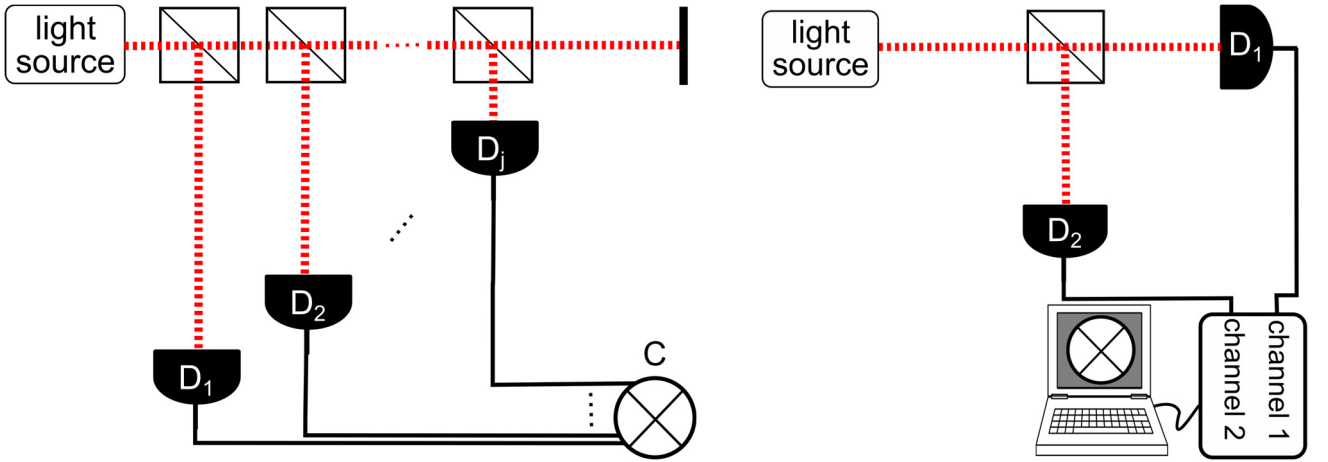


Figure 4. **Detection schemes for determining higher order temporal correlations.** Left:  $j$  detectors connected to a correlator unit for measuring the  $j$ -th order correlation function with  $j - 1$  time delays. Right: Two detectors connected to a time-tagging unit acquiring individually and synchronously the photon count time-traces. The  $j$ -th order correlation function with one time delay are evaluated by calculation.

<sup>5</sup> In principal, the two-time higher-order auto-correlations  $G^{(l,m)}(t, t + \tau)$  can be determined by a single detector. After having measured  $I(t)$  with a single detector, Eq. (26) can be evaluated. However, the dead-time and the integration time of even fast detectors restrict the applicability to light of long coherence times only. Modern time-tagging modules offer far better timing resolution for  $\tau$  as well as real-time  $G^{(l,m)}(t, t + \tau)$  monitoring options which is not feasible with a one-detector system. Note that a multi-pixel CCD camera yielding appropriately fast frame rates with respect to the coherence time can replace the two-detector spatial intensity interferometer. By measuring time-resolved intensity profiles  $I(\vec{r}, t)$ , the same argument holds as above including the space variable. Thereby, the transverse coherence length  $\sigma_c$  can be determined experimentally with one single camera [29]. Again, this method is only practical if the coherence time is slower than the CCD frame rate.

---

Applications of higher-order temporal correlations are closely linked to second-order correlation applications (see application discussion in the previous section). However, they are not routinely measured, even though they can reveal new information or better correlation visibility, in part because of the added experimental complexity (see Figure 4) [54].

This introductory section about some fundamentals on the correlations of light with special focus on second-order and higher-order temporal auto-correlations is now followed by a comprehensive introduction of the key topic of the thesis: Ghost Imaging.

---

## 2.2. Ghost Imaging

The ghost imaging (GI) phenomenon is the principal object of this thesis. This chapter gives a brief historical background as well as an introduction to the main classical physics of the field. Moreover, the current research status is outlined focusing on established GI detection methods and state-of-the-art GI light sources.

**Introduction.** A “ghost image” is obtained by measuring the total intensity of the transmitted or reflected light of an illuminated object and the spatially resolved intensity of a highly-correlated reference beam which itself does not interact with the object. The information of both intensities alone is not enough to form an image of the object. However, image reconstruction can be achieved by correlating the two intensities. Intriguingly, spatial resolution is achieved by the non-interacting reference beam.

The ghost imaging (GI) phenomenon has been demonstrated originally with entangled photon pairs from a parametric down-conversion (PDC) source [15]. Whereas a transmission mask was illuminated by signal photons, the beam path of the idler photons was spatially resolved by a scanning fiber. The correlations between the detector signals of the signal and the idler beam path using a coincidence count circuit, resulted in the first ghost image. Due to the use of non-classical light, the GI phenomenon was initially claimed to be a pure quantum effect. However, already at that time, it was suggested that *some type of classical source could be imagined* that is able to mimic this type of imaging behavior [15].

It was in 2002 that a ghost imaging experiment was achieved by using classical angularly correlated laser pulses [16]. Quickly, other experimental realizations followed [55] using pseudo-thermal light [56, 18, 57] and even spectrally filtered hollow cathode lamps [58, 59]. The latter was claimed to be *truly* thermal in the sense that thermal statistics - or classical photon-bunching - was directly emitted by the source. However, as only a marginal number of atomic emission lines were contributing, a considerable degree of first-order coherence was present (see Eq. (7)). Indeed, the optical power spectrum of *true* thermal radiation obeys a Planck distribution with very large optical bandwidths.

These GI experiments by classical light engendered an intense debate on the physical origins, whether GI with thermal light can be considered as a quantum effect due to the superposition between indistinguishable two-photon alternatives, or rather as a classical effect due to the statistical correlation of intensity fluctuations [60, 61, 62, 63, 64, 65, 66, 67]. The debate was kind of a revival of the basic question about the quantum-ness of photon-bunching from thermal light and its enhanced intensity correlations. One of the emerging aspects from sometimes controversial discussions, was that GI takes place in the near-field of a light source rather than in the far field as for the original HBT experiment. Still today, open questions about the quantum aspect of thermal light in correlation experiments remain [68]. Experimentally, there have been numerous approaches to GI studying (i) fundamental aspects in close connection to the above-mentioned theories, [57, 18, 56, 68, 29, 69] as well as (ii) experimental parameters such as visibility, resolution, polarization, and coherence length dependencies regarding also the connection between GI and ghost diffraction [69, 70, 71, 72, 73, 74]. This intense period on fundamental research lead to a profound gain of knowledge in the field by recognizing both, a quantum non-local two-photon interference description as well as an intensity-fluctuation correlation interpretation of lensless pseudo-thermal GI [64].

In the following, a classical introduction to the functional principle of GI shall suffice in order not to go beyond the scope of the thesis. This is also justified by the fact that the main results of this thesis regarding GI, are built on the exploitation of classical light sources with light fields of very high photon numbers. And beyond, the here proposed novel GI experiment (Section 5.2 and 5.3) aims to even excel the degree of classicality in state-of-the-art GI by introducing totally incoherent light.

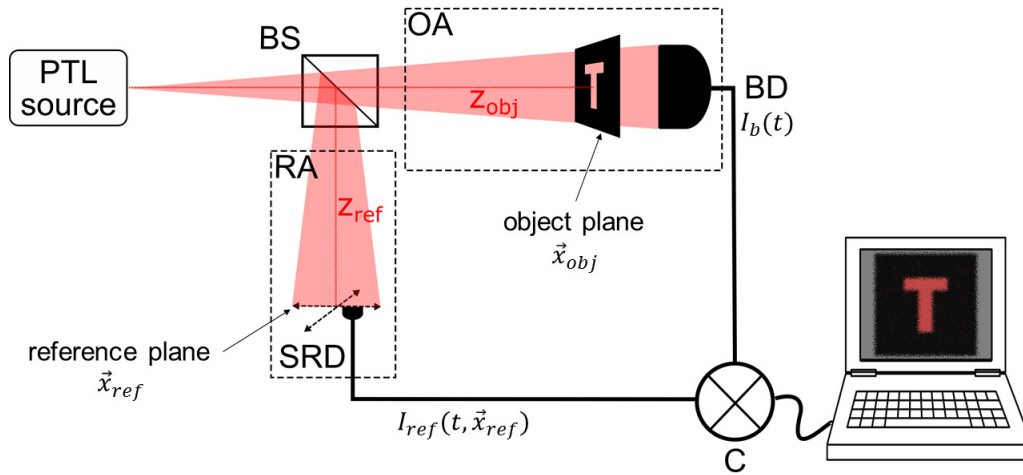


Figure 5. Typical schematics of a classical GI experiment using a pseudo-thermal light (PTL) source and a spatial HBT configuration with a beamsplitter (BS), the object arm (OA) comprising the object and the bucket detector (BD), the reference arm (RA) comprising the spatially resolving detector (SRD) and finally the correlator (C).

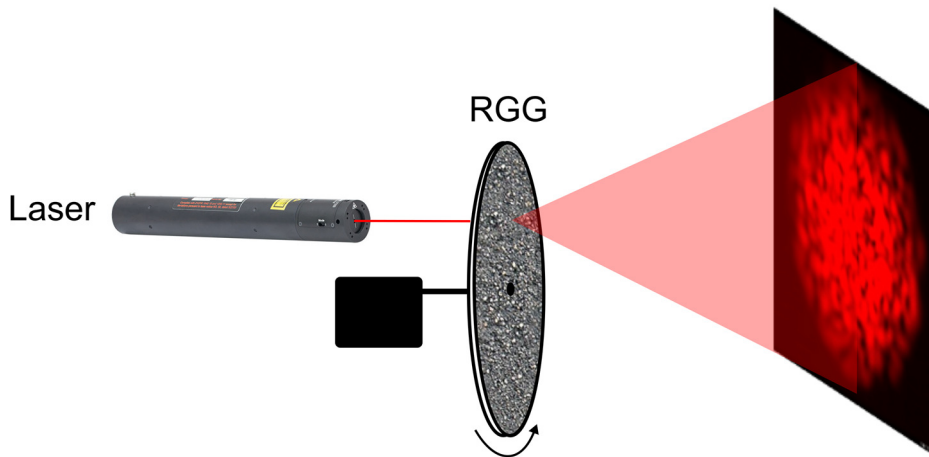


Figure 6. Schematic of the pseudo-thermal light source. Here, a He-Ne laser is depicted illuminating a rotating ground glass (RGG) which leads to the generation of speckle patterns in a specific far-field plane.

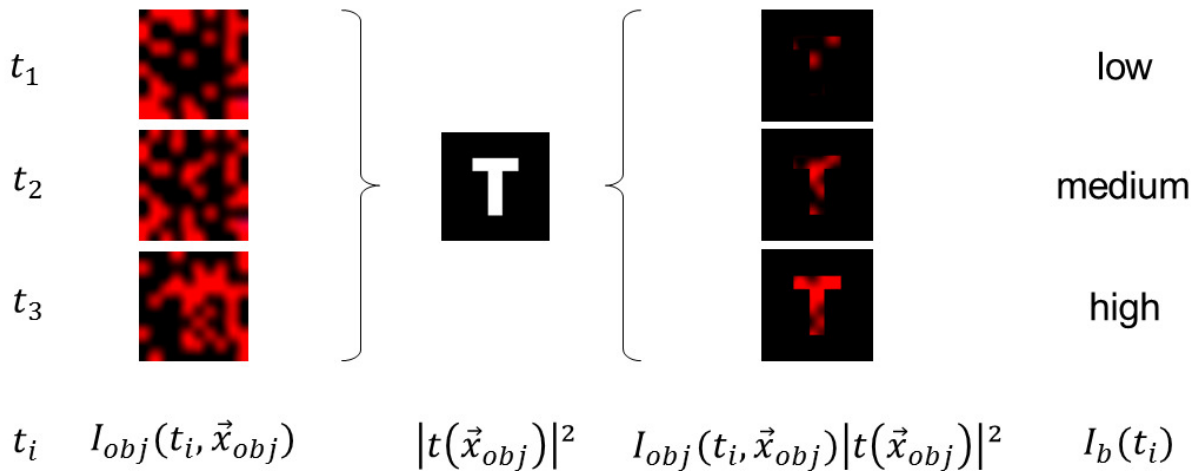


Figure 7. Illustration of the speckle pattern transmission in the object arm. Three possible speckle patterns generated at times  $t_i$  are impinging with an intensity distribution  $I_{obj}(t_i, \vec{x}_{obj})$  onto a transmission mask with the field-transmission function  $t(\vec{x}_{obj})$ . Behind the mask, different levels of intensity are recorded by the spatially integrating bucket detection  $I_b(t_i)$ . Further propagation effects between the object and the bucket detector are neglected such that Eq. (28) holds strictly.

### Classical ghost imaging.

Figure 5 is a typical schematic drawing of a classical GI experiment. It comprises a *pseudo-thermal* (PT) light source [75] consisting of highly coherent laser light and a rotating ground glass (RGG) (Figure 6). This light source generates random light spot patterns in the far field of the source plane (ground glass plane) due to random diffraction of the impinging laser light at the granularity of the glass surface; e.g. [76, 77]. The size of these random light spots  $\sigma_c$ , also called speckles, can be calculated by the well-known VCZ-theorem [27, 26] if the light spot  $D_0$  on the ground glass is considerably larger than the grain size and if the grain size is in the range of the wavelength  $\lambda$ . The commonly used approximation is expressed by [29]

$$\sigma_c = \frac{\lambda z}{D_0}, \quad (27)$$

where  $z$  denotes the distance from the scattering plane. The speckle patterns are split by a beam splitter generating two statistically highly correlated light beams. One of the beams is projected onto the targeted object with an intensity distribution  $I_{obj}(t, \vec{x}_{obj})$ . In Figure 5, a transmission mask with a field object transmission function  $t(\vec{x}_{obj})$  [78] serves as a representative object yielding a step function with values between 0 and 1. However, note that the following physics are also valid for a configuration with reflective and non-binary objects. For this exemplary scenario, the transmitted light is collected by a single detector, the so-called *bucket* detector, which signal is<sup>6</sup>

$$I_b(t) = \int I_{obj}(\vec{x}_{obj}, t) |t(\vec{x}_{obj})|^2 d\vec{x}_{obj}. \quad (28)$$

It is assumed that the near-field of the object is imaged onto the spatially integrating bucket detector. The bucket signal can obviously not form an image of the object, as it holds only a single-pixel information  $I_b(t)$  (Eq. (28)). However, keep in mind that the object information  $|t(\vec{x}_{obj})|^2$  leads to a specific value of  $I_b(t)$  at the bucket detector. In the opposite arm, the so-called *reference arm*, sometimes referred to as the *test arm*, the speckle pattern is spatially resolved, e.g. by a scanning detector. The recorded reference intensity  $I_{ref}(t, \vec{x}_{ref})$  is then correlated with the bucket signal, resulting in

$$\begin{aligned} GI(\vec{x}_{ref}) &= \langle I_{ref}(t, \vec{x}_{ref}) I_b(t) \rangle = \left\langle \int I_{ref}(t, \vec{x}_{ref}) I_{obj}(t, \vec{x}_{obj}) |t(\vec{x}_{obj})|^2 d\vec{x}_{obj} \right\rangle \\ &= \int \langle I_{ref}(t, \vec{x}_{ref}) I_{obj}(t, \vec{x}_{obj}) \rangle |t(\vec{x}_{obj})|^2 d\vec{x}_{obj}. \end{aligned} \quad (29)$$

Supposing that  $I_{ref}(t, \vec{x}_{ref})$  and  $I_{obj}(t, \vec{x}_{obj})$  are identical intensity distributions  $I_{ref}(t, \vec{x}_{ref}) = I_{obj}(t, \vec{x}_{obj}) = I(t, \vec{x})$ , i.e. no magnification nor distortion are present within the reference and the object paths, Eq. (29) can be rewritten as

$$GI(\vec{x}_{ref}) = \int \langle I(t, \vec{x}_{ref}) I(t, \vec{x}_{obj}) \rangle |t(\vec{x}_{obj})|^2 d\vec{x}_{obj} \quad (30)$$

Thus, the intensity-intensity correlations between the bucket signal and the spatially resolved reference signal retrieves the previously *lost* object information by the spatial integration of the bucket detector, even though the reference arm has never seen the object. This is specifically the reason for the established wording *ghost image*, although the term can be misleading when recognizing that neither of the two detectors can form an image of the object on its own. Eq. (29) and Eq. (30) reveal that the cross-correlations between the intensity distribution of the object- and the reference arm are critical to the visibility of the object information in the ghost image  $GI(\vec{x}_{ref})$ . The brackets  $\langle \rangle$  denote the ensemble average over space and time. This indicates the need of a large number of random pattern realizations

<sup>6</sup> Here, the notation  $d\vec{x}_{obj}$  and more generally  $d\vec{x}$  denote the increments of a surface integral, which is used consistently throughout the thesis. Therefore,  $\int f(\vec{x}) d\vec{x}$  is a surface integral of the form  $\iint f(\vec{x}) dx dy$ . It must not be confused with a line integral.

in order to reconstruct the ghost image accurately. An illustrative way to understand the image formation functionality, is depicted in Figure 7. There, three different speckle patterns are depicted - producible by rotating the ground glass of a PT light source (Figure 6) - together with a transmission mask of the letter  $T$  as well as the transmitted shape of the patterns. The latter visualizes the amount of light that the bucket detector is exposed to. The bucket detector measures various levels of intensity depending on the *similarity* of the actual speckle pattern and the object. The bucket signal  $I_b(t)$  thus serves as a weighting of the *test* patterns. By averaging over an ensemble of test patterns, the object information is finally retrieved.

**Coherence properties of a ghost imaging light source.** Furthermore, Eq. (30) shows that specific intensity cross-correlations between the object- and the reference plane must hold for GI. The correlations

$$G^{(2)}(\tau = 0, \vec{x}_{ref}, \vec{x}_{obj}) = \langle I(t, \vec{x}_{ref}) I(t, \vec{x}_{obj}) \rangle = \langle I(t, \vec{x}_{ref}) I(t, \vec{x}_{ref} + \Delta\vec{x}) \rangle \quad (31)$$

must not take a constant value. Otherwise, Eq. (29) wouldn't comprise any spatial dependency and hence, no ghost image is formed. Let's consider a *lensless* GI configuration [79, 80] as shown in Figure 5. Neither magnification, nor attenuation or distortion disturb the propagation of the two equally split light fields towards the imaging planes which are located equally far from the source plane  $z_{ref} = z_{obj}$ . Consequently, the cross-correlation function of Eq. (31) corresponds to the light source intensity auto-correlation function having propagated to the imaging planes. This function becomes constant if no enhanced correlations exist for any displacement  $\Delta\vec{x} = \vec{x}_{obj} - \vec{x}_{ref}$  resulting in  $\langle I(t, \vec{x}) \rangle \langle I(t, \vec{x} + \Delta\vec{x}) \rangle = \langle I \rangle^2$  being the square of the mean intensity. In order to enable image reconstruction by the GI protocol (Eq. (29)), the light field must yield locally enhanced intensity correlations. Therefore, two conditions on the coherence of light must apply:

1. Temporal *incoherence* in second-order such that enhanced correlations are present at a fixed position  $\vec{x}$ :

$$G^{(2)}(\tau, \vec{x}) = \langle I(t, \vec{x}) I(t + \tau, \vec{x}) \rangle \geq \langle I \rangle^2 . \quad (32)$$

In terms of photon statistics, the classical light source must not follow a Poissonian distribution. A minimum level of photon-bunching is mandatory [81]:

$$g^{(2)}(\tau = 0) > 1 . \quad (33)$$

2. Spatial *incoherence* such that Eq. (32) is only locally valid ( $\Delta\vec{x} = 0$ ). In other terms, a finite size of the spatial width of the cross-correlation term (Eq. (31)) is needed for preventing a covering of the transmission function  $t(\vec{x}_{obj})$  in Eq. (29) and Eq. (30):

$$G^{(2)}(\tau = 0, \Delta\vec{x}) \geq \langle I \rangle^2 \quad (34)$$

with

$$\lim_{|\Delta\vec{x}| \rightarrow \infty} \{G^{(2)}(\tau = 0, \Delta\vec{x})\} = \langle I \rangle^2 . \quad (35)$$

Enhanced correlations thus reduce close to  $\langle I \rangle^2$  for  $\Delta\vec{x} > \sigma_c$  where  $\sigma_c$  is the transverse coherence length [29]. This also means that  $\sigma_c$  must be equal or smaller than the object features to be resolved in the ghost image. The corresponding coherence area,  $A_c \propto \sigma_c^2$ , represents the minimum *pixel size* in GI [53].

### Speckle statistics of pseudo-thermal light.

The PT light source was invented by Martienssen and Spiller in 1964 at the Physikalisches Institut der Universität Frankfurt am Main. This quasi-thermal, quasi-monochromatic light was specifically developed for fundamental investigations *concerning the relations between coherence and fluctuations* [75]. This paragraph explains briefly why speckle patterns generated by PT light sources (Figure 6) fulfill the above stated coherence conditions.

Located at a specific far-field plane, a speckle pattern can be considered as a random interference pattern caused by the diffraction of coherent laser light focused onto the rough surface of a ground glass. Ideally, subsequent speckle patterns induced by the rotation of the ground glass are completely independent. In this case, the amplitude  $E$  and the phase  $\theta$  of the EM wave of individual speckles vary randomly. Therefore, also the intensity of the speckles evolves randomly in time. The electric field of a single speckle  $\vec{E}(t)$  results from the interference of an ensemble of  $N$  EM waves generated at different scattering positions in the diffusive plane [82]:

$$\vec{E}(t) = E e^{i\theta(t)} \vec{e} = \frac{1}{\sqrt{N}} \sum_{n=1}^N E_n e^{i\phi_n(t)} \vec{e}_n \quad (36)$$

where  $\vec{e}$  is the unit vector defining the field polarization. Under the above-mentioned conditions,  $\vec{E}(t)$  can be described by a two-dimensional *random walk* [82]. With the large number assumption, the amplitude  $E$  obeys a Rayleigh distribution and independently, the phase  $\theta$  is uniformly distributed. The resulting intensity fluctuations follow an exponential distribution

$$p(I) = \frac{1}{\langle I \rangle} e^{-I/\langle I \rangle} \quad (37)$$

with statistical moments expressed by

$$\langle I^j \rangle = \langle I \rangle^j j! . \quad (38)$$

Using Eq. (37) and (38), it can be quantified how well the GI coherence conditions are fulfilled by ideal PT light. Indeed, thermal statistics prevail which can be understood by recalling the Siegert-relation [83]:

$$\begin{aligned} G^{(2)}(\tau) &= \langle I(t) \rangle \langle I(t + \tau) \rangle + |G^{(1)}(\tau)|^2 \\ \Rightarrow G^{(2)}(\tau = 0) &= 2\langle I \rangle^2 , \end{aligned} \quad (39)$$

which coincides with the second statistical moment of Eq. (38). In particular, Eq. (39) takes twice the value of vanishing correlations, which is the classical limit of photon-bunching. The Siegert-relation is not only valid for the time domain but also for the space domain, expressed by

$$G^{(2)}(\Delta\vec{x}) = \langle I(\vec{x}) \rangle \langle I(\vec{x} + \Delta\vec{x}) \rangle + |G^{(1)}(\Delta\vec{x})|^2 . \quad (40)$$

If isotropy as well as a uniform illumination are assumed such that  $\langle I(\vec{x}) \rangle = \langle I \rangle$  for every position in the imaging planes, a global coherence area can be calculated according to

$$A_c = \int \frac{|G^{(1)}(\Delta\vec{x})|^2}{|G^{(1)}(0)|^2} d\Delta\vec{x} . \quad (41)$$

In the picture of random speckle pattern generation, the coherence area is a measure for the mean speckle size with  $\sigma_c \propto \sqrt{A_c}$ .

### Ghost imaging detection and application.

Regarding the measurement of the intensity correlation signals, the GI coherence conditions which could be put at disposal by the just discussed speckle statistics of a PT light source, imply that

- the time resolution of the detection system must be adapted to the coherence time  $\tau_c$ . As Eq. (32) takes a maximum at equal timing (i.e.  $\tau = 0$ ) and vanishes on the timescale of  $\tau_c$ , an appropriate time resolution must be ensured in order to register properly prevailing enhanced intensity correlations<sup>7</sup>.
- the reference detector should yield a minimum spatial resolution of  $\sigma_c$ . In case of a detector scanning procedure, the scanning aperture must be adjusted or in case of a CCD camera, the pixel size must be chosen accordingly<sup>8</sup>.

Note that the explanatory approach of spatio-temporal correlations in GI can be generalized to more complex, lens-based GI configuration considering impulse response functions of the speckle fields propagating through the optical system [84]. Also, the GI signal definition (Eq. (29)) represents the most basic GI detection protocol which is based on the classical definition of the intensity-intensity correlation function [52, 34]. There are several different definitions of the GI signal based on other GI detection protocols such as differential GI [85], polarimetric GI [86], higher-order GI [53, 87], DC-analog block detection [60], positive-negative correlation detection [88], to name a few, all aiming to enhance imaging performances such as the visibility and the resolution in specific GI scenarios.

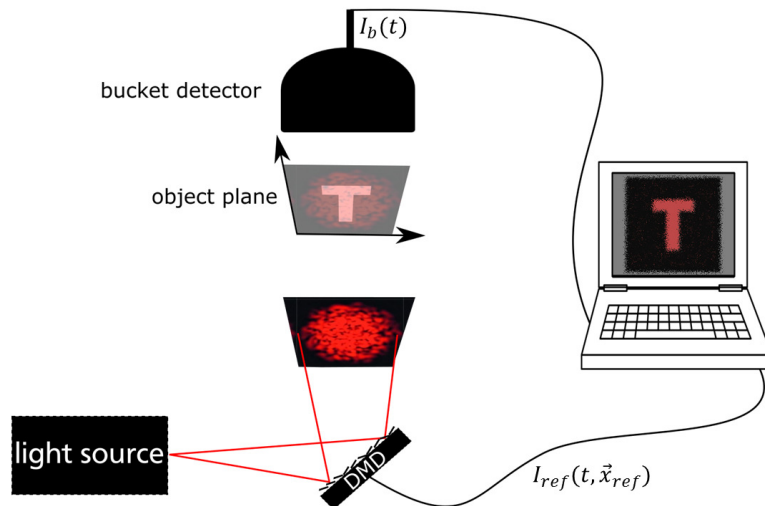


Figure 8. **Schematics of a computational ghost imaging scheme.** A light source illuminates here a digital micro-mirror device (DMD) which produces random light spot patterns guided onto an object. Correlations between the pre-computed random patterns and the single-pixel bucket detector signal are computed to form a ghost image.

Over the past years, a lot of effort has been invested in finding GI applications with advantageous imaging properties. In a certain sense, GI *decouples* the spatial resolution from the object. This offers the possibility for imaging in a harsh environment where environmental conditions (e.g. vacuum [89], industrial processing, biological or even living surrounding [20]) impede the placement of imaging optics near the object. GI is also promising for imaging through turbulent media via more robust intensity correlation signals in certain scattering regimes [90, 91, 92]. Alongside, *computational* GI was developed which relies on artificially generated spatially random beam patterns, e.g. by illuminating a spatial light modulator [93, 94] or a digital micro mirror device (DMD). Figure 8 shows a generic schematic of a computational GI configuration. Light impinges on a DMD which generates random light

<sup>7</sup> There is previous work on how the detection bandwidth can be smaller than the modulation speed of artificially generated speckle patterns [232].

<sup>8</sup> Using compressive sensing techniques, this condition can be circumvented up to a certain level [109]

spots using an appropriate algorithm [95, 96]. These patterns are guided onto the targeted object and just as in Figure 5, the totally transmitted (or reflected) light is collected onto a single-pixel bucket detector. The knowledge about the spatial intensity distribution of the pattern, set by the DMD mirror position, makes the reference arm obsolete. Closely connected to computational and compressed sensing methods [97, 98, 99], this concept enables single-pixel camera systems which considerably reduce the complexity of the detection setup.

Although numerous GI experiments have been demonstrated with modified (or expanded) configurations and advanced detection protocols, all of them build upon the following two basic *state-of-the-art GI detection schemes*:

- the spatial HBT scheme with two detectors - one bucket and one spatially resolving reference detector located at the object and the reference plane, respectively - followed by a coincidence count unit or synchronous signal acquisition with subsequent correlation evaluation.
- the computational approach using artificially randomized light and post-computed correlations between the signal of a single-pixel bucket detector and the precomputed spatial patterns.

Moreover, the strive towards a real-world application has led to several proof-of-principle demonstrations such as GI LIDAR [100], ghost holography [101], GI microscopy [102], GI using sunlight [103, 104], GI with adaptive imaging techniques [105], temporal GI [106, 107, 108], compressive GI for high image resolutions [109], image encryption based on a GI protocol [110], GI using atoms [111], fluorescence GI [112], to name a few. Very recently, calibration-free ellipsometry for homogenous thin films and interfaces has been proposed based on a GI scheme [113].

#### **State-of-the-art ghost imaging light sources.**

One major goal of this thesis is the expansion of state-of-the-art GI light sources. Therefore, an overview of existing light sources is given by Table 1.

As this thesis deals with classical GI, this overview is limited to one example of a quantum light source taken from the very first GI experiment [114, 15]. There, a type-II phase-matched spontaneous parametric down conversion (SPDC) source consisting of laser light (pump) and a nonlinear crystal produced orthogonally polarized signal and idler beams. The frequency-entangled photon pairs are propagating in a different direction with respect to the incoming laser beam and two photons of the same pair exhibit an angle of opposite sign. When the signal and the idler photons arrive at the same time at their corresponding imaging plane, enhanced coincidence probabilities are measured ( $g^{(2)}(0) > 1$ ). The quantum nature of the source becomes apparent for a three-detector coincidence experiment. There, anti-bunched intensity correlations are observed ( $g^{(2)}(0) < 1$ ).

The first classical GI light source consisted of a continuous wave laser source and a rotating mirror placed on a galvanometer. This pseudo-random deflection together with an asynchronously operated chopper-wheel (with respect to the galvanometer) generated angularly correlated laser *pulses*. With this light source, the first classical counterpart of quantum ghost imaging and quantum ghost diffraction was demonstrated [16, 55].

Very quickly, the PT source was established in classical GI experiments; e.g. [56, 18, 57]. As already introduced in this chapter, laser light is focused onto a rotating diffusing element (transmitting ground glass or diffuse reflector). The angular velocity  $\omega_r$  of the rotating diffuser determines the rate at which the speckle patterns change, which can yield mHz or even below if required. The upper limit is given by the motor capability which no more than a few kHz for conventional DC motors. The coherence time of PT sources can be approximated by [115]

$$\tau_c = \frac{\omega_0 \sqrt{\pi}}{r \omega_r} \quad (42)$$

---

with the focus radius  $\omega_0$  and the distance of the focus  $r$  from the rotation center<sup>9</sup>. The PT intensity correlations can reach the ideal thermal value of  $g^{(2)}(0)=2$ ; however often, residual ballistic photons and other scattering issues reduce that value considerably. The use of laser light ensures good brightness per spatial mode (speckle cell). Moreover, the control of the amount and the size of speckles as well as the coherence time, makes this type of GI source attractive for laboratory use. One challenge for high-resolution imaging with PT light, i.e. exploiting a high number of speckle cells from the pattern, consists in ensuring the uniformity of the intensity distribution.

The concept of light sources for computational GI has already been introduced in this chapter. The SLM or DMD based PT light generation has several advantageous. Firstly, high resolution can be achieved by choosing a device with high pixel amount. DMDs are constantly developed by projector technologies (e.g. Digital Light Processing, DLP technology by Texas Instruments) and thus high-tech devices are available at reasonable prices. Uniformly distributed, random square-shaped patterns can be easily generated. The binary modulation rate can reach several kHz. The key advantage is the non-necessity of measuring the spatial distribution in a reference arm. The intensity of the bucket detector signal is recorded separately with a time resolution matching the pattern modulation rate. Post-computing of the correlations between the known intensity distribution of the random patterns and the bucket intensity produces the ghost image. Computational light sources offer great adjustability of the light source parameters by SLM or DMD control. Since the correlations are evaluated after the signal acquisition (in contrast to electronic coincidence count units), the coherence time is purely depending on the random modulation speed regardless of the light source coherence properties of the impinging light. A wide range of wavelengths is accessible due to the use of mirrors in DMDs (visible spectral range). The liquid crystal technology offers the possibility to extend that range from the UV up to the long wavelength infrared regime of several tens of  $\mu\text{m}$  in terms of wavelength.

Finally, there are several demonstrations of GI using *truly* thermal light. In a first case, hollow-cathode-lamps were used where the resonance lines in the near-infrared (NIR) were spectrally filtered [58, 79]. The large source size was exploited for the required spatial incoherence. The brightness per solid angle is relatively low for any type of discharge lamp and the demonstrations within Refs. [58, 79] are restricted to a transverse mode number lower than 10. The coherence times in the range of nanoseconds is indeed among the shortest. However, the correlator did not provide enough time resolution and the degree of photon-bunching was extremely low ( $g^{(2)}(0) < 1.1$ ). In this case, the terminology *thermal* is only valid regarding the photon-bunching property, i.e. intrinsic second-order incoherence. However, no *true* thermal radiation, in the sense of the Planck radiation, applies. The implementation of a GI experiment exploiting sunlight does indeed make use of thermal radiation [103, 104]. In this case, sunlight was gathered by a telescope-like collector and subsequently spectrally filtered by a Faraday anomalous dispersion optical filter with a bandpass width of 0.01nm in terms of wavelength. This *true* thermal radiation with *natural* photon-bunching was also made considerably coherent regarding the first correlation order. And beyond, the time resolution of the detection system failed again to gather a high degree of photon-bunching ( $g^{(2)}(0) < 1.05$ ). Obviously, there is a tradeoff between lowering the coherence time of the light source and providing enough time resolution of the intensity correlation detection system. It is also clear from here that no *truly* thermal radiation power spectrum has ever been employed in a GI experiment or in other words: no high first-order temporal incoherence is possible with state-of-the-art GI detection systems.

In this thesis, it is shown how the portfolio of classical GI light sources can be expanded based on opto-electronic emitters. In particular, the *classicality will even be excelled* by increasing step-by-step the degree of incoherence.

---

<sup>9</sup> This approximation holds for Gaussian beam profiles of the laser.

Table 1. Overview of light sources used in Ghost Imaging<sup>10</sup>.

Light source	components	1st order temporal coherence	Degree of photon-bunching	Spatial coherence	Refs	Notes
<b>Spontaneous parametric down-conversion source</b>	Laser + nonlinear crystal	<ul style="list-style-type: none"> <li>• ~GHz</li> <li>• depending on spectral filter and coincidence time window</li> </ul>	<ul style="list-style-type: none"> <li>• Anti-bunched photon pairs</li> <li>• Enhanced photon-photon correlation</li> </ul>	N/A	[114, 15]	Quantum GI light source: Here restricted to one example.
<b>Angularly correlated laser pulses</b>	Laser + mirror on galvanometer	<ul style="list-style-type: none"> <li>• N/A</li> <li>• depending on mirror rotational speed</li> </ul>	<ul style="list-style-type: none"> <li>• N/A</li> <li>• Enhanced angular correlations</li> </ul>	- N/A + high brightness per "spatial mode"	[16]	Pseudorandom deflection of mirror and asynchronous chopper wheel
<b>Pseudo-thermal light</b>	Laser + rotating ground glass	<ul style="list-style-type: none"> <li>• mHz-kHz</li> <li>• depending on motor speed</li> </ul>	<ul style="list-style-type: none"> <li>• medium to high</li> <li>• depending on scattering quality</li> </ul>	+ High and controllable - uniform distribution	e.g. [56, 18, 57, 29]	<ul style="list-style-type: none"> <li>• Most widespread</li> <li>• big range of wavelengths implemented</li> </ul>
<b>Computational sources</b>	Laser or lamp + spatial light modulator	<ul style="list-style-type: none"> <li>• Up to several 10kHz</li> <li>• Device modulation speed dependent</li> </ul>	<ul style="list-style-type: none"> <li>• High</li> <li>• algorithm based</li> </ul>	+ High (pixel amount of device) + uniform distribution	e.g. [93, 94]	• spatial light modulators: SLMs or DMDs
<b>Hollow-cathode-lamp</b>	Lamp + filter	<ul style="list-style-type: none"> <li>• ~GHz</li> <li>• Depending on spectral lines</li> </ul>	<ul style="list-style-type: none"> <li>• Naturally high</li> <li>• Detector time resolution critical</li> </ul>	+ highly incoherent source - low brightness per solid angle	[58, 79]	References show a low degree of photon-bunching, $g^{(2)}(0) < 1.05$
<b>Sunlight</b>	Collector (into MM fiber) + filter (FADOF)	<ul style="list-style-type: none"> <li>• ~10GHz</li> <li>• Spectral filtering: <math>\Delta\lambda = 0.01\text{nm}</math></li> </ul>	<ul style="list-style-type: none"> <li>• Naturally high</li> <li>• Detector time resolution critical</li> </ul>	- relatively low - given by MM fiber	[103, 104]	<ul style="list-style-type: none"> <li>• Telescope sized collector</li> <li>• References show a low degree of detected photon-bunching, <math>g^{(2)}(0) &lt; 1.05</math></li> </ul>

<sup>10</sup> This table should be regarded as an attempt to compare the diverse source implementations in GI. However, there is no claim of completeness in respect of more than 20 years of GI research. For instance, a recent publication on x-ray GI, which reports a special PT source by x-ray synchrotron radiation [266], is omitted in this overview.

### 3. Experimental methods

This chapter is dedicated to a detailed description of the two main measurement methods for determining the second-order coherence degree. First, the photon counting method using a single detector is introduced (Chapter 3.1.) which can retrieve photon number probability distributions  $P(n)$  and the central second-order coherence degree  $g^{(2)}(0)$ . Then, two-photon-absorption interferometry is presented which allows a very high time resolution for measuring the full second-order correlation function  $g^{(2)}(\tau)$  (Chapter 3.2.).

#### 3.1. Determining photon statistics by one single-photon-counting detector

In this part, the experimental method for determining photon number distributions  $P(n)$  based on single-photon-counting detection with one single detector (Figure 9) is presented.

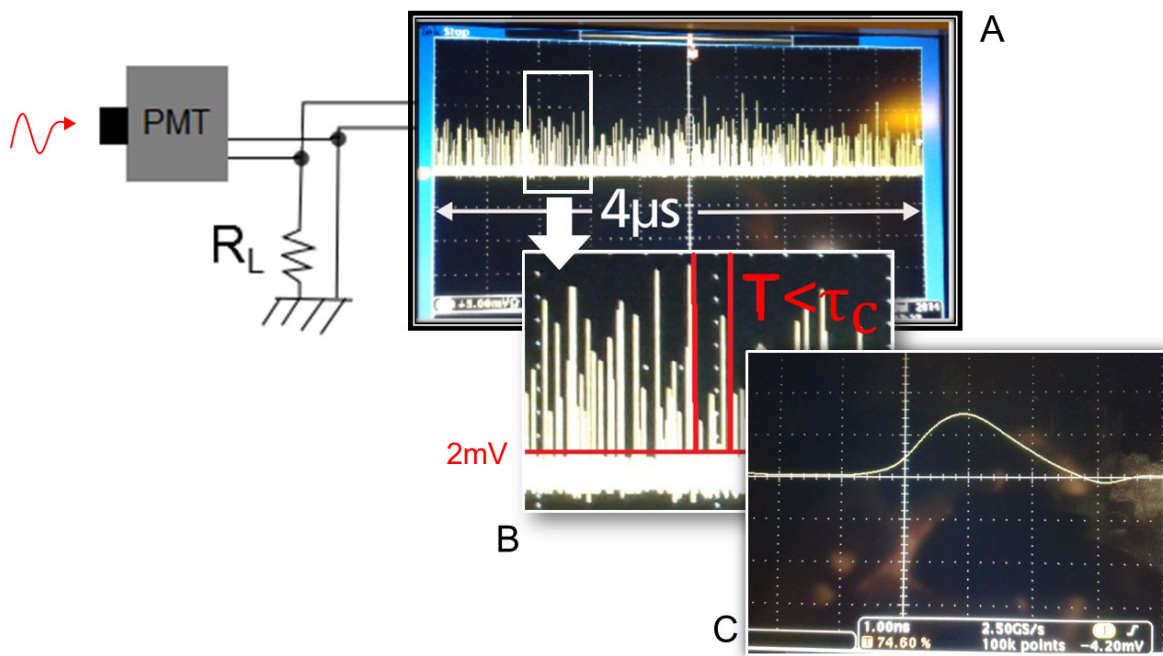


Figure 9. **Diagrammatic scheme of the single-photon-counting detection.** A single-photon-counting detector (Hamamatsu H10330A-45,  $V_{PMT}=700V$ ) is connected to an oscilloscope (TEK 3032, 300MHz (2.5 GS/s)) to acquire single-photon-count time traces (A). A 2mV threshold has a discrimination functionality to minimize the data acquisition by LabView control, which subsequently counts photon counts within a time-binning window  $T$  adjusted to be smaller than the coherence time of the investigated light (B). A magnified picture of the oscilloscope shows a single-photon-count of  $\sim 7mV$  amplitude and 2ns width. The oscilloscope voltage scale is 5mV (C) [116].

**Principle and setup.** The determination of photon number distributions by single-photon-counting is the basis for the GI scheme presented in Chapter 5.1. The probability distribution of photon numbers  $P(n)$  quantifies the statistics of how many photons arrive per time unit. It reflects directly the emission process of a light source. Spontaneous, stimulated and single-photon emission of photons exhibit fundamentally different distributions along the timeline of a specific propagation direction. The most intuitive approach to measure the photon statistics of a light field, is counting single-photon events with a sensitive detector and investigating the recorded photon count time traces.

This is precisely the approach taken here. The following procedures are based on the experimental schemes of earlier work [117, 118]. The implemented single-photon-counting detector is a

photomultiplier tube (PMT, H10330A-45) which yields a high sensitivity at the cost of reduced quantum efficiency (2%) in comparison to avalanche photodiodes. The high sensitivity comes from a high signal gain by multiplication of photo-electrons generated at the photo-cathode which are accelerated towards the PMT-anode, where single-photon signals generate photocurrent pulses. Figure 9 (C) shows an oscilloscope sweep of one single-photon count pulse. It has an amplitude of roughly 7mV and a pulse width of approximately 2ns which coincides with the PMT specifications (rise time + fall time = 2.6ns). The good signal quality – marginal pulse ringing and reasonable pulse heights – proves that the PMT is well suited for counting single-photons.

**Data acquisition and photon number counting.** For recording single-photon count time traces, i.e. acquiring a lot of photon events, which are the data basis for the reconstruction of the photon statistics, a rather simple and instructive approach has been implemented. Photon counts are acquired by reading out multiple oscilloscope traces (Figure 9, A) using an appropriate time span and sample rate in order to resolve every photon count pulse. Then, these time traces are divided into time windows by a time-binning  $T_{bin}$ . Within these time windows, the number of occurring pulses is counted according to a simple LabView-based pulse finding algorithm [116]. Thereby, photon numbers per adjustable time unit can be retrieved.

**Dark counts.** A particularly delicate aspect is that not solely photo-electrons are released when photons impinge on the photocathode inducing the well-known photoelectric effect [119]. Dark counts are generated upon thermally induced electron release due to the low work function of the material at high PMT voltages. Depending on the characteristics of a specific PMT and its operation conditions (voltage, temperature), dark counts can have diversely pronounced properties such as the rate, maximum and minimum amplitude. Figure 10 (left) shows the amplitude distribution in terms of voltage signals measured by an oscilloscope for an illuminated PMT by laser light (black data) and for a light-shielded PMT (closed shutter, red data). One can derive from the overlap of the two measurements in the low voltage range that up to a level of 2mV, solely dark counts are present. This allows setting a discrimination threshold, leaving only data with  $V > 2\text{mV}$  to the analysis. However, even if being much less frequent (at least by a factor of 20), dark counts occur up to a level of  $\sim 8\text{mV}$ . A higher discrimination level would clearly dismiss signal data [120]. Therefore, a dark count correction is implemented considering the actual dark count probability distribution  $P_{dark}(n)$ . Typical dark count statistics are depicted in Figure 10 (right) which obeys a Poissonian distribution, as can be expected [37, 121], here with a mean dark count number of  $\bar{n}_{dark} = 0.43$ . For each measurement, a dark count measurement is conducted and the corrected histogram is retrieved according to the following convolution formula:

$$H_{corr}(n) = \sum_{i=0}^{N_{max}} H(n+i)P_{dark}(i). \quad (43)$$

Thereby, the missing events  $H(n_i)$  of a specific photon number  $n_i$  from the measured histogram  $H(n)$ , due to the addition of dark counts, are recycled.  $N_{max}$  denotes the highest measured number of photons from the histogram  $H(n)$ . Finally, the probability distribution  $P(n)$  is retrieved by normalization:

$$P(n) = \frac{H_{corr}(n)}{\sum_0^{N_{max}} H_{corr}(n)}. \quad (44)$$

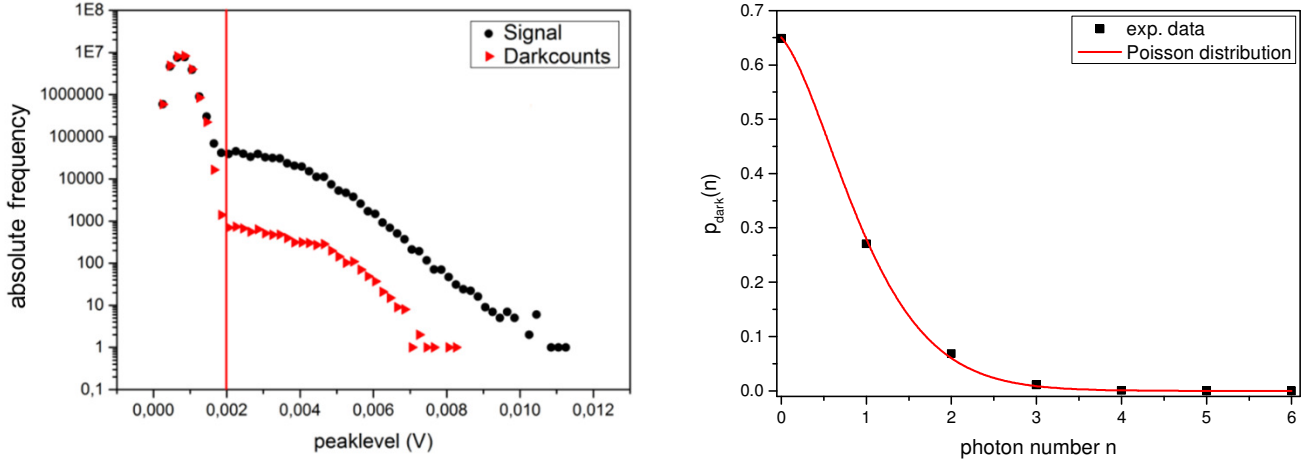


Figure 10. **Dark count analysis.** Left: Voltage distribution when laser light illuminates the PMT (black data) and when the PMT shutter is closed (red data). Right: Dark count probability distribution determined from a closed PMT shutter measurement adjusting  $T_{\text{bin}}=250\text{ns}$  resulting in  $\bar{n}_{\text{dark}} = 0.43$  [116].

**Calculation of the coherence degree.** On the basis of Eq. (44), a photon statistics analysis of the measured light field is possible due to the complete knowledge of the probability distribution of the photon numbers. In particular, the calculation of statistical moments

$$\langle n^m \rangle = \sum P(n) n^m \quad (45)$$

allows one to evaluate the coherence degrees. Using the first and the second moment,  $\langle n \rangle$  and  $\langle n^2 \rangle$ , one can easily derive the central second-order coherence degree (reproduced from Section 2.1.2)

$$g^{(2)}(\tau = 0) = 1 + \frac{\Delta n^2 - \langle n \rangle}{\langle n \rangle^2} \quad (46)$$

with the variance  $\Delta n^2 = \langle (n - \langle n \rangle)^2 \rangle = \langle n^2 \rangle - \langle n \rangle^2$ .

More generally, every central coherence degree of higher-order  $j$  can be calculated [122] according to

$$g^{(j)}(0) = \frac{\sum_n \prod_{i=0}^{j-1} (n - i) P(n)}{[\sum_n n P(n)]^j}. \quad (47)$$

It should be emphasized that having the possibility of extracting arbitrary higher-order coherence degrees with one measurement, represents a strong advantage of this technique. Note that the evaluation of higher correlation orders is limited by the accuracy of the experimental  $P(n)$ . With increasing order  $j$ , Eq. (47) relies on terms of larger photon numbers  $P(n > j)$ . At some point, the calculation of higher-order coherence degrees becomes meaningless as will be demonstrated next.

**Experimentally determined probability distributions.** In order to demonstrate the functionality of the method, two representative measurements are presented and discussed.

Firstly, laser light from a discrete mode semiconductor laser is investigated (Figure 11, left row). The measurement has been performed with a time resolution of  $T_{\text{bin}}=250\text{ns}$  matching the linewidth specifications of the manufacturer ( $\Delta\nu < 2\text{MHz}$  which corresponds to  $\tau_c > 500\text{ns}$ ). A total number of 440000 counting events were registered within a measurement time of 20min. In Figure 11A and Figure 11B, the corrected probability distribution is depicted on a linear scale and on a logarithmic scale, respectively. A good agreement with a Poisson distribution (Eq. (16)) using the experimental mean value

of  $\langle n \rangle = 13.98$  is observed. Figure 11A illustrates the exponential shape of the dark count distribution whereas Figure 11B reveals the precision of the measurement. Below probabilities of  $1 \cdot 10^{-4}$ , the experimental values deviate from the ideal trajectory. This is attributed to the finite number of acquired photon counts, which is especially limited by relatively slow oscilloscope acquisition speed. Note that experimental values of  $P(n)=0$  are left out in the logarithmic graph. The evaluation of the coherence degree as a function of the correlation order  $j$  is shown in Figure 11C. The experimental values are calculated according to Eq. (47) using the data of Figure 11A. Supposing ideal coherent light emitted by pure stimulated emission from a laser source, the Glauber coherence formalism predicts a constant correlation function regardless of the correlation order [34] (compare with Figure 1):

$$g_{coh}^{(j)} = 1 \quad (48)$$

Figure 11C uncovers the accuracy of the measured probability distribution. Whereas  $g^{(j)}(0)$  remains very close to 1 for correlation orders below 5, a considerable false increase is observed up to a level of  $g^{(16)}(0) = 2.03$ . A 5% deviation from Eq. (48) is ensured up to  $j=8$ . In particular, the central second-order coherence degree amounts to  $g^{(2)}(0) = 1.0007$  which is practically unity.

Secondly, PT light is measured. The PT light source is based on the classical concept of coherent laser light being focused onto a RGG plate (compare with Figure 6.). Here, the same semiconductor laser is utilized exploiting the excellent coherence behavior as described above. A commercial sand-blasted transmission diffusor is fixed onto the motor shaft of a DC electric motor which is driven at low speed ( $< 5\text{Hz}$ ) [116]. The RGG plate is located close to the focal point of a lens generating clearly visible randomly distributed speckle spots in the far field. A single-mode (SM) optical fiber selects light from a single speckle cell, which is guided into the PMT. The results of the photon statistics analysis are shown in Figure 11 (right row). A total amount of 22300 photon events were registered and the time resolution has been kept ( $T_{bin} = 250\text{ns}$ ) for the binning procedure. Just like for the laser light analysis, Figure 11D and E display the probability distribution  $P(n)$  on a linear and a logarithmic scale, respectively. Figure 11D illustrates the exponential decay of the thermal statistics behavior of the PT light, which is validated by comparing the data (black squares) with a Bose-Einstein (BE) distribution (Eq. (17)) using the experimentally obtained mean value  $\langle n \rangle = 4.63$ . The logarithmic graph reveals how well the experimental data matches the exponential trajectory for the full range of  $n$ . More and more fluctuation around the BE line is observed for  $n > 20$  when probabilities are below 0.008. Figure 11F pictures the quantitative consequences in terms of higher-order coherence degrees of the PT light. For correlation orders  $j > 6$ , the experimental results deviate at an exponential rate from ideal thermal coherence degrees (Eq. (25)). The 5% accuracy is valid up to  $j=5$ , lower than for the laser light measurement which is due to the lower number of photon counts. Nevertheless, the experimental second-order coherence degree takes a value of  $g^{(2)}(0) = 2.04$ , nicely reproducing the thermal degree of photon-bunching. It is emphasized that the here implemented PT light source is of high quality and simultaneously of remarkable simplicity with respect to the compactness and handling (commercial LD, model construction motor and diffusor). It is not evident that such ideal thermal values of  $g^{(2)}(0) \approx 2$  are experimentally obtained. In practice, often residual ballistic photons have to be eliminated [123] or further randomized [29]. Additionally, the randomization of the incoming coherent light field by the surface scattering of the diffusor does not always obey a random walk, i.e. yielding non-Gaussian scattering processes [83]. Or on the contrary, multiple scattering processes lead to the reduction of the coherence degree [124]. The here implemented, high-quality PT light source will be utilized within the novel classical GI concept in Section 5.1.

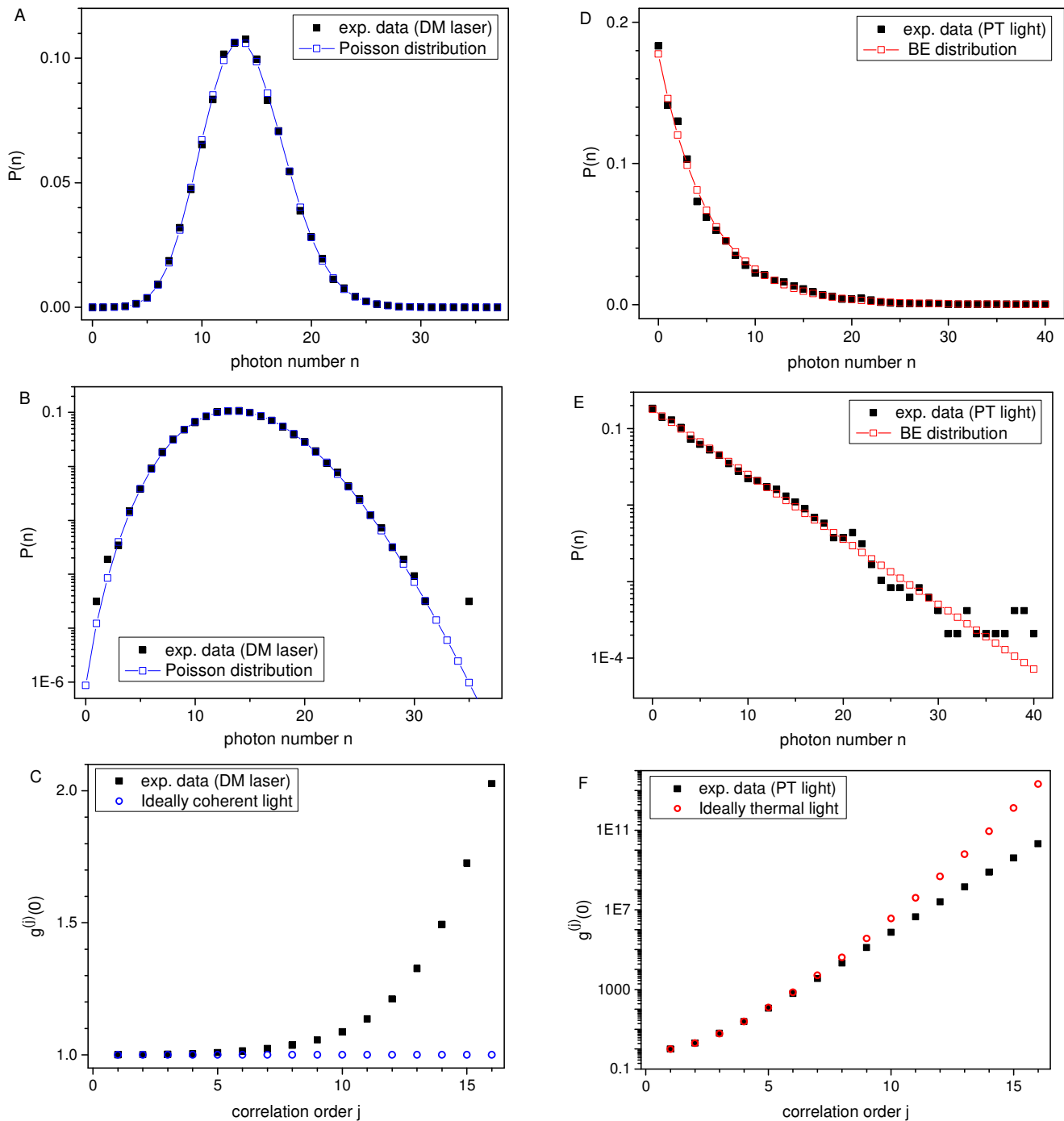


Figure 11. **Exemplary measurements** of (left row, A-C) laser light (discrete mode (DM) diode laser) and (right row, D-F) pseudo-thermal (PT) light. A, B and D, E show measured probability distributions (black data) together with theoretical distributions (red data) of Poisson and Bose-Einstein, respectively. C and F depict the calculated coherence degrees (black data) according to Eq. (47) together with the theoretical values for ideally coherent and ideally thermal light (red data).

---

---

This chapter has introduced the concept of measuring the photon statistics of light by single-photon-counting using one single detector following the methods of [118, 117]. The photon count time traces contain the full information about the temporal correlation behavior of a light field quantified by the photon number probability distribution  $P(n)$ . The knowledge of  $P(n)$  allows one to calculate higher-order coherence degrees  $g^{(j)}(0)$ . The here implemented setup consists of a single-photon-count resolving PMT and an oscilloscope. The precision of the system has been tested by two classical light sources: a coherent semiconductor laser and a laser diode-based PT light source. The dark count consideration on the basis of a convolution-correction has led to a good reproduction of Poisson and Bose-Einstein distribution functions. It can be stated that the accuracy of here implemented direct detection technique based on a single-photon-counting correlation system with one detector is sufficient up to a correlation order of  $j = 5$  within a reasonable measurement time. The precision could be further enhanced by acquiring more photon events at the cost of considerable longer measurement times.

It should be noted that the oscilloscope read-out stands out by its instructive value and its simplicity. Sophisticated time-tagging modules for time-correlated single-photon-counting (TCSPC) applications such as fluorescence lifetime correlation spectroscopy (FLCS) could considerably reduce the measurement time and thus enable much higher precision (see discussion on perspectives in Chapter 6). Due to high costs of such time-tagging electronics, the choice of an oscilloscope read-out solution was taken.

This detection concept is the basis for the GI scheme presented in Chapter 5.1, where PT light with a long coherence time is exploited. The intensity correlation detection method presented in the next section is crucial for measuring the second-order coherence degree of spectrally broadband light utilized for the investigations of ASE emitted by SLDs (Chapter 4) as well as for the GI schemes in Sections 5.2 and 5.3.

### 3.2. Determining intensity correlations by two-photon-absorption interferometry

This section introduces a relatively recent concept for determining experimentally the intensity correlation function of spectrally broadband light based on nonlinear interferometry [9].

**Correlation timescales.** In this context, it is important to recall that the spectral width of a light field  $\Delta\nu$  defines the timescale on which its temporal correlations of any order occur (see Section 2.1.1) by reconsidering Eq. (7):

$$\tau_c = \frac{1}{\Delta\nu} \approx \frac{\bar{\lambda}^2}{c \Delta\lambda} \quad (49)$$

with the central wavelength  $\bar{\lambda}$  and the spectral width  $\Delta\lambda$  in terms of wavelength based on the relationship  $c = \lambda \nu$ .

Table 2 provides an overview of coherence timescales for different spectral widths. As the light sources applied in this thesis exhibit NIR emission, these numerical examples (Eq. (49)) are calculated with an exemplary central wavelength of 1300nm. Additionally, typical semiconductor light sources corresponding to these coherence properties are listed. The kHz linewidth regime can be reached by external-cavity diode lasers (ECDL) with ms coherence timescales which correspond to long coherence lengths of multiple km [125]. The MHz linewidth range exhibits  $\mu$ s correlation timescales and several meters of coherence lengths, which is easily covered by distributed feedback (DFB) laser diodes [126]. Typical Fabry-Pérot (FP) laser diodes yield multiple GHz wide spectra depending on the number of emitted longitudinal modes which together show coherence length of cm-scale reaching spectral widths of sub-nm. Around 1THz, few nm-wide optical spectra show ps coherence times, typically observed for highly MM laser diodes such as broad-area laser diodes. This can already be considered as a broadband semiconductor emitter, i.e. an emitter of large optical bandwidth. Finally, LEDs and SLDs yield emission without longitudinal mode selection. The optical spectra can reach FWHM of 10nm to 100nm corresponding to sub-ps coherence times and  $\mu$ m coherence lengths. These numerical examples emphasize that light with optical spectra as large as several THz, exhibits correlation timescales being orders of magnitude shorter than monochromatic semiconductor emitters of any kind. This justifies the terminology applied throughout the thesis of spectrally *ultra-broadband* light.

Table 2. **Numerical examples of Eq. (49)** illustrating the time and length scales of the temporal coherence depending on the prevailing spectral width of a light field with a central wavelength of  $\lambda=1300$ nm. The column on the far right-hand side mentions a selection of related semiconductor (SC) light sources using the following abbreviations: Whispering gallery mode (WGM), external cavity diode laser (ECDL), distributed feedback diode laser (DFB DL), discrete mode diode laser (DM DL), multimode diode laser (MM DL), light emitting diode (LED) and superluminescent diode (SLD).

Spectral width $\Delta\nu$	Spectral width $\Delta\lambda$	Coherence time $\tau_c$	Coherence length $l_c = c \tau_c$	SC light sources
1Hz	5.64E-12nm	1s	2.998E+8m	WGM ECDL [127]
1kHz	5.64E-9nm	1ms	299.8km	(Actively stabilized) ECDL
1MHz	5.64E-6nm	1 $\mu$ s	299.8m	DFB DL, DM DL
1GHz	5.64E-3nm	1ns	29.98cm	DL
1THz	5.64nm	1ps	299.8 $\mu$ m	MM DL
10THz	56.4nm	100fs	29.98 $\mu$ m	LED, SLD, highly MM DL

A central aspect of this thesis consists in investigating and exploiting the coherence properties of superluminescent diodes. In case of a first-order correlation measurement, e.g. determining the field auto-correlation function  $\langle E^*(t)E(t + \tau) \rangle$ , one can make use of standard interferometry. A detector measures the intensity of the light field, which is proportional to  $\langle E^2 \rangle$ , where small optical path delays  $\Delta d$  translate into very short time delays  $\tau$  due to the speed of light:  $\tau = \Delta d/c$ . Thus, first-order coherence is resolved by employing an appropriate path delay assembly. However, measuring temporal correlations of higher orders is a major challenge when the optical bandwidth is *ultra-broad*. In second order, intensity-intensity correlations  $\langle I(t)I(t + \tau) \rangle$  need to be temporally resolved on the timescale of  $\tau_c$ . There are several techniques to achieve excellent time resolution for  $g^{(2)}(\tau)$ -measurements such as sophisticated time-tagging modules in combination with ultrafast detectors (tens of picoseconds) [128], streak camera approaches (few picoseconds) [7], ultrafast RF spectrum detection by highly nonlinear fibers (picosecond) [129], dual-pulse homodyne detection (sub picosecond) [130] as well as superconducting detectors (femtosecond regime) [11]. Here, a nonlinear detection method is exploited combining interferometry with ultrafast intensity-intensity detection by two-photon-absorption in a semiconductor detector reaching sub-fs correlation time resolution. In the following, the two-photon-absorption process is briefly discussed.

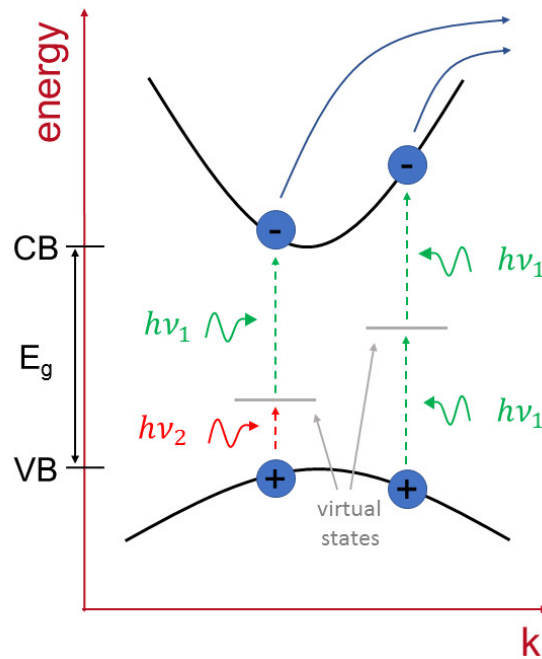


Figure 12. **Schematic representation of two-photon-absorption (TPA) inside a semiconductor material.** The energy band diagram as a function of wave vector  $k$  (conduction band (CB), valence band (VB)) is shown for the direct band gap ( $E_g$ ) case with two exemplary TPA events of different photon energy combinations  $h\nu_1$  and  $h\nu_2$ .

**Two-photon absorption.** Inside a semiconductor detector, an electron-hole pair is conventionally created by one absorbed photon which frequency overcomes the energy band gap  $E_g$ . This linear absorption induces a photocurrent which is directly proportional to the incident optical power. Under certain conditions, electron-hole pairs can be generated by two simultaneously arriving photons, which individually possess lower energy than  $E_g$ , however, their sum is greater than  $E_g$  (Figure 12). This phenomenon is called two-photon-absorption (TPA) and the resulting photocurrent scales with the square of the impinging optical power. TPA is part of third-order optical nonlinear processes such as third-harmonic generation, the optical Kerr effect and Raman scattering.

Nonlinear light propagation in a transparent medium is fundamentally described by the relationship between the electric polarization of the medium  $\vec{P}$ , the nonlinear susceptibilities  $\chi^{(i)}$  and the impinging light field  $\vec{E}$  [131]:

$$\vec{P}(\omega) = \varepsilon_0 \sum_i \chi^{(i)}(\omega) \vec{E}^i(\omega). \quad (50)$$

The electric dipole moment per unit volume of the medium is called the electric polarization [132].  $\chi^{(1)}$  is the linear susceptibility representing the linear response, i.e. the linear absorption and the refractive index of the material. The third-order Fourier components  $P_i^{(3)}$  of the electric polarization with frequency  $\omega_p$  is expressed by [131]

$$P_i^{(3)}(\omega_p) = \varepsilon_0 D^{(3)} \sum_{jkl} \chi_{ijkl}^{(3)}(\omega_p; \omega_1, \omega_2, \omega_3) E_j(\omega_1) E_k(\omega_2) E_l(\omega_3). \quad (51)$$

$\varepsilon_0$  is the vacuum electric permittivity,  $\chi^{(3)}$  is the third-order nonlinear susceptibility tensor (3x3x3x3 dimensional tensor) where  $i, j, k$  and  $l$  refer to the Cartesian components of the fields. Note that Eq. (51) implies that three optical fields interact to produce a fourth field representing a four-photon process. In general, each optical field has a different frequency  $\omega_1, \omega_2$  and  $\omega_3$ . The exclusive third-order nonlinear polarization frequencies occur at frequencies of  $\omega_p = \omega_1 + \omega_2 + \omega_3$ . For TPA, the frequency dependency

$$\omega_1 = \omega_2 = -\omega_3 \quad (52)$$

holds. Respecting two other possible combinations, the degeneracy factor  $D^{(3)}$  takes a value of 3. Assuming an isotropic medium and an incoming linearly polarized plane wave with frequency  $\omega$ , one can show that the TPA coefficient writes [133, 134]

$$\beta_{TPA} = \frac{1}{I^2} \frac{dI}{dz} = \frac{3\omega}{2\varepsilon_0 n^2 c^2} \text{Im}(\chi^{(3)}). \quad (53)$$

with the intensity of the field  $I$  and the index of refraction  $n$ . Note that the two-photon-absorption coefficient is indeed related to the imaginary part of the susceptibility tensor  $\text{Im}(\chi^{(3)})$ . Let  $I = P_{opt}/S$  be the intensity of the field with a total optical power  $P_{opt}$  impinging on the dielectric medium with a constant spot area  $S$  along the absorption length  $\Delta z$ . Then, the change in optical power due to TPA can be approximated to [133]

$$\Delta P_{TPA} = S \Delta I = \frac{\beta_{TPA} \Delta z}{S} P_{opt}^2. \quad (54)$$

The quadratic dependency on  $P_{opt}$  is verified for the TPA detector used in this thesis within an exemplary measurement. The photomultiplier tube (PMT) (Hamamatsu H7421-40) is sensitive to visible light in the range of 380nm to 720nm in terms of wavelength. Hence, a TPA response in the range of 760nm to 1420nm is expectable. The choice of this specific sensitivity was made upon the fact that NIR light sources are employed. The energy of two NIR photons is needed to induce a photon count event at the PMT anode. Fundamental absorption events from ambient light are inhibited by placing a long-pass-filter ( $\lambda < 1000\text{nm}$ , Schott RG1000) covering the PMT window. For the demonstration purpose, an ASE light source (Exalos EXS13G1-2311) emitting a central wavelength of 1300nm is utilized. The light is focused onto the photocathode plane ensuring a sufficiently high TPA photon count rate. More specifically, the focal plane of the focusing lens is located at the depletion region of the GaAsP-

photocathode<sup>11</sup> reducing the spot size  $S$  to a minimum and thus maximizing the value of Eq. (54) for a given optical power (Figure 13, left). Figure 13 (right) shows the TPA photon count rate as a function of impinging optical power. The latter is a rather rough approximation of the amount of power impinging on the photocathode respecting the transmission of the LP filter<sup>12</sup>. The graph reveals a clear nonlinear absorption behavior with a slope of  $1.96 \pm 0.01$  (nonlinear fit parameter) within a range of two decades of impinging power and four decades of TPA photon count rate. Deviating values below  $1 \mu\text{W}$  are attributed to dark counts and to residual ambient light photons. Above  $300 \mu\text{W}$ , a slight saturation of the photocathode is visible. Note that a considerable amount of optical power is focused on a small part of the photocathode, which is conceived to detect very low levels of light in the visible spectrum. With these applied NIR intensities, thermal effects on the GaAsP crystal structure as well as changes in the refractive index are very likely. Figure 13 (right) also illustrates the overall low quantum efficiency of TPA detection. Considering the number of impinging photons per second corresponding to the abscissa, TPA quantum efficiencies below  $10^{-9}$  are estimated.

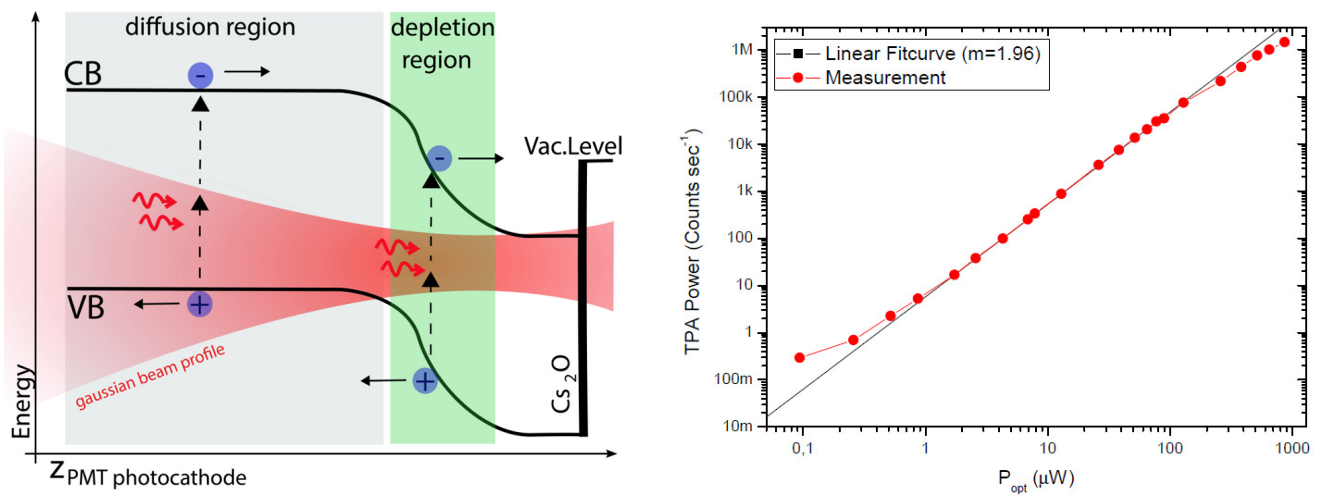


Figure 13. **Two-photon-absorption in a semiconductor-based photomultiplier.** Left: Energy band diagram of the VIS sensitive PMT photocathode (Hamamatsu H7421-40) illuminated by NIR photons. Right: TPA photon count rate as a function of incoming optical power recorded by the counting box (Hamamatsu C8855-01) of the PMT.

The suitability of the PMT (H7421-40) as a TPA detector has been investigated in more detail in [135]. On the basis of a semi-classical consideration [133], the measured TPA count rates should obey a Poissonian distribution. This has been verified experimentally for the total operation range. Furthermore, the TPA absorption coefficient  $\beta_{TPA}(\lambda)$  has been determined by a z-scan measurement for a number of relevant wavelengths ranging from 1180nm to 1340nm ( $30 \text{ cm/GW} > \beta_{TPA}(\lambda) > 1 \text{ cm/GW}$ ) verifying the functionality of the TPA-PMT in the operation range of interest<sup>13</sup>. In addition, one expects differing counting rates for coherent and thermal light illuminating the TPA detector. Due to the photon-bunching property of thermal light beams ( $g^{(2)}(0) = 2$ ), the probability for inducing a TPA process is twice as large as for coherent light ( $g^{(2)}(0) = 1$ ) [136]. This has been also validated experimentally by employing

<sup>11</sup> According to the specification of Hamamatsu Photonics [264], the photocathode is located about 16mm away from the module window. The most uncertain value is  $\Delta z$  since Hamamatsu doesn't communicate any information due to corporate secret. The value of  $\sim 1 \mu\text{m}$  given in Ref. [133] is assumed.

<sup>12</sup> Further optical power reduction is expected due to a possible AR coating of the PMT window and the photocathode surface, neglected in Figure 13 (right).

<sup>13</sup> In Ref. [133, 9], a similar PMT has been employed. There, a GaAs photocathode (H7421-50) has been utilized to match the light source NIR emission around 1500nm ( $\beta_{TPA}(\lambda = 1550 \text{ nm}) = 10.25 \text{ cm/GW}$ ). Here, the GaAsP option was taken to match the lower wavelengths around 1300nm. Also, a higher TPA sensitivity can be expected based on the overall improved quantum efficiency [264]. Besides, other TPA detectors can even yield higher absorption coefficients ( $\beta_{TPA} \sim 60 \text{ cm/GW}$ ) [262, 263], however without multiplication of the signal.

a coherent laser diode and an incoherent ASE source at the same central wavelength of 1300nm with a TPA counting ratio of  $\sim 2:1$  [137].

**The TPA interferometer.** As the TPA rate is proportional to the incoming intensity square [9, 24, 138],

$$\langle \hat{E}^{(-)}(t) \hat{E}^{(-)}(t) \hat{E}^{(+)}(t) \hat{E}^{(+)}(t) \rangle, \quad (55)$$

it is obvious that intensity correlation measurements with a suitable TPA detector is possible. In accordance with the methods of [9, 139, 140], a Michelson interferometer scheme is implemented which introduces a path delay  $\Delta x$  or equivalently a time delay  $\tau = 2\Delta x/c$  to Eq. (55). Figure 14 shows a schematic drawing of the TPA interferometer. The investigated light is coupled into a single-mode optical fiber for practicality and for ensuring a small spot size. The latter becomes advantageous when it comes to adjust a small focus of the light of the two interferometer arms (denoted by 1 and 2) onto the photocathode of the TPA PMT at the interferometer output. The focal plane of the output lens is located at the photocathode plane (depletion region) to maximize the possible TPA count rate (Eq. (54)). Also, it is important to ensure a good (transverse) overlap of the two foci in the photocathode depletion region to actually enable the correlation measurement. The employed beamsplitter is broadband, anti-reflection coated and non-polarizing such that neither frequency- nor polarization components are privileged to enter one of the interferometer arms which could lead to uncontrolled and unwanted cross-correlation effects instead of the targeted intensity auto-correlation measurement. The time resolution of this intensity auto-correlation system can be approximated by the Heisenberg time-energy uncertainty given by [133]

$$\Delta\tau = \frac{2\hbar}{E_g} \quad (56)$$

representing the lifetime of the virtual energy state inside the energy band gap (see Figure 12). From the results of a z-scan measurement of the TPA PMT, the energy band gap of the GaAsP photocathode has been approximated to  $E_g = 2.04\text{eV}$  [137]. This means that an estimated time resolution of  $\Delta\tau = 0.32 \cdot 10^{-15}\text{s}$  is available.

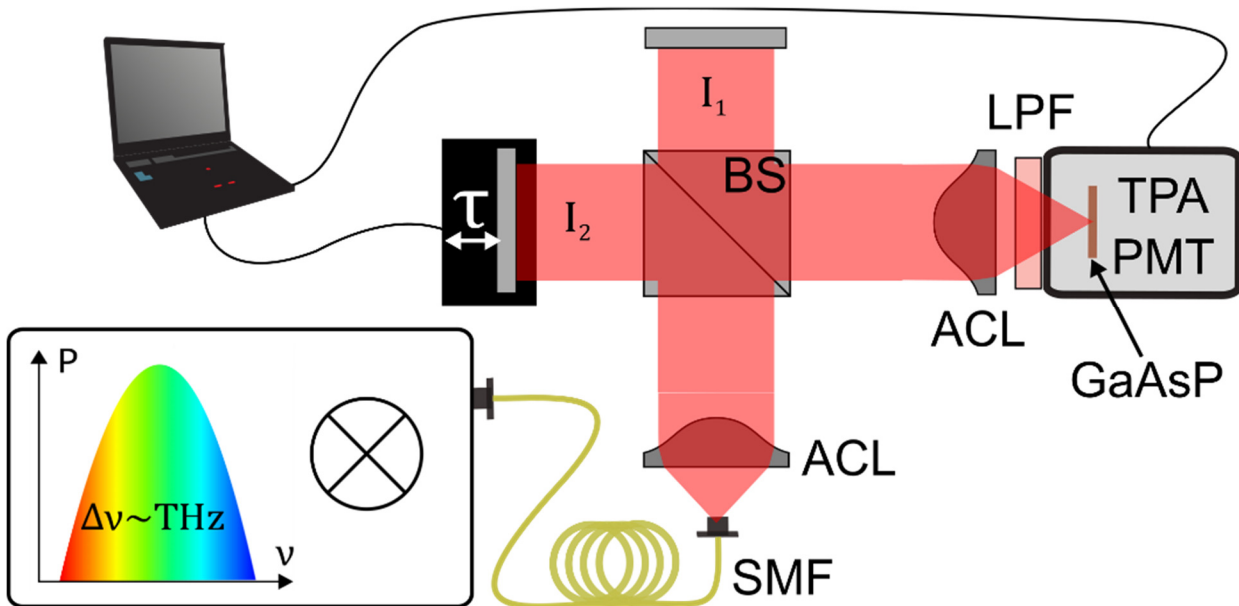


Figure 14. **Schematic of the implemented TPA Michelson interferometer.** The light source is fiber-coupled into a single-mode optical fiber (SMF). The mean intensities of the individual interferometer arms are denoted by  $I_1$  and  $I_2$ . Further components: Non-polarizing beamsplitter (BS), high-precision linear stage ( $\tau$ ), achromatic lenses (ACL), long-pass filter blocking visible light (LPF) to suppress fundamental absorption.

**The TPA interferogram.** In the following, a representative measurement using a broadband ASE source (Exalos EXS13G1-2311) shall serve as a description of the interferometric TPA signal as well as the correlation information extraction.

Figure 15 shows the TPA interferogram data in terms of the TPA count rate as a function of the optical path delay. The mirror has been displaced by a total distance of  $120\mu\text{m}$  within the Michelson interferometer. The TPA interferogram shows interference signature on a path delay scale of  $\pm 40\mu\text{m}$  which corresponds to short time delays (top abscissa) in the range of  $\pm 130\text{fs}$ . The TPA count rates vary between  $0\text{Counts/s}$  and  $29\text{kCounts/s}$  where a dark count level of  $10\text{Counts/s}$  has been subtracted from the data. Figure 15 (right) is a zoom into the TPA interferogram data showing highly resolved interference fringes where the data point density depends on the displacement speed of the motorized actuator (Newport LTA-HS) and the integration time of the photon counting module (Hamamatsu C8855-01). Note that the interference fringe distance indeed reflects the mean wavelength of  $1.3\mu\text{m}$ .

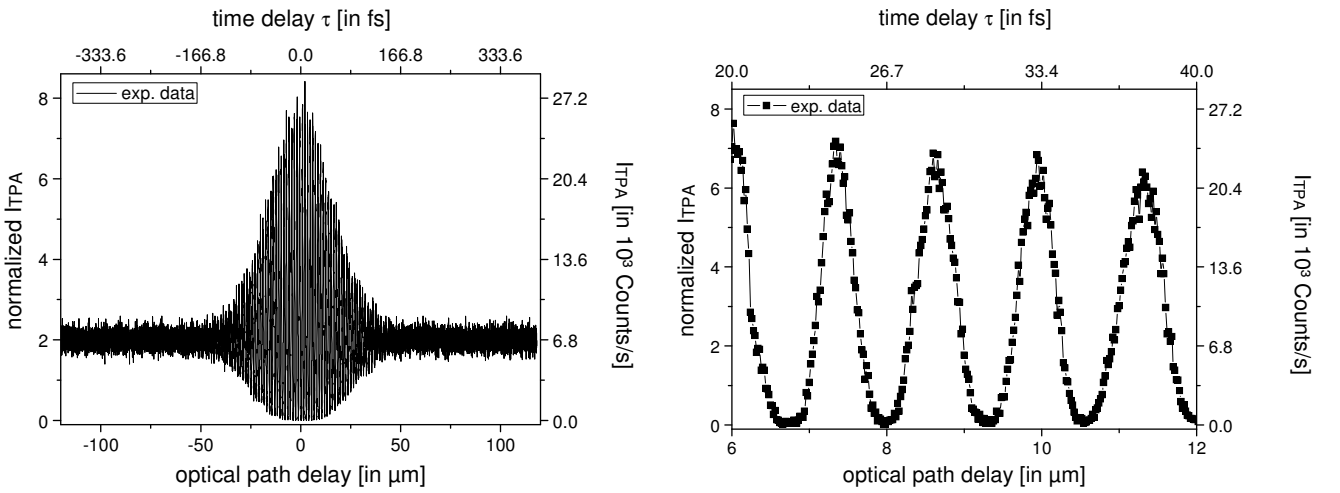


Figure 15. **Representative TPA interferogram** of light emitted by a broadband ASE source. Left: Full interferogram in terms of TPA Counts/s (right axis) and normalized TPA count rate (Eq. (57), left axis) as a function of optical path delay (bottom abscissa) as well as the corresponding time delay  $\tau$  (top abscissa). Right: Zoom-in of the left graph showing highly resolved TPA interference fringes.

The features of the TPA interferogram such as the frequency composition as well as the observed asymmetry with respect to the mean intensity axis at time delays far off coherence can be understood by considering a generalization of [141] which was fully investigated in the thesis of F. Boitier [133] as well as in Ref. [140]:

$$\frac{I_{TPA}(\tau)}{I_1 + I_2} = 1 + 2G^{(2)}(\tau) + 4\text{Re}[F_1(\tau)e^{-i\omega_0\tau}] + \text{Re}[F_2(\tau)e^{-2i\omega_0\tau}] . \quad (57)$$

$I_{TPA}(\tau)$  is the interferogram signal.  $I_1$  and  $I_2$  correspond to the mean TPA signal of the individual interferometer arms (see Figure 14). The full term on the left side of Eq. (57) forms the normalized TPA interferogram, denoted as such in Figure 15. The right-hand side of Eq. (57) describes the frequency composition of the TPA interferogram by three main terms. An appropriate illustration for identifying all three components is a fast Fourier transform (FFT) of Figure 15 which is depicted in Figure 16 (left). Here, the FFT amplitudes are plotted against the frequency  $\nu = \omega/2\pi$  in units of  $\text{THz} = 10^{12}\text{Hz}$ . In the low frequency range (i), below  $20\text{THz}$ , information about the second-order correlation is located, which corresponds to the first term of Eq. (57).  $G^{(2)}(\tau)$  represents the non-normalized second-order correlation function (see Eq. (12)). The two other summands of Eq. (57) are fast oscillating terms, one going with

the mean optical frequency  $\omega_0 = 2\pi c/\lambda_0$  and the other with  $2\omega_0$  denoted by (ii) and (iii) in Figure 16 (left) at frequencies of 230THz and 460THz, respectively.  $F_1(\tau)$  and  $F_2(\tau)$  can be expressed in terms of the electric field [141] by

$$F_1(\tau) \propto \frac{1}{2} \langle (|E(t)|^2 + |E(t+\tau)|^2) E(t)E^*(t+\tau) \rangle$$

$$F_2(\tau) \propto \langle E^2(t)E^{*2}(t+\tau) \rangle$$
(58)

One can realize that  $F_1(\tau)$  is reminiscent of the first-order correlation function and that  $F_2(\tau)$  is related to the optical nonlinear process of the TPA detection. Indeed, a zoom into the optical frequency range around  $\nu_0$  (Figure 16, right) reveals that the TPA interferogram comprises the optical spectrum. The direct comparison with a measurement using a commercial optical spectrum analyzer (OSA) (blue line) shows a nice agreement with the FFT data and thus consolidates the accuracy of the implemented TPA interferometer.

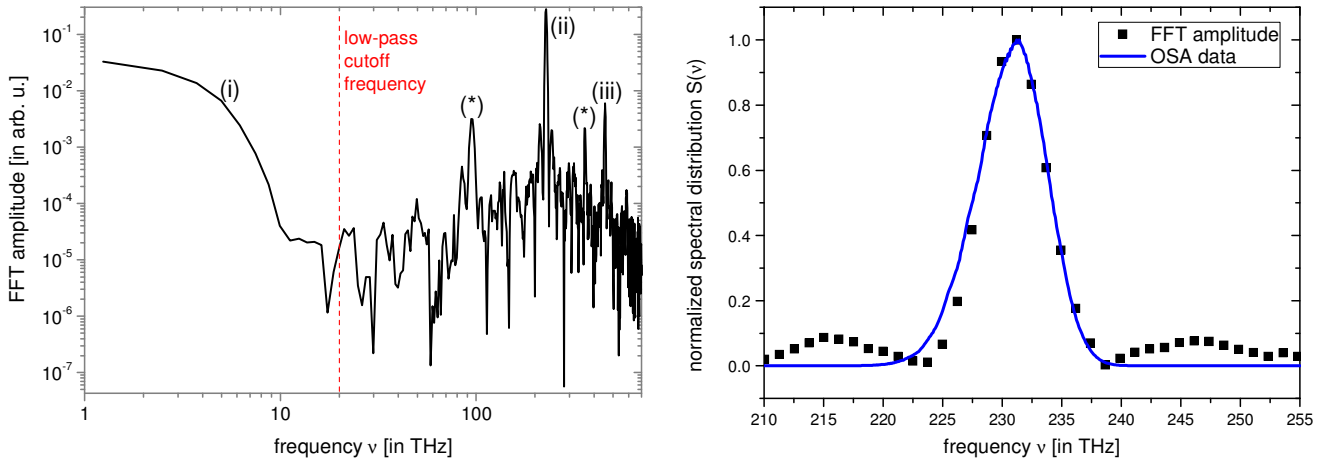


Figure 16. **Fourier transformation (FFT) of the TPA interferogram from Figure 15** (double logarithmic scale). Left: Full FFT spectrum with indications of the three frequency components of Eq. (57): (i) low-frequency range ( $\propto G^{(2)}(\tau)$ ), (ii) optical frequency range, (iii) frequency-doubled component as well as additional frequency contributions (\*) due to interferometric artifacts<sup>14</sup>. The vertical dashed line (red) denotes the low-pass cut-off frequency utilized for the extraction of  $G^{(2)}(\tau)$ . Right: Zoom into (ii) with comparison to an optical spectrum measured by a commercial optical spectrum analyzer (linear scale).

### Correlation signal extraction.

Moreover, the individual signals can be recovered by applying an inverse FFT (IFFT) to appropriately selected bandpass windows. Figure 17 shows the retrieved signals corresponding to  $F_1$  (left) and to  $F_2$  (right) which have been obtained by using a bandpass window of 223-238THz and 452-469THz, respectively. In both graphs, the timescale on which inference is visible is determined by the coherence time. Using the mean of  $\bar{\lambda} = 1300nm$  and the spectral width  $\Delta\lambda = 59nm$  of the measured optical spectrum (Figure 17, left), the coherence time (Eq. (7)) takes a value of 96fs which matches the interference fringe amplitude decay.

<sup>14</sup> These interferometric artifacts are probably due to the accidental formation of FP cavities. Reflections from the surface of the detector as well as from the back of the photocathode can occur. Furthermore, possibly applied AR coatings within the detector are designed for visible wavelengths and could additionally enhance the amount of undesired reflections. The frequency spacing of these artifacts is  $\nu_0 \pm 132THz$  which suggests a cavity length of less than  $1\mu m$ . These effects point out the delicate sensitivity of the TPA detector to the quality of the absorption material as well as to its surface quality. A detailed analysis of such artifacts has been investigated in Ref. [134].

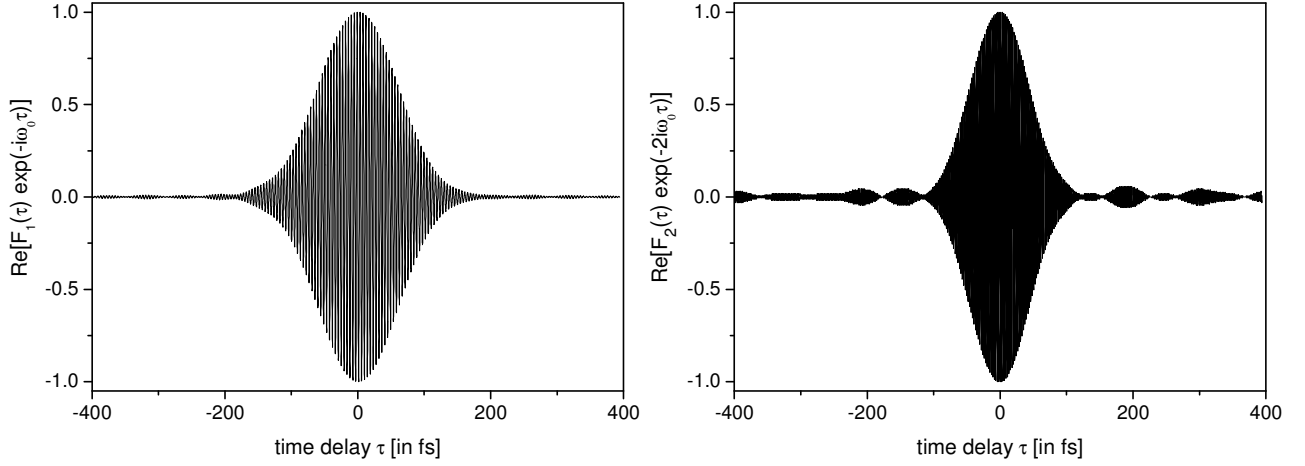


Figure 17. Retrieved fast oscillating contributions of the TPA interferogram from Figure 15. Left: First-order frequency components (ii) using an IFFT of the bandpass window: 223-237THz. Right: Frequency-doubled oscillation components (iii) using an IFFT of the bandpass from 450 to 467THz.

After all, the second-order correlation signal,  $G^{(2)}(\tau)$ , can be retrieved as well. Due to the clear separation from the high-frequency components (Figure 16, left), a low-pass filter is implemented by setting an appropriate cut-off frequency in the Fourier domain<sup>15</sup> and applying an IFFT. Thereby, Eq. (57) reduces to

$$\frac{I_{TPA}^{LP}(\tau)}{I_1 + I_2} = 1 + 2G^{(2)}(\tau) \quad (59)$$

where  $I_{TPA}^{LP}$  stands for the low-pass (LP) filtered TPA interferogram signal. To determine a second-order correlation function in units that are independent of TPA signal levels, a normalization to values far-off coherence ( $\tau \gg \tau_c$ )

$$G^{(2)}(\tau \gg \tau_c) = \frac{1}{2} \left( \frac{I_{TPA}^{LP}(\tau \gg \tau_c)}{I_1 + I_2} - 1 \right) \quad (60)$$

is applied resulting in

$$g^{(2)}(\tau) = \frac{G^{(2)}(\tau)}{G^{(2)}(\tau \gg \tau_c)} \quad (61)$$

The latter is the normalized second-order auto-correlation function according to the Glauber coherence formalism. Figure 18 (left) shows the extraction result for the TPA interferogram of Figure 15 having set a cut-off frequency of 20THz (see Figure 16, left). Again, short correlation timescales are observed in agreement with the coherence time  $\tau_c = 96fs$  with  $g^{(2)}$  values reducing to 1 for  $\tau > \tau_c$ . A pronounced intensity correlation signal is visible which can already be surmised by the pronounced asymmetry of the TPA interferogram with respect to the horizontal baseline (defined by TPA Counts at  $\tau \gg \tau_c$ ) in Figure 15. The second-order coherence degree  $g^{(2)}(\tau = 0)$  amounts to 2.01 representing a nearly ideal thermal photon-bunching level. In order to quantify the precision of the  $g^{(2)}(0)$  determination, the statistics of a set of 90 repeated measurements has been evaluated. The histogram of experimentally determined  $g^{(2)}(0)$  values is depicted in Figure 18 (right) together with a normal distribution (Gaussian)

<sup>15</sup> Note that the appropriate choice of the cut-off frequency is strongly dependent on the coherence time of the investigated light. It is instructive to think of the width of the interference signal being described by an explicit amount of low frequencies. Hence, the cut-off frequency needs to be adjusted to the spectral width of the light source. Furthermore, the spectral shape and the data point density can affect the bandwidth of adequate cut-off frequencies for determining correct values of the second-order coherence degree.

fit. The latter appears as a reasonable adaptation of the observed statistical distribution. Therefore, the Gaussian parameters are a good representation of the statistical mean and the deviation for possibly occurring  $g^{(2)}(0)$  values in the experiments. The Gaussian mean and variance amount to  $\overline{g^{(2)}(0)} = 2.01$  and  $\Delta^2 g^{(2)}(0) = 0.04$ , respectively.

It should be mentioned that apart from the nature of the photon emission process, other optical properties act on the second-order auto-correlation function and consequently influence the degree of second-order coherence. Control and knowledge of the polarization, the transverse beam characteristics and possible dispersion effects are crucial for a correct interpretation of the experimental results.

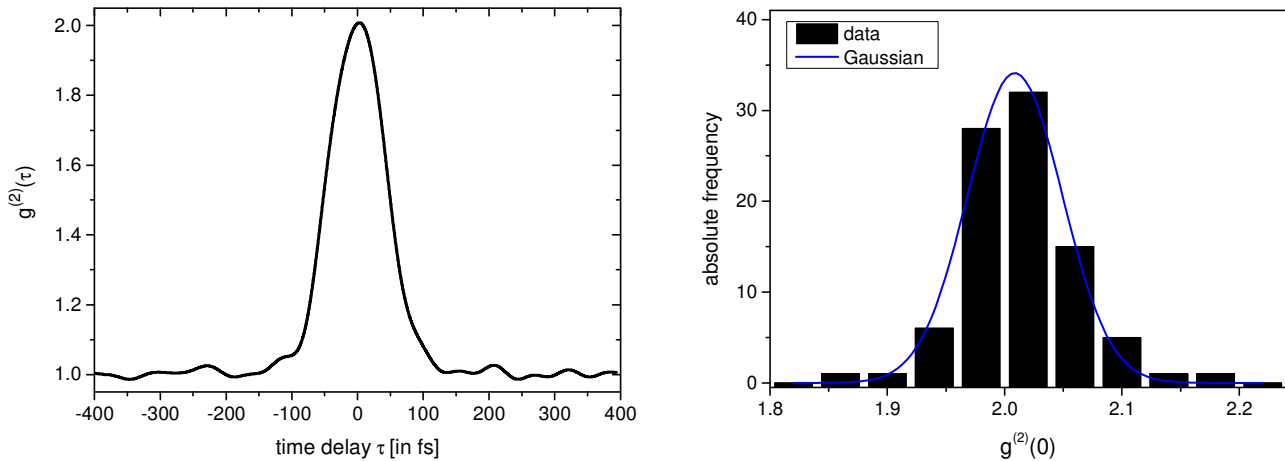


Figure 18. **Second-order correlation extraction from the TPA interferogram.** Left: Data extracted from the TPA interferogram of Figure 15. Right: Statistics of the extracted second-order coherence degree taken from a set of 90 TPA interferograms. A Gaussian fit (blue line) yields a mean value of  $\overline{g^{(2)}(0)} = 2.01$  and a variance of  $\Delta^2 g^{(2)}(0) = 0.04$ .

**TPA interferometry application.** Finally, it is worth noticing that TPA interferometry enabled the experimental observation of the photon-bunching effect of true thermal light sources [142], more than 50 years after the famous HBT experiment [4]. In this context, the terminology *true* refers to non-processed, *pure* thermal light sources which usually emit many different wavelengths leading to large spectral widths. In fact, the literal sense of *thermal light* (blackbody radiation) is EM radiation from objects, in thermal equilibrium with their environment, generated by the thermal motion of their constituent atoms [143]. The corresponding spectral distribution is described by Planck’s radiation law which is inherently linked to the temperature of the emitting body. Indeed, Boitier and coworkers were the first to measure experimentally the photon-bunching level of a Halogen lamp operated at  $\sim 3000\text{K}$  where the intensity correlation signal was apparent on timescales below 37fs [9], as nearly the full spectrum of the lamp was guided onto the detector.

In this thesis, TPA interferometry is exploited for investigating the second-order coherence behavior of amplified spontaneous emission from quantum dot superluminescent diodes (Chapter 4). As these light sources yield THz-wide optical spectra, a sub-ps time resolution is required. Furthermore, TPA interferometry is key to the introduction of broadband light sources to ghost imaging (Chapter 5.2.). Finally, the demonstration of a highly incoherent GI experiment is only possible by intensity cross-correlation detection based on TPA interferometry (Chapter 5.3.).

For the sake of completeness, since its publication in 2009, the TPA interferometry method has been used as an experimental tool in a multitude of fundamental research work. In a certain sense, this method has extended the fundamental research on higher-order coherence of light, which was pioneered in the early years of the laser, to highly MM light states: the measurement of super-bunching in broadband parametric down conversion sources [38], the coherence analysis of SLD light [23] also in comparison with intensity noise measurements [144, 145], the superposition of broadband incoherent

---

light sources [146] and the investigation of partially polarized optical beams [147]. Also, there have been a few propositions on applications such as second-order OCT tomography based on TPA interferometry [50] and the verification of enhanced TP excitation in fluorescence microscopy [136]. Besides the incorporation into interferometry for second-order correlation measurements, TPA in semiconductors has already been exploited for other applications [148] such as short pulse characterization by TPA auto-correlators [141, 149], pulse compression by TP gain [150], TPA-based signal processing for e.g. optical demultiplexing at very high bit rates [151], optical thresholding [152], pulse chirp measurements [153], TPA spectroscopy [154] and also a reflectometry system based on TPA detection [155], just to name a few.

This chapter was dedicated to the introduction of two-photon-absorption (TPA) interferometry as the second, central experimental method of this thesis. The fundamental physics of the TPA process has been explained within the context of a semiconductor-based PMT (Figure 12 and Figure 13) utilized as the TPA detector. The appropriateness of TPA detection for second-order correlation measurements, or intensity-intensity detection, can be resumed by the following key facts:

- TPA is an *ultra*-fast process due to the *very* short lifetime of the virtual state inside the energy bandgap.
- The TPA rate is proportional to  $\langle I(t)I(t) \rangle$ .
- TPA is broadband because virtual states can emerge at any energy level within the bandgap.
- Being a pure intensity effect, TPA does not require phase matching.

The implemented TPA interferometer in a Michelson configuration (Figure 14) adds a time delay to intensity-intensity detection. The fast response time of the TPA detector is approximated by the Heisenberg time, corresponding in this specific case to a time resolution of  $\Delta\tau = 0.3fs$ . The extraction of the second-order auto-correlation function  $g^{(2)}(\tau)$  (Figure 18) from the TPA interferogram (Figure 15) is performed by applying a low-pass filter to the acquired data (Figure 16) and an appropriate normalization (Eq. (61)). Intensity correlations of light on sub-ps timescales can thus be experimentally determined which is a prerequisite in pursuit of the aims of this thesis. Also, a reasonable precision of the implemented system for determining the second-order coherence degree  $g^{(2)}(0)$  has been verified showing a statistical deviation of  $\sim 2\%$ .

Hence, the TPA Michelson interferometer scheme put forward in this chapter is well suited for fundamental intensity auto-correlation analysis of light (Chapter 4). Different interferometer configurations with TPA detection are certainly conceivable. In particular, a modified configuration will be put in place for accessing intensity cross-correlations in view of a GI scheme based on TPA interferometry (Sections 5.2. and 5.3.). However, the following first result-section is based on the Michelson version for investigating the second-order coherence behavior of a particularly interesting type of light generation: amplified spontaneous emission from superluminescent diodes.

---

## 4. Tailoring first- and second-order coherence properties of light emitted by SLDs

---

In this chapter, the temporal coherence of light emitted by a special type of opto-electronic emitter is investigated. Superluminescent diodes (SLDs) generate photons by neither purely spontaneous nor purely stimulated emission processes. The prevailing amplified spontaneous emission (ASE) represents a hybrid light generation process thus constituting an interesting object of fundamental research. Investigations on higher-order coherence properties of ASE from SLDs have been given lively attention in recent years [48, 23, 145, 144], in part due to new experimental possibilities [9] (Section 3.2). This thesis contributes to this topic with two experiments on simultaneously tunable first- and second-order coherence properties of SLD light, thereby exploring fundamental physics at the edge of ASE to stimulated emission.

At first, a general introduction to the structure and the operation principle of SLDs is given (Section 4.1). Also, the gain material of the devices in operation is briefly described and discussed for understanding the shape and the bandwidth of optical spectra. A brief overview of the status of research regarding higher-order correlations of SLD light is provided. In the first experiment (Section 4.2), intrinsic coherence tuning is achieved by applying well-controlled broadband optical feedback onto a SLD. The second experiment is based on an extrinsic approach mixing incoherent SLD light with coherent light from a SM diode laser (Section 4.3). The full control of the second-order coherence degree by the power-ratio can be considered as a revival of some results on mixed-light in the early days of coherence analysis. The obtained results from both experiments are backed up by direct comparison to a theoretical model. In particular, a quantum state of light is postulated for describing spectrally broadband ASE of SLDs. The work presented in Chapter 4 has resulted in two scientific publications [156, 157], the latter of which is referred to concerning the outlined theoretical part at the end of Section 4.1. and in Section 4.3.

### 4.1. Superluminescent diodes (SLDs)

At first, the structure and the functional principle of superluminescent diodes are explained by comparison to related opto-electronic emitters. The dedication of a full section to the introduction of SLDs is justified by the facts that, for one thing, Chapter 4 deals with fundamental investigations on SLD light and secondly, SLDs are exploited as the light sources for realizing incoherent ghost imaging experiments presented in two sections of Chapter 5.

**Device structure.** Superluminescent diodes (SLDs) are semiconductor-based opto-electronic emitters capable of emitting spectrally broadband light with several tens to hundreds of nanometers spectral width in terms of wavelength together with high output powers. These characteristics are enabled by a broadband optical gain material embedded inside an edge-emitting diode structure featuring a waveguide geometry (see Figure 19, right). To prevent longitudinal mode formation as in laser resonators, the facets are anti-reflection (AR) coated and slightly tilted (typ.  $5^\circ$ - $7^\circ$ ) with respect to the waveguide optical axis inhibiting optical feedback. The length of the waveguide, typically several millimeters, allows spontaneously emitted photons to be amplified significantly on their one-way travel towards one of the two output facets generating so-called amplified spontaneous emission (ASE). Due to the waveguide dimensioning (several mm length vs. few  $\mu\text{m}$  width), SLD emission combines low temporal coherence of light emitting diode (LED) and high directionality of LDs. Table 3 summarizes the important optical properties of LEDs, SLDs and LDs. Furthermore, narrow-stripe SLDs yield transverse single-mode emission which provides efficient broadband light for practical implementation. Already in the 1970s, double-hetero-structured SLDs were fabricated in view of fiber-based sensing applications [158]. Today, SLDs are commercially available, e.g. by Denselight, EXALOS, InPhenix and Superlum. By selecting appropriate gain materials, the wavelength range between 400nm and 1700nm

is accessible. Most recently, high-brightness blue light SLDs in combination with phosphor achieved high quality white light emission [159]. SLDs are purely injection-current pumped thus constituting easy-to-handle, extremely compact, miniaturized and robust light sources (see Figure 19, left) for a vast field of applications such as OCT [160, 161, 162], white light interferometry [163], distance measurements [164], fiber optical gyroscopes [165] and self-mixing interferometry for flow measurements [166]. Note that the SLD structure is principally identical to that of a semiconductor optical amplifier (SOA). The difference in usage as a stand-alone broadband light source or as an optical amplifier for injected laser light motivates the differentiation in notion. Hence, different approaches for designing an appropriate active medium and device features (facet coatings, waveguide geometry, etc.) are necessary.

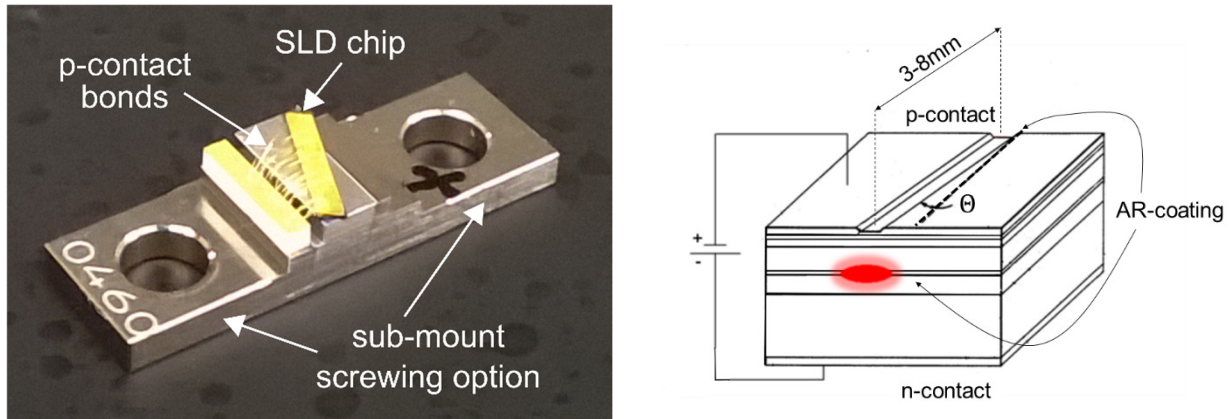


Figure 19. **The superluminescent diode.** Digital camera image of a mounted SLD (left) and schematic diagram of the diode structure with indications of some typical characteristics and emission region (right). The three-dimensional schematic has been adapted from Ref. [167].

Table 3. Overview of important optical properties of different types of opto-electronic emitters [168].

Optical property	LED	SLD	Laser diode
<b>Bandwidth</b>	Large	Large	Small
<b>Coherence length</b>	Short	Short	Long
<b>Emission</b>	Divergent	Directional	Directional
<b>Output power per solid angle</b>	Low	Medium	High
<b>Photon emission process</b>	Spontaneous	Amplified-spontaneous	Stimulated

**Quantum dot gain material.** All SLDs utilized in this thesis are based on quantum dot gain media. A brief background on quantum dots with focus on inhomogeneously broadened InAs/InGaAs quantum dot layer systems is given in this paragraph.

A quantum dot (QD) is a nanoscale semiconductor material. Its properties thus differ strongly from those of bulk semiconductors. In particular, opto-electronic properties change with the shape and the size of specific QDs. Embedded within a material of different energy band gap, charge carriers are confined in all three space and wave vector dimensions. The nanoscale size leads to quantized energy states where electron-hole pairs can recombine by radiation emission with defined frequencies. This property is similar to that of single atoms which justifies the consideration of QDs as *artificial atoms*. The lowest

optical transition is commonly referred to as the ground state (GS) transition followed by the first excited state (ES) transition, second excited state (SES) transition, and so forth (see Figure 20, left). The exact position of the energy levels in the *conduction* and *valence* band, responsible for the specific radiation energies, is determined by a variety of intrinsic parameters such as the QD material, the material composition, the size, the shape and the temperature [169]. Because of their wide-range tunability, QDs are not only of high interest for modern research fields such as quantum computing and quantum optics serving as qubits [170] and single-photon emitters [171], but also for applications in bio-imaging as fluorescent markers for bio-particle tracking or flow cytometry [172], in solar cells [173] and even in display technology for replacing RGB (red, green and blue) color filtering [174].

The incorporation of self-assembled epitaxially grown QD layers in semiconductor lasers (Figure 20, right) has been pioneered in the later 1990s [175, 176]. Higher differential gain, lower threshold currents and improved temperature stability were the key benefits for pushing forward the technology mainly involving InAs- and InGaAs-QDs embedded in GaAs confinement layers and GaAs or InP substrate materials [177] covering the wavelength range from  $1.0\mu\text{m}$  to  $1.9\mu\text{m}$ . Moreover, properties like extremely broad gain bandwidth, large output saturation intensity, ultra-fast gain recovery and uniform pulse amplification under gain saturation has led to QD-based semiconductor optical amplifiers (SOAs) [178]. Furthermore, the high quality of QD saturable absorbers has enabled efficient, compact and high repetition-rate mode-locking [179] such as in monolithic multi-section passively mode-locked laser diodes [180]. QD-based SLDs have been developed 15 years ago [181, 182] and they are commercially available since 2008 (Innolume GmbH). Owing to a tailorable, spectrally broadband gain, QD SLDs allow better sensitivity and spatial resolution for low-coherence applications. Grown by the Stranski-Krastanow method, self-assembled QDs nucleate spontaneously on the growth surface driven by the strain of lattice mismatch between epitaxial layer and the substrate when molecular beam epitaxy or metalorganic vapor phase epitaxy techniques are applied [183]. This leads to a large inhomogeneity of QD sizes inside a growth layer with an approximately Gaussian size distribution [169]. Thus, each of the originally discrete emission wavelengths of GS, ES and SES (Figure 20, left) are broadened when the full ensemble of QDs is radiating. The SLD structure mostly preserves the available gain spectrum for the actual edge-emission.

A representative behavior of the here utilized Dot-in-Well (DWELL) InAs/InGaAs QD layer system with a GaAs waveguide is shown in Figure 21. On the left-hand side, the optical power output  $P_{opt}$  as a function of injection current  $I_p$  (P-I characteristic) reveals typical SLD attributes. For low injection currents, here below 200mA, only slight power increase is observed which can be attributed to dominating spontaneous emission, likewise in LEDs. Around 200-250mA, a clear enhancement of the P-I curve steepness is visible. Due to more available charge carriers with significant population of the QD states, ASE starts to be the dominant light generation process. More net modal gain results in a steeper increase of optical output power, here showing a nearly linear behavior above 300mA. Note that compared to LD, no distinct amplifying threshold is formed by ASE. The latter is considered as a disturbing emission contribution in LD which delays the onset of laser threshold and which is usually tried to be suppressed. The spectral properties belonging to the P-I curve are depicted in Figure 21 (right). Three optical spectra were measured by a commercial OSA (ADVANTEST Q8384) at representative injection current values: 50mA (spontaneous emission regime), 400mA (ASE regime), 900mA (close to the thermal rollover). At 50mA, one central wavelength around 1310nm is radiating which is attributed to pure GS emission. An additional spectral contribution at a second central wavelength of 1230nm reflecting the ES emission, sets in for increasing injection currents which is already dominating at 400mA. At a high pump current of  $I_p=900\text{mA}$ , the SES centered at 1160nm is also contributing. Also, GS emission is slightly reduced which indicates thermally induced depopulation (losses) of lower energy states in combination with gain saturation effects. Figure 21 (right) illustrates the spectrally broadband property of QD SLDs with multiple Gaussian-like spectral distributions with varying shape and width depending on the amount of injection current. It is obvious that common spectral width measures such as the FWHM or the 10dB-width would not capture the complexity of all different contributions. Therefore, the integrating Suessmann measure introduced in Eq. (9) is applied. For discrete spectral power values, the expression can be written as

$$\Delta\lambda_s = \left( \sum_{i=1}^N P_i \Delta\lambda_i \right)^2 / \left( \sum_{i=1}^N P_i^2 \Delta\lambda_i \right) \quad (62)$$

in terms of wavelength with the sampled optical power data  $P_i$  and the wavelength increment  $\Delta\lambda_i$ . The spectral widths corresponding to the three measurement examples in Figure 21 (right) amount to 76.2nm, 75.4nm and 95.8nm for 50mA, 400mA and 900mA, respectively. The corresponding frequency-domain values are 13.3THz, 14.9THz and 19.0THz, which can indeed be classified as ultra-broadband in the sense of

Table 2. There are further special designs for achieving extreme large bandwidths of QD SLDs which can easily exceed 150nm [184] or even 200nm when different QD layers are stacked on top of each other (chirping) [185].

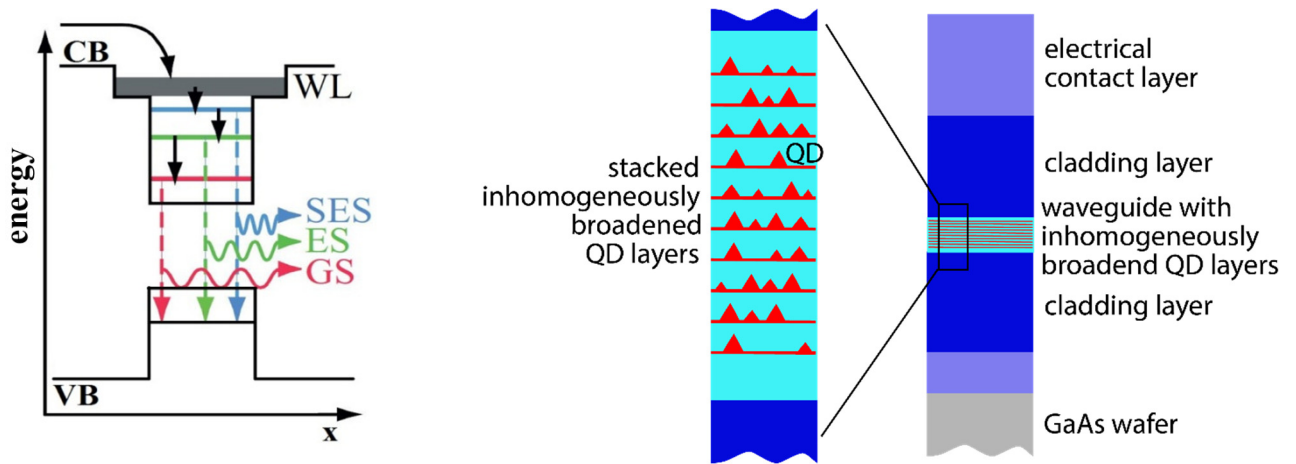


Figure 20. **Quantum dot gain material.** Left: Energy band diagram in the space domain of a single quantum dot. The solid arrows indicate possible electron relaxations from the conduction band (CB) of the bulk material into the QD wetting layer (WL) and the radiative energy levels (SES, ES, GS) to finally recombine with electron holes located in the valence band (VB). Right: Schematic cross-section of 10 inhomogeneously broadened QD layers within a possible epitaxial structure comprising GaAs space layers (turquoise), cladding layers (darker blue) and electrical contacts (light blue).

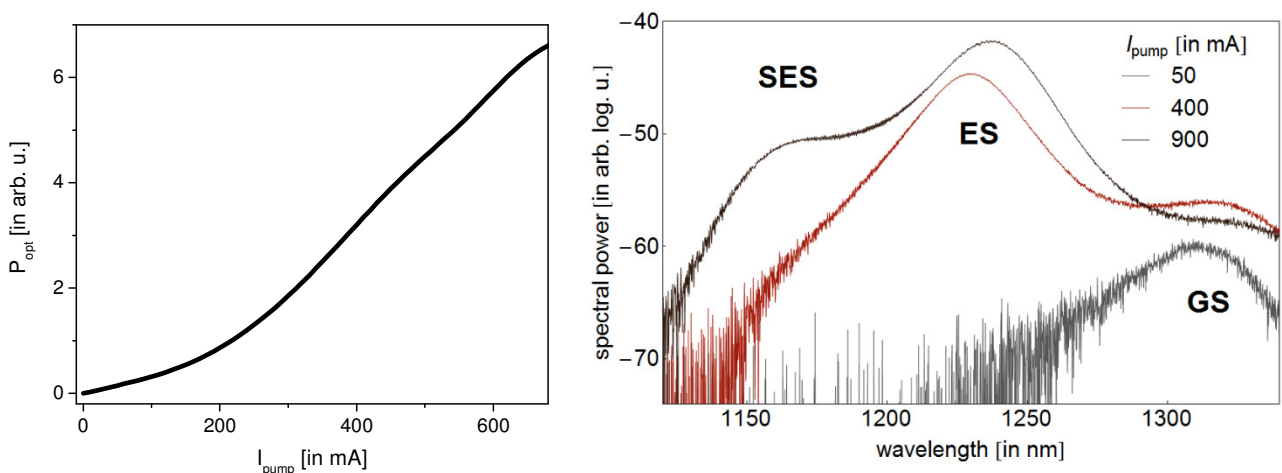


Figure 21. **Opto-electronic characteristics of a quantum dot SLD.** Left: P-I curve showing the optical power  $P_{opt}$  behavior as a function of injection current  $I_{pump}$ . Right: Representative optical spectra at different injection current levels revealing ground state (GS), first excited state (ES) and even second excited state emission (SES) of inhomogeneously broadened QD layers.

---

**The coherence of light emitted by QD SLDs.** The motivation for the following experiments on tailoring first- and second-order coherence of QD SLD light, presented in the next two Result-Sections 4.2 and 4.3, lies in three main aspects.

Firstly, ASE represents an intriguing fundamental light generation process being a mixture of spontaneously and stimulated emitted photons. Since the invention of the laser in 1960, ASE has been continuously studied in terms of statistical and noise behavior because of its disturbing influence at the laser threshold [186, 6, 187, 188]. In the 1970s, Allen and Peters were the first to address the ASE phenomenon, putting it into context with Dicke's superradiance [189]. They defined ASE as *highly directional radiation emitted by an extended medium with a randomly prepared population inversion in the absence of a laser cavity*. Supported by theoretical studies and He-Ne gas discharged tube-amplification experiments, they established the ASE threshold condition, the pump-output-intensity behavior, saturation effects, and spatial coherence properties [190, 191, 192, 193]. Even nowadays, the analysis of photon statistics of ASE is of interest for determining the onset of stimulated emission in new laser concepts, e.g. in random lasing [194], for microcavity laser [10] and for monolayer excitonic laser [195]. However, the experimental access to photon statistics and higher-order correlations is challenging due to the intrinsic nature of ASE not being frequency-selective. Often, the electrical bandwidth of detection systems cannot keep up with the spectral bandwidth [196] (see Section 3.2). As already introduced at the beginning of Section 4.1, SLDs are ideal ASE sources. Their strong directionality which leads to high radiance and high output power values, indicates a significant amount of amplified photon events. In combination with their ultra-broadband optical spectra, SLDs generate particularly interesting, extremely high MM states of light, using quantum optical terminology. It is important to recall that the introduction of the TPA interferometry method by Boitier et al. in 2009 is key for investigating the related photon statistics being the footprint of the quantum nature of light. Only then could second-order auto-correlation functions  $g^{(2)}(\tau)$  of broadband light states be analyzed in their entirety, in the sense that all contributing spectral components are simultaneously detected. Few higher-order coherence investigations of SLD- or SOA-ASE were conducted prior to 2009 [196, 130], however filtering or reducing the spectral contributions significantly below  $\Delta\lambda=1\text{nm}$ .

Secondly, SLDs are already established light sources in low-coherence applications such as in commercial OCT imaging systems [197]. Some say that OCT was the main driving force for the development of SLD technology [160]. Still today, there is a continuous effort to introduce QD SLDs in OCT systems [162, 198, 199] where the ultra-large bandwidth designs in combination with high output powers can enhance the axial resolution as well as the penetration depth into samples. The quality of first-order correlation functions is generally of paramount importance in low-coherence measurement techniques [200] for e.g. localizing the interferometric signal or improving point-spread-functions [201]. In this context, the first-order coherence functions of QD SLDs have been investigated focusing on the increase of spectral bandwidth as well as on the flatness of optical spectra for suppressing side lobes of the correlation signals [202, 203]. Apart from first-order coherence features, further fundamental light source properties are relevant to applications. Describing the intensity fluctuations of a light source, the relative intensity noise (RIN) constitutes a significant factor for the sensitivity in OCT systems [204]. The RIN of QD SLD light has been conducted in the past decade regarding spectral and polarization dependencies [205], differences with QD laser noise [206], temperature-induced ASE noise reduction [48] as well as shot noise and excess noise levels [145]. RIN is commonly determined from the spectral noise power density  $S_i(\omega)$  of a photocurrent  $i(t)$  from a detector, which is related to second-order correlations by a Fourier transform:  $S_i(\omega) = \int G^{(2)}(\tau)\exp(i\omega\tau) d\tau$  [207]. Hence, investigating the second-order coherence properties of QD SLD light means, in a wider sense, exploring the application potential of QD SLD regarding expectable detector fluctuations due to quantum noise.

And thirdly, the exploitation of QD-based gain media in SLD structures introduces a non-negligible quantum aspect for the carrier dynamics in the semiconductor material, as well as for the generation of photons. The quantized zero-dimensional carrier systems of the inhomogeneously broadened QDs generate a strong emission-state hierarchy (compare with Figure 21 (right)), which has been

investigated regarding its impact on coherence properties in recent years [145]. Further studies on QD SLD light coherence have revealed a temperature-induced reduction of the intensity correlations, while the ultra-broadband spectral emission remains unchanged [23]. This novel hybrid light state exhibits very low first-order coherence with a coherence length of  $l_c = 24\mu\text{m}$  corresponding to  $\Delta\nu_s = 12.5\text{THz}$  by simultaneously suppressing the central second-order coherence degree to  $g^{(2)}(0) = 1.33$  suggesting a considerably enhanced ratio of stimulated to spontaneous emission processes [48]. Furthermore, active media based on QDs offer reduced spontaneous emission with respect to bulk media by the higher efficiency of population inversion and smaller waveguide losses [208, 209]. All these aspects support QD SLDs as excellent candidates (platform) for quantum optics investigations at the border between ASE and stimulated emission.

**Postulation of a quantum optical state of light emitted by SLDs.** To foster the technological progress of QD SLDs, it is indispensable to develop theoretical models in close adaption to specific material systems. Sophisticated numerical models based on rate equations [210, 211] but also analytical models have been proposed [212], also in the context of QD SOAs [213] which guides future progress. However, fundamental quantum optical studies on SLD light emission regarding higher-order coherence properties have not been addressed so far<sup>16</sup>.

The outlined theory in the following is based on a quantum optical approach. This is justified by the fact that the physical nature of photon generation manifests itself in its statistics. Temporal second-order correlations are the first level of coherence at which photon statistics are reflected. Specifically, the approach is based on an assumed quantum optical state of light targeting to capture the experimental observations on first- and second-order correlations of QD SLD light. The experimental results on  $g^{(2)}(\tau)$  and  $g^{(2)}(0)$  in Section 4.2 and 4.3 will be directly compared with their calculated counterparts to identify relevant physical parameters<sup>17</sup>.

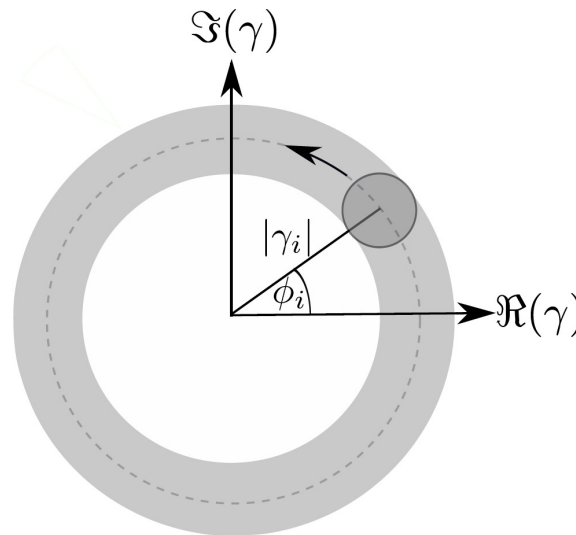


Figure 22. **Phase space diagram of a single phase-randomized Gaussian state.** This state is prepared in a thermal state displaced by  $\gamma_j = |\gamma_j|\exp(i\phi_j)$  with randomized phase angles according to Eq. (63). [Courtesy of Franziska Friedrich taken from [157]]

<sup>16</sup> Of course, quantum dot-based laser and related novel laser systems have been treated by quantum optical theory, e.g. for considering carrier-photon correlations describing higher-order correlation functions [269]. However, only recently, first approaches towards a microscopic quantum model for QD SLD light have been carried out [268]. These quantum theoretical investigations on ASE from QD SLDs are currently pursued driven by possible quantum optical mechanisms for the generation of hybrid coherent states of light [23].

<sup>17</sup> The here outlined theory has been developed by Franziska Friedrich from the theoretical quantum dynamics group lead by Prof. R. Walser at the Institute of Applied Physics (TU Darmstadt). By courtesy of F. Friedrich, all formulas are reproduced from Ref. [157] which was written in a collaborative work.

Two *ingredients* are assumed to form an appropriate quantum state of ASE generated by a QD SLD:

1. The total light state should reflect the ultra-large optical bandwidth by incorporating a high number of individual states with adaptable amplitudes for matching the observed optical power distribution of a specific experimental situation.
2. The incoherent character, mostly observed for QD SLD operated at room temperature [145], should be taken into account. It is assumed that the individual modes are not correlated with each other which is considered by no fixed phase relationship.

Accordingly, a *multimode phase-randomized Gaussian (MM PRAG) state of light* is postulated expressed by

$$\hat{\rho}_{PRAG} = \frac{1}{(2\pi)^N} \int_0^{2\pi} d^N \phi \hat{D}(\gamma) \hat{\rho}_T \hat{D}^\dagger(\gamma) \quad (63)$$

which comprises  $N$  individual PRAG states. A natural choice for an equilibrium state is the canonical operator

$$\hat{\rho}_T = e^{-\hat{H}/k_B T} / \text{Tr}\{e^{-\hat{H}/k_B T}\} \quad (64)$$

with the temperature  $T$ , the Boltzmann constant  $k_B$  and energies obeying

$$\hat{H} = \sum_{j=1}^N \hbar \omega_j \hat{a}_j^\dagger \hat{a}_j . \quad (65)$$

The multimode displacement operator

$$\hat{D}(\gamma) = \exp \left\{ \sum_{j=1}^N \gamma_j \hat{a}_j^\dagger - \gamma_j^* \hat{a}_j \right\} \quad (66)$$

allows one to account for a selectable number of modes  $N$  attributing an individual amplitude  $\gamma_j$  to each individual state (ingredient 1). By phase-randomizing the displaced state  $\hat{D}(\gamma) \hat{\rho}_T \hat{D}^\dagger(\gamma)$ , the incoherent character (ingredient 2) is included. The optical power of a specific angular frequency  $\omega_j$  is written as

$$p_j \equiv p(\omega_j) = \frac{\hbar \omega_j c}{L} |\gamma_j|^2 \quad (67)$$

where  $L$  is the length of the optical system characterizing the mode volume for an appropriate field normalization. Note that the contribution of optical power from the original thermal field  $\hat{\rho}_T$  is neglected to eliminate low frequency contributions in accordance with pure NIR emission from QD SLDs. Thus, the total optical power is

$$P = \sum_{j=1}^N p_j . \quad (68)$$

In order to calculate the temporal first-order correlation function

$$G^{(1)}(t, t + \tau) = \langle \hat{E}^{(-)}(t) \hat{E}^{(+)}(t + \tau) \rangle , \quad (69)$$

expressed here in a quantum manner according to [3] (compare with Eq. (2)), the quantized electric field with a single transverse mode and one linear polarization orientation  $\vec{e}_y$  is considered:

$$\hat{E}(t) = \sum_{j=1}^N i \sqrt{\frac{\hbar\omega_j}{2\epsilon_0 V}} \hat{a}_j e^{i(k_j z - \omega_j t)} \vec{e}_y + h.c. = \hat{E}^{(+)}(t) + \hat{E}^{(-)}(t). \quad (70)$$

Here, the plane wave propagation direction is  $z$  with wave numbers  $k_j = 2\pi j/L$ ,  $\epsilon_0$  is the vacuum permittivity and  $V$  is the mode volume comprising the longitudinal part  $L$  and the transverse single-mode cross-section. The normalized temporal first-order correlation function of a MM PRAG state results in

$$g_{PRAG}^{(1)}(\tau) = \frac{1}{P} \sum_{j=1}^N p_j e^{-i\omega_j \tau}. \quad (71)$$

The second-order correlation function is defined in a quantum manner by [3]

$$G^{(2)}(t, t + \tau) = \langle \hat{E}^{(-)}(t) \hat{E}^{(-)}(t + \tau) \hat{E}^{(+)}(t + \tau) \hat{E}^{(+)}(t) \rangle \quad (72)$$

respecting normal ordering. The normalized temporal second-order correlation function of a MM PRAG state can be evaluated to

$$g_{PRAG}^{(2)}(\tau) = 1 + \left| g_{PRAG}^{(1)}(\tau) \right|^2 - \frac{\sum_{j=1}^N p_j^2}{P^2}. \quad (73)$$

This expression resembles the Siegert-relation (Eq. (39)) which describes the second-order coherence degree as a function of first-order correlations for ideal thermal light [82]. For the here postulated PRAG state, second-order correlations are also fully determined by first-order correlation features. However, the Siegert-relation is expanded by an additional term which reduces the second-order coherence degree by a constant value depending on the optical power distribution  $p(\omega)$  of the contributing states. Using statistical parameters of  $p(\omega)$ , the central second-order coherence degree reads

$$g_{PRAG}^{(2)}(0) = 2 - \frac{\left(1 + \frac{\Delta^2 p}{\langle p \rangle^2}\right)}{N} \quad (74)$$

with the mean power  $\langle p \rangle = (\sum_j p_j)/N$  and the variance  $\Delta^2 p = \sum_j (p_j - \langle p \rangle)^2/N$ . It is interesting to realize that the photon statistics of the PRAG state depend on the number of modes  $N$  and the moments of its power distribution.

These theoretical predictions about the second-order correlation behavior for ASE generated by QD SLDs are confronted with experimental observations, presented in the following two sections. First, the number of modes  $N$  emitted by a QD SLD is manipulated for testing the validity of Eq. (74) (Section 4.2). In a second experiment, QD SLD light and coherent laser light are superposed, which leads to slight extensions of Eq. (73) and (74). Direct comparison between experimentally obtained and calculated  $g^{(2)}(0)$ -values as well as  $g^{(2)}(\tau)$ -functions are performed (Section 4.3).

## 4.2. Coherence control via broadband optical feedback

Eq. (74) predicts a crucial dependency of the central second-order coherence degree on the number of modes  $N$ . The ideal thermal value of  $g^{(2)}(0) = 2$  is reduced by a term which is inversely proportional to  $N$ . Figure 23 shows trajectories of  $g^{(2)}(0)$  as a function of  $N$  for four different values of the statistical parameter  $\Delta^2 p / \langle p \rangle^2$ . Figure 23 (left) suggests that for a high number of modes,  $g^{(2)}(0)$  should take values very close to 2. In contrast, these values are supposed to decrease significantly when  $N$  reduces below 50. All four calculated trajectories show a steep drop down to  $g^{(2)}(0) = 1$  for values of  $N < 10$ . The enlarged section for high number of modes (Figure 23, right) reveals small deviations from 2. With respect to the TPA interferometer precision (Section 3.2, Figure 18), an appropriate experiment should provide a strong impact on the number of modes emitted by the QD SLD for accessing the regime of central second-order *coherence drop*.

An experimental technique which yields generally a considerable influence on the optical properties of an opto-electronic emitter, is the application of optical feedback. In this case, well-controlled broadband optical feedback (OFB) is applied to a QD SLD.

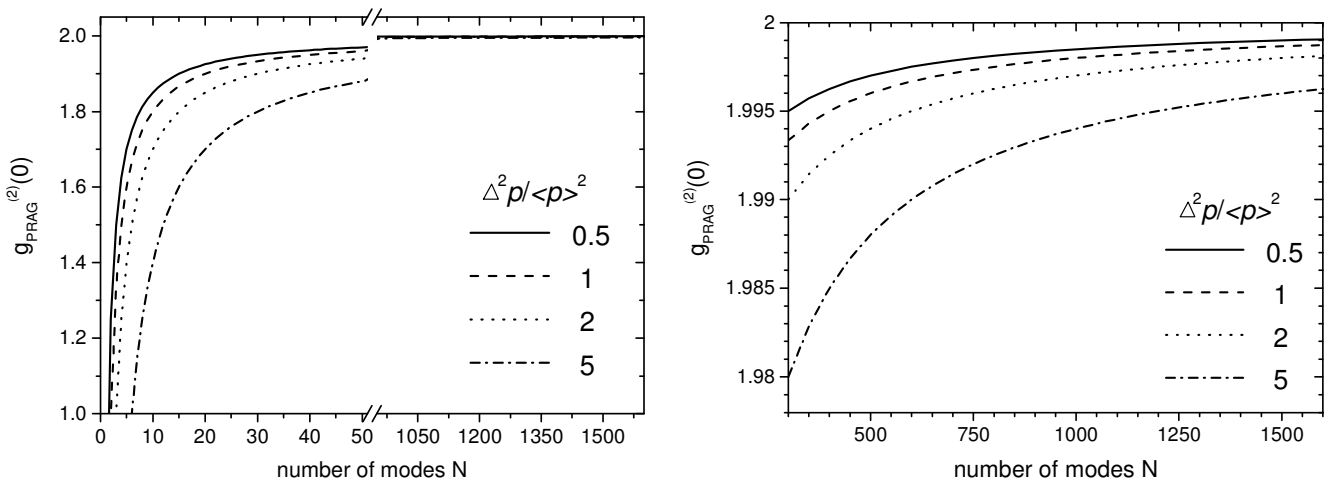


Figure 23. Central second-order coherence degree of a MM PRAG state as a function of the number of contributing modes  $N$ . Exemplary trajectories for four different values of  $\Delta^2 p / \langle p \rangle^2$  are depicted for a range of  $0 < N < 1650$  (left) and an enlarged section for higher number of modes  $300 < N < 1600$  revealing the trajectories on a small  $g^{(2)}$ -scale (right).

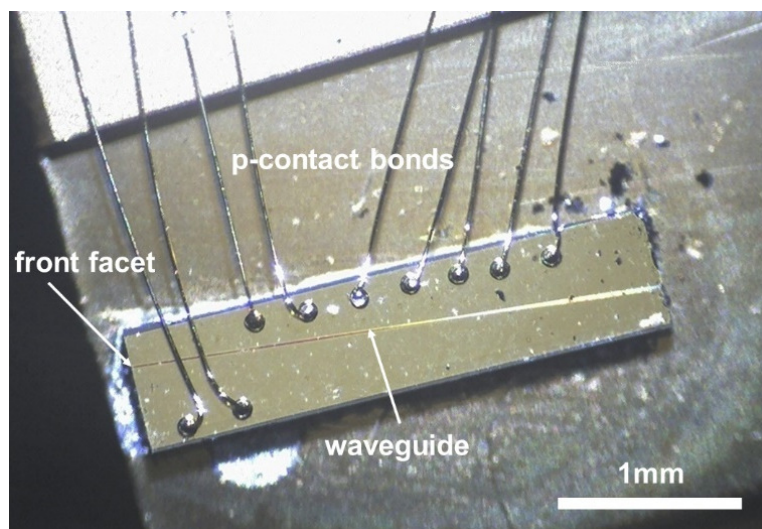


Figure 24. Microscopic picture of the SLD. The SLD was epitaxially grown by the University of Sheffield and processed by Thales III-V Lab (Palaiseau, Paris) within the European project Nano UB-Sources (device number: VN590).

**The QD SLD device.** The active medium of the investigated QD SLD consists of six identical self-assembled InAs QD layers embedded in InGaAs quantum-well layers (DWELL system [205]) realizing light emission in the NIR in the range between 1120 and 1340 nm with a maximum output power of about 1 mW. The device is a 3 mm long, 5°-tilted, AR coated ridge waveguide QD SLD (Figure 24) driven by a DC current source (Thorlabs LDC 8020) up to 900 mA and it is temperature-stabilized at 20.5°C (Thorlabs TED 8020). Without OFB, the broadband emission of the QD SLD is governed by a hierarchic emission of GS, ES and SES yielding spectral bandwidths between 120nm and 60nm. The P-I characteristic as well as the optical spectrum behavior with increasing injection current of this specific QD SLD have been already presented in Section 4.1 (Figure 21).

**Optical feedback experiment.** Front-facet OFB is realized straightforwardly by splitting the collimated light emission from the QD SLD by a broadband 50:50 beamsplitter and reflecting the light back into the waveguide with a mirror forming a total feedback distance of 600 mm (Figure 25). The amount of OFB intensity is controlled via a variable attenuator. Small feedback strengths<sup>18</sup> below 5% result in a smooth narrowing of the ultra-broadband optical spectra down to  $\Delta\lambda_s = 15\text{nm}$ , with ASE ripples becoming more and more significant. High feedback strengths up to the maximum of 25% induces strong spectral narrowing with MM emission operation. There, the frequency spacing of the modes clearly corresponds to the QD SLD waveguide length of 3mm. It is emphasized that system dynamics caused by OFB operation are avoided by delicately choosing OFB adjustments where the permanently monitored optical spectrum shows a stable, static emission during the measurement. In this study, dynamical regimes where OFB on QD-based emitters can lead to highly nonlinear and chaotic behavior [214], especially when one deals with low-gain regimes [215], are explicitly not of interest. For the purpose of stability, an interference filter with a FWHM of 10nm was optionally inserted whenever instabilities were observed, especially at higher feedback strengths. The beamsplitter output is utilized to couple the light into a SM fiber which guides the light into the TPA interferometer for analyzing the second-order coherence degree. In this case, the TPA detector was a reflection-mode photomultiplier (Hamamatsu R928) incorporating a multi-alkali photocathode. The experimental  $g^{(2)}(0)$  determination was performed according to the methods described in Section 3.2.

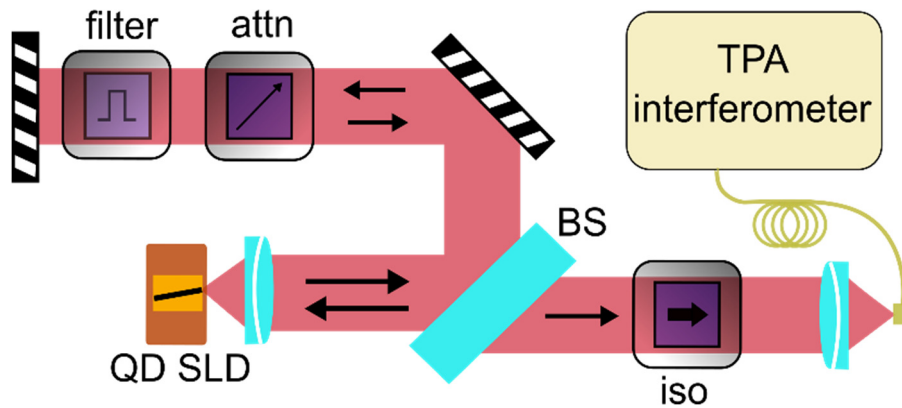


Figure 25. **Schematic diagram of the optical feedback experiment.** The free-space emitting SLD is split by a non-polarizing 50:50 beamsplitter (BS). The broadband feedback arm comprises a variable attenuator (attn) and an optional interference filter (filter) yielding  $\Delta\lambda_{FWHM}=10\text{nm}$ . The second BS output is guided through an optical isolator (iso) to prevent further optical feedback effects and finally the light is sent to  $g^{(2)}(\tau)$ -analysis.

<sup>18</sup> The feedback strengths are estimated by utilizing the second output direction of the beamsplitter (Figure 25) respecting the 50:50 split ratio. Note that these values are ideal values not taking into account coupling losses into the waveguide.

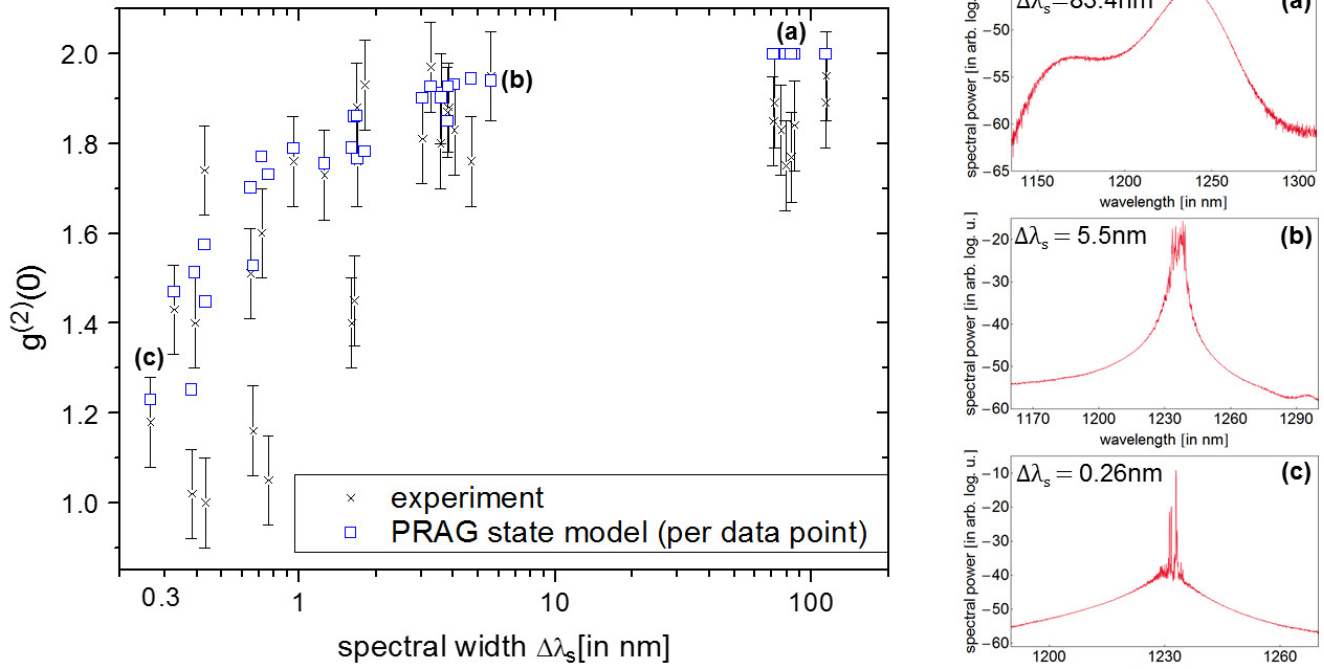


Figure 26. Central second-order coherence degree under broadband optical feedback as a function of the spectral width. The indications (a), (b) and (c) are exemplary data points for which the optical spectra (over wavelength) are depicted on the right-hand side.

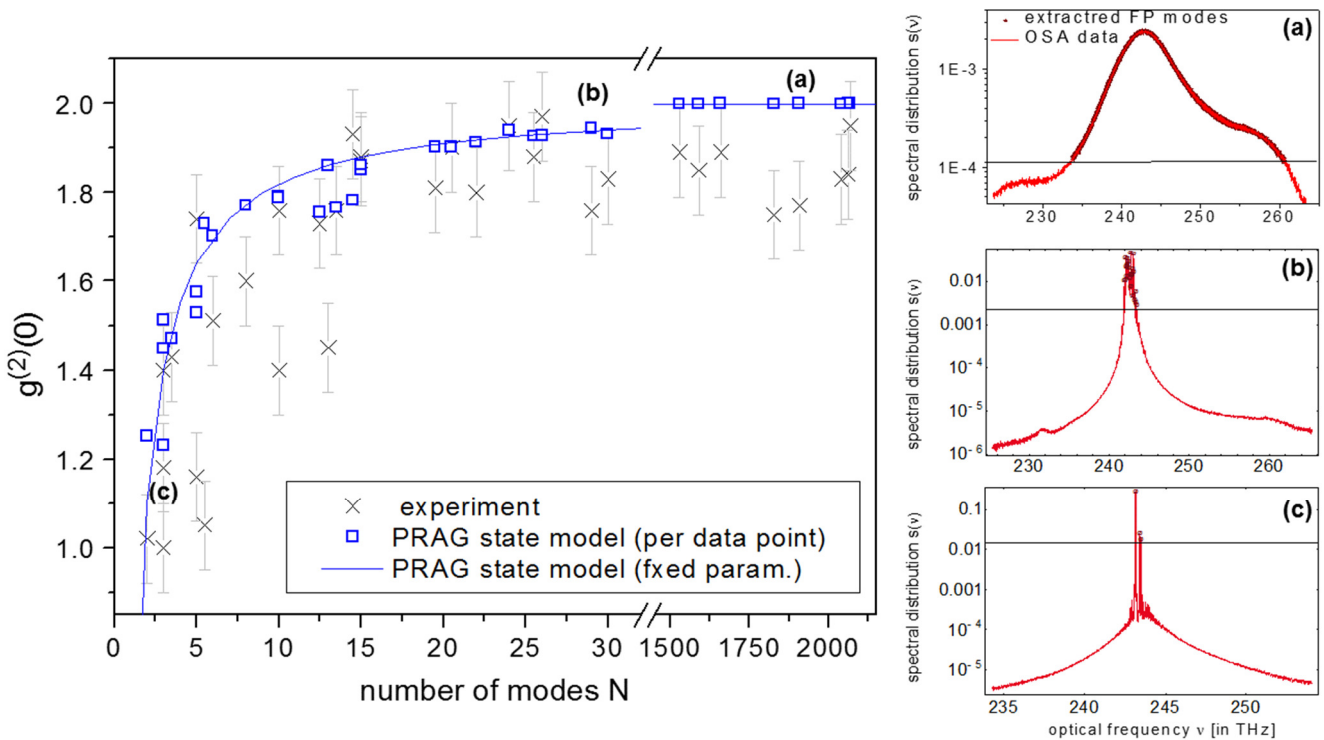


Figure 27. Central second-order coherence degree under optical feedback as a function of the number of modes. The indications (a), (b) and (c) are exemplary data points for which the optical spectra (over optical frequency) are depicted on the right-hand side, together with indications of the extracted modes (darker red data) on the basis of the 13dB threshold (horizontal solid line).

**Results.** Figure 26 shows the experimental results of  $g^{(2)}(0)$  as a function of the spectral bandwidth  $\Delta\lambda_s$  together with three selected spectra to illustrate the corresponding different emission conditions. For broadband emission with  $\Delta\lambda_s > 60\text{nm}$ , an average value of  $\overline{g^{(2)}(0)} = 1.83$  is found which indicates nearly thermal photon statistics<sup>19</sup>. Even for high feedback intensities with strong spectral narrowing down to  $\Delta\lambda_s = 3\text{nm}$ , thermal statistics is maintained with  $g^{(2)}(0)$  values between 1.75 and 1.98. By decreasing the spectral bandwidth even further, a reduction of  $g^{(2)}(0)$  from 1.85 down to 1.0 is clearly visible thus reflecting a change in second-order coherence from a thermal to a coherent state. The ultimate coherent limit  $g^{(2)}(0) = 1.0$  is reached for two data points at a spectral bandwidth of approximately 0.4nm. Despite a high experimental variability of  $g^{(2)}(0)$  values in the vicinity of the photon statistics transition, probably due to complex MM emission compositions, this first result demonstrates that a simultaneous tailoring of first- and second-order coherence of light emitted by a QD SLD via well-controlled OFB can be achieved. Figure 26 reveals a complete coherence transition from spectrally broadband emission with thermal-like photon statistics to spectrally narrow emission with Poissonian photon statistics.

Table 4. Representative set of data of the OFB experiment.

$\Delta\lambda$ [in nm]	$N$	$\Delta^2 p / \langle p \rangle^2$	$g_{exp}^{(2)}(0)$	$g_{PRAG}^{(2)}(0)$
0.26	3	1.31	1.18	1.23
1.26	13	2.12	1.73	1.76
4.04	30	1.08	1.83	1.931
83.4	1908	0.81	1.84	1.999

In order to draw a direct comparison with the PRAG state predictions, the number of modes emitted by the QD SLD has to be considered. The continuous transition of the central second-order coherence degree (Figure 26) is now depicted in Figure 27 as a function of the number of emitted modes  $N$ , extracted from the measured optical spectra. Note that it is essential to exclude non-relevant spectral contributions which can falsify the statistical parameters of  $p(\omega)$  (Eq. (67)). Thus, solely power levels with a maximum deviation of 13dB below the maximum  $p_{max}(\omega)$  are taken into account. The corresponding theoretical values according to Eq. (74) are evaluated per data points with the experimentally extracted parameters  $N$ ,  $\langle p \rangle$  and  $\Delta^2 p$  in order to reproduce the experimental conditions as best as possible. Numerical values are tabulated in Table 4 for reference. For ultra-broadband QD SLD emission,  $N$  reaches very high values. Here, the number of modes could not be enumerated straightforwardly by counting spectral peaks because smooth Gaussian-like spectral shapes dominate (Figure 27, a)). Therefore,  $N$  remains experimentally undeterminable. However, a lower bound estimate is given by the number of FP modes matching the length  $L=3\text{mm}$  of the QD SLD waveguide similar to a MM laser but here with strongly broadened and overlapping longitudinal modes. In practice,  $N$  has been determined by fitting modes to the measured optical spectra with a spacing according to the free spectral range (FSR) in terms of frequency

$$\Delta\nu_{FSR} = \frac{c}{2n_{GaAs}L} \approx 1.465 \times 10^{10} \text{Hz}. \quad (75)$$

<sup>19</sup> The discrepancy of  $\Delta g^{(2)}(0) \approx 0.17$  between the experimental values and the ideal thermal value of 2 is attributed to two main experimental issues at this early stage of TPA interferometer development. First, the multi-alkali based PMT exhibits a relatively low sensitivity compared to the later implemented semiconductor-based PMT (Section 3.2). Additionally, a utilized plate beamsplitter introduced a non-negligible dispersion effect within the TPA interferometer acting on  $g^{(2)}(0)$ , which was later eliminated by the use of beamsplitter cubes.

by assuming a refraction index of the GaAs waveguide of  $n_{GaAs}=3.41$  and respecting the previously mentioned 13dB cutoff. In this broadband regime, mode numbers  $N>1000$  are observed together with experimental values of  $g^{(2)}(0)$  fluctuating around 1.85 while theoretical values (blue data) amount to  $g_{PRAG}^{(2)}(0) = 1.999$ , very close to the limit value of 2 for pure thermal states. Again, the specified mode numbers  $N$ , indicated in Figure 27 (a) (darker red points), are lower bound estimates. However, regarding Figure 23 (right), the experimentally determined values of  $\Delta^2 p / \langle p \rangle^2$  (see Table 4) of about 0.8 lead to values of  $g_{PRAG}^{(2)}(0)$  at  $N>1000$  being clearly restricted to values above 1.99 taking the uncertainties of  $\Delta g_{PRAG}^{(2)}(0)$  to below 1%. Entering the regime of directly countable mode numbers  $N=30$  down to  $N=15$ , high central second-order coherence degrees above 1.8 are observed but already with a slightly decreasing tendency. This agrees with the calculated values (Figure 27, blue data) which show a less-fluctuating trajectory. The steep transition is located in the range of  $1<N<15$  (compare with extracted  $p(\omega)$  data in Figure 27 (b) and (c)) where experimental values are reducing from  $g^{(2)}(0) = 1.8$  to  $g^{(2)}(0) = 1.0$ . The calculated values reveal that the model agrees with the region of coherence transition which is also valid with respect to the spectral width (see blue data in Figure 26). However, a residual photon-bunching degree of  $g_{PRAG}^{(2)}(0) = 1.23$  doesn't agree completely with the experimentally obtained minimum value. Strongly deviating values are due to challenging experimental conditions concerning the stabilization of the QD SLD emission under OFB during the measurement.

**Conclusion.** This first result-section demonstrates that in a wide range, a simultaneous tailoring of first- and second-order coherence properties of light emitted by a QD SLD can be achieved by well-controlled OFB. The central second-order coherence degree as a function of both, the spectral width  $\Delta\lambda_s$  and the number of modes  $N$  is tailorable in the range of 1.98 to 1.0. Despite considerably fluctuating experimental values and some disagreeing data points between theory and experiment, the overall coincidence and the observed trends of theory and experiment are more than obvious. Therefore, it can be confirmed that the coherence transition is indeed triggered by the strongly reduced number of existing emission modes  $N$  and the slightly enhanced ratio of  $\Delta^2 p / \langle p \rangle^2$ . Beyond the here presented second-order correlation results, relative intensity noise investigations from earlier work confirm the coherence transition in terms of a change from pure excess noise to shot noise behavior [135, 156]. Very recently it has been shown that coherence properties of thermal-like photons can be shaped subsequently after emission [216]. In contrast, here a direct intervention into the emission process was realized.

Unfortunately, the coherence transition is observed for a very low number of modes where the QD SLD no longer exhibits smooth broadband spectra. The reason for significant second-order coherence changes only for  $N<15$  lies in the relatively small values of  $\Delta^2 p / \langle p \rangle^2$  in the range between 1 and 3. For broadband emission with tens of nanometer spectral widths and Gaussian-like spectral shapes, even lower values  $\Delta^2 p / \langle p \rangle^2 < 1$  are found which fix second-order coherence degrees quickly to  $g^{(2)}(0) \approx 2$  by increasing  $N$  (Figure 23). The drawback of these results is therefore the loss of the broadband emission property of the QD SLD, and hence the accuracy of the PRAG state as an accurate model for the broadband ASE regime of the QD SLD still requires more evidence. Additionally, instabilities due to OFB induced carrier dynamics could act on the correlations of the light generation [215].

Consequently, a second experimental approach with priority on the conservation of the broadband ASE regime of QD SLD operation is taken, which is presented in the next section.

---

### 4.3. Coherence control by mixing incoherent SLD light with coherent laser light

This section deals with a second, now extrinsic approach on tailoring first- and second-order coherence properties of QD SLD light. Following the concluding reasoning of the previous section, the QD SLD emission is now left unaffected in order to preserve its characteristic ultra-broadband ASE regime. To introduce significant changes in the coherence behavior, a fully coherent light state from a single-mode laser emission is superimposed onto the broadband QD SLD emission. Consequential, extrinsic control for changing the combined first- and second-order correlation properties, is given by the intensity ratio between both light components. The coherent light state thereby probes the accuracy of the assumed PRAG state via the combined photon statistical behavior.

This approach is based on the concept of *mixed-light* which has been subject to extensive experimental and theoretical studies starting shortly after the invention of the laser in the 1960s, in connection with photon counting methods and the newly developed HBT experiment [217, 218, 219, 220, 221]. Recently, mixed-light states with PT light have been investigated demonstrating the continuous tunability of photon statistics [123]. In the next section, the mixed-light phenomenon is extended to highly first-order incoherent light sources which is termed *ultra-broadband mixed-light*.

**The ultra-broadband mixed-light scheme.** A schematic diagram of the mixed-light experiment is shown in Figure 28. Coherent light is provided by a commercial discrete-mode diode laser (single-mode (SM) laser, Eblana Photonics). Similar to a DFB laser, a waveguide grating structure provides single frequency emission with a narrow linewidth ( $\Delta\nu < 2\text{MHz}$ , manufacturer's specifications) when operated well-above laser threshold. The QD SLD exhibits a 4mm long waveguide consisting of a triple-chirped epitaxial structure made of 10 InAs/InGaAs DWELL QD layers (grown by Innolume GmbH). Figure 29 (right) depicts a schematic diagram of the chip (processed by Thales III-V Lab). The waveguide has a bended structure which is barely visible in the microscopic picture (see Figure 29, left). From the AR coating indications, one can derive that this device was designed as a gain chip for external-cavity configurations. However, the diode is operated without OFB and with a continuous forward bias, which enables ultra-broadband ASE emission. The emitted light beams from both sources are guided through optical isolators, ensuring controlled emission conditions. The superposition of the two light sources is implemented by fiber-coupling both beams into a 50:50 fiber combiner. Variable attenuators enable a controlled tuning of the power ratio between the coherent and the incoherent light constituents. In Figure 30, a representative optical spectrum of the superposed light is depicted. In this case, the power ratio was adjusted to 1:1, monitored at the second output of the fiber BS. On the one hand, one can recognize spectrally separated spectral distributions of the two sources. The SM laser is located at  $\bar{\lambda}_L = 1300.0\text{nm}$  whereas the QD SLD (operated at  $I_p = 300\text{mA}$ ) is centered at  $\bar{\lambda}_{SLD} = 1237.0\text{nm}$  which leads to an expectable beat frequency of  $\omega_{SLD} - \omega_L \approx 7.38 \cdot 10^{13} \text{ 1/s}$ . On the other hand, the differing optical bandwidths are clearly visible. While the ultra-broad spectral width of the QD SLD amounts to 65.7nm or 12.9THz in terms of wavelength and frequency, respectively, the linewidth of the SM laser cannot be resolved by the utilized OSA. The operating conditions of the two light sources corresponding to the spectral properties described above, are fixed. It is however clear that with varying the power ration between the two light constituents, the overall mean wavelength as well as the mean spectral width are changing. Finally, the superimposed light within the SM fiber is guided into the TPA interferometer for the second-order coherence analysis.

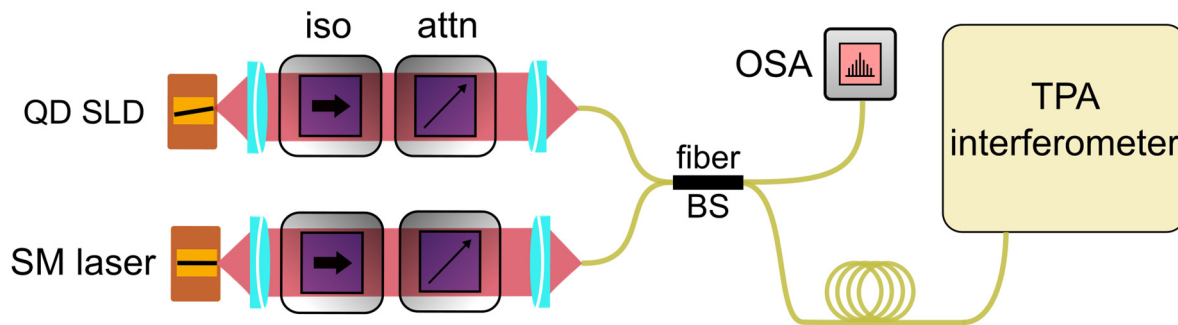


Figure 28. **Schematic diagram of the mixed-light experiment.** The power ratio between laser light (SM laser) and SLD light (QD SLD) is controlled by variable attenuators (attn). Optical isolators (iso) prevent back-reflections into the emitters. A fiber combiner (fiber BS) enables a simple implementation of the two light fields, which is then guided into the TPA interferometer and to a commercial OSA (ADVANTEST Q8384). Note, the TPA detector from Section 4.2 (Hamamatsu R928) has been exchanged by a semiconductor-based head-on PMT (Hamamatsu H7421-40) with enhanced sensitivity [135].

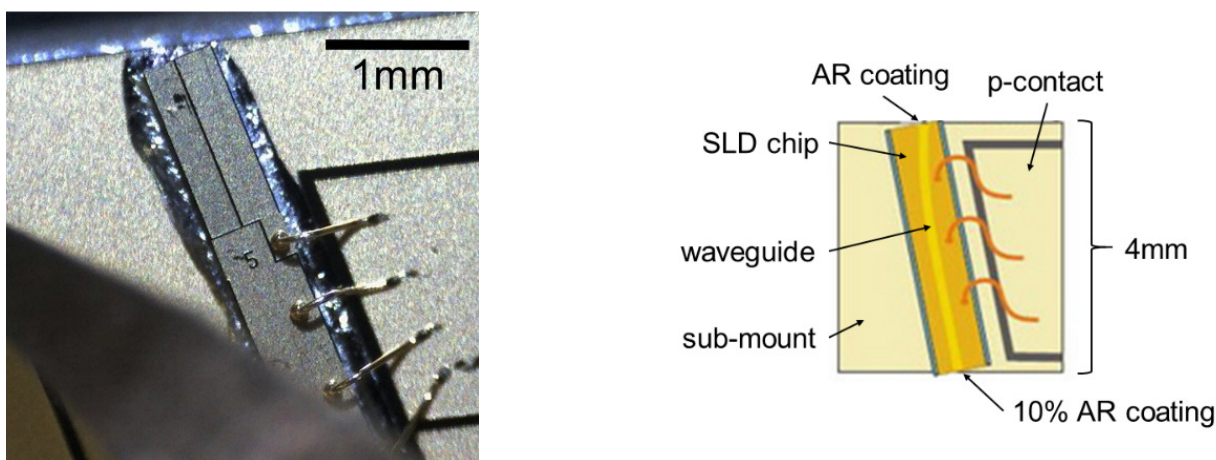


Figure 29. **SLD in operation.** Left: Microscopic picture from top. Right: Chip schematics showing the bended waveguide structure, the sub-mount dimensions and the AR coating specifications.

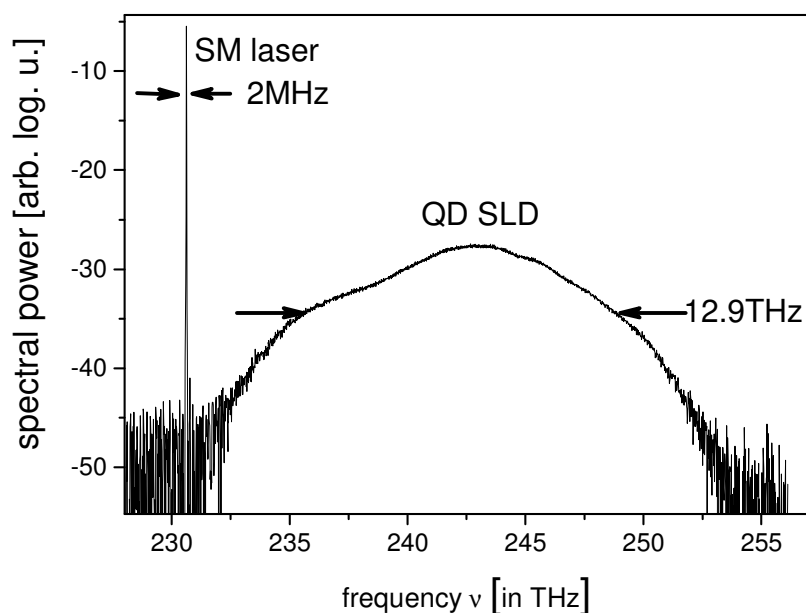


Figure 30. **Representative optical spectrum of the superimposed light** measured by a commercial OSA. The optical frequencies have been translated from a measured wavelength abscissa. The indications on the spectral width is assumed according to the manufacturer specification (SM laser) and determined by the Suessmann measure (QD SLD). Here, a power ratio of 1:1 between laser and SLD light has been adjusted.

**The mixed-light state.** For deriving theoretical counterparts of experimentally obtained second-order coherence degrees, the PRAG state model must be expanded by a coherent contribution. From the experimental setup (Figure 28), it is obvious that the two sources are independent from each other. Thus, one can express the superposition by

$$\hat{\rho}_m = \hat{D}(\alpha_k) \hat{\rho}_{PRAG} \hat{D}^\dagger(\alpha_k) \quad (76)$$

with the single-mode displacement operator  $\hat{D}(\alpha_k) = \exp\{\alpha_k \hat{a}_k^\dagger - \alpha_k^* \hat{a}_k\}$ . In other words, a coherent amplitude  $\alpha_k$  in mode  $k$  with angular frequency  $\omega_k$  is added to the PRAG state. Neglecting again the thermal state contributions of the PRAG state definition, the first-order correlation function of the mixed-light state results in

$$G_m^{(1)}(\tau) = \sum_{j=1}^N e^{-i\omega_j \tau} \{p_j^{PRAG} + p_j^c\} \quad (77)$$

with the power of the single-mode coherent contribution of

$$p_j^c = \frac{\hbar \omega_j c}{L} |\alpha_j|^2 \delta_{jk} . \quad (78)$$

One can show that the modulus of the normalized first-order correlation function reads

$$\left|g_m^{(1)}(\tau)\right|^2 = \frac{1}{(P_{PRAG} + P_c)^2} \left\{ P_c^2 + \left| \sum_{j=1}^N p_j^{PRAG} e^{-i\omega_j \tau} \right|^2 + 2P_c \sum_{i,j=1}^N p_j^{PRAG} \cos\{(\omega_j - \omega_k)\tau\} \right\} , \quad (79)$$

$P_{PRAG}$  and  $P_c$  being the total optical powers of the PRAG state and the coherent state, respectively. The last term results from the beat frequency between the coherent mode and the  $j$ -th mode of the PRAG state. The normalized second-order correlation function can then be derived to

$$g_m^{(2)}(\tau) = 1 + \left|g_m^{(1)}(\tau)\right|^2 - \frac{P_c^2 + \sum_{j=1}^N (p_j^{PRAG})^2}{(P_{PRAG} + P_c)^2} \quad (80)$$

where the time-dependence only arises from the modulus of Eq. (79). Just like Eq. (73), the coherence degree reduction term (third term in Eq. (80)) is time-independent and fully determined by first-order coherence properties, however here with PRAG state as well as coherent state components. Finally, it should be noted that the exact derivations of the above outlined expressions can be found in detail in Ref. [157] (see Footnote 17).

**Results: Temporal second-order correlations.** In the first place, the second-order correlation functions of both light sources are investigated separately to establish the initial states. Figure 31 depicts measured TPA interferograms (bottom, black line), the correspondingly extracted  $g^{(2)}(\tau)$ -functions (top, red line) as well as calculated counterparts  $g_m^{(2)}(\tau)$  (blue line) of the QD SLD (left) and the SM laser (right).

The extremely large spectral width of the QD SLD, synonymous for a highly pronounced first-order incoherence, results in very short correlation timescales. This is confirmed in Figure 31 (bottom, left) where correlations are visible solely on the scale of approximately  $\pm 125$ fs on the recorded TPA interferogram. Figure 31 (top, left) depicts  $g^{(2)}$ -functions determined experimentally as well as calculated by the PRAG state model (Eq. (73)) using experimental parameters taken from the corresponding optical spectra:  $N$ ,  $p_j^{SLD}(\omega)$ ,  $P_{SLD}$  and  $\left|g_{SLD}^{(1)}(\tau)\right|^2$  using Eq. (71). Note that an index *SLD*

is introduced to differ its experimental parameters from those of the laser which will be indexed by  $L$ . Just as for the OFB experiment,  $N$  is estimated by taking the lower bound of possibly contributing modes, namely the number of FP modes fitting into the measured spectral distribution function with spacing corresponding to the FSR with respect to the 4mm long waveguide:  $\Delta\nu_{FSR} \approx 1.099 \times 10^{10}$  Hz. One can recognize that the experimental and the theoretical functions coincide well. The experiment reveals an ultrashort coherence time<sup>20</sup> of  $\tau_c = (100 \pm 2)$  fs as well pronounced intensity correlations with a central second-order coherence degree of  $g^{(2)}(0) = 1.91 \pm 0.05$ . The theoretical counterpart agrees nicely with the time-dependence and certifies a globally, highly incoherent state of light with thermal-like photon statistics ( $g_{PRAG}^{(2)}(0) = 1.999$ ) for the QD SLD emission. In contrast, the second-order correlation analysis of the SM laser delivers an approximate constant value of  $g^{(2)}(\tau) = 1.01 \pm 0.04$  (Figure 31, top, right) which reveals a highly coherent light source character, not only showing high-quality monochromaticity reflected by the fully modulated interference fringes of the TPA interferogram (Figure 31, bottom) but also a central second-order coherence degree of  $g^{(2)}(0) = 1.00 \pm 0.01$  reflecting a Poissonian photon statistics behavior<sup>21</sup>. Obviously, a constant value of  $g_c^{(2)}(\tau) = 1$  is depicted as the theoretical expectation according to Eq. (24).

In case of superimposed light fields, the combination of the fiber-coupled optical powers of the two light sources can be quantified by a power ratio between the SM laser  $P_L$  and the QD SLD  $P_{SLD}$ . Taking a closer look at Eq. (80), the importance of the power ratio can already be surmised. To make its dependency on second-order correlations of the mixed-light even more clear, a relative quantity is introduced which is

$$\zeta = \frac{P_L}{P_L + P_{SLD}} \quad (81)$$

constraining the power ratio measure  $\zeta$  to a range between 0 (exclusive QD SLD emission, Figure 31 (left)) and 1 (exclusive laser emission, Figure 31 (right)). Applying  $\zeta$  to the theoretical results of the mixed state of light, Eq. (80) can be rewritten as

$$g_m^{(2)}(\tau) = 1 + |g_m^{(1)}(\tau)|^2 - \zeta^2 - \frac{(1 - \zeta)^2}{N} \left\{ 1 + \frac{\Delta^2 p^{SLD}}{\langle p^{SLD} \rangle^2} \right\} \quad (82)$$

which will be used for calculating the theoretical counterparts in the following mixed-light coherence investigation. Figure 32 (bottom) shows an exemplary TPA interferogram corresponding to a power ratio adjustment of  $\zeta = 0.6$ . The interferogram exhibits a shape that includes features from both sources: (i) a long range ( $\tau \gg \tau_c$ ) intensity modulation originating from the laser emission but with non-zero destructive interference maxima that show already the interplay of both light fields, and (ii) an enhanced correlation for ( $\tau < \tau_c$ ) originating from the QD SLD emission. Additionally, a clear modulation of the envelope is visible indicating the beating of the two light fields. The experimentally extracted as well as the calculated  $g^{(2)}$ -functions in Figure 32 (top) show well-coinciding trajectories. The beat-like signal modulation of the envelope of the interferogram translates into secondary maxima  $g^{(2)}(\pm\tau_2)$  originating from the beating of the ensemble of all mixed-light frequencies. The dominating beat occurs from the beating of the mean frequencies of both fields resulting in a beat-time of  $\tau_{beat} = \tau_2 \approx 76$  fs. The theoretical model reproduces both the proper time scales,  $+\tau_2$  and  $-\tau_2$ , and the absolute values of the secondary maxima,  $g^{(2)}(\pm\tau_2) = 1.1$ . Regarding vanishing time delays, the experiment reveals second-order coherence degree of  $g^{(2)}(0) = 1.64$ , clearly differing from values of both individual emission states

<sup>20</sup> The coherence time is determined by extracting the real part of the absolute square of  $g^{(1)}(\tau)$  applying a bandpass method to the TPA interferogram. Subsequently, Eq. (9) can be applied such that the given coherence time coincides with the Suessmann measure which is utilized consistently throughout the thesis. See Section 5.3 for more details about the extraction method.

<sup>21</sup> Due to the limited range of the translation stage moving the mirror inside the interferometer, this value has been double-checked via the photon-counting experiment determining the explicit photon number distribution  $P(n)$ , validating  $g^{(2)}(0) = 1.00$ . This allows one to normalize the TPA interferogram in the regime of pure laser modulation, still showing interference. The reader is referred to Section 3.1 where the identical laser has been considered.

which is also confirmed by theory with a value  $g_m^{(2)}(0)=1.63$ . Slight deviations between theory and experiment are observed in the range of  $-\tau_2 < \tau < 0$  and  $0 > \tau > \tau_2$  where the experimental resolution does not allow recording the theoretically predicted minima falling below  $g_m^{(2)}(\tau) = 1$  (at  $25\text{fs} < \tau < 60\text{fs}$  and  $-60\text{fs} < \tau < -25\text{fs}$ ).

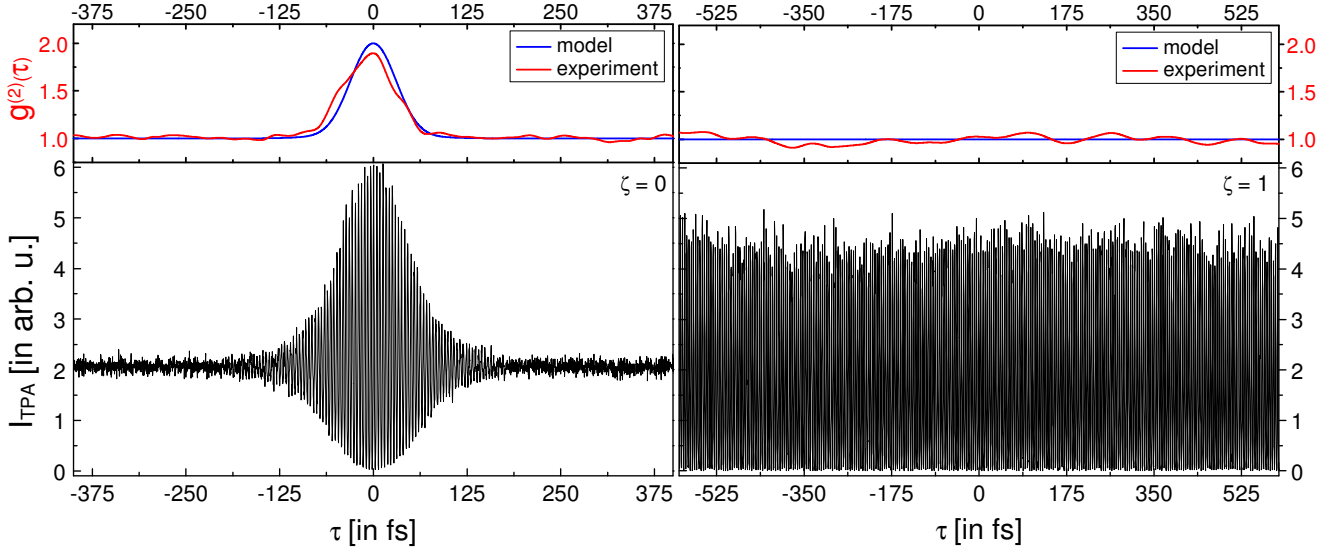


Figure 31. **Individual second-order correlations** of (left) SLD light and (right) laser light. Bottom: Measured TPA interferogram. Top: Extracted second-order correlations functions (red) and calculated functions (blue) according to Eq. (73) on the basis of measured optical spectra (Figure 30).

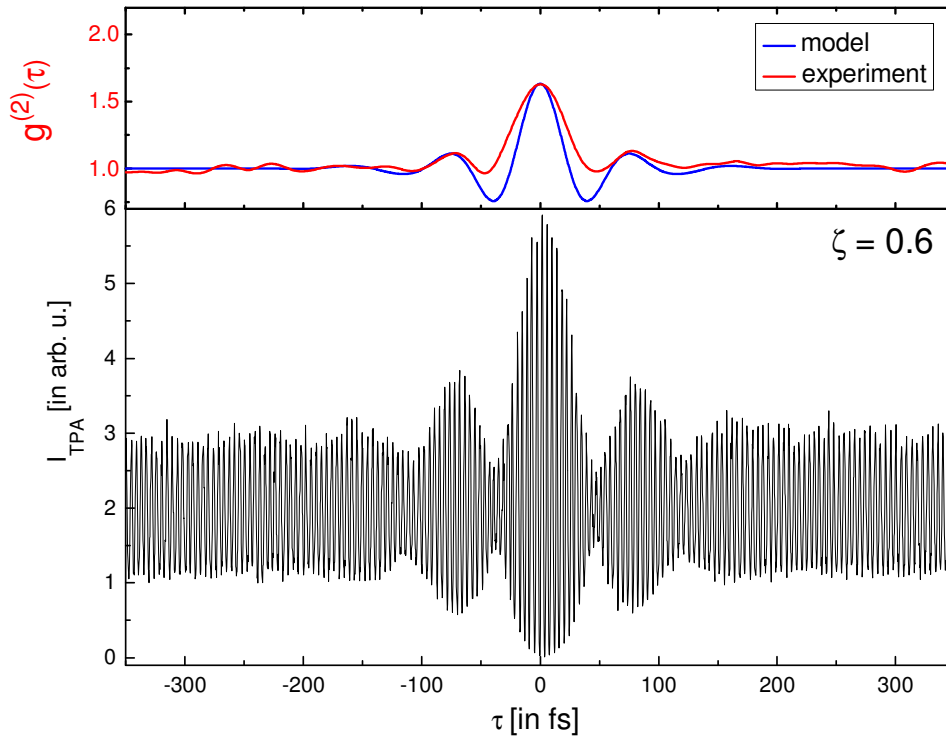


Figure 32. **Exemplary second-order correlations of a mixed-light scenario with a power-ratio of  $\zeta = 0.6$** . Bottom: TPA interferogram. Top: Extracted second-order correlations functions (red) and calculated functions (blue) according to Eq. (82) on the basis of a measured optical spectrum (comparable to Figure 30).

### Results: Continuous tuning of the central second-order coherence degree.

Investigating  $g^{(2)}(0)$  as a function of  $\zeta$  (Figure 33), a full-range, continuous tunability in the range of 1.91 and 1.0 with a parabola-like trajectory is observed. To the best of one's knowledge, this is the first demonstration of the mixed-light phenomenon that includes an ultra-broadband light source. Figure 33 also depicts the theoretical values (blue data) obtained from the derived analytical expression (Eq. (82)) calculated with the experimentally determined parameters. In Table 5, two exemplary sets of data are given representing one high and one low coherence degree. Comparing the theoretical and the experimental trajectories, an overall good agreement with excellently coinciding values for  $\zeta \geq 0.6$  within the statistical uncertainties is noted whereas slight deviations for  $\zeta < 0.6$  are apparent. The latter is again attributed to the previously discussed experimental challenges such as TPA sensitivity and dispersion effects<sup>22</sup>. Nevertheless, an overall good reproduction of photon statistical behavior is observed in this mixed-light experiment by the analytical quantum theoretical considerations based on the superposition of a well-known coherent light state and the assumed PRAG state. Thus, one can deduce that the broadband light states generated by the ASE of the QD SLD are well described by the PRAG states.

Table 5. **Exemplary mixed-light data.** Experimentally obtained and calculated values according to Eq. (80)

$\zeta$	$N$	$\Delta^2 p^{SLD} / \langle p^{SLD} \rangle^2$	$g_m^{(2)}(0)$	$g^{(2)}(0)$ (exp.)
$0.83 \pm 0.03$	1990	0.83	1.28	$1.28 \pm 0.03$
$0.34 \pm 0.03$	1990	0.83	1.86	$1.79 \pm 0.04$

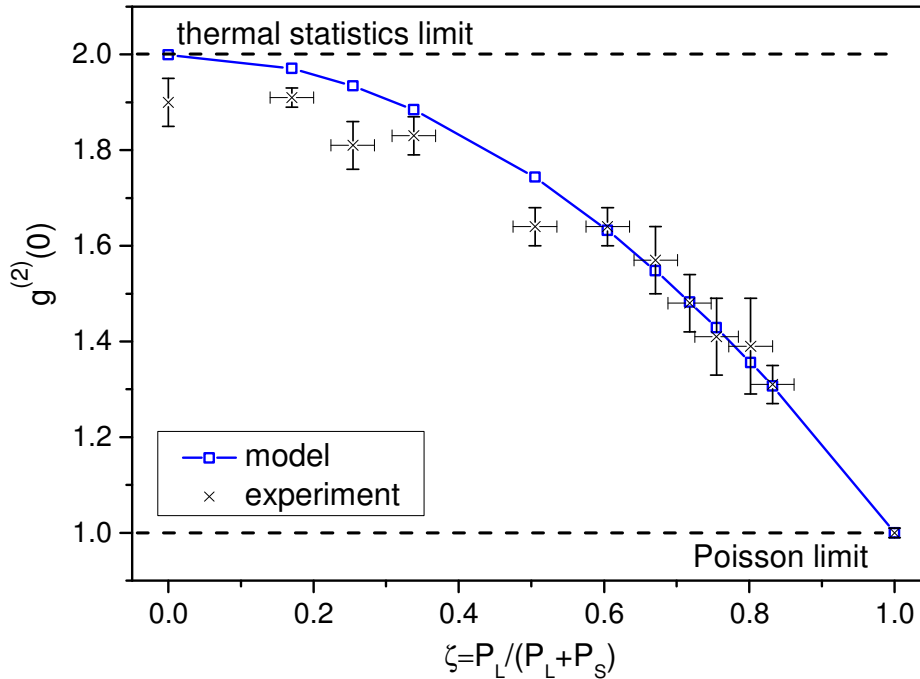


Figure 33. **Ultra-broadband mixed-light: experimental data and model values of the central second-order coherence degree.** The theoretical limits of ideal thermal and coherent light values are indicated by horizontal lines as a guide-to-the-eye. Model values are calculated according to Eq. (82) at  $\tau = 0$  on the basis of measured optical spectra (Figure 30).

<sup>22</sup> Note that the aspect ratio of the TPA interferogram in Figure 31 (bottom, left) is 1:3 with respect to the horizontal axis. An ideal thermal behavior would yield an aspect ratio of 1:4 (see Figure 15). However,  $g^{(2)}(0)$  values have already been improved compared to the OFB experiment due to the use of a more sensitive PMT (Footnote 19). The main coherence degree reduction-mechanism is chromatic dispersion in the TPA interferometer, which is supported by the fact that for increasing the values of  $\zeta$ , i.e. an overall narrowing of the mixed spectral distribution, the experimental trajectory and the mixed-light theory match nearly perfectly.

---

**Conclusion.** In conclusion, a second experiment on simultaneous tailoring first- and second-order coherence properties of QD SLD light has been realized. The drawback of spectrally narrowing the QD SLD emission in the OFB experiment was rectified by the mixed-light approach. The superposition of high quality coherent light from the SM laser and steady-state ultra-broadband QD SLD emission allowed tuning in a wide range the combined statistical nature of photon streams. As a main result, a full transition from thermal-like to coherent statistics has been achieved by varying the power ratio of the two light sources. Here, the coherence transition showed a smoother trajectory compared to the OFB experiment (compare Figure 27 and Figure 33).

This experiment can be considered as revival of some pioneering work from Arecchi [218], Scarl [220], Lachs [221] or also Perina [222]. Experimental and theoretical studies on the superposition of Gaussian or chaotic fields with coherent fields have been a hot topic in the coherence analysis of - at that time - recently developed lasers. To the best of one's knowledge, it is the first demonstration of the mixed-light phenomenon that includes a highly incoherent light component, i.e. where strong incoherence is given in both first- and second-order correlations. The good agreement between theory and experiment for  $g^{(2)}(0)$  as well as  $g^{(2)}(\tau)$  in the mixed-light scenario, supports also the highly MM PRAG state model as an appropriate description of QD SLD emission and more generally for ASE generated by SLDs.

It is worth noticing that the developed mixed-light scheme (Figure 28) represents an easy-to-handle light source with tunable photon statistics which could be useful for testing the sensitivity of optical application systems to the second-order coherence degree such as two-photon microscopy [136], second-order OCT [50] and also ghost imaging [81, 223].

Chapter 4 has presented experimental results on the simultaneous tailoring of first- and second-order coherence properties of light emitted by quantum dot superluminescent diodes (QD SLDs). Particular effort was made to achieve a maximum impact on the second-order correlations. Indeed, two different experimental approaches enabled the complete control of the second-order coherence degree. Both experiments showed a continuous transition from thermal-like to highly coherent photon statistics.

With regard to the coherence transition, an essential aspect of novelty is the presence of ultra-broadband light leading to ultra-short correlations timescales, which was put at disposal by amplified spontaneous emission from QD SLDs. Under those conditions ( $\Delta\nu > 10\text{THz}$ ), the associated second-order coherence degrees are only pronounced on correlation timescales below 100fs. The time resolution requirement to the intensity-intensity detection system could be met by exploiting TPA interferometry which was introduced only some years ago [9].

This presented work contributes to the research on the coherence of ultra-broadband ASE generated by QD SLDs. It is the first time that QD SLD light states are considered. The postulated quantum optical state of light captures the complex NIR spectral distribution of real QD SLD emission assuming uncorrelated longitudinal modes. The  $N$ -mode *phase-randomized Gaussian (PRAG) state* represents an incoherent superposition of thermal Gaussian states shifted by a complex amplitude for each individual mode. The derived analytical expressions for first- and second-order correlations were directly tested by the two experiments.

Applying broadband optical feedback (OFB) onto a QD SLD, the number of emitted modes  $N$  was reduced by narrowing the spectrum. The observed range of coherence transition,  $1 < N < 25$ , coincides with PRAG state expectations.

The ultra-broadband *mixed-light experiment* allowed preserving the natural bandwidth of QD SLD light. The adjustable superposition of high quality coherent light from a SM laser engendered full control on the combined second-order coherence degree agreeing well with theory for which the PRAG state was extended by a coherent amplitude. As discussed in the last section, mixed-light was already a major aspect of coherence studies starting in the 1960s. Here, the key advancing aspect is the consideration of ultra-large spectra, or in other words of extremely high multimode states of light.

This comprehensive study on tailored first- and second-order coherence properties supports the simple PRAG state ansatz for QD SLD ASE. Relevant parameters to changes of  $g^{(2)}$  were identified such as the number of modes  $N$  and the statistical properties of their spectral distribution  $p^{SLD}(\omega)$ ,  $\langle p^{SLD} \rangle$  and  $\Delta^2 p^{SLD}$ . Together with earlier work [145, 23], it can be stated that pure ultra-broadband ASE from QD SLDs operated at room-temperature, yields a state of light of considerably *robust second-order incoherence*. Both experimental approaches, whether intrinsic or extrinsic, had to act significantly on the optical properties to induce observable photon statistics changes. Future microscopic modeling of QD SLD light generation will benefit from these insights [268].

Fundamental investigations on intensity correlations of light are still carried out today appearing in various fields, e.g. in fluorescence correlations spectroscopy applications studying scattering processes [267]. With the emergence of ghost imaging and its development towards application, several studies on higher-order coherence mention its relevance [23, 223, 38]. It is in that same context that the comprehensive temporal coherence investigations discussed in Chapter 4 can be considered, namely as preliminary work for understanding and characterizing the light source exploited in the next chapter. Indeed, room-temperature operated QD SLDs provide the temporal incoherence condition required for a GI source. Chapter 5 deals with novel classical and highly incoherent GI experiments where QD SLDs enable the latter concepts.

---

## 5. Ghost imaging (GI) with opto-electronic emitters

---

Until today, ghost imaging remains a vivid and fascinating topic in quantum optics or quantum imaging [224]. The introduction of thermal light sources to GI engendered the field of classical GI, where more feasible light sources are utilized in view of application. However, also quantum GI is still striving towards practical implementations [225]. The actual hot topic directions in classical GI are the development of computational GI with a simplified experimental scheme offering single-pixel cameras closely related to the compressive imaging field [226], the search for new applications, such as imaging in turbulent media [20], and even new GI techniques, such as imaging of temporal objects by time-domain GI [106], to push forward its acceptance into the real world.

To contribute to the development of GI, Chapter 5 aims to extend the portfolio of classical light sources for GI with concepts based on opto-electronic emitters. Furthermore, new GI detection schemes are developed with the expectation to provide a broader platform for enabling applications in future work. Here, two completely new detection concepts are developed and the proof of their functionality is demonstrated. In particular, the classicality of established GI schemes is *surpassed* by increasing step-by-step the degree of incoherence (Section 5.1→5.2→5.3). Three GI experiments are presented subsequently which follow the thesis guideline: *from novel to highly incoherent concepts*. Together with the title of this chapter the two-fold research objective is emphasized: new detection concepts *and* new light sources.

State-of-the-art light sources have been presented in detail within Section 2.2 (see Table 1). They all consist of multiple elements forming in most cases complex, bulky devices. In this thesis, opto-electronic emitters are utilized to develop compact and easy-to-handle GI light sources which beyond comprise new properties. One central finding of Chapter 4 is the robust, high temporal incoherence of light emitted by QD SLDs. Regarding the high level of photon-bunching ( $g^{(2)}(0) \approx 2$ ), QD SLD light fulfills excellently the temporal incoherence requirement to GI (see page 18) which is explicitly exploited for the development of new GI light sources. Specifically, three opto-electronic GI light source concepts are developed:

- I. A high-quality pseudo-thermal light source based on a semiconductor laser diode
- II. A hybrid pseudo-thermal-superluminescent diode (PT-SLD) light source based on a narrow-stripe QD SLD
- III. A broad-area SLD based on a tapered QD SLD

Regarding state-of-the-art GI detection, two basic schemes are well-established. On the one hand, the original spatial HBT-based scheme with two detectors (one bucket and one spatially resolving reference detector) and a coincidence count unit or synchronous signal acquisition (time tagging) with subsequent correlation evaluation remains the most utilized method. On the other hand, the computational approach using artificially randomized light and post-computed correlations between the signal of a single-pixel bucket detector and the precomputed spatial patterns has led to a significant reduction of the setup complexity. Therefore, application-oriented developments often change over to computational GI where newest DMD technology allows high-resolution ghost images by taking advantage of computational methods such as compressive and adaptive imaging techniques [227]. Although, numerous improved GI protocols have been demonstrated, also with modified configurations such as polarimetric GI [86], differential GI [85], normalized GI [228], iterative GI [229], positive-negative corresponding GI [230], DC-analog block GI [60], marked GI [231], speckle-averaged GI [232], pseudo-inverse GI [233], just to enumerate a few. However, all of them adhere to the two basic configurations discussed above.

---

---

In this chapter, two completely novel GI detection schemes are proposed, namely

- I. Photon statistics-based ghost imaging (PS-GI) based on one single-photon-counting detector
- II. Ultra-broadband ghost imaging (UBB-GI) using TPA interferometry

At first, the photon statistics-based GI concept is presented where the semiconductor laser-based PT light source is incorporated (Section 5.1). The ability of evaluating higher-order ghost images is studied. Section 5.2 introduces ultra-broadband GI detection applying TPA interferometry and hybrid PT-SLD light. Finally, the broad-area SLD is implemented into the ultra-broadband GI scheme (Section 5.3). It should be noted that the following results were achieved having targeted proofs of concept. Therefore, all experiments are restricted to one-dimensional ghost images. The potential for two-dimensional imaging and further developments is discussed within each section and in Appendix 8.1.

Please note that a major part of this chapter has been published in scientific (peer-reviewed) journals (see page 135). Hence, important content overlap of results about photon statistics-based GI (Section 5.1) and ultra-broadband GI (Section 5.2 and 5.3) is given within Refs. [234, 235] and Refs. [236, 237], respectively.

---

## 5.1. Photon statistics-based GI with pseudo-thermal light

The first developed classical GI detection scheme is presented in this first section about novel GI concepts with opto-electronic light sources.

The key idea is that instead of measuring correlations between the signal of the bucket detector originating from the object beam and the reference signal of another detector located in the reference beam such as in standard GI schemes (Figure 5), the two beams are optically superposed at the rear of the imaging planes. The joint photon statistics are analyzed by one single-photon-counting detector and appropriate photon count acquisition. Using the statistical parameters, one can evaluate central coherence degrees (Eq. (15)) and thus obtain GI signals. The fundamental physical idea of this proposed concept consists in exploiting the complementarity of intensity auto- and cross-correlations of light in the context of GI.

For the experimental GI scheme, a pseudo-thermal light source has been implemented. In particular, a laser diode is utilized for illuminating a rotating diffuser enabling a maximum of simplicity in handling and system incorporation.

The performance of the implemented photon-statistics-based ghost imaging (PS-GI) system is investigated in detail. The visibility, the resolution and the quality of the GI signals are analyzed within simple GI scenarios. Furthermore, the possibility of evaluating higher-order ghost images with one single detector is demonstrated by proof-of-principle experiments on third- and fourth-order GI.

The experimental realization of PS-GI is supported by a simple model in which analytical expressions for the spatial correlations are derived. The superposition of object and reference beam is the main characteristic of the concept, which leads to the terms of *mixed-light* GI signal and *mixed-light* GI model. For the development of the model, the mode properties of the speckles from a classical PT source are considered. The direct comparison between model values and PS-GI measurements explains deviating characteristic features in comparison to state-of-the-art GI detection and provides physical insight into the functional principle of the PS-GI concept.

Section 5.1 comprises the four following sub-sections: First, the PS-GI scheme is introduced together with photon distribution measurements. Section 5.1.2 presents the mixed-light GI model step-by-step from the very basic ansatz up to the characteristic properties of higher-order ghost image signals. Experimental results on higher-order spatial correlations and a one-dimensional proof-of-principle GI experiment are discussed in direct comparison to the mixed-light GI model predictions in Section 5.1.3. Finally, the imaging of objects with higher complexity is discussed by a numerical example (Section 5.1.4) in view of two-dimensional PS-GI in future work. A summary and some perspectives for future PS-GI developments will conclude Section 5.1.

### 5.1.1. GI scheme

Figure 34 is a relatively abstract representation of the PS-GI scheme. For its implementation, the PT source from Section 3.1 is utilized consisting of a highly monochromatic laser diode and a RGG plate. The emitted laser light ( $\lambda = 1300.0\text{nm}$ ,  $\Delta\nu < 2\text{MHz}$ ,  $g^{(2)}(\tau = 0) = 1.00$ ) is focused onto the diffusing surface producing random interference patterns in the far-field (Figure 35). The scattering ground glass plane represents the primary light source in terms of irradiating individual speckles. A collimation lens with a focal length of 40mm captures the speckle patterns and creates an approximately collimated light beam which then is separated by a beamsplitter into two highly position-correlated light fields, the object beam and the reference beam (Figure 34). At a distance of  $z_{obj} = z_{ref} \approx 520\text{mm}$  from the source plane, the object and the reference plane with the placed object mask and the spatially resolving element are located, respectively. Note that a lensless GI experiment is implemented [238], exploiting the self-correlation of the transverse wave vector for classical thermal light [84] thus assuring a maximum of

experimental simplicity. The superposition of the reference and the object beam passing the imaging planes is realized by collecting the two beams individually in optical fibers. Whereas all light transmitted through the object is collected into the fiber, corresponding to the *bucket-functionality* in standard GI schemes without spatial information, the reference fiber enables the spatial resolution by selecting a small area of the impinging speckle pattern and by scanning the reference plane. Both fiber-coupled light fields are superposed using a fiber combiner, subsequently guided into a light-shielded single-photon-counting PMT (Hamamatsu H10330A-45) which photon counts are registered by an oscilloscope. Applying the experimental method of Section 3.1, the mixed-light photon statistics are determined and coherence degrees can be calculated. For all following experimental results, the same settings of the oscilloscope as well as of the parameters for the evaluation of  $P(n)$  as described in Section 3.1 apply.

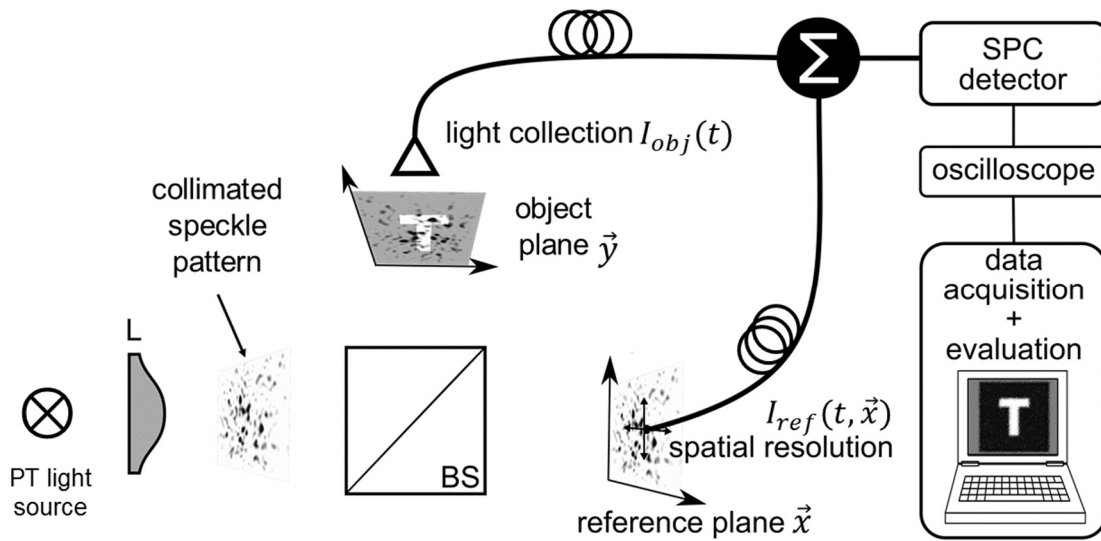


Figure 34. **Schematic diagram of the photon statistics-based ghost imaging experiment** with the PT light source, a collimation lens (L), the beamsplitter (BS) and the imaging planes  $\vec{x}$  and  $\vec{y}$  located at  $z_{ref}$  and  $z_{obj}$ , respectively. The right part of the figure shows the superposition (e.g. by optical fibers and a fiber combiner) of the reference and the object beam ( $\Sigma$ ) with subsequent detection (single-photon-counting (SPC) detector) and data acquisition (oscilloscope with LabView-based read-out and evaluation). Additionally, a measured, static speckle pattern (negative image) originating from the PT source is depicted within the beam paths to illustrate the speckle pattern propagation within the lensless GI configuration.

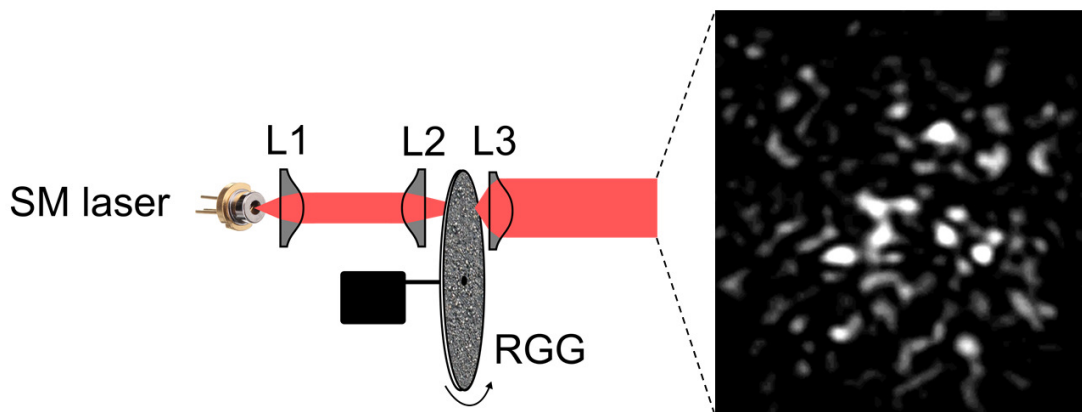


Figure 35. **The implemented pseudo-thermal light source.** Left: Schematic drawing comprising the packaged discrete mode laser (single-mode laser (SM laser)), the collimation and focussing lenses for the speckle size control (L1, L2 and L3) and the rotating diffusor (RGG). Right: Representative speckle-pattern in the imaging plane of the PS-GI setup measured with a CCD camera (Apogee AP1).

The thermal photon statistics behavior of the implemented PT light source has already been verified in Section 3.1. Additionally, Figure 36 shows representative photon distributions measured within the implemented PS-GI scheme. When analyzing the light originating from one single speckle cell either in the reference or in the object plane, experimentally determined photon distributions  $P(n)$  depicted in Figure 36 (A) and (B) (black squares) are obtained, respectively. For each measurement, the light from the correspondingly opposite arm is blocked and SM fibers with a core diameter of  $\sim 9.3\mu\text{m}$  are positioned in the imaging planes (Figure 34). The core of the fibers serves as an appropriate aperture since clearly visible speckles have been adjusted ( $> 100\mu\text{m}$ ). Both measured distributions are in excellent agreement with a BE distribution, which can be directly compared in Figure 36 (A) and (B) (red lines). A specific BE distribution (Eq. (17)) is calculated here with the experimentally obtained mean photon number without any fitting procedure. Quantitatively, a fidelity

$$F = \sum_{n=0}^{N_{max}} \sqrt{P_{exp}(n)P_{theory}(n)} \quad (83)$$

of 0.999 holds for both distributions. The corresponding normalized central second-order correlation coefficients calculated according to Eq. (15) amount to  $g^{(2)}(0) = 1.95$  (Figure 36 (A)) and  $g^{(2)}(0) = 1.99$  (Figure 36 (B)).

In case of superposition, i.e. single speckle fiber-coupling in both arms, the photon distributions depicted in Figure 36 (bottom) are obtained. Figure 36 (C) has been determined when the same speckle cell is fiber-coupled in each arm meaning that the positions in both planes are correspondingly identical ( $\vec{x} = \vec{y}_0$ ). Additionally, the same optical power-coupling is ensured. The measured photon distribution still coincides with a BE distribution validated by a high fidelity of 0.999. The value of the central second-order correlation coefficient also confirms the persisting thermal photon statistics with  $g^{(2)}(\tau = 0, \vec{x} = \vec{y}_0) = 2.04$ . In contrast, Figure 36 (D) shows a measurement for two different, superimposed speckles having displaced the reference arm transversely by a distance of  $|\Delta\vec{x}| \approx 1.5\text{mm}$  with respect to the previous measurement. The experimentally obtained photon distribution differs clearly from BE (Figure 36 (D)). This deviation leads to a reduced coherence degree of  $g^{(2)}(\tau = 0, \vec{x} = \vec{y}_0 + \Delta\vec{x}) = 1.51$  as well. On the one hand, the here observed spatial correlations  $g^{(2)}(\tau = 0, \vec{x} \neq \vec{y})$  seem to behave differently than in standard GI methods where instead, intensity *cross*-correlations between reference and object arm are exploited. On the other hand, these basic experimental results are motivating regarding the GI functionality which relies on spatially confined correlations.

To show even more evidence of a GI functionality of the proposed scheme, a full one-dimensional transverse fiber displacement ( $x$ -coordinate) is performed while fixing the fiber in the other plane at  $y_0 = 0$  to study the so-called *position-position correlation* between the object and the reference plane<sup>23</sup> [57, 84] in terms of  $g^{(2)}(\tau = 0, x)$ . Figure 37 shows the results for two selected, different speckle diameters of the PT source. The mean speckle diameter has been varied by moving the focus of the semiconductor laser beam out-of-plane on the scattering surface. Adapting a Gaussian, the maximum is  $g^{(2)}(\tau = 0, x = 0) = 2.00$  for the case of the smaller speckle (left) and  $g^{(2)}(\tau = 0, x = 0) = 1.98$  for the larger speckle (right). In the periphery of the fiber scan range, correlations drop down to a constant, spatially independent value of  $g^{(2)}(\tau = 0, x \gg 0) = g^{(2)}(\tau = 0, x \ll 0) = 1.57$  for the small speckle diameter and to  $g^{(2)}(\tau = 0, x \gg 0) = g^{(2)}(\tau = 0, x \ll 0) = 1.58$  for the larger speckle diameter. Moreover, mean speckle sizes of  $(0.68 \pm 0.11)\text{mm}$  and  $(1.01 \pm 0.07)\text{mm}$  for the smaller and the larger speckle-size adjustment are derived from the FWHM of the Gaussian fits, respectively. These values are also reflecting the transverse coherence length  $\sigma_c$  of the field (see Eq. (11) and Eq. (27)). It is worth noticing that this experiment represents a first, one-dimensional PS-GI experiment.

<sup>23</sup> The absolute value of  $y_0$  can be defined arbitrarily, as only relative positions between the reference coordinate  $x$  and the object coordinate  $y$  matter. For making it easier to the reader,  $y_0$  has been set to zero.

---

---

In the following section, a developed model for this novel mixed-light GI concept is presented. It aims to reproduce characteristic properties of the spatial correlation function in order to (i) understand the underlying physics and furthermore (ii) characterize the visibility performance of the experimental PS-GI method.

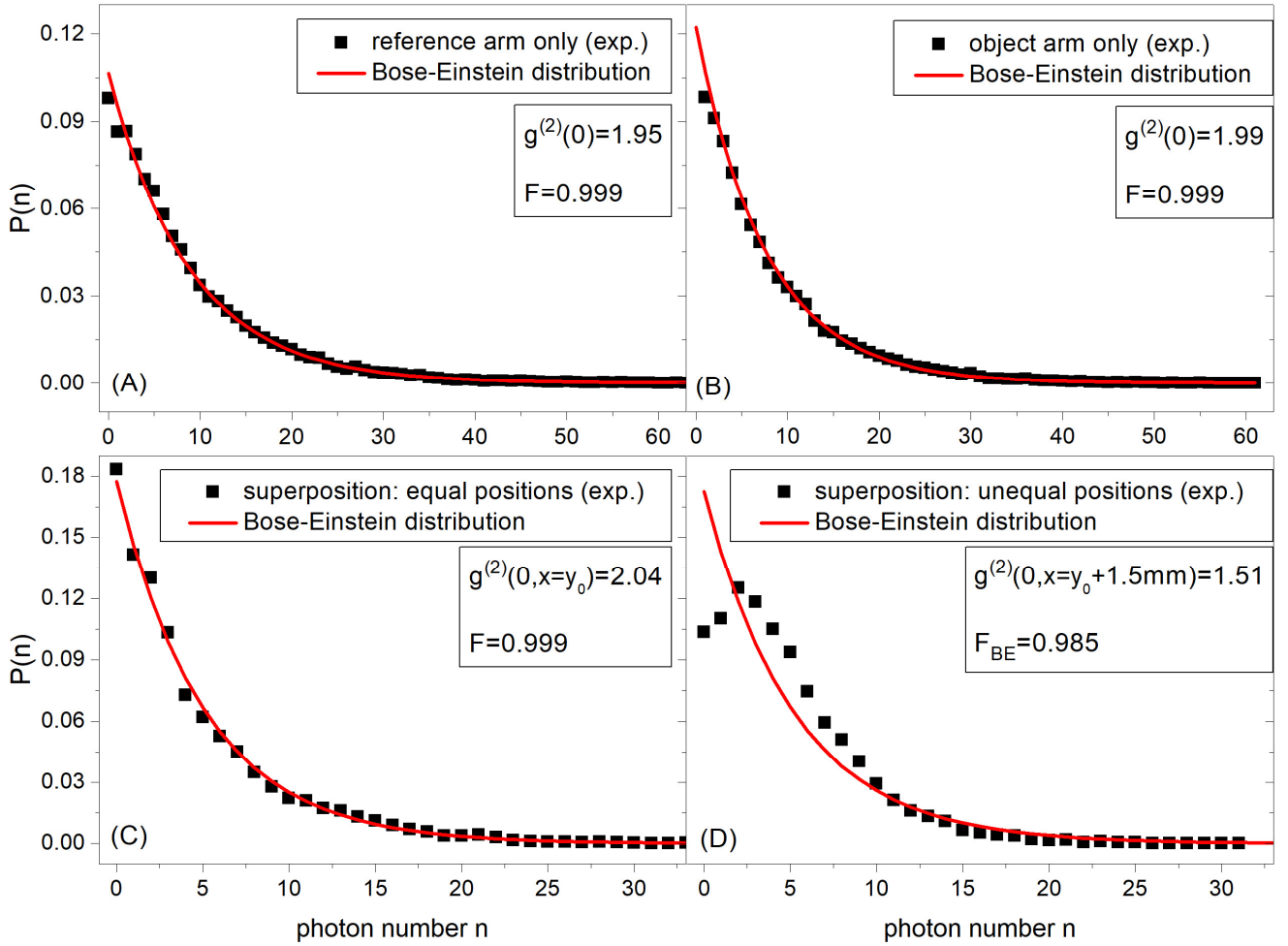


Figure 36. **Representative probability distributions of photons** originating from a single speckle cell exclusively in the reference plane  $\vec{x}$  (A) and exclusively in the object plane  $\vec{y}$  (B) as well as for superimposed speckle cells at correspondingly equal,  $x = y_0$  (C), and unequal positions,  $x = y_0 + 1.5\text{mm}$  (D). Additionally, the central second-order coherence degree as well as the fidelity factor are given in each graph. In (D), the fidelity is explicitly denoted by  $F_{BE}$  for reasons of comparison with the next section (Figure 38).

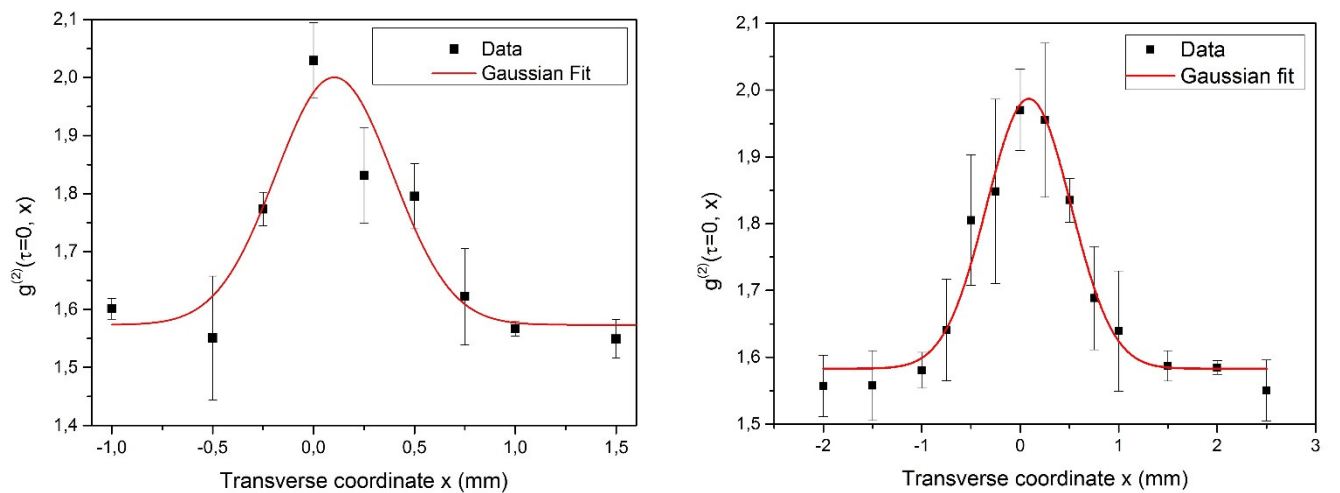


Figure 37. **Measured position-position correlations**  $g^{(2)}(\tau = 0, x)$  in terms of a transverse displacement  $x$  in the reference plane having fixed the position in the object plane at  $y_0 = 0$  for two selected, different speckle diameters [116]: 0.68mm (left) and 1.01mm (right).  $x = 0$  corresponds to the equal positioning of object and reference aperture. Errors bars represent the statistical variance of a set of 3 measurements. The fitted functions (red line) are based on assuming a Gaussian respecting error bar weights.

## 5.1.2. Model

The section is organized as follows: First, the basic ansatz for the central second-order correlation degree of mixed-light GI is presented. This ansatz will then be applied to the very basic scenario of position-position correlations between the reference plane and the object plane. The visibility behavior will be investigated. Additionally, a photon number distribution calculation is performed with regard to the preliminary results in Figure 36 (D) complementing the position-position correlation results. From comparison with literature [83], the mixed-light GI correlation behavior is generalized to an arbitrary amount of speckle illumination in view of imaging more complex objects. Again, by the help of [83], the characteristic properties of higher order mixed-light ghost images are finally derived. The main physical insights into mixed-light GI will be summarized from there.

**Ansatz.** The central second-order correlation degree  $g^{(2)}(\tau = 0, \vec{x})$  with  $\vec{x}$  being the spatial coordinate in the reference plane, represents the image signal in GI. Here, the developed model shall describe the characteristic properties of the spatial correlation function in mixed-light GI  $g_{mix}^{(2)}(\tau = 0, \vec{x})$ , in particular the maximum and the minimum values. This allows for a direct comparison with the performance of state-of-the-art GI technologies by concentrating on the visibility aspect.

The ansatz is intuitively based on the experimental principle (Figure 34), namely the superposition of the reference and the object beam generated by a PT source which is classical light originating from random emission processes exhibiting photon-bunching. Adopting a classical approach, the superposition is a simple addition of two intensities, namely *the collected intensity*  $I_{obj}(t)$  of the object beam and the intensity of the reference beam  $I_{ref}(t, \vec{x})$ . The resulting intensity  $I_{mix}(t, \vec{x})$  which is detected by the PMT, is equal to

$$I_{mix}(t, \vec{x}) = I_{obj}(t) + I_{ref}(t, \vec{x}) \quad (84)$$

where interference effects are neglected for simplicity<sup>24</sup>. By inserting the mixed intensity term in the classical definition of the second-order correlation function (Eq. (12)), one obtains

$$g_{mix}^{(2)}(\tau, \vec{x}) = \frac{\langle I_{obj}(t) I_{obj}(t + \tau) \rangle + \langle I_{obj}(t) I_{ref}(t + \tau, \vec{x}) \rangle}{\langle I_{obj}(t) + I_{ref}(t, \vec{x}) \rangle \langle I_{obj}(t + \tau) + I_{ref}(t + \tau, \vec{x}) \rangle} + \frac{\langle I_{ref}(t, \vec{x}) I_{obj}(t + \tau) \rangle + \langle I_{ref}(t, \vec{x}) I_{ref}(t + \tau, \vec{x}) \rangle}{\langle I_{obj}(t) + I_{ref}(t, \vec{x}) \rangle \langle I_{obj}(t + \tau) + I_{ref}(t + \tau, \vec{x}) \rangle}. \quad (85)$$

Within the presentation of the model,  $\langle \rangle$  represents the time average  $\langle \rangle_t$  unless otherwise noted. Eq. (85) contains four correlation terms in the numerator which must be evaluated according to the specific scenarios at the object and the reference plane. The GI signal is defined at  $\tau = 0$ , namely where the maximum amplitude, with respect to time, is expected. Therefore,  $g_{mix}^{(2)}(\tau = 0, \vec{x}) \equiv g_{mix}^{(2)}(0, \vec{x})$  is considered in the following.

**Position-position correlations of speckles.** As the very basic scenario, already mentioned in Section 5.1.1, the position-position correlations between individual speckle cells in the reference and the object plane are investigated. It is commonly assumed that different speckle cells are statistically independent [82]. In the time domain, they obey individually Gaussian statistics (Eq. (37)) synonymous

<sup>24</sup> The omission of interference terms is a rather strong assumption for describing the experimental PS-GI scheme, in particular because a Mach-Zehnder like configuration is implemented. However, one will see how well the model coincides with experimental data in Chapter 5.1.3. In future developments of the model, interference terms could well be inserted together with appropriate experimental investigations.

for BE distributed photons. The following relation for the spatial correlation behavior of intensities  $I_m(t, x_m)$  and  $I_k(t, y_k)$  of two speckle cells m and k holds [83]<sup>25</sup>:

$$\langle I_m(t, x_m) I_k(t, y_k) \rangle = \begin{cases} 2 \langle I_m(t, x_m) \rangle \langle I_k(t, y_k) \rangle & \text{for } m = k \\ \langle I_m(t, x_m) \rangle \langle I_k(t, y_k) \rangle & \text{for } m \neq k \end{cases} . \quad (86)$$

In order to investigate the position-position correlations originating from two speckle cells,  $I_1(t, x_1)$  located in the reference plane ( $\vec{x}$ ) and  $I_2(t, y_2)$  located in the object plane ( $\vec{y}$ ), the relations above are plugged into Eq. (85). Note, that only the one-dimensional case is considered and thus  $\vec{x} \rightarrow x$  and  $\vec{y} \rightarrow y$  apply for the transverse imaging axes. The two-dimensional case of transverse imaging planes can be easily extrapolated and does not include any additional physics. When the reference and the object arm are at the correspondingly same position, i.e. fiber coupling *the identical speckle cell*, one obtains

$$g_{mix}^{(2)}(0, x_1 = y_2) = 2 , \quad (87)$$

whereas considering *two different speckles* by a transversely displaced speckle selection in the reference arm, one gets

$$g_{mix}^{(2)}(0, x_1 \neq y_2) = 2 - \frac{2 \langle I_1(t, x_1) \rangle \langle I_2(t, y_2) \rangle}{(\langle I_1(t, x_1) \rangle + \langle I_2(t, y_2) \rangle)^2} . \quad (88)$$

One recognizes a parameter-free maximum value of  $g_{mix}^{(2)} = 2$  which is reduced for the case of  $x_1 \neq y_2$  depending on the individual speckle intensities. With Eq. (87) and (88), the visibility behavior of the position-position correlations can be analyzed. The visibility is defined by

$$V^{(j)} = \frac{g_{max}^{(j)} - g_{min}^{(j)}}{g_{max}^{(j)} + g_{min}^{(j)}} \quad (89)$$

and serves as a quality criterion of GI systems. A simple visibility dependency on the intensity ratio  $\zeta = \langle I_1 \rangle / (\langle I_1 \rangle + \langle I_2 \rangle)$  can be deduced:

$$V_{mix}^{(2)}(\zeta) = \frac{\zeta(1 - \zeta)}{2 - \zeta + \zeta^2} . \quad (90)$$

$\zeta$  takes values between 0 and 1, representing a relative measure for the intensity discrepancy between the two speckles. Whereas  $\zeta = 0.5$  corresponds to perfectly balanced intensities,  $\langle I_1 \rangle = \langle I_2 \rangle$ ,  $\zeta = 0$  and  $\zeta = 1$  signify a total imbalance of  $\langle I_1 \rangle \ll \langle I_2 \rangle$  and  $\langle I_1 \rangle \gg \langle I_2 \rangle$ , respectively. This definition of the ratio between the intensities of the two speckles  $\langle I_1 \rangle$  and  $\langle I_2 \rangle$ , located at opposite imaging planes, covers all possible intensity distribution circumstances in a finite range of values.

The visibility  $V_{mix}^{(2)}(\zeta)$  increases when both intensities approximate each other. The maximum value of 14.3% is reached for  $\zeta = 0.5$  corresponding to  $g_{mix}^{(2)}(0, x_1 \neq y_2) = 1.5$  (Eq. (88)). The visibility trends towards 0 for  $\zeta$  approaching its limits 0 and 1. There, the individual auto-correlation behavior of one of the two speckles is dominating and thus superposition is not apparent, hence  $g_{mix}^{(2)}(0, x_1 \neq y_2) = g_{mix}^{(2)}(0, x_1 = y_2) = 2$ .

<sup>25</sup> Here, the spatial coordinates  $x$  and  $y$  are already adapted to the GI scheme referring to the reference plane and the object plane, respectively. In general, Eq. (86) is expressed in terms of one single plane and thus one single spatial coordinate, e.g.  $x$  [83].

These results agree already with the experimental results of Figure 36 regarding the determined  $g^{(2)}$ -values. Next, the assumed statistical *independency* of speckles shall be applied further to the underlying photon distributions  $P(n)$ .

**Mixed-light photon distributions.** This paragraph is dedicated to explaining the observed photon distribution of Figure 36 (D) where a clear discrepancy between the experimental and the BE distribution is observed. There, the position-position correlations between two different speckles was measured. Just as discussed above, correlation degrees have been derived on the basis of statistically independent speckles. The assumption is now transferred to the photon distributions  $P(n)$ . In the following, solely an exemplary calculation is considered since this is a mathematical topic which has been already treated in the past [239]. However, the following results will (i) complement the understanding of the physics of mixed-light GI and (ii) illustrate the accuracy of the PS-GI method.

From statistics theory, it is well-known that the statistics of the sum of two different random variables are obtained by the convolution of the individual statistics. Within one single speckle cell, the light obeys thermal photon statistics with a BE distribution. Figure 36 (A) and (B) demonstrate the high quality of the implemented PT source as well as the high accuracy of the detection method by reproducing BE statistics.

The convolution of two discrete distributions with positive integer variables are defined as [240]

$$P_{12}(n) = \overline{(P_1 \cdot P_2)}(n) = \sum_{n'=0}^n P_1(n') P_2(n - n') . \quad (91)$$

With the assumptions of equal mean photon numbers<sup>26</sup>  $\bar{n}_1 = \bar{n}_2 = \bar{n}$ , the convolution of two BE distributions results in

$$P_{12}(n) = \frac{(1+n)\bar{n}^n}{(1+\bar{n})^{(n+2)}} . \quad (92)$$

It comprises similar terms compared to the BE distribution (Eq. (17)) but differs from it in two main points. First, the exponent of the denominator ( $n + 2$ ) is enhanced by 1, which leads to a steeper decline of  $P_{12}(n)$  and second, the additional factor  $(1 + n)$  in the nominator leads to a displaced maximum from  $n = 0$  towards higher photon numbers. This distribution is now depicted in Figure 38 (blue line) together with the data of Figure 36 (D) where the experimental mean photon number  $\bar{n} = 2.39$  was inserted. One can clearly see the good reproduction of the experiment by the convolution of two BE distributions instead of the sole BE distribution (red line). Furthermore, the high fidelity-value  $F = 0.999$  of the other measurements (Figure 36 (A)-(C)) has been restored. From there, one can reliably deduce the validity of the convolution ansatz of two BE distributions. By examining  $P_{12}(n)$  in more detail, the corresponding mean photon number reads

$$\bar{n}_{12} = \sum_n P_{12}(n) n = 2\bar{n} \quad (93)$$

which coincides with the intuitive addition of photon numbers. With simple math, the variance reads

$$\Delta^2 \bar{n}_{12} = \sum_n P_{12}(n) n^2 - \bar{n}_{12}^2 = 2\bar{n}(1 + \bar{n}) \quad (94)$$

<sup>26</sup> The case  $\bar{n}_1 \neq \bar{n}_2$  can be calculated as well, but it leads to larger, more complex terms.

which happens to be twice the variance of a single BE distribution. Inserting  $\bar{n}_{12}$  and  $\Delta^2 \bar{n}_{12}$  into Eq. (15), one finds  $g^{(2)}(0) = 1.5$  coinciding with the result of  $g_{mix}^{(2)}(0, x_1 \neq y_2)$  at  $\zeta = 0.5$  from the previous subsection (Eq. (88)).

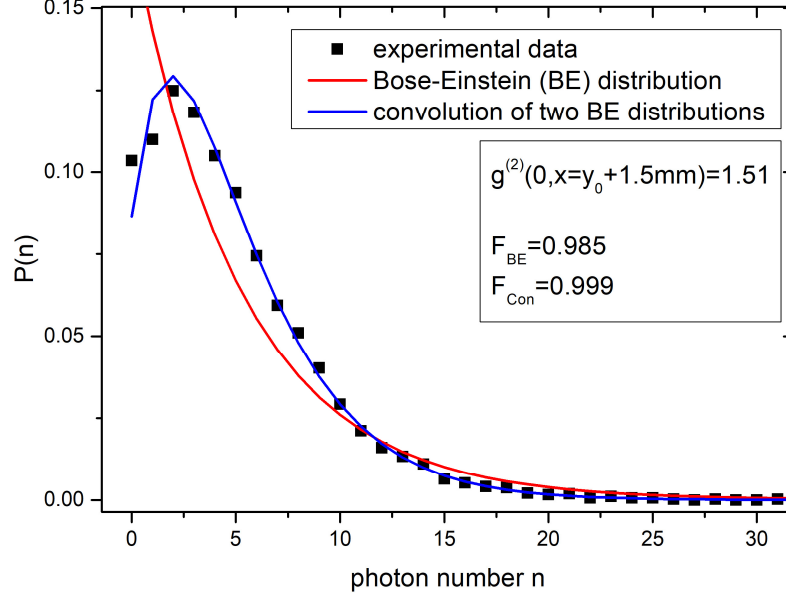


Figure 38. **Photon distributions of two different superimposed speckle-cells.** Experimental data and BE distribution taken from Figure 36 (D) and calculated convolution of two BE distributions reconstructing the experimentally obtained photon statistics. Experimentally, the SM fiber in the reference plane has been displaced by  $\Delta x = 1.5\text{mm}$  with respect to  $x = y_0$  (equal positions within the speckle pattern at each planes) in order to ensure the superposition of two different speckle cells (compare with Figure 37).

**Multiple speckle correlations.** So far, the theoretical considerations generate satisfactory results regarding the position-position correlations in mixed-light GI. In view of imaging more complex objects, the model is expanded to higher numbers of contributing speckles, which makes the evaluation of the nominator in Eq. (85) more complex. Eq. (87) and Eq. (88) are the derived characteristic properties of the position-position correlations, namely the maximum value in the center and the minimum value in the periphery of the spatial correlation function. These two formulas happen to coincide with the results of Ref. [83] which provides  $j$ -th-order auto-correlation functions of Gaussian scattering processes. There, the second-order correlation function at  $\tau=0$  is expressed by

$$g_N^{(2)}(0) = 1 + \frac{\sum_{k=1}^N \langle I_k \rangle^2}{(\sum_{k=1}^N \langle I_k \rangle)^2} = 1 + \beta_N(2) \quad (95)$$

with

$$\beta_N(j) = \frac{\sum_{k=1}^N \langle I_k \rangle^j}{(\sum_{k=1}^N \langle I_k \rangle)^j} \quad (96)$$

which scales with the number of speckles or spatial modes  $N$  with individual mean intensities  $\langle I_k \rangle$ . As  $g_N^{(2)}(0)$  takes a value of 2 for  $N=1$  and as one can easily rewrite Eq. (88) for  $N=2$ , it is inferred that

$$g_{mix}^{(2)}(\tau = 0, \vec{x}) \equiv g_{N(\vec{x})}^{(2)}(0) \quad (97)$$

holds. It can be concluded that the mixed-light GI concept exploits the spatial intensity auto-correlations of multiple speckles. Recalling the design of this novel GI scheme, the beamsplitter generates two

statistical copies of the PT light beam; the scanning reference arm serves as a selection aperture of the total number of speckles  $N(\vec{x})$  contributing to the measured, superposed reference and object light. Consequently, Eq. (97) is exploited to predict the characteristic maximum  $g_{max}^{(2)}$  (at  $N_{min}(\vec{x}_{max})$ ) and minimum  $g_{min}^{(2)}$  (at  $N_{max}(\vec{x}_{min})$ ) signal amplitudes of an arbitrary GI scenario if the number of speckles passing the object  $N_{obj}$  and the number of selected speckles by the reference aperture  $N_{ref}(\vec{x})$  as well as their respective intensities are known.

**Higher order correlations.** So far, it was found that the  $g^{(2)}$ -signal in mixed-light GI relies on auto-correlation functions of multiple superimposed speckles. However, one can further exploit the higher-order correlation formalism provided by Ref. [83]. The following equations for the third- and fourth-order correlations are reproduced in a reduced manner for  $\tau = 0$ :

$$g_N^{(3)}(0) = 1 + 3\beta_N(2) + 2\beta_N(3) \quad (98)$$

and

$$g_N^{(4)}(0) = 1 + 6\beta_N(2) + 3\beta_N(2)^2 + 8\beta_N(3) + 6\beta_N(4) \quad (99)$$

with  $\beta_N(j)$ -values corresponding to Eq. (96). These relations allow making predictions on the characteristic properties of a specific higher-order GI scenario, i.e. the maximum and the minimum values of a ghost image. In analogy to Eq. (97), the higher-order mixed light signal can thus be expressed by

$$g_{mix}^{(j)}(\tau = 0, \vec{x}) \equiv g_{N(\vec{x})}^{(j)}(0). \quad (100)$$

To demonstrate the well-known benefit of higher-order GI [53, 238] in the here proposed mixed-light GI concept, the position-position correlations for the third- and fourth-order case is investigated. Therefore,  $N = 1$  and  $N = 2$  are inserted for the maximum and the minimum value, respectively, into both Eq. (98) and Eq. (99).

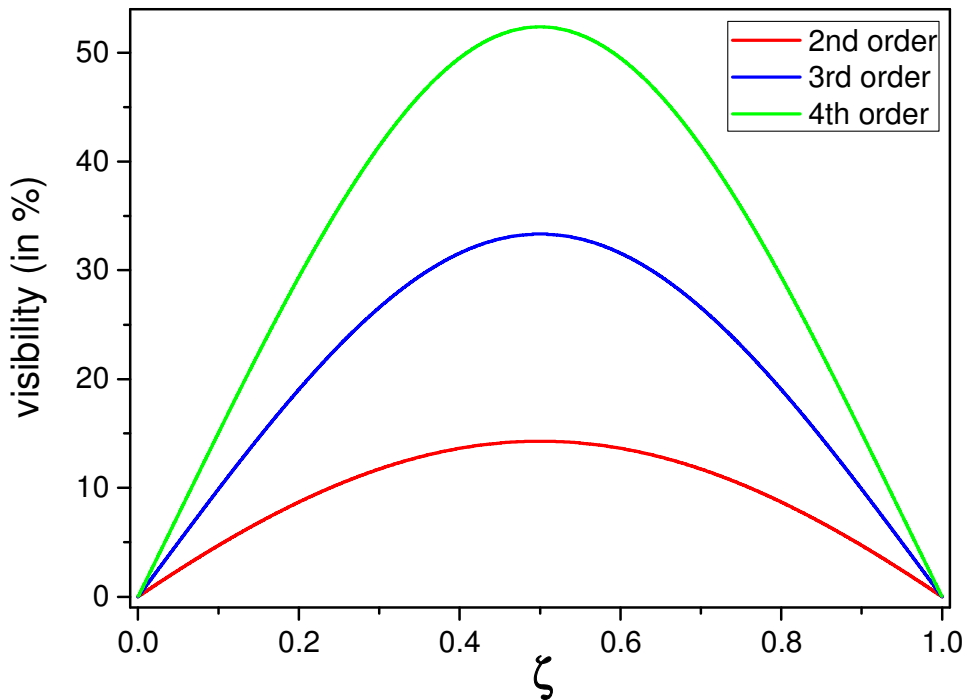


Figure 39. **Visibility of the higher-order position-position correlations in mixed-light GI for the orders 2, 3 and 4 as a function of  $\zeta = \langle I_1 \rangle / \langle I_1 \rangle + \langle I_2 \rangle$ .**

In analogy to Eq. (90), visibility expressions as a function of the relative intensity ratio  $\zeta = \langle I_1 \rangle / (\langle I_1 \rangle + \langle I_2 \rangle)$  are obtained:

$$V_{mix}^{(3)}(\zeta) = \frac{\zeta(1 - \zeta)}{1 - \zeta + \zeta^2} \quad (101)$$

and

$$V_{mix}^{(4)}(\zeta) = \frac{\zeta(3 - 4\zeta + 2\zeta^2 - \zeta^3)}{2 - 3\zeta + 4\zeta^2 - 2\zeta^3 + \zeta^4} . \quad (102)$$

These two functions are depicted together with the second-order expression (Eq. (90)) in Figure 39. **Visibility of the higher-order position-position correlations in mixed-light GI** for the orders 2, 3 and 4 as a function of  $\zeta = \langle I_1 \rangle / (\langle I_1 \rangle + \langle I_2 \rangle)$ . Figure 39. Similar visibility dependencies on  $\zeta$  appear for all orders. The graph illustrates the significance of the intensity ratio which can deteriorate the contrast to 0 in the worst cases of  $\zeta \rightarrow 0$  as well as  $\zeta \rightarrow 1$  regardless of the correlation order. The correspondent maximum visibility value is attained for speckles of equal intensities ( $\zeta = 0.5$ ). The most important insight here is that a clear improvement of the visibility-performance is attained with increasing correlation order. The maximum values are 14.3%, 33.3% and 52.4% with ascending correlation order. Compared to state-of-the-art GI where

$$V^{(j)} = \frac{j! - 1}{j! + 1} \quad (103)$$

holds for the spatial correlations [241], a lower visibility-performance is identified. This can be fully attributed to the mixed-light characteristic of the detection concept.

Additionally, one can predict the visibility performance in a GI scenario of higher complexity than the basic point-to-point correspondence which solely addresses the spatial correlation behavior. It is assumed that a *single speckle* with intensity  $\langle I_{ref}(t, \vec{x}) \rangle$  is selected in the reference arm and an *arbitrary number of speckles*  $N_{obj}$  is collected in the object arm where the total intensity  $\langle I_{obj}(t) \rangle$  is uniformly distributed between all speckles ( $\langle I_k(t) \rangle = \langle I_{obj}(t) \rangle / N_{obj}$ ). The latter ensures an equal consideration of all features of a given object. Analogous to the previous analysis, an intensity ratio parameter  $\zeta$  is defined:

$$\zeta = \frac{\langle I_{ref}(t, \vec{x}) \rangle}{\langle I_{ref}(t, \vec{x}) \rangle + \langle I_{obj}(t) \rangle} , \quad (104)$$

covering all possible circumstances of intensity distribution between the reference and the object plane<sup>27</sup>. Figure 40 depicts numerically generated visibility-functions depending on  $\zeta$ , comparable to Eq. (90), (101) and (102). Here, instead of selecting one single speckle in the object plane, multiple speckles are contributing to the intensity of the object arm as precisely needed for imaging an object. The graph comprises the full trajectories for  $N_{obj} = 2$  (solid lines) and  $N_{obj} = 20$  (dashed lines) for the correlation orders 2 (red), 3 (blue) and 4 (green). The shifts of the maximum positions of all trajectories for  $N_{obj} = 2$  up to  $N_{obj} = 20$  are indicated with arrows. As expected, one can clearly see the decrease in visibility when the number of contributing speckles rises [29], i.e. when the complexity of a targeted object is increased. Just as for Figure 39, a vanishing visibility holds when  $\zeta$  takes its limits 0 and 1. The enhancement in visibility with higher correlation order remains for all speckle amounts  $N_{obj}$ . An important aspect here is the behavior of the maximum visibility with increasing  $N_{obj}$ . A clear shift from

<sup>27</sup> Because of the assumption of a uniform intensity distribution in the reference and the object plane, the intensity ratio  $\zeta$  does not exhibit a spatial dependence. However, the most general case of an anisotropic intensity profile of generated speckle patterns would yield an intensity ratio  $\zeta(\vec{x})$ . The spatial dependence of the intensity  $I_{ref}(t, \vec{x})$  is used consistently for reminding the spatially resolved detection in the reference plane.

$\zeta = 0.5$  (for  $N_{obj} = 1$ ) towards lower values is observed. Concurrently, the visibility trajectories no longer exhibit a symmetry axis (compare with Figure 39). Moreover, the optimal intensity distributions  $\zeta$  varies for different correlation orders at a given value  $N_{obj} > 1$ .

To conclude this part, the presented model allows to predict the contrast of a specific ghost image. The optimal intensity distribution between reference arm and object arm to maximize the contrast of a specific GI scenario, is profoundly dependent on the number of contributing speckles in each individual arm and their corresponding intensity distribution.

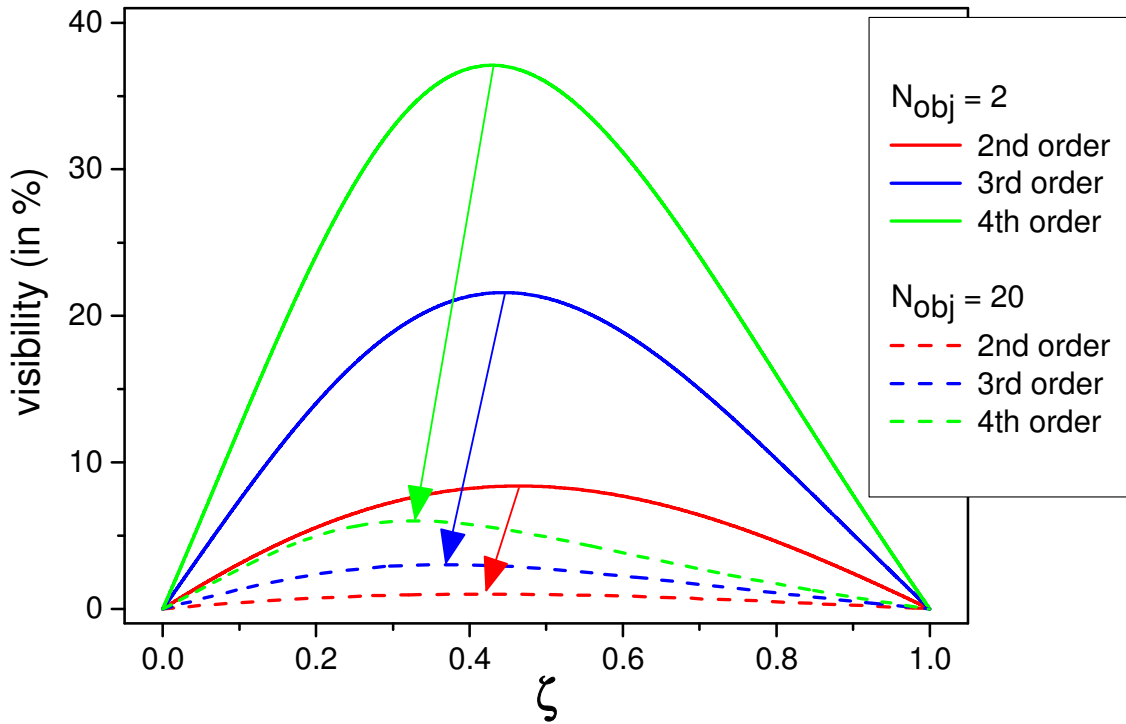


Figure 40. **Visibility of an object with multiple speckle transmission** for the correlation orders 2 (red), 3 (blue) and 4 (green) as a function of the relative intensity ratio  $\zeta = \langle I_{ref} \rangle / (\langle I_{ref} \rangle + \langle I_{obj} \rangle)$ . The arrows illustrate the shift of maximum visibility from  $N_{obj} = 2$  to  $N_{obj} = 20$  of a given correlation order. To get a better idea of possible imaging scenarios:  $N_{obj} = 2$  could image a maximum of two features, i.e. a double pinhole mask, whereas a total number of  $N_{obj} = 20$  - coupled into the object arm - would resolve a maximum of 20 different object features.

At this stage, the implications of the model on the functionality of the PS-GI detection method are summarized:

- I. The total number of superimposed speckles  $N$  selected by the apertures of the reference and the object arm determines the joint correlation behavior, thus the image signal  $g_{mix}^{(2)}$ , on the basis of independent speckles obeying Gaussian statistics.
- II. The reference aperture - located in the reference plane - varies the amount of identical and independent transverse modes

$$N(\vec{x}) = N_{obj} \cup N_{ref}(\vec{x}) \quad (105)$$

since it selects speckle intensities from the same speckle pattern as in the object plane. Thus  $g_{mix}^{(2)}(\tau = 0, \vec{x})$  is modulated between

$$g_{min}^{(2)}(\tau = 0, \vec{x}_{min}) = g_{N_{max}(\vec{x}_{min})}^{(2)}(\tau = 0) \quad (106)$$

and

$$g_{max}^{(2)}(\tau = 0, \vec{x}_{max}) = g_{N_{min}(\vec{x}_{max})}^{(2)}(\tau = 0). \quad (107)$$

The specific values of  $N(\vec{x})$  and hence of  $g_{min}^{(2)}$  and  $g_{max}^{(2)}$  depend upon the object complexity (object size) and the aperture sizes with respect to the mean speckle size (or transverse coherence area  $A_c$ ).

- III. The intensity ratio between reference and object arm  $\langle I_{ref}(t, \vec{x}) \rangle / \langle I_{obj}(t) \rangle$  plays a crucial role regarding the ghost image visibility performance.
- IV. Analogous to (I.), higher-order mixed-light is based on the joint higher-order correlation behavior of multiple statistically independent speckles. Their Gaussian statistics are indeed responsible for enhanced  $g_{mix}^{(j)}$ -values with increasing orders  $j$ . A clear visibility improvement with increasing correlation order  $j$  holds, however with a lower increase than state-of-art GI detection techniques due to the superposition property of the detection scheme.

In order to demonstrate the validity of the mixed-light GI model and the functionality of the PS-GI detection technique especially at higher correlation orders, a direct comparison between measured and calculated spatial correlations as well as the cross-section of a simple object are presented in the next section.

### 5.1.3. Experimental results

In this section, experimental results obtained by the implemented PS-GI setup are presented together with theoretical counterparts calculated with parameters which are consistent with the actual experimental situation. Already mentioned in Section 5.1.1 (Figure 37), the spatial correlations of a specific speckle pattern adjustment are analyzed in detail. Higher-order correlations are extracted and directly compared with the model expectations regarding also the visibility. Afterwards, an actual ghost image demonstration is presented by a cross-section of a double-pinhole mask<sup>28</sup>.

**Spatial correlations.** A simple GI scenario is represented by a spatial correlation measurement between the reference and the object plane. In Figure 37, a spatial correlation measurement has been already shown. More precisely, the position-position correlations between speckle cells from both imaging planes are pictured. Since (i) the implemented scheme is a lensless GI configuration (see Figure 34), meaning that no magnification in any of the GI arms exists, and (ii) the apertures are smaller than the size of the speckle cells, the true space-scales of the spatial correlations are reproduced by the measurement in Figure 37 (see Section 5.1.1 for more details). With regard to the mixed-light model, Eq. (87) and (88) apply strictly. Therefore, the data from Figure 37 (right) are reconsidered for drawing a direct comparison between model and experiment.

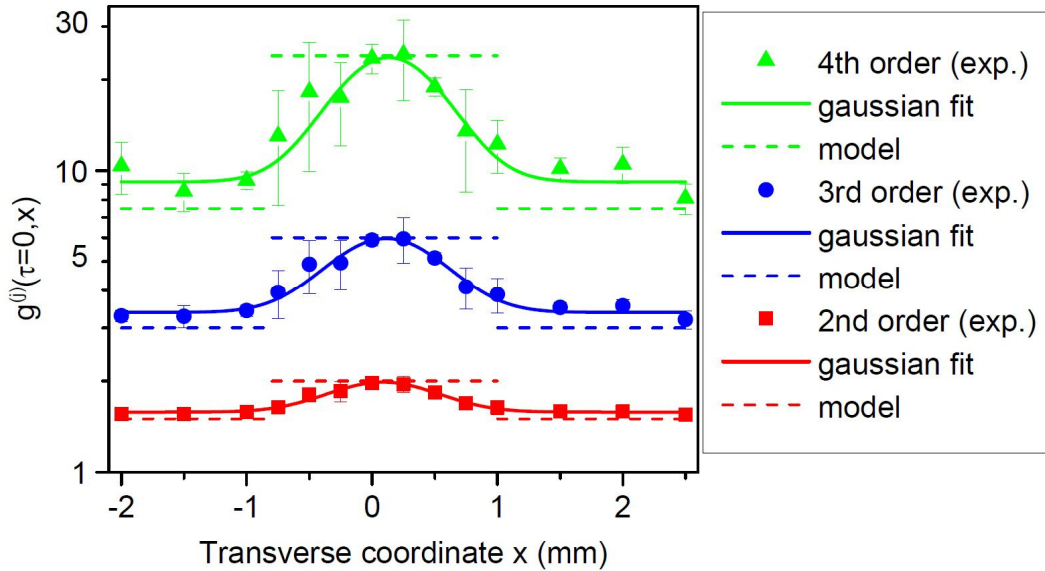


Figure 41. Experimentally determined spatial higher-order correlations ( $\zeta=0.5$ ). The fitted Gaussians (solid lines) take the error bar weights into account originating from the statistical variance of set of 3 measurements. The dashed lines denote the calculated minimum and maximum values by the model, also listed in Table 6. Note that this solely serves as an indication and not as a spatial trend description.

Table 6. Characteristic values of the spatial higher-order correlations ( $\zeta = 0.5$ ) derived from the experiment and calculated according to the mixed-light GI model.

Correlation order $j$	Mixed light model		Experimental values	
	$g_{mix}^{(j)}$ min	$g_{mix}^{(j)}$ max	$g_{exp}^{(j)}$ min	$g_{exp}^{(j)}$ max
2	1.5	2	$1.57 \pm 0.01$	$1.97 \pm 0.02$
3	3.0	6	$3.4 \pm 0.1$	$5.9 \pm 0.2$
4	7.5	24	$9.3 \pm 0.4$	$32.6 \pm 1.3$

<sup>28</sup> The experiments have been performed in the course of a supervised master thesis of S. Kuhn [116] (see Supervised theses, page 138).

As described in Section 5.1.1, the applied detection method (Section 3.1) determines the photon distribution  $P(n)$  of the mixed-light GI signal. Hence, not only second-order but in principal all higher GI orders  $j$  are accessible with one measurement using the expression of Eq. (47). Experimentally, the accuracy of  $P(n)$ , especially at high values of  $n$ , increases with longer measurement times or equivalently with a greater number of registered photons. At some point, the evaluation of a specific measurement  $P(n)$  at higher orders  $j$  is no more reasonable due to a large degree of signal uncertainties (see Figure 11). For this reason, the experimental data is evaluated up to the correlation-order  $j = 4$  depicted in Figure 41. A clear maximum value of  $g^{(j)}(0, x)$  within a Gaussian shape is observed for each correlation order  $j$  as it is expected from spatial correlations of speckles generated by a PT source [67]. Note that the widths of the trajectories are considerably large compared to the aperture size (directly related to the mean speckle size, see Section 5.1.1) leading to the gradual decrease of the  $g^{(j)}$ -signal from the maxima towards the periphery ( $x \gg \sigma_c$ ). From a Gaussian fit to each set of data (solid lines), the maximum and minimum signal values are extracted in order to compare the absolute values of equal and unequal position as well as to investigate the corresponding visibility performances. The extracted maximum and minimum values of the central  $j$ -th-order coherence degree  $g_{exp}^{(j)}(0)$  and the model values  $g^{(j)}(0)$  are summarized in Table 6. Concerning the maximum value which is expected to occur for the simultaneous contribution of the same speckle in the reference and object arm ( $x = y_0$ ), one can recognize a very good agreement between the model and the experimental data for all correlation orders. The values 2, 6 and 24 are experimentally well reproduced within the error bars which are taken from the fit parameter uncertainties by the regression analysis considering a weighting by the statistical variance of a set of 3 measurements. In the periphery, when two different speckles are superimposed ( $x \neq y_0$ ), reduced correlation values are expected. The experimentally determined values show a slightly reduced coincidence with the model when considering the error bars. Still, a clear reduction of the  $g_{exp}^{(j)}$ -signal from the previously discussed maxima as well as the predicted non-constant, gradual increase of periphery values with increasing order  $j$  (Eq. (98) and Eq. (99) with  $N = 2$ ,  $\zeta = 0.5$ ) are observed. Here, one can realize the increase of measurement uncertainty with increasing correlation order attributed to the mathematical properties of Eq. (47).

Table 7. Visibility of the spatial higher-order correlations with  $\zeta = 0.5$ , determined experimentally and calculated according to the mixed-light GI model.

Correlation order $j$	Visibility model (in %)	Visibility experiment (in %)
2	14.3	11.4±0.5
3	33.3	27.8±1.5
4	52.4	43.7±2.9

The values of Table 6 allow calculating straightforwardly the corresponding visibility (Eq. (89)). Compared to standard GI schemes which measure the true cross-correlations between reference and object arm with completely vanishing correlations in the periphery of the ghost image ( $g^{(j)} = 1$ ), the here implemented PS-GI method yields a reduced but nevertheless improving visibility behavior with increasing correlation order (see. Figure 41). Table 7 summarizes the visibility-values for the higher-order spatial correlations calculated with the model and determined from the experiment. The increasing tendency of the visibility with higher correlation order is experimentally validated, here by enhancement factors of 2.3 and 3.7 between  $V^{(2)}$ ,  $V^{(3)}$  and  $V^{(4)}$ , respectively. Good coincidence with the model values is observed taking into account the experimental uncertainties. The overall slightly reduced experimental  $V^{(j)}$ -values are ascribed to the slightly enhanced  $g^{(j)}$ -values of the measurement in the periphery (Table 6).

Deliberately detuning the adjusted power ratio  $\zeta$  between the reference and object arm away from optimum visibility ( $\zeta = 0.5$ ), the predicted impact on the visibility (Figure 39) can be examined. Figure

42 shows measured second-order spatial correlations, where inserted variable neutral density filters within each GI arm enabled different power ratio adjustments  $\zeta$ . Unfortunately, the experimental value at the optimum condition  $\zeta = 0.5$  shows the highest deviation from the theoretical trajectory (Eq. (90) and Table 7). For all the other measurements, experimental and theoretical values match quite well with respect to the error bars. Deviations are attributed to the experimental challenge keeping a constant power ratio during a measurement time of 1h for collecting 3 sets of data. Throughout the measurements, a high central coherence degree of 2.0 has been kept for the spatial correlation peak, whereas the periphery value subsequently increased from values of 1.57 up to 1.8 with deteriorating the power balance ( $\zeta \neq 0.5$ ), thus leading to a reduced visibility of roughly 6% for a power ratio of 1:4. Clearly, the predicted trend by the mixed-light model is confirmed.

It should be mentioned that further quality criteria of ghost images such as the contrast-to-noise ratio (CNR) [232] which reflects the noise impact of  $g^{(j)}$ -signals on the ghost image, are available. A rigorous analysis of the CNR behavior in mixed-light GI would need further assumptions of the model such as the number of measurements (number of speckle patterns) to describe the fluctuations  $\Delta g_{mix}^{(j)}$ . Also, photon detection theory should be considered with regard to the measured quantity  $P_{exp}(n)$  which is at the basis of the  $g_{mix}^{(j)}$ -evaluation in the experiment. These aspects should be studied in future work. For the sake of comparability with literature, absolute CNR values are given here according to the definition of Ref. [242]

$$CNR(j) = \frac{g_{max}^{(j)} - g_{min}^{(j)}}{\sqrt{\frac{1}{2}(\Delta^2 g_{max}^{(j)} + \Delta^2 g_{min}^{(j)})}} \quad (108)$$

with the ghost image noise being assessed by the correlation signal variance  $\Delta^2 g^{(j)} = \langle g^{(j)2} \rangle - \langle g^{(j)} \rangle^2$ . It is determined here by using the statistical standard deviations (error bars from Figure 41). The resulting CNR values are 7.4, 6.3 and 5.2 with ascending correlations order 2, 3 and 4. These values reveal the typical CNR deterioration when increasing the correlation order [243]. The trade-off between visibility enhancement and simultaneous rise of the noise level is thus also valid for the mixed-light GI concept.

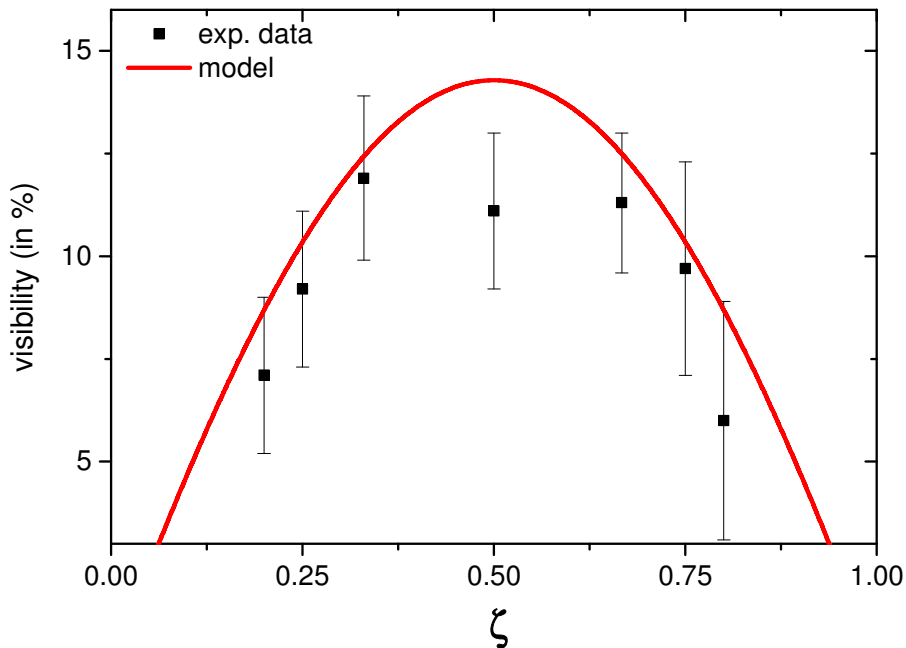


Figure 42. Visibility of the spatial second-order correlations in PS-GI as a function of the adjusted power ratio  $\zeta$  between both imaging planes.

**Double-pinhole experiment.** Having demonstrated a good agreement between the model and the experiment for the simple scenario of the point-to-point correspondence, a more complex situation is approached next, aiming to prove the full GI-functionality of the PS-GI concept. As often occurring in literature, the next level of complexity is realized by a two-point object, here implemented by a double pinhole mask with individual pinhole dimensions again smaller than one speckle cell. The mask is made of aluminum and precision-drilled holes yielding diameters of 0.85mm and a pinhole distance of 2.55mm. For the GI experiment, the power ratio between the object and the reference plane is adjusted to 2:1 where the transmission of each 3 apertures contribute equally by  $\langle I_{pinhole1} \rangle = \langle I_{pinhole2} \rangle = \langle I_{ref} \rangle = \langle I \rangle$ . It should be mentioned that the imaging plane distance  $z_{ref}$  has been readjusted after the insertion of the object to  $z_{ref} = z_{obj}$  to ensure the in-focus condition for preventing ghost image blurring effects within the lensless GI configuration. The transmitted light through the object mask is subsequently gathered by a collimation package coupling the light into the SM fiber. Cross-sections of the measured ghost images of the double pinhole mask with evaluated correlation orders 2, 3 and 4 are shown in Figure 43. In analogy to the analysis of the previous scenario, Gaussian functions (solid lines) are adapted to the experimental data in order to extract the characteristic properties of the ghost images. Applying double Gaussians, one can clearly observe two maxima corresponding to the pinhole positions in the object plane. The object dimensions are accurately reproduced by the ghost image. Of course, no sharp mask edges are reproduced due to the use of a small number of speckles ( $\sim 5$  within the measurement range). However, the Gaussian fit parameters give rise to a pinhole separation of  $(2.62 \pm 0.12)mm$  matching the value of 2.55mm determined by a microscopic image (see Figure 43, right). The characteristic properties of the ghost image, the maximum and minimum  $g^{(j)}$ -values for both the experiment as well as the model, are summarized in Table 8. One notices the overall reduced values of  $g^{(j)}$  compared to Table 7 due to the contribution of one additional speckle cell in the mixed-light signal. The model values are calculated according to Eqs. (97), (98) and (99). For the minimum values, three different ( $N_{max} = 3$ ) but equally contributing ( $\langle I \rangle$ ) speckle cells are considered. Two different ( $N_{min} = 2$ ) speckles contribute to the expected maximum values, yet one of the two is twice as intensive ( $2\langle I \rangle$ ) due to equal positioning of the reference aperture with one transmission feature of the object. Although having recorded a ghost image showing clear evidence for the double pinhole mask, the model predicts lower  $g_{max}^{(j)}$ - and  $g_{min}^{(j)}$ - values. For both experimentally determined values, there seems to be an additional offset of roughly 0.3, 1.9 and 9.7 for the orders 2, 3 and 4, respectively. This can be explained by a reduced number of contributing speckles within the object plane illumination. This could be induced by the proximity of the two pinholes and fairly large speckles ( $> 0.85mm$ , see Figure 41) illuminating the object together with a possible instability of the ground glass mount leading to a speckle cell center position motion during the measurement. Further influences could be due to the fiber coupling scheme either limiting or imposing some spatial restrictions. In future, these issues should be investigated by additional experiments comparing e.g. a free-space configuration with the fiber approach. Also, this rather simple model should be extended by taking into account speckle light propagation through the imaging setup comprising proper object transfer functions and also polarization effects.

These discrepancies between the model and the experimental observation are logically transferred to the visibility performance (Table 8). In contrast to the increase in visibility from 5.9% to 34.8% for the correlation order 2 to 4 is predicted by the calculations, the experimental results show a less important but nevertheless positive enhancement up to 15.4% at  $j=4$ . The considerably large uncertainties of the measured GI signal  $\Delta g_{exp}^{(j)}$  (see Figure 43) are responsible for the large uncertainty of the determined visibility values up to a relative error of 85% in the case of  $j=2$  and thus a careful interpretation needs to be made.

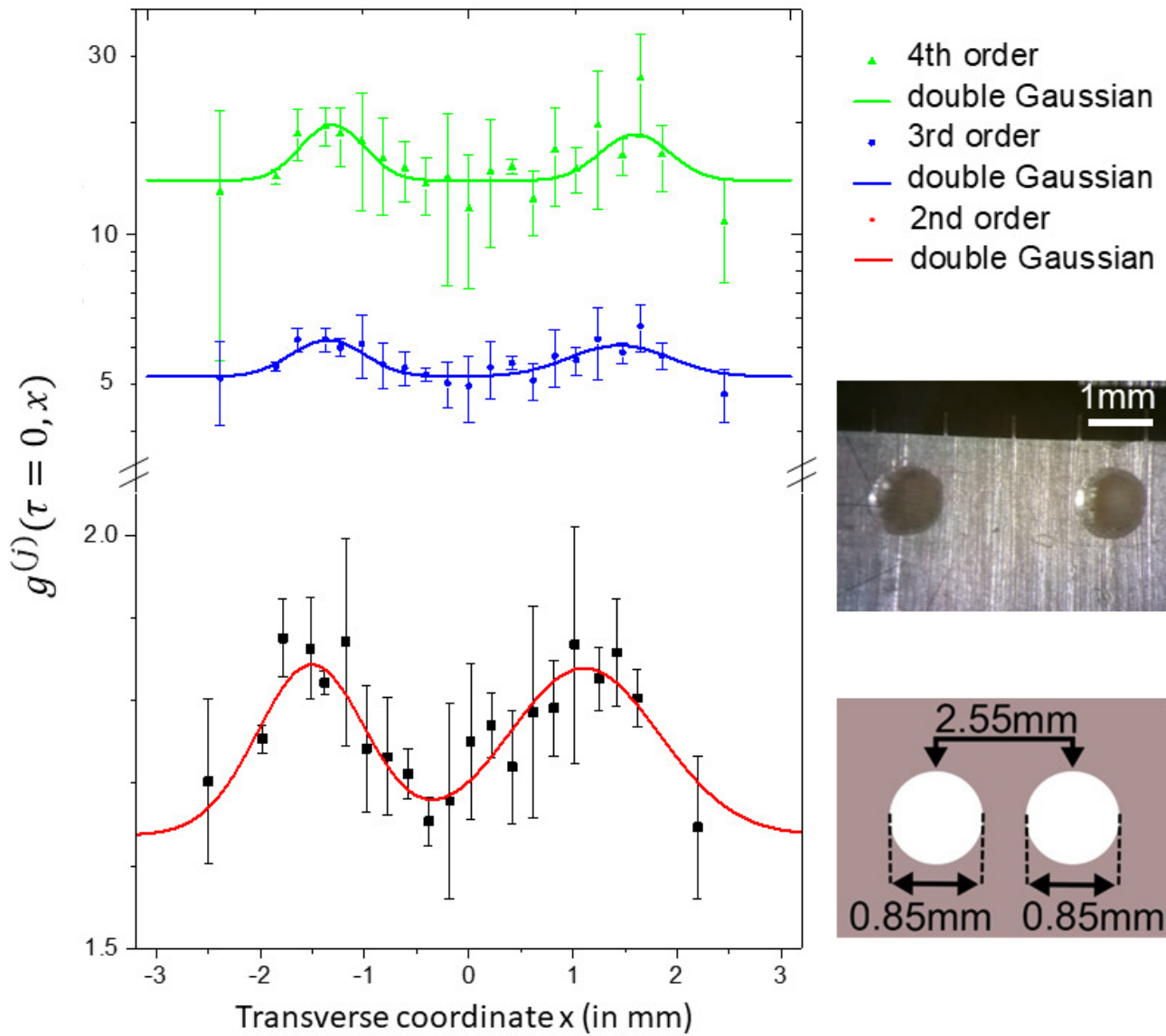


Figure 43. **Ghost image cross-section of a double-pinhole mask.** Left: Experimentally obtained higher-order ghost image cross-sections. Right: Legends of graphs (top), microscopic picture of the transmission mask (middle) made of an aluminium plate together with a schematic drawing of the object with dimensioning indications (bottom).

Table 8. **Characteristic properties and visibility values of the double-pinhole cross-section PS-GI demonstration** compared to theoretical values according to the mixed-light GI model.

Correlation order $j$	2	3	4
$g_{exp}^{(j)}$ min	1.64±0.10	4.19±0.15	14.0±0.7
$g_{exp}^{(j)}$ max	1.84±0.14	5.15±0.27	19.1±1.8
$g_{mix}^{(j)}$ min	1.33	2.22	4.44
$g_{mix}^{(j)}$ max	1.50	3.33	9.20
Visibility model (in %)	5.9	20.0	34.8
Visibility experiment (in %)	5.7±4.9	10.3±3.1	15.4±5.2

### 5.1.4. Numerical 2D ghost images

A proof-of-principle GI experiment has been demonstrated in the previous section. In view of developing a practical imaging system, it is evident that two-dimensional, complex objects must be addressed. This section deals briefly with the expected visibility behavior of PS-GI depending on the object complexity. Additionally, a numerical example of a 2D ghost image is presented giving a clear illustration of a possible imaging scenario with a PS-GI camera-system of future development<sup>29</sup>.

The decreasing visibility with increasing object complexity is an inherent issue of GI. As a reminder: for imaging a specific number of object features, at least the same number of transverse modes must be projected onto the object which then are all contributing to the GI signal. As intensity correlation signals decrease with a higher number of transverse modes, also the visibility of the entire ghost image deteriorates consequentially. Tremendous effort has been invested into developing new protocols and exploiting modern technologies for improving the visibility aspect (see the introductory Section 2.2). The analysis of the visibility performance of GI is often carried out by considering the dependence of the object complexity [29, 238, 53, 85]. Therefore, the visibility of the here proposed PS-GI scheme is briefly analyzed and compared to conventional higher-order GI detection in that same manner. As already mentioned, the complexity of an object to be resolved, can be captured in terms of numbers of coherence areas  $A_c$  (Eq. (11)). It is appropriate to use the relative measure  $A_{obj}/A_c$ , where  $A_{obj}$  stands for the object area. In conventional higher-order GI detection [53]

$$G^{(j)}(\vec{x}) = \langle I_{bucket}^{j/2} I_{ref}^{j/2}(\vec{x}) \rangle \quad (109)$$

holds using here an adapted correlation order definition for comparability. The corresponding visibility behavior of a binary object with uniform intensity distribution at the imaging planes as a function of object complexity reads [53, 243]

$$V^{(j)}(A_{obj}, A_c) = 1 - 2 \left\{ 1 + \frac{\left(\frac{A_{obj}}{A_c} + j - 1\right)! \left(\frac{A_{obj}}{A_c} - 1\right)!}{\left[\left(\frac{A_{obj}}{A_c} + \frac{j}{2} - 1\right)\right]^2} \right\}^{-1}. \quad (110)$$

Note that this expression is valid only for even values of  $j$  and  $A_{obj}/A_c$  being an integer. Figure 44 depicts these visibility functions for the correlation order 2 (black solid line) and 4 (black dotted line) as a function of  $A_{obj}/A_c$ . In direct comparison, numerically determined visibility values of the mixed-light GI scheme for the orders 2 (red data), 3 (blue data) and 4 (green data) are depicted as well. Note that

- i. a uniform intensity distribution and binary objects are likewise assumed in the presented mixed-light model.
- ii. additionally, the power ratio  $\zeta$  for the optimum contrast condition holds.

The latter has been numerically derived for each  $A_{obj}/A_c$  value which prohibits formulating a general visibility expression with those specific boundary conditions.

The accordance of the decrease of all trajectories in the double-logarithmic scale is striking showing an exponential decay of the visibility with increasing  $A_{obj}/A_c$ . Furthermore, the overall lower visibility performance of PS-GI with respect to conventional GI for a specific correlation order  $j$  is visible. This fact is clearly attributed to the mixed-light characteristic of PS-GI. However, the reduced number of detectors and thus the reduction of complexity of the setup achieving higher-order GI with one single detector

<sup>29</sup> A supervised master thesis deals with that subject (see page 138, L. Fischer).

---

easily justifies the PS-GI scheme. Besides, the visibility of PS-GI in correlation order  $j = 3$  already surpasses conventional GI with  $j = 2$ .

In order to be more precise, a concrete numerical example is illustrated by an exemplary binary transmission mask. Figure 45 (A) shows a possible transmission mask of an acronym of the *Technische Universität Darmstadt* (TUD) in a 24x24pixel image. A number of 62 coherence areas shall fit into the transmission area of the mask. Figure 45 (B), (C) and (D) are calculated PS-GI ghost images with the same assumptions as for Figure 44 corresponding to the correlation order 2, 3 and 4, respectively. For all three ghost images, the image signals are depicted on a gray-scale within a range of  $g_{max}^{(j)} - g_{min}^{(j)} = 0.2$ , illustrating the improvement of the visibility by evaluating higher correlation orders. For  $j$  equals 2, 3 and 4, the precise maximum visibility values amount to 0.32%, 0.91% and 1.69%, respectively, whereas conventional GI yields  $V^{(2)} = 0.80\%$  and  $V^{(4)} = 3.15\%$ .

It can be concluded that the visibility behavior of PS-GI is very similar to that of conventional higher-order GI, however with globally lower absolute values for a given correlation order  $j$ . The computed visibility, representatively shown in a range of  $1 \leq A_{obj}/A_c \leq 1000$ , allows one to identify the requirement in experimental precision for imaging an object of a specific complexity. The mixed-light model, presented in this chapter, thus constitutes a simple framework for predicting image characteristics of a PS-GI system.

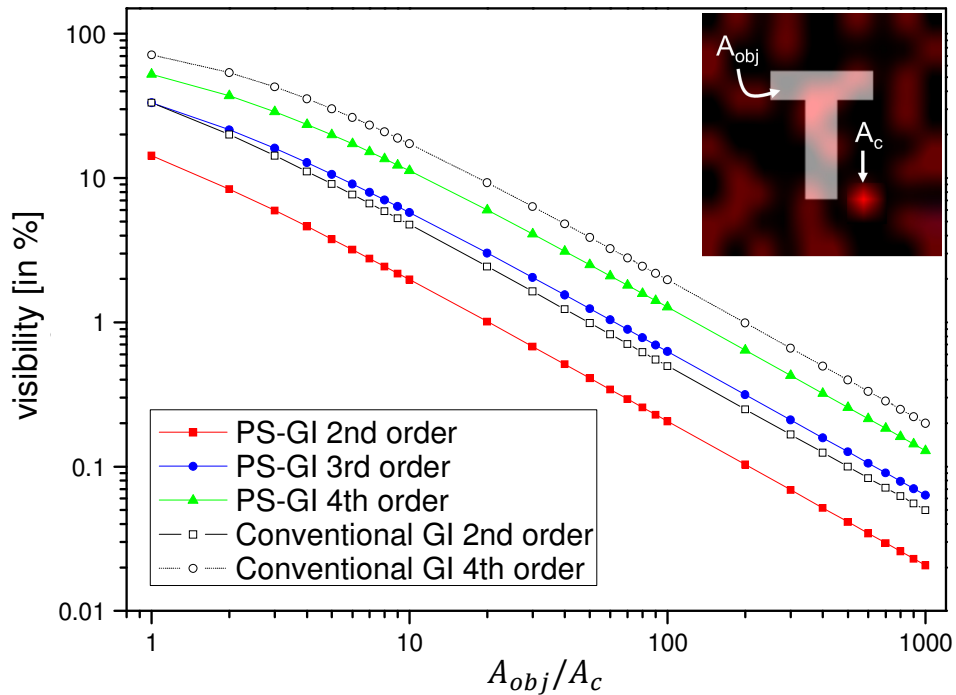


Figure 44. **Visibility as a function of object complexity** in terms of number of coherence areas fitting into an object transmission mask ( $A_{obj}/A_c$ ). Coloured and black trajectories correspond to the PS-GI model and conventional higher-order calculations, respectively. Inset: Illustration of the coherence area  $A_c$  and the object area  $A_{obj}$  for an exemplary binary object of the letter "T".

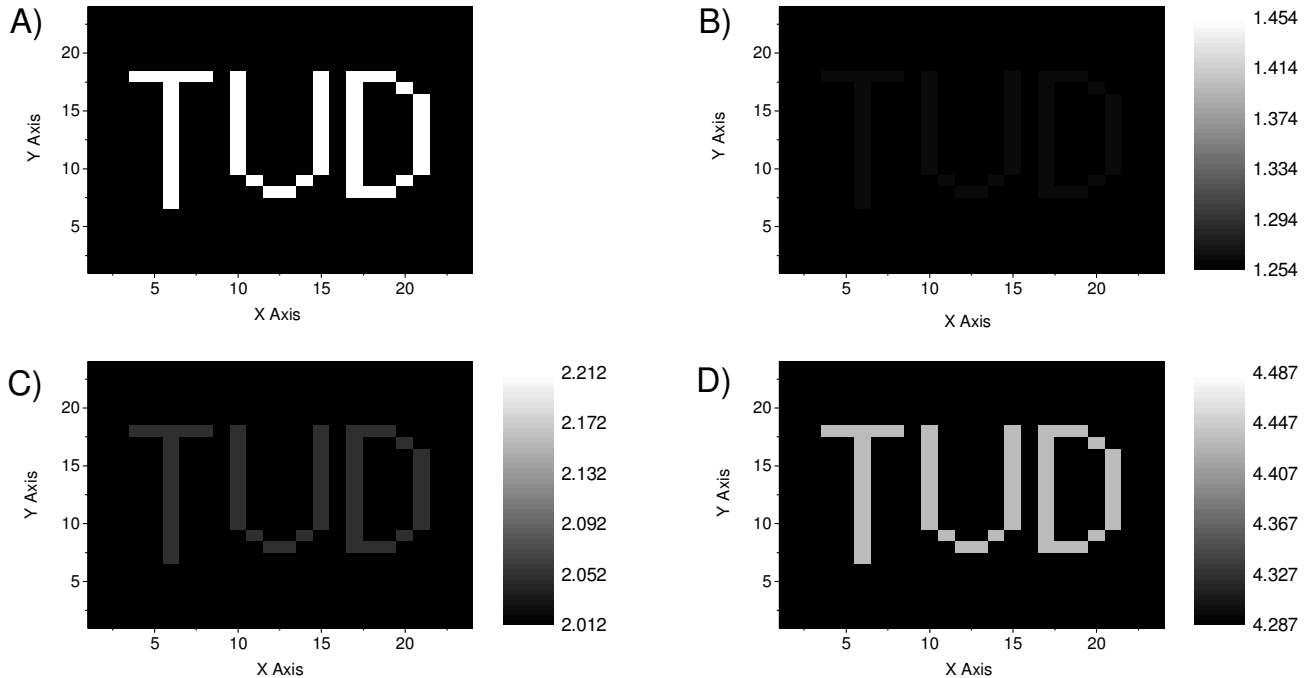


Figure 45. **Calculated higher-order PS-GI images (maximum and minimum values) of a two-dimensional transmission mask (A)** depicting the acronym of the *Technische Universität Darmstadt* (TUD). The expected PS-GI signal amplitudes for the correlation order 2 (B), 3 (C) and 4 (D), assuming optimal visibility conditions (see Section 5.1.2), are visualized as a contour-plot with an adjusted equal scaling of 0.2 for illustrating the visibility enhancement with increasing correlation order.

Section 5.1 dealt with a novel classical GI detection method which is termed *photon statistics-based ghost imaging* (PS-GI). Instead of detecting the bucket signal and the reference signal by two different detectors which are subsequently correlated, the reference and the object light selected in the respective imaging planes are optically superimposed. The joint photon number probability distribution of this combined (*mixed-*) light is then determined by one single-photon-counting detector with appropriate photon-count acquisition and statistical evaluation. A unique feature of this concept is that higher-order ghost images can be evaluated with the same measurement using a single detector. The physical concept is based on the idea of exploiting the complementarity of intensity auto- and cross-correlations of light in the context of GI.

A simple model of the novel PS-GI scheme based on the superposition of the intensities of the object and the reference beam with independent speckles obeying Gaussian statistics has been presented. The functionality of the ghost image formation is ascribed to the joint intensity auto-correlation behavior of a varying amount of multiple speckle cells contributing to the detected mixed-light. The spatially resolving reference arm operates as the selecting aperture for the amount of contributing speckle cells. As already shown in the very early days of photon statistics [218, 220] and also in Chapter 4, mixed-light phenomena are strongly dependent on the power ratio between the different light contributions. This does also apply in the case of mixed-light GI. The visibility performance of a specific mixed-light GI scenario is significantly dependent on the ratio between the collected object intensity and the selected reference intensity as well as on the distribution of all individual speckle cell intensities at the imaging planes. Note that conventional GI does also exhibit a dependence on the partition ratio of the intensities on the two detectors, however with less importance [238]. Also, the higher-order functionality of the PS-GI method using only one detector has been confirmed by the mixed-light GI model. With this model, it was possible to gain insights into the underlying physics of the PS-GI concept explaining the fundamental differences with respect to state-of-the-art GI schemes. In particular, the visibility of conventional GI and PS-GI has been analyzed as a function of the object complexity. It has been found that the well-known exponential decay of GI-visibility with increasing the number of object features to be resolved is valid in the exact same manner for mixed-light. The main difference lies in lower absolute values of the visibility due to the mixed-light characteristic.

Furthermore, the direct comparison between experimental results and values calculated by the model showed a good agreement regarding the photon distribution analysis as well as the position-position correlations. A proof-of-principle GI demonstration has been achieved by recording a cross-section of a double-pinhole mask.

Future practical implementation of a 2D PS-GI system will benefit from the here presented work. In view of a feasible PS-GI camera system, it is indispensable to develop a faster data acquisition which will also enable further robustness analysis of the PS-GI method, e.g. investigations of the contrast-to-noise ratio (CNR). The PS-GI can be seen as a complement to already existing GI detection methods (Section 2.2) enabling a broader platform for applications, thus fostering the entrance into practical GI metrology in future work. True to this motto, the following section presents another novel GI detection principle yet with a totally different approach based on temporally incoherent light and nonlinear interferometry.

## 5.2. Spectrally ultra-broadband GI with hybrid pseudo-thermal-SLD light

This section deals with the development of another GI detection scheme which is a prerequisite for enabling highly incoherent GI experiments. The detection concept is based on two-photon-absorption in a semiconductor detector, as presented in Section 3.2 and as already utilized for fundamental superluminescent diode coherence studies in Chapter 4.

A first building block towards highly incoherent GI concepts is laid by developing a spatial HBT scheme where the two-detector concept and a subsequent correlator apparatus is replaced by TPA interferometry. This will allow measuring a ghost image with femtosecond-correlation timescales.

First, a detailed description of the GI scheme is given together with the implemented light source (Section 5.2.1). *Hybrid pseudo-thermal-superluminescent diode light* is generated for ensuring the required coherence properties appropriate to GI. Then, a point-to-point correspondence between the light fields at the reference and at the object plane is demonstrated in Section 5.2.2. Finally, the cross-section of a double-pinhole object is imaged as a proof-of-principle GI experiment (Section 5.2.3). The quality and the visibility of the obtained GI signals are discussed.

### 5.2.1. GI scheme

**The QD SLD.** The here utilized light source is the same device as in Section 4.3, namely a free-space emitting SLD based on a QD active region consisting of inhomogeneously broadened InAs/InGaAs - quantum dot layers. Here, the SLD is continuously forward-biased at even higher pump currents ( $I_p = 1.2A$ ) compared to the mixed-light investigations in Section 4.3 ( $I_p = 300mA$ ). Thus, high output powers up to 200mW are generated at the front facet. Ultra-broadband emission in the NIR is observed at an approximate central wavelength of  $\lambda_c = 1203nm$  with a spectral width of  $\Delta\lambda_s = 70nm$  (see Figure 46, left). The shape of the optical distribution functions reveals three central wavelength contributions with conceivable Gaussian distributions from which the lowest central wavelength, i.e. the highest energy state, is dominating. This is clearly attributed to the triple-chirped QD epitaxial structure of the SLD [244]. The non-uniform spectral shape with a pronounced tail supports again the use of the Suessmann measure for quantifying the spectral width (compare the indications of different values in Figure 46).

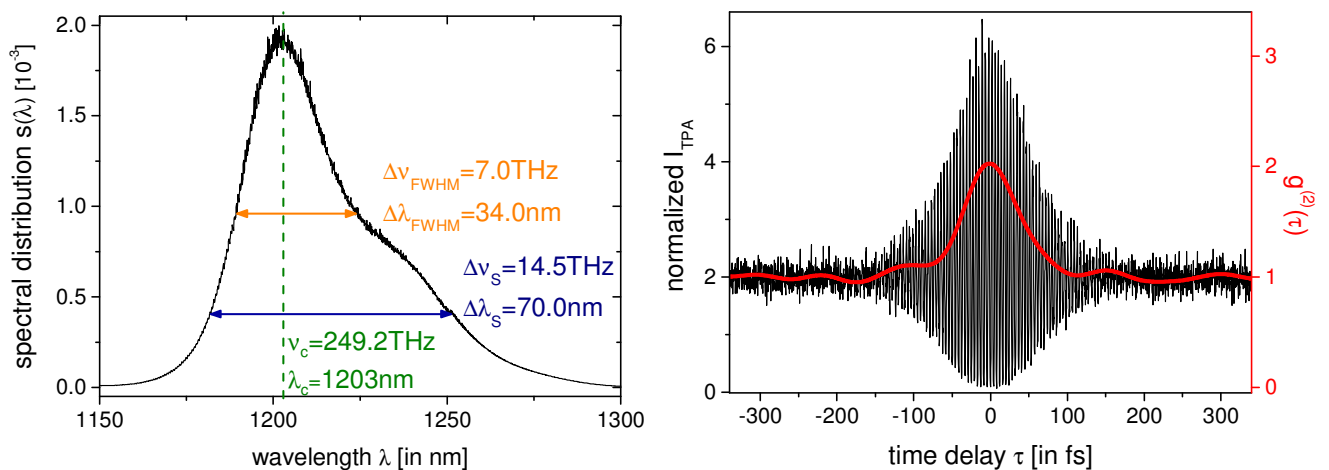


Figure 46. **First- and second-order coherence of the QD SLD light:** Left: Optical power spectrum (measured by an OSA, ADVANTEST Q8384) as a function of wavelength with various indicated measures: the central wavelength/frequency (green) as well as the spectral widths in terms of wavelength/frequency according to the FWHM (orange) and to the Suessmann measure (blue). Right: Representative TPA interferogram (black line) of a single measurement and extracted second-order correlation function (red line).

Figure 46 (right) depicts a representative TPA interferogram of the QD SLD emission corresponding to the operation conditions from Figure 46 (left). It shows constructive and destructive interference fringes which vanish for time delays  $\tau$  exceeding  $\pm 100\text{fs}$ . Furthermore, Figure 46 (right) unveils a clear thermal correlation behavior with  $g^{(2)}(\tau) \geq 1$  and a central degree of second-order coherence  $g^{(2)}(0) = 2.03 \pm 0.05$  being conform with the thermal limit value of 2. A coherence time  $\tau_c = 67\text{fs}$  has been determined directly from the extracted correlation function  $g^{(2)}(\tau)$  at the  $1/e^2$ -decay with respect to  $g^{(2)}(0)$ . To underline the good functionality of the TPA detection method, the excellent coincidence with the predicted coherence time corresponding to the spectral width  $\Delta\nu_s = 14.5\text{THz}$  (Eq. (7)).

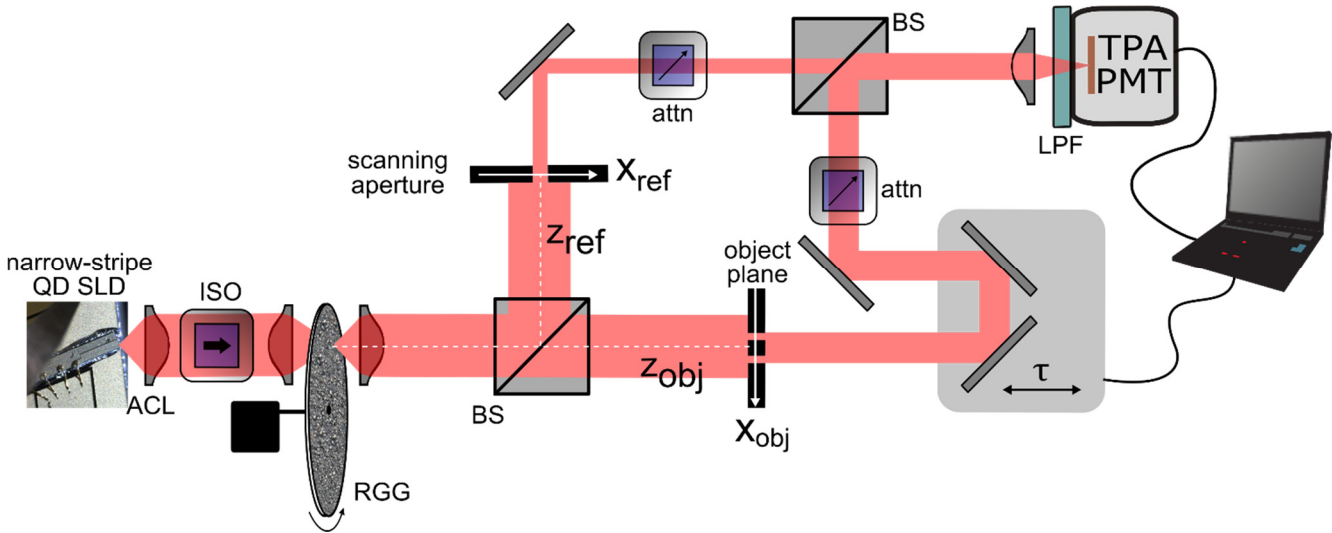


Figure 47. **Schematic diagram of the experimental setup for ultra-broadband ghost imaging** using the hybrid pseudo-thermal-SLD light: free-space emitting superluminescent diode (narrow-stripe QD SLD), achromatic lenses (ACL), optical isolator (ISO), rotating ground glass plate (RGG), broadband 50:50 beam splitters (BS), long pass filter (LPF) blocking fundamental absorptions ( $\lambda < 1000\text{nm}$ , SCHOTT RG1000), variable attenuator (attn) for optimizing the intensity distribution between both interferometer arms, motorized (Newport LTA-Series) linear translation stage ( $\tau$ , Newport M-443) and the photomultiplier in TPA mode (TPA PMT).

### Ultra-broadband ghost imaging scheme.

This comprehensible highly incoherent light with respect to time emitted by the SLD is incorporated into a the new, TPA interferometry-based GI configuration depicted in Figure 47. However, the SLD exhibits strongly directional emission, predefined by its waveguide geometry and by the small output facet of  $< 1\mu\text{m}$  height and  $5\mu\text{m}$  width (narrow-stripe edge emitter). Unfortunately, this results in a highly pronounced spatial coherence property, inappropriate to a light source for GI. This issue is circumvented by focusing the SLD beam onto a RGG diffuser (Thorlabs N-BK7 diffuser, 220 grit) generating a spatially incoherent light beam consisting of changing random speckle patterns (analogue to Figure 35). It is important to note, that the here implemented rotating diffuser solely acts on the spatial coherence of the light beam and has no influence on the temporal coherence as it does for PT light sources. The angular speed of the diffusive ground glass plate of approximately  $0.2\text{kHz}$  modulates the intensity in time-regimes more than 7 orders of magnitudes slower than the coherence time of the light source. This high temporal incoherence ( $\tau_c = 67\text{fs}$  and  $g^{(2)}(\tau = 0) = 2.03$ ) combined with artificially generated spatial incoherence is termed as hybrid PT-SLD light. Thus, the requirements as a GI light source are fulfilled (see Section 2.2). The divergent speckle-patterned beam is then collimated and split by a broadband beam splitter generating two highly correlated beams with a beam diameter of  $\sim 25\text{mm}$ . The object plane and the reference plane are adjusted to be equally apart at distances  $z_{ref} = z_{obj} = 200\text{mm}$  with respect to the ground glass plane such that blurring of the ghost image is prevented [69]. The implemented TPA detector requires the two beams to be recombined via a second beam splitter forming an overall Mach-Zehnder interferometer-like geometry. The time delay  $\tau$  is introduced via a high precision, motorized translation stage with a retro reflector-like mirror alignment. Special care is taken to adjust the beam overlap between the

reference and the object arm behind the second beamsplitter in order to assure an accurate overlap of the two foci at the photocathode plane. Occasionally, a re-adjustment during the measurement is needed such that spatial drifts or object focus-scanning is prevented. Also, it is noteworthy that this setup represents a lensless GI configuration and hence intrinsically works within the near-field plane of the object without the need of any further imaging component [245]. It can be summarized that the proposed GI scheme relies on a modified spatial HBT configuration where the two-detector system with a subsequent correlator is replaced by TPA interferometry.

### 5.2.2. Point-to-point correspondence

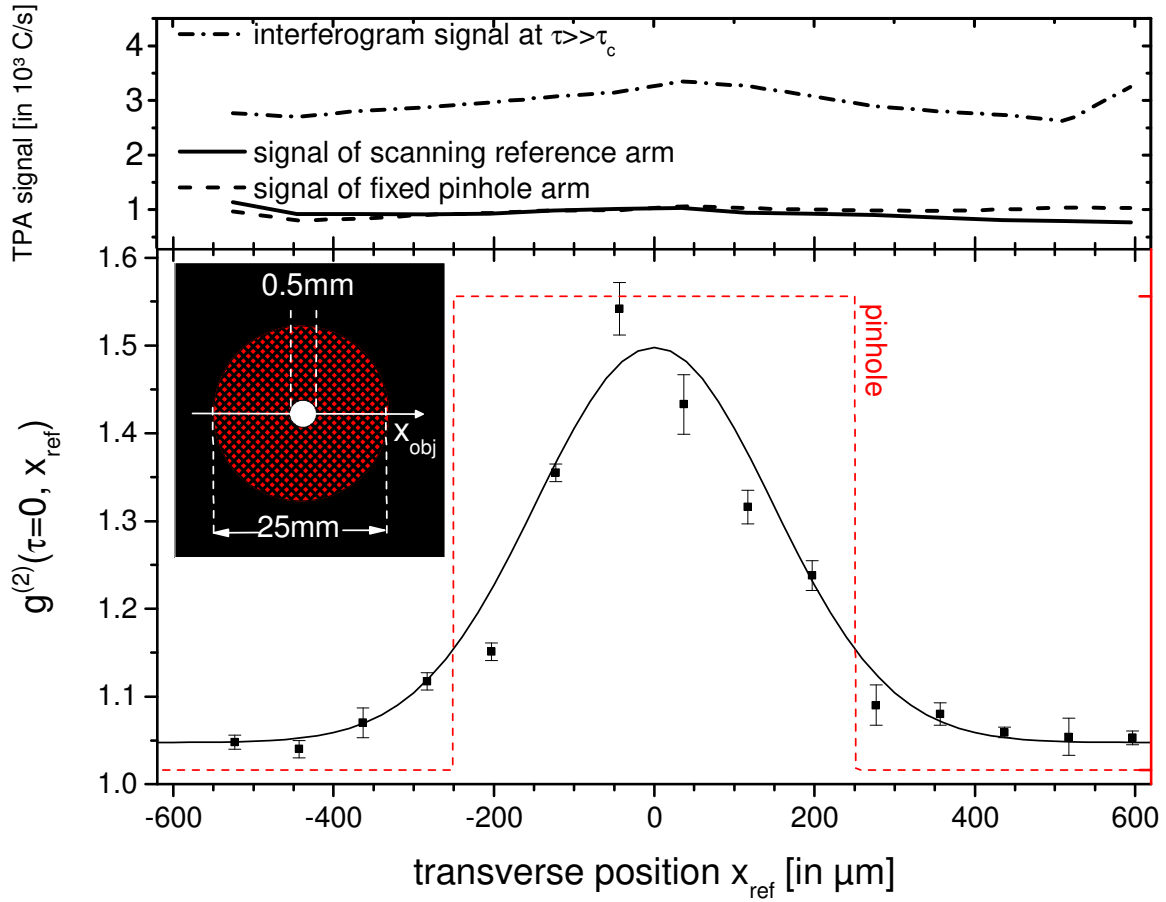


Figure 48. **Representative point-to-point correspondence of ultra-broadband GI using the hybrid PT-SLD light.** Top: TPA signals corresponding to the intensities of the single arms (reference pinhole and fixed pinhole) as well as the combined intensities taken from the interferogram at time delays far from coherence. Bottom: Central second-order coherence degree as a function of the relative transverse displacement of the two split beams. A Gaussian fit is depicted as a guide-to-the-eye. The error bars correspond to the statistical variance of a set of 3 subsequent measurements. Inset: Schematic illustration (not to scale) of the speckle-pattern size and the fixed pinhole in the object plane ( $x_{obj}$ ) which cross-section is also indicates in the graph (red dashed line).

In a first experiment, a point-to-point correspondence between the two split beams at the object and the reference plane shall be verified. Therefore, two pinholes with diameter  $d=500\mu\text{m}$  are placed in the interferometer, one in each interferometer arm at distances corresponding to the object plane  $z_{obj}$  and the plane of transverse resolution  $z_{ref}$ . Relative transverse displacement is realized by keeping the pinhole in the object plane fixed at the center of the collimated beam ( $x_{obj}=0\mu\text{m}$ ) (Figure 48, inset) and by scanning the pinhole in the reference plane along the transverse  $x_{ref}$ -axis, where  $x_{ref}=0\mu\text{m}$  also corresponds to the center of the beam. Figure 48 (top) shows mean TPA signals corresponding to the

intensities of the reference pinhole transmission and the fixed pinhole transmission as well as the combined intensities taken from the TPA interferograms at time delays  $\tau$  far from  $\tau_c$ . Considerably constant values remain with overall position averaged TPA counting rates (counts per second (C/s)) of  $(922 \pm 95)$ C/s (reference),  $(968 \pm 73)$ C/s (object) and  $(2956 \pm 228)$ C/s (superimposed far off coherence). Clearly, no information about a point-to-point correspondence can be retrieved. The approximately constant TPA signal behavior as a function of transverse position  $x$  is due to the fact that the speckle-patterned beam of 25mm diameter impinging onto each pinhole plane exhibits a nearly constant intensity distribution in the vicinity of the pinholes. Figure 48 (bottom) depicts the central second order coherence degree  $g^{(2)}(0)$  as a function of the transverse position  $x_{ref}$  obtained from experimentally determined intensity-intensity cross-correlation functions  $g^{(2)}(\tau = 0, x_{obj} = 0\mu m, x_{ref})$ . Enhanced correlations near  $x_{ref} = 0\mu m$  up to  $g^{(2)} = 1.54$  with decreasing values for  $|x_{ref}| > 0\mu m$  are observed. Beyond  $|x_{ref}| > 250\mu m$ , which corresponds to the edges of the pinhole dimensions in the object plane,  $g^{(2)}(0)$  reduces below 1.15 and correlations almost entirely vanish for  $|x_{ref}| > 450\mu m$  with values around  $g^{(2)} = 1.05$ . The reason why these values do not fully approach 1 is due to the large diameter of the two pinholes leaving some residual correlations which are also the origin of the reduced values of  $g^{(2)}$  at  $x_{ref} = 0\mu m$  in comparison to the measured value of  $g^{(2)} = 2.03$  in Figure 46 (right). The simultaneous detection of a larger number of uncorrelated speckles corresponds to spatially integrated intensity correlations leading to a correlation reduction and thus to a reduced visibility from 31% (Figure 46 (right)) to 18% (Figure 48, bottom). The adjusted transverse coherence length of approximately  $\sigma_c \approx 320\mu m$  is slightly smaller than the pinhole sizes<sup>30</sup>. This minimizes the amount of transverse modes (speckle cells) that contributes to the correlation signals for observing a pronounced point-to-point correspondence. Additionally, this explains the maximum value of  $g^{(2)}(\tau = 0, x_{obj}, x_{ref} = 0\mu m)$  not reaching the maximum spatial correlation value of  $\sim 2$ , as more than 1 speckle cell are selected in each of the planes.

### 5.2.3. GI experiment

In order to demonstrate a GI experiment with an object of rather simple complexity, a double-pinhole mask is placed into one of the interferometer arms at the object plane ( $\vec{x}_{obj}$ -plane, see Figure 47). Each of the two pinholes exhibits a diameter of  $d = 500\mu m$  and they are separated by a distance of  $s = 1$ mm (Figure 49, inset). At the reference plane ( $\vec{x}_{ref}$ -plane), a simple pinhole is used with a diameter of  $500\mu m$  to scan the transverse  $x_{ref}$ -axis (one-dimension) where a total range of 2.2mm is covered in steps of  $80\mu m$ . Figure 49 (top) shows TPA signals corresponding to the individual intensities of the reference pinhole transmission and the fixed double-pinhole transmission as well as the combined intensities taken from the TPA interferograms at time delays  $\tau$  far from  $\tau_c$ . Just as for the point-to-point correspondence in the previous section, quasi constant values prevail over the total scan range with overall position averaged TPA counting rates (counts per second (C/s)) of  $(1228 \pm 68)$ C/s (reference),  $(1743 \pm 112)$ C/s (object) and  $(4168 \pm 276)$ C/s (superimposed far off coherence). Clearly, these TPA signals do not provide any spatial information about the object excluding any shadowing effects within the free-space TPA interferometer. Figure 49 (bottom) depicts the second-order coherence degree  $g^{(2)}(0)$  as a function of the transverse position  $x_{ref}$  obtained from experimentally determined intensity-intensity cross-correlation functions  $g^{(2)}(0, x_{obj}, x_{ref})$ , where  $x_{ref} = 0\mu m$  is the central position of the reference beam corresponding to the center of one of the two holes of the fixed double-pinhole in the object plane (see Figure 49, inset). Two distinct maxima  $g^{(2)}(x_{ref}^{max,1} = -40\mu m) = 1.63$  and  $g^{(2)}(x_{ref}^{max,2} = 920\mu m) = 1.60$  are apparent. The correlations reduce nicely beyond  $x_{ref} > 1250\mu m$  and  $x_{ref} < -250\mu m$  to values below  $g^{(2)} = 1.1$  reflecting the periphery dimensions of the double-pinhole object. Most importantly, the correlation reduction holds also for positions  $x_{ref}$  in between the two pinholes for  $250\mu m < x_{ref} < 750\mu m$ , again with values below  $g^{(2)} = 1.1$  revealing a clear object signature. The reason why these values do

<sup>30</sup> This value has been estimated by using Eq. (27).

not fully approach  $g^{(2)} = 1.0$  is attributed to the large diameter of the scanning pinhole with respect to the speckle size and the pinhole separation leaving some residual correlations. Together with an expected correlation reduction due to the object complexity (here: two transparent features), a considerable visibility of 21% is achieved. Despite the coarse scanning procedure, the double-pinhole signature is well imaged. A double Gaussian fit function Figure 49 (bottom, black solid line) reproduces the pinhole separation  $s$  with 99.6% accuracy.

Finally, two representative interferograms are depicted in Figure 50 together with their low-pass filtered counterparts from single measurements at positions  $x_{ref} = 1000\mu\text{m}$  and  $x_{ref} = 600\mu\text{m}$  to support further the good functionality and quality of the proposed GI scheme. At  $x_{ref} = 1000\mu\text{m}$ , enhanced correlations  $g^{(2)}(0, x_{ref} = 1000\mu\text{m}) = 1.58$  are measured (Figure 49, bottom). The underlying correlations signal as a function of the time delay  $\tau$  (Figure 50, left, red line) shows a pronounced modulation despite the ground glass influence on the TPA interferogram [50] (Figure 50, left, black line) reflected by the non-ideal constructive and destructive interference fringes during the measurement. In contrast, at  $x_{ref} = 600\mu\text{m}$ , a quasi Poissonian-like second-order degree of  $g^{(2)}(0, x_{ref} = 600\mu\text{m}) = 1.02$  is apparent. The underlying correlations are in fact non-visible without any interferogram signature (Figure 50, right, black line) yielding a constant second-order correlations signal (Figure 50, right, red line).

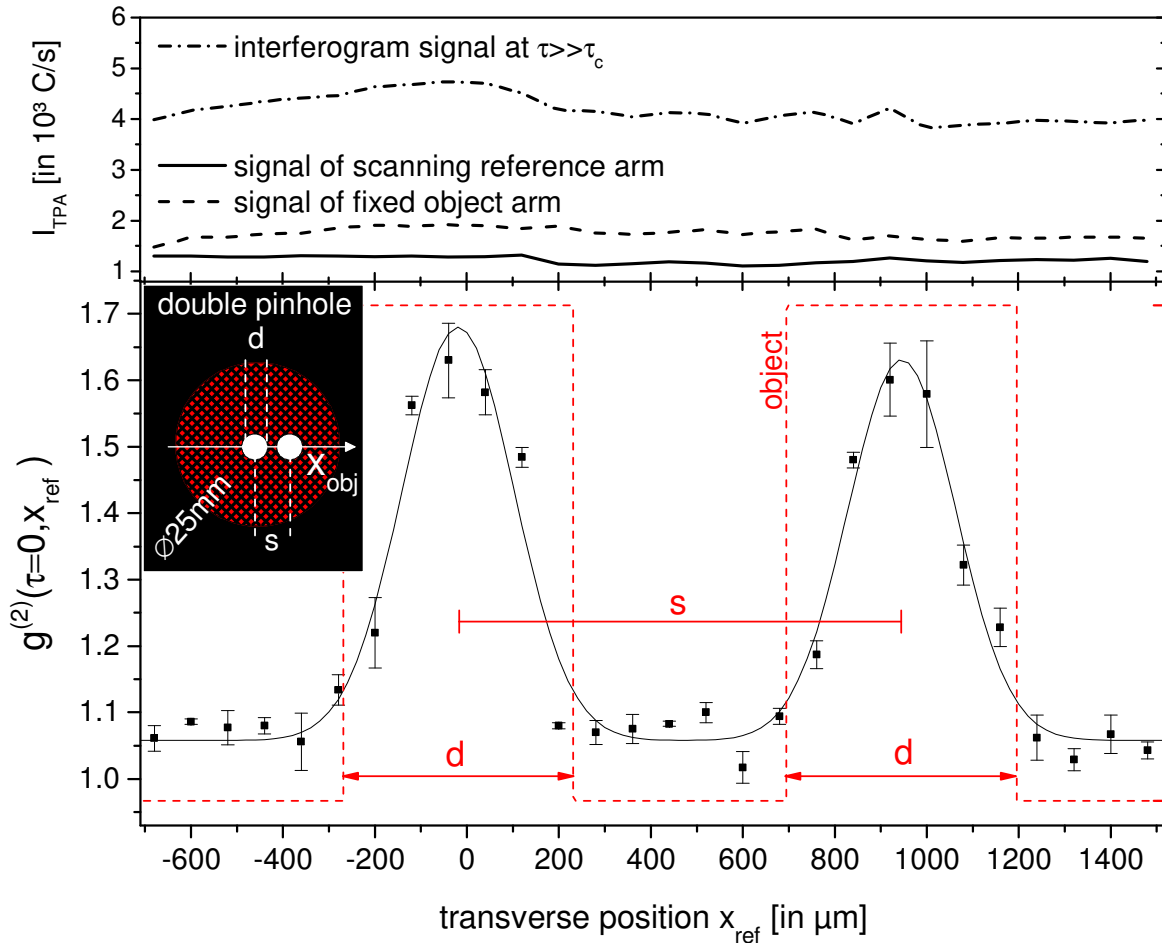


Figure 49. **Ultra-broadband GI with a double-pinhole object:** Top: TPA signals corresponding to the intensities of the single arms (reference pinhole and fixed double-pinhole object) as well as the combined intensities taken from the interferogram at time delays far from coherence  $\tau \gg \tau_c$ . Bottom: Ghost image cross-section (central second-order coherence degree as a function of the relative transverse displacement between reference and object beam) with error bars corresponding to the statistical variance of a set of 3 subsequent measurements. A double Gaussian fit (black solid line) is depicted as a guide-to-the-eye. Inset: Schematic drawing of the object and the beam size (not to scale) with object details given: the individual pinhole diameter  $d=500\mu\text{m}$  and the pinhole separation  $s=1000\mu\text{m}$ , which are depicted as a cross-section (red dashed line) in the bottom graph.

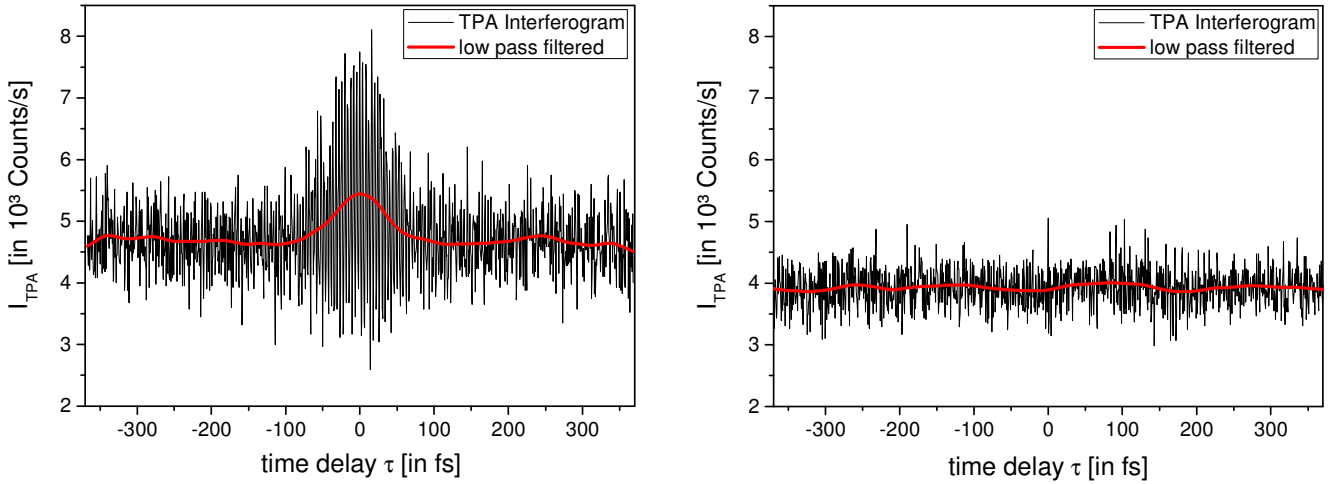


Figure 50. Measured (black line) and low-pass filtered (red line) TPA interferograms of single measurements corresponding to the ghost image (Figure 49, bottom) at  $x_{ref}=1000\mu\text{m}$  (left) and at  $x_{ref}=600\mu\text{m}$  (right).

Section 5.2 presented a new GI experiment based on temporally incoherent light and TPA interferometry. The interferometric nonlinear detection technique for temporal second-order auto-correlation measurements of real black body sources, developed in 2009 [9], has been exploited for realizing a GI scheme. Its functionality has been proven by verifying a point-to-point correspondence as well as by recording a proof-of-principle one-dimensional ghost image of a double-pinhole mask. This scheme can be considered as another, fourth complement to already existing GI detection methods (original two-detector-based GI, computational GI and PS-GI (Section 5.1)). It is interesting to note that the potential of TPA interferometry for addressing spatial correlations of light has already been suggested by F. Boitier within the outlook of his PhD thesis [133] finding here its realization in the context of GI.

While the focus of this section was the implementation of the GI detection scheme by TPA interferometry, the experiment itself holds a noteworthy progress in the field of fundamental GI research. Indeed, a *GI experiment with light comprising the highest degree of temporal first-order incoherence* has been realized. Induced by the ultra-broadband spectral width ( $\Delta\nu_S = 14.5\text{THz}$ ) originating from opto-electronic amplified spontaneous emission exhibiting thermal-like photon statistics, the corresponding femtosecond-correlation timescales had to be managed ( $\tau_c = 67\text{fs}$ ).

Hence, the level of incoherence has been strongly increased regarding the temporal domain by means of a QD SLD. However, in the spatial domain, a residual coherent characteristic persists due to relatively *slow* speckle-pattern generation ( $<1\text{kHz}$ ) by the rotating diffusor, which can be associated with ms-timescales. This justifies once again, the terminology of *hybrid pseudo-thermal-superluminescent diode light*. Also, this light source concept holds a multi-component, rather bulky design just as for state-of-the-art GI light sources (Table 1), hence does not really contribute to an improved applicability of GI.

This aspect is taken up by the next section. In particular, a QD SLD exhibiting an enlarged waveguide structure is employed within the here presented TPA interferometry-based GI scheme.

---

### 5.3. Spectrally ultra-broadband GI with a broad-area SLD

In pursuit of realizing a highly incoherent GI experiment without restriction on any aspect of coherence, the ultra-broadband GI scheme introduced in the previous section, is exploited further using a novel source of light.

Recalling the historical development of GI light sources (see Section 2.2), GI was initially demonstrated with entangled light from parametric down conversion which, still today, is at the heart of quantum GI research [225]. Classical light sources were later introduced with the development of thermal light GI concepts. State-of-the-art classical GI light sources rely either on complex combinations of coherent light with spatially randomizing optical elements or on incoherent lamps with monochromating optics generating artificial thermal statistics. However, these concepts suffer strong losses of efficiency and directionality (see Table 1). There are mainly two reasons for the development of such multi-component sources for classical GI which both relate to the detection schemes. The limited time resolution of HBT configuration-based GI schemes with one bucket detector and a spatially resolving reference detector makes artificially generated position-correlations a necessary technical solution. Coherence times can be adjusted to significantly high values for matching long detector integration times. For certain, computational GI is currently the concept with the most promising potential and with the most advanced developments towards application [246, 247], even if being gradually replaced by computational imaging methods such as single-pixel Hadamard imaging using structured light [248, 249]. In such imaging techniques, the computed spatial patterns rely on the combination of a light source with a spatial light modulator, mostly realized by sophisticated DMDs. Thus, such GI schemes inherently possess the multi-component source-approach together with a time resolution limited by the modulation speed of the modules.

Here, a completely different light source for classical ghost imaging is proposed: a broad-area superluminescent diode. Its structure specificities are presented in Section 5.3.1. The coherence behavior of this spectrally broadband-emitting opto-electronic light source is investigated in detail. TPA interferometry is applied for quantifying the coherence time and the photon statistics in direct comparison with thermal coherence expectations (Section 5.3.2). Developing further the Mach-Zehnder-type TPA interferometer from Section 5.2, the number of emitted spatial modes are quantified. Thereby, the suitability of BA SLDs as a GI light source is evaluated. Showing finally a one-dimensional proof-of-principle GI experiment (Section 5.3.4), these compact, single-component emitters are introduced to the field.

#### 5.3.1. The broad-area SLD

The here investigated SLD (see Figure 51) is based on QD active medium consisting of 15 inhomogeneously broadened InAs/InGaAs QD layers which form a total active layer of  $0.620\mu\text{m}$  thickness. The 6mm long waveguide is overall tilted by  $7^\circ$  with respect to the facets which are both AR coated. The tapered waveguide structure consists of a straight section of  $500\mu\text{m}$  length and  $14\mu\text{m}$  width followed by the tapered section of  $5500\mu\text{m}$  length and a resulting facet width of  $110\mu\text{m}$ . The processing has been made by photolithographic technique and proton implantation inducing a gain-guided waveguide structure in combination with slight index-guiding [250]. Hence, strong amplification with high output powers as well as broad-area (BA) emission at the tapered output facet is implemented. The BA-SLD is operated at room temperature and the pump current is set to approximately 1.3A, well above ASE threshold. An optical spectrum is shown in Figure 51 (right) revealing NIR emission at 1250nm. The FWHM amounts to 13nm which corresponds to 2.5THz in terms of frequency. The Gaussian-like shape of the spectrum is due to single state (ground state) emission of the optically active QDs [169].

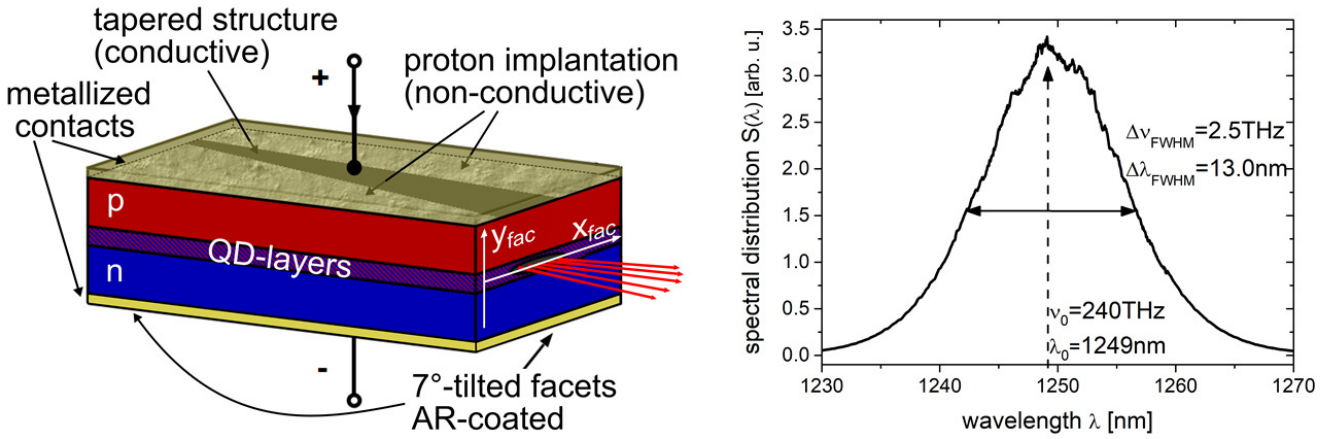


Figure 51. **The broad-area superluminescent diode.** Left: Schematic of the BA-SLD structure. Note that this drawing does not represent the actual proportions. The GaAs (100) substrate (n-doped) of the device with about 200 $\mu\text{m}$  thickness is more than 100 times larger than the diode transition. The broad-area facet coordinates are denoted as  $x_{fac}$  and  $y_{fac}$ , perpendicular and along the epitaxial growth direction, respectively. Right: Optical spectrum measured with a commercial OSA (ADVANTEST Q8384) with indications of the spectral distribution center and the FWHM both in terms of frequency and wavelength. The corresponding Suessmann measure amounts to  $\Delta\nu_S = 4.29\text{THz}$ .

Additionally, the state of polarization has been characterized using the Stokes polarization parameter formalism [251]. An expected high degree of polarization ( $\text{DOP} > 0.95$ ) was found above the ASE threshold with a dominant linear polarization component (circular Stokes vector component  $< 0.003$ ) whose orientation coincides well with the horizontal structure of the QD layers [135].

### 5.3.2. Temporal correlations

This section presents a quantitative temporal coherence analysis of the BA-SLD light. For this purpose, the Michelson-type TPA interferometer is used (see Section 3.2). The different temporal correlation orders can be analyzed considering the individual terms of Eq. (57) by applying appropriate bandpass filters to the recorded TPA interferogram data (see Figure 17 and Figure 18).

In first place, first-order temporal correlations are considered which are reflected by the  $F_1(\tau)$ -term (see Eq. (57)). According to the formalism of Ref. [140] which assumes a thermal statistics behavior of the field<sup>31</sup>, one can derive

$$F_1(\tau) = \exp\{-i2\pi\nu_0\tau\} g^{(1)}(\tau). \quad (111)$$

Hence, the third term of Eq. (57) is directly proportional to  $\text{Re}\{g^{(1)}(\tau)\}$ . Consequently, a bandpass filter is applied onto the measured TPA-interferogram using a 40THz window in order to match the full range of emitted wavelengths (compare with Figure 51, right). The bandpass filtered TPA interferogram is depicted in Figure 52 (left, black line). The  $\text{Re}\{g^{(1)}(\tau)\}$ -function can be exploited to quantify the coherence time  $\tau_c$  defined by Eq. (6). Given that  $\text{Re}\{g^{(1)}(\tau)\}$  and  $\text{Im}\{g^{(1)}(\tau)\}$  are inherently linked by a Hilbert transform owing to the analytical signal nature of the electric field,  $|g^{(1)}(\tau)|^2$  can be accessed by determining the envelope of  $\text{Re}\{g^{(1)}(\tau)\}^2$  [252]. Employing the discrete form of Eq. (6), one obtains a coherence time of  $\tau_c = 233\text{fs}$  which specifies the time window in which the higher-order correlations are pronounced. Equivalently, the spectral width, according to the Suessmann definition, amounts to  $\Delta\nu_S = 4.29\text{THz}$  or  $\Delta\lambda_S = 22.3\text{nm}$  in terms of frequency and wavelength, respectively. To verify this result, a comparison with a  $g^{(1)}$ -function exhibiting Gaussian distributed optical frequencies expressed by [133]

<sup>31</sup> It shall be later revealed how well this assumption holds.

$$\text{Re}\{g^{(1)}(\tau)\} = \text{Cos}(2\pi\nu_0\tau)\exp\left\{-\frac{\pi}{2}\left(\frac{\tau^2}{\tau_c^2}\right)\right\} \quad (112)$$

is undertaken. Figure 52 (left) and the inset therein illustrate the excellent coincidence of experimentally determined and thermal light expected  $\text{Re}\{g^{(1)}(\tau)\}$ -functions. Slight deviations in the periphery of the interference fringes are attributed to the limited experimental frequency resolution of 0.5THz and the non-ideal Gaussian-distributed optical spectrum. The latter is explicitly examined in Figure 52 (right) showing the Fourier transform of the experimental  $\text{Re}\{g^{(1)}(\tau)\}$  (black squares), the measured optical spectrum (black line) as well as the Gaussian distribution  $S(\lambda)$  (red line) corresponding to Eq. (112) which is calculated by the Wiener-Khintchine theorem (Eq. (4)):

$$S(\nu) \propto \exp\{-2\pi^2(\nu - \nu_0)^2\tau_c^2\}. \quad (113)$$

The excellent correspondence of all three distributions shall be emphasized supporting strongly (i) the accuracy of the implemented measurement system as well as (ii) the correctness of the assumption of a Gaussian-like spectral distribution of the BA-SLD light.

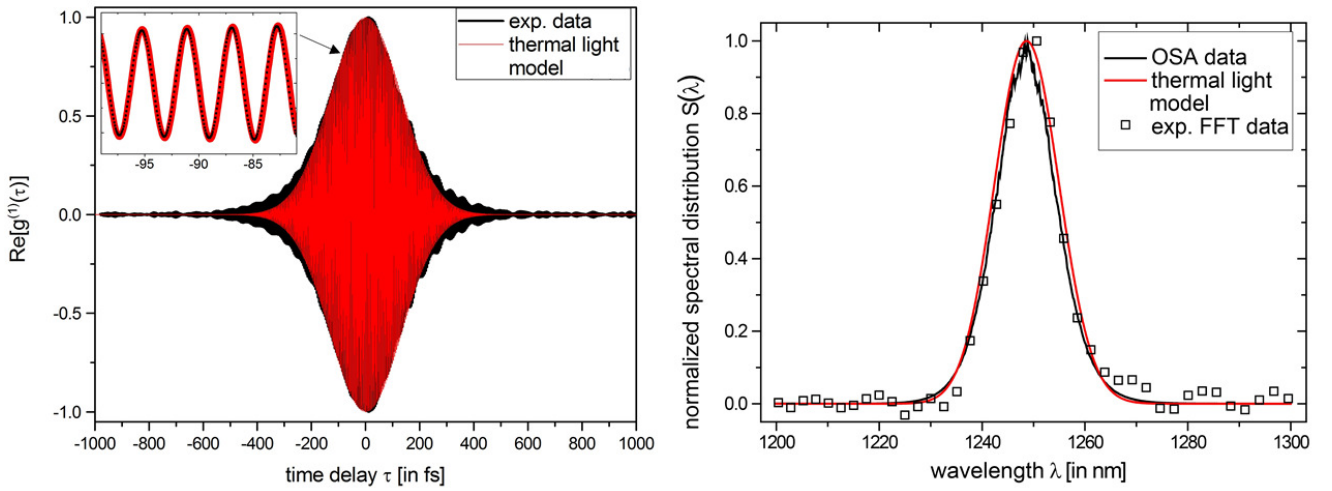


Figure 52. **First-order temporal correlations of the BA-SLD light.** Left: Experimentally determined  $\text{Re}\{g^{(1)}(\tau)\}$  function (black) and thermal light model with Gaussian-distributed optical frequencies calculated with the experimentally determined coherence time  $\tau_c=233\text{fs}$  (red line); inset: zoom-in showing highly resolved interference fringes; Right: optical spectrum obtained by three different methods: an OSA trace (black line), experimental FFT data (black squares) from the left graph and the Gaussian distribution with  $\tau_c=233\text{fs}$  (red line).

In order to analyze temporal second-order correlations, the low frequency contributions of the TPA interferogram are considered (Eq. (59)). Second-order correlation function extraction is carried out according to the method set out in Section 3.2 using a cutoff frequency of 10THz in the Fourier domain of the TPA interferogram. The normalized second-order auto-correlation function, shown in Figure 53 (black line), is conform with ultrafast decaying correlations dictated by the coherence time of  $\tau_c=233\text{fs}$ . Most importantly, the central second-order coherence degree reveals an ideal thermal value of  $2.01 \pm 0.04$ . Analogous to the first-order investigation, this experimental result is compared with theoretical expectations assuming an ideal thermal  $g^{(2)}$ -behavior based on a Gaussian spectral distribution [133]:

$$g^{(2)}(\tau) = 1 + e^{-\pi\left(\frac{\tau}{\tau_c}\right)^2} \quad (114)$$

Figure 53 (red line) depicts this function with the experimentally determined value of  $\tau_c$  coinciding excellently with the experimental  $g^{(2)}(\tau)$ -data.

Summarizing this section, the temporal coherence properties of the BA-SLD equal literally ideal thermal light behavior for both, first-order correlations revealing femtosecond coherence timescales as well as second-order correlations obeying photon-bunching governed photon statistics (see [39,43,44] for comparison).

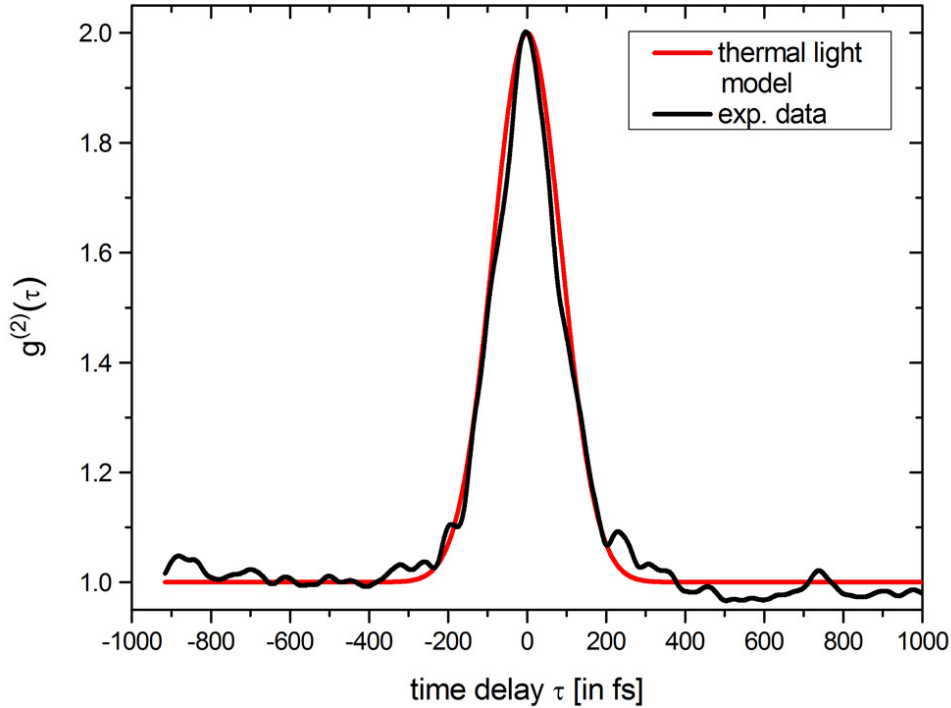


Figure 53. **Second-order temporal correlations of the BA-SLD light.** Extracted correlation function (black) from a measured TPA interferogram and theoretically expected second-order correlation function for thermal light with Gaussian distributed frequencies calculated with the experimentally determined coherence time  $\tau_c=233$ fs (red line).

### 5.3.3. Spatial correlations

For providing a complete coherence analysis, the spatial coherence of the BA-SLD light is investigated in this sub-section. Exploiting TPA detection within a spatial HBT configuration enables the measurement of the transverse coherence length  $\sigma_c$  and then the deduction of the number of emitted spatial modes. Concurrently, the potential spatial resolution for GI is determined. In fact, the transverse coherence area ( $\sim\sigma_c^2$ ) determines the scale on which a targeted object can be resolved in GI (see Section 2.2) without using compressive imaging techniques [109].

Coherent semiconductor laser sources with small-area facets typically emit a transverse single-mode, elliptical spatial profile. In contrast, the here employed BA emitter is expected to emit a multitude of spatial modes on the axis perpendicular to the growth direction ( $x_{fac}$ -axis, Figure 51 (left)), and a single mode parallel to the growth direction ( $y_{fac}$ -axis, Figure 51 (left)). Its dimensions resemble strongly BA laser structures where spatially multimode emission and even dynamic filamentation are well-known phenomena [253, 254, 255].  $\sigma_c$  shall be determined at the planes of interest, namely at the imaging planes of a GI experiment. The implemented scheme in Figure 54 represents a fiber-based version of the UBB-GI scheme of the previous section. However there, the narrow-stripe emitter had to be combined with a RGG in order to adjust appropriate pseudo-thermal spatial correlations. On the contrary, the here exploited BA-SLD shall serve as a stand-alone GI light source with completely different spatio-temporal

mode properties. The emission at the BA facet is collimated by the combination of a short focal length lens ( $f=4.5\text{mm}$ ) and a cylindrical lens ( $f=100\text{mm}$ ). The first beamsplitter (BS1) creates a statistical copy of the collimated BA-SLD beam and both beams impinge on their corresponding planes, which are both located equidistantly at  $600\text{mm}$  from the source, without magnification. The second-order spatial cross-correlations  $\langle I_{ref}(\vec{x}_{ref})I_{obj}(\vec{x}_{obj}) \rangle$  of the light field between the reference plane  $(x, y)_{ref}$  and the object plane  $(x, y)_{obj}$  are thus equivalent to spatial auto-correlations:

$$G^{(2)}(\tau = 0, \Delta\vec{x}') = \langle I(\vec{x})I(\vec{x} + \Delta\vec{x}') \rangle . \quad (115)$$

$\langle \rangle$  denotes the average over space  $\langle \rangle_x$ . At first, slit apertures are inserted into each of the two planes with a slit dimensioning of  $\Delta x \cdot \Delta y = 0.1 \cdot 4\text{mm}$ . In order to implement the relative horizontal displacement  $\Delta\vec{x}'$ , one slit is scanned transversely relatively to the other, here in  $x_{ref}$ -direction. By recombining the light transmitted through both planes via BS2 and subsequent focusing onto the TPA detector (Figure 54),  $G^{(2)}(0)$ -signals are acquired stepwise by measuring a TPA interferogram at each position  $x_{ref}$ . The result is shown in Figure 55 (left, black data) where  $g^{(2)}(0)$  is depicted as a function of the transverse position  $x_{ref}$ . Values ranging from 1.00 to 2.02 are observed. The fact that these values reflect both, no correlation ( $g^{(2)} = 1$ ) and maximum thermal correlation ( $g^{(2)} = 2$ ), supports the choice of apertures to describe correct spatial auto-correlations. It also indicates the full linear polarization state of the BA-SLD light<sup>32</sup> (see Section 5.3.1). An estimate for the transverse coherence width  $\sigma_s$  is given by adapting a Gaussian [29]:

$$g^{(2)}(\tau = 0, x_{ref} - x_0) = 1 + A \exp \left\{ -\frac{(x_{ref} - x_0)^2}{2 \sigma_G^2} \right\} \quad (116)$$

The fit procedure to the experimental data yields an amplitude of  $A=0.94 \pm 0.05$  and a Gaussian width of  $\sigma_G = (128 \pm 6)\mu\text{m}$ . The transverse coherence width is approximated by  $\sigma_c \approx 2\sigma_G$  [29] which takes a value of  $(256 \pm 12)\mu\text{m}$ . In Figure 55 (left), the data of two additional measurements is shown where one of the slits is enlarged to  $\Delta x = 375\mu\text{m}$  (green data) and  $\Delta x = 800\mu\text{m}$  (blue data). One can recognize the typical behavior of contrast reduction and signal broadening when multiple transverse coherence areas contribute to the intensity correlation signal [87]. For  $\Delta x$ -values of  $1.5\sigma_c$  and  $3.1\sigma_c$ , the signal amplitudes decrease from 1.94 to 1.64 and to 1.27, respectively. This proves that the implemented GI setup works correctly in the sense that spatial coherence properties are preserved and not affected by e.g. fiber-coupling. Next, two slit apertures are aligned along the vertical  $y_{ref}$ -axis with aperture dimensions of  $\Delta x \cdot \Delta y = 1.5\sigma_c \cdot 0.1\text{mm}$ . The transverse scan  $g^{(2)}(\tau = 0, y_{ref})$  (Figure 55, right) shows no significant correlation modulation. The overall reduced value from 2 to 1.58 is due to the detection of multiple spatial modes from the horizontal dimension. This measurement thus proves experimentally the transverse single-mode emission in epitaxial growth direction caused by the small dimensioning of  $0.62\mu\text{m}$  height of the BA-SLD active layer structure.

It should be emphasized that the implemented spatial HBT configuration with interferometric TPA detection for determining the transverse coherence length of the BA-SLD light field in the imaging planes (Figure 54) represents an alternative method for measuring spatial auto-correlations of light sources with ultra-fast spatio-temporal mode dynamics. It is particularly challenging to address the second-order spatial correlations of such light fields. Established methods use streak-camera approaches [255] or first-order interferometry systems addressing solely first-order spatial correlations [256].

<sup>32</sup> Otherwise, the central second-order coherence degree could range between  $1.5 \leq g^{(2)}(0) < 2$  according to *partially* polarized light leading to *partially* coherent light from a single phase-space cell.

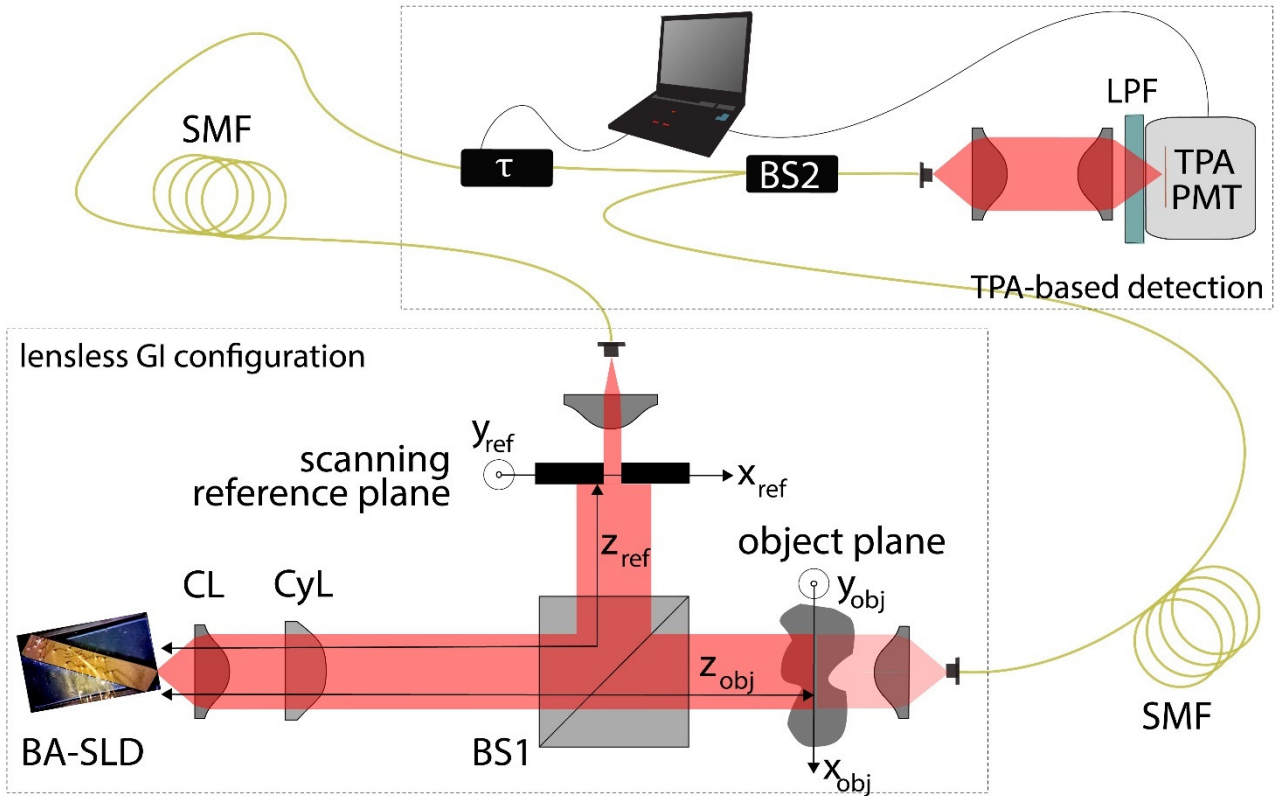


Figure 54. **Diagrammatic drawing of the fiber-based ultra-broadband GI setup:** Free-space emitting BA-SLD as the GI light source, collimation lens (CL), cylindrical lens (CyL), two broadband 50:50 beam splitters (BS1, fiber-based BS2), single-mode fibers (SMF), long pass filter (LPF) blocking fundamental absorptions ( $\lambda < 1000\text{nm}$ , SCHOTT RG1000), and the photomultiplier in TPA mode (TPA-PMT).

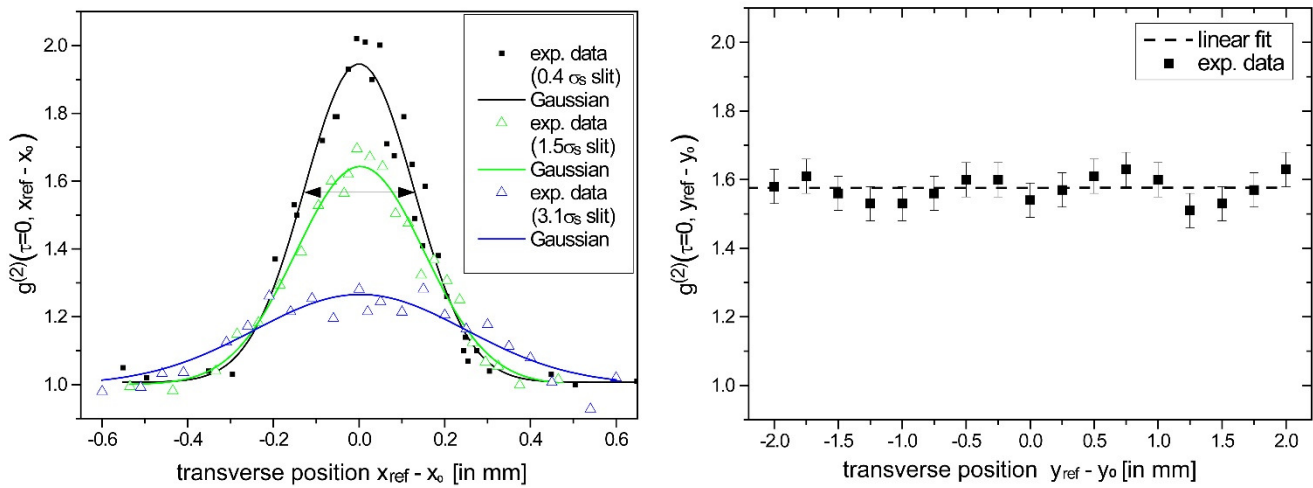


Figure 55. **Spatial correlations of the BA-SLD light at the imaging planes.** Experimentally determined spatial intensity auto-correlations (left) along the horizontal  $x_{ref}$ -axis with different slit widths (the deduced mode expansion  $\sigma_c \approx 2\sigma_G$  is illustrated by the arrow) and (right) along the vertical  $y_{ref}$ -axis. A slope of a linear fit (dashed line) amounts to 0 with a constant function of 1.58.

The spatial coherence analysis is completed by investigating the beam profile in the imaging planes. Figure 56 shows a fiber scanning measurement ( $62.5\mu\text{m}$  core MM fiber) of the spatial intensity profile of the BA-SLD light in the reference plane. As the GI scheme is lensless, the beam profile in the opposite plane remains identical except of being horizontally inverted. At first, one can see the trapezoid shape of the spot which is characteristic for tapered semiconductor emitters. Secondly, one can recognize the spot dimensions of  $\sim(2.5 \times 4.5)\text{mm}^2$ . Most importantly, the intensity distribution reflects nicely the findings of the spatial coherence properties: On the one hand, a relatively smooth cross-section along the vertical  $y_{ref}$ -axis is observed reflecting transverse SM emission along the growth direction. On the other hand, intensity modulations up to 40% are recorded for the horizontal  $x_{ref}$ -axis clearly caused by the multiple spatial modes perpendicular to the growth direction of the BA-SLD. From these observations, the number of emitted spatial modes, exhibiting here a pronounced oblong shape, can be estimated. The number of dominant spatial modes (within a 10dB range) emitted by the BA-SLD amounts to 11. These modes are indicated in the top cross-section of Figure 56 as a histogram. As these spatial modes are aligned next to each other along the  $110\mu\text{m}$  wide BA facet, they should feature an approximate mean near-field mode expansion of  $10\mu\text{m}$  coinciding well with literature data [255].

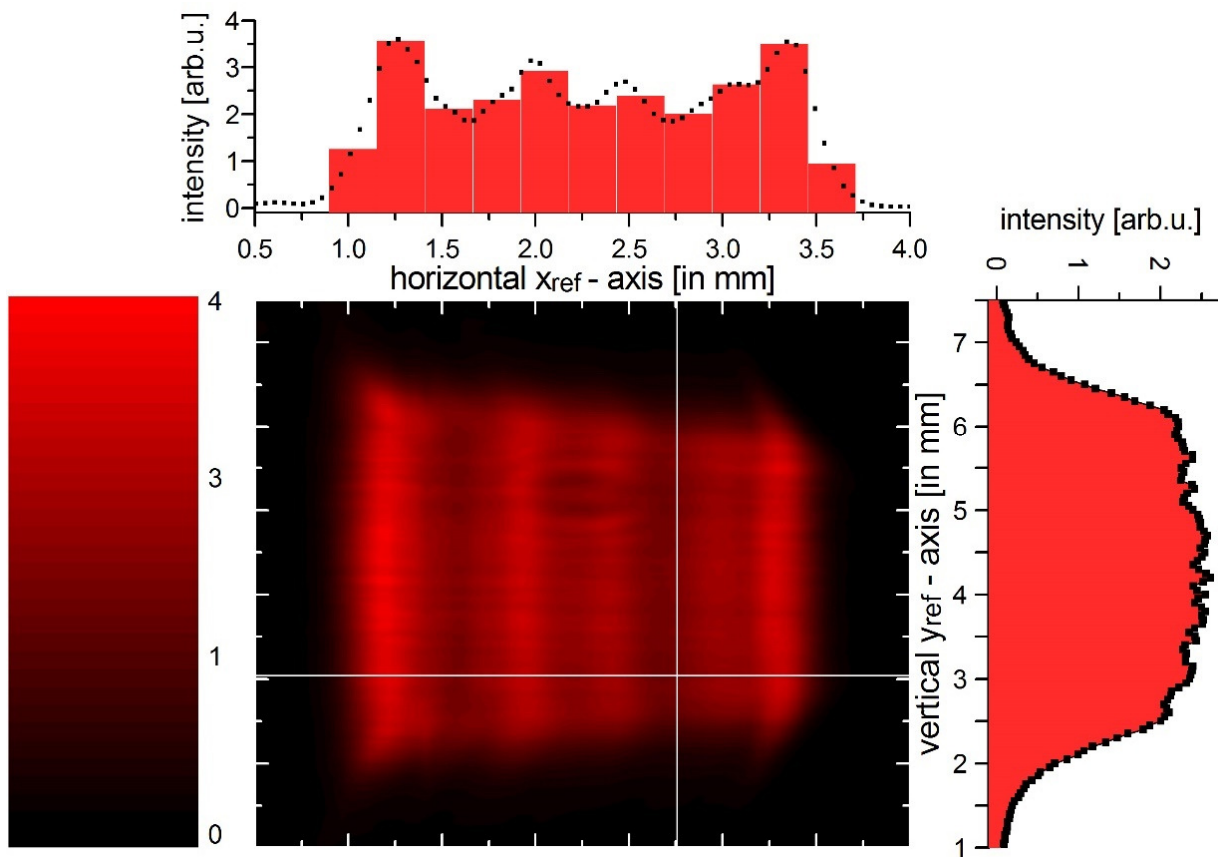


Figure 56. **Light spot profile at the imaging planes.** The two white lines denote the selected cross-sections depicted as additional graphs at the top and on the right-hand side of the contour plot. In the top graph, the histogram bars illustrate the dominant spatial modes yielding the experimentally determined mode expansion of  $\sigma_c = 256\mu\text{m}$ .

### 5.3.4. GI experiment

The comprehensive coherence analysis showed clear evidence that the BA-SLD features intrinsically all requirements as a classical GI light source (see page 18). Even though the here employed device imposes a relatively low image resolution constraint (11x1 “pixels”), a proof-of-principle GI experiment using an object of next level complexity can be performed. Therefore, a double-slit object made of standard reprographic paper and deliberately self-made slits producing an unbalanced object structure (Figure 57 (right)) is placed at the object plane within the GI setup. The object and the reference plane are located both at the same distance from the source of  $z_{obj} = z_{ref} = 600\text{mm}$  in order to avoid blurring effects. For the sake of clarity, the detection protocol of the implemented UBB-GI scheme (Figure 54) using GI terminology is specified:

$$g_{GI}^{(2)}(\tau = 0, x_{ref}) = \frac{\langle I_b(t) I_{ref}(t, x_{ref}) \rangle}{\langle I_b(t) \rangle \langle I_{ref}(t, x_{ref}) \rangle}. \quad (117)$$

Note that this detection protocol is based on the classical definition of the second-order Glauber correlation function which represents the most basic GI signal detection. The transmitted light through the mask is collected into an optical fiber constituting the bucket intensity  $I_b(t)$ . The scanning reference arm, comprising a spatially resolving slit width of  $\Delta x = 100\mu\text{m}$  and subsequent fiber coupling, acts as the reference intensity  $I_{ref}(t, x_{ref})$ . Here, a one-dimensional space scale is considered as the BA-SLD provides multiple spatial modes solely on the horizontal x-axis.

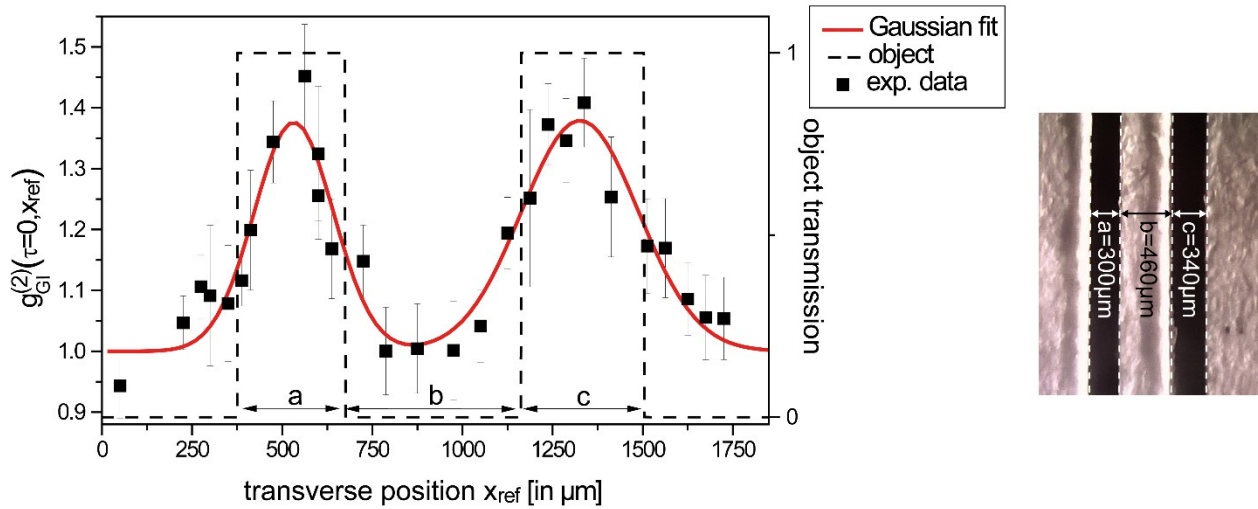


Figure 57. **Ghost image cross-section of a double-slit object.** Left: Experimental data (black squares) with error bars corresponding to the statistical variance of a set of three measurements, fitted double Gaussian function (red line) respecting the error bar weights and indications of the object dimensions (dashed line). Right: Digital camera record of the object through a microscope, which cross-section is depicted in the graph (blue dashed line).

A cross-section of the double-slit is imaged by the stepwise transverse displacement of the aperture in  $x_{ref}$ -direction. The obtained values of  $g_{GI}^{(2)}$  reveal two distinct maxima,  $g_{GI}^{(2)}(560\mu\text{m}) = 1.45$  and  $g_{GI}^{(2)}(1340\mu\text{m}) = 1.41$ , separated clearly by vanishing correlations of  $g_{GI}^{(2)} = 1.0$  around  $x_{ref} = 900\mu\text{m}$ . Correlations are completely vanishing at the outer borders of the object at  $x_{ref} > 1600\mu\text{m}$  and  $x_{ref} < 300\mu\text{m}$ . By applying a double Gaussian fit function to the experimental data (Figure 57, left, red line), more image details are revealed. Compared to the microscopic picture (Figure 57, right), the ghost image indeed reflects the unbalanced slit widths  $a = 300\mu\text{m}$  and  $c = 340\mu\text{m}$ , the latter featuring a broader FWHM ( $FWHM^{(c)} = 380\mu\text{m}$ ) than for slit a ( $FWHM^{(a)} = 260\mu\text{m}$ ). The slit distance of  $780\mu\text{m}$  is nicely reproduced reflected by the center position difference of the double Gaussian distribution:  $s_{GI} = 795\mu\text{m}$ .

Furthermore, the overall visibility (Eq. (89)) amounts to 16% which is a notable value compared with second-order GI expectations with thermal light [67] and compared with ghost images using *true* thermal light [103, 79] of *two-bit objects*. This good visibility value is achieved at the cost of relatively low image resolution limited by the amount of contributing transverse modes.

**Discussion.** It is highlighted that this is the first GI experiment with intrinsically highly incoherent light by means of the BA-SLD respecting temporally first-order, temporally second-order as well as spatial incoherence. This semiconductor-based opto-electronic emitter unifies all required coherence properties for GI which were analyzed in detail and which are summarized in Table 9. In Section 5.2, the photon-bunching properties of ASE emitted by SLDs are already exploited for GI, however, the spatial coherence had to be adjusted by a rotating diffuser. Here, the photon-bunching and the spatial incoherence are the intrinsic characteristics of a BA edge-emitter due to the MM filamentation dynamics along the BA facet coordinate caused by the ultra-fast coupled charge carrier-photon dynamics of semiconductor devices [255]. Adhering to broad-area laser diodes with similar output facet dimensioning, the spatio-temporal dynamics of the SLD near-field are expected to take place on picosecond timescales [255].

As there is no need for pre-treatment or post-conditioning of the emitted light, the BA-SLD represents, to the best of one's knowledge, the most compact light source in the field. The relatively low image resolution ( $\sim 256\mu\text{m}$ ) realized in Figure 57 (see also Table 9) could be improved in terms of *pixel-size* by either choosing shorter focal-length collimation optics or by refocusing the beam (Figure 56) onto the object. Here, the near-field expansion of a single transverse mode amounts to  $\sim 10\mu\text{m}$ . Furthermore, the number of transverse modes could be increased by designing a BA-SLD with a larger output facet. Also, a straight waveguide instead of the here utilized tapered waveguide would be preferable in order not to impose restrictions on transverse mode generation caused by the small area back facet. Application specific BA-SLDs could be designed on demand regarding optimal image resolution, optical power and directionality (spot size) properties. Despite their BA facet, BA-SLDs maintain a strong directionality suitable for long range imaging [20, 89]. Note that for the here presented experiments, the working distance has been chosen rather arbitrarily. On the one hand, the directional emission of the BA-SLD is well-suited for projecting small light spots at long distances from the source. On the other hand, short working distances of a few mm are well accessible by conceiving miniaturized collimation optics. In view of real imaging applications with complex objects, BA-SLD array structures could considerably scale-up the resolution and also overcome the one-dimensional restriction due to edge-emission.

Table 9. Coherence properties of the BA SLD light.

coherence	measure	impact on optical property
temporal 1 <sup>st</sup> order	$\tau_c = (233 \pm 20)fs$	(i) ultra-broadband optical spectrum ( $\Delta\lambda_s=22.3\text{nm}$ ) (ii) fs-timescale correlation decay
temporal 2 <sup>nd</sup> order	$g^{(2)}(0) = 2.01 \pm 0.04$	thermal-like photon statistics (i.e. distinct photon-bunching)
spatial	$\sigma_c^{far-field} = (256 \pm 13)\mu\text{m}$ $\sigma_c^{near-field} = (10 \pm 0.5)\mu\text{m}$	11x1 transverse modes

In this final section about research results, a completely novel light source has been introduced to ghost imaging: *the broad-area superluminescent diode (BA-SLD)*. It is the first time that such a semiconductor light source is exploited for GI: a stand-alone, compact emitter (<200mm<sup>3</sup> in volume) based on *opto-electronic amplified spontaneous emission*, here in terms of a quantum dot tapered superluminescent diode.

In first place, the intrinsic incoherence of the utilized BA-SLD has been quantified comprehensively regarding the temporal domain (first- and second-order) as well as the spatial domain. Ideal thermal intensity correlations have been identified with prevailing ultra-short correlation timescales below 300fs, an ideal thermal photon-bunching degree as well as multiple uncorrelated transverse modes (see Table 9). The transverse mode expansion as well as the number of dominant transverse modes has been determined developing a spatial HBT configuration in combination with TPA interferometry. To be precise, the high degree of temporal second-order coherence ( $g^{(2)}(0) = 2$ ) relates to each individual transverse mode. Due to the fact, that all coherence measures yield values classified as *incoherent*, one could state that light emitted by BA SLDs is *completely incoherent*. However, note that in the strict sense of correlation function definition, real light sources remain always partially coherent due to finite spectral bandwidths, potential photon-bunching enhancements and limited amounts of spatial modes.

Hence, from a fundamental point-of-view, it can be stated that the proof-of-principle GI experiment reconstructing the cross-section of a double-slit transmission mask demonstrates, for the first time, the GI phenomenon with an *intrinsically completely incoherent light source* in the same sense as Boitier et al. demonstrated the first real black body source photon-bunching measurement [9].

As discussed extensively, state-of-the-art classical GI light sources rely on combinations of coherent light with spatially randomizing optical elements or on incoherent lamps with monochromating optics. It shall be recapitulated that the most prominent ones are the pseudo-thermal light source, light sources impinging on a spatial light modulators and less often thermal emitters (incandescent lamps, the sun,...) in combination with narrowband spectral filters. In Section 5.2., ultra-broadband GI (UBB-GI) is already realized by means of a QD SLD. However there, a hybrid pseudo-thermal-SLD approach was indispensable for generating the spatial incoherence due to single transverse mode emission by the narrow-stripe SLD structure. Hence, the BA-SLD represents the *most compact light source* in the field of GI. This completely new type of light source holds interesting features in view of potential GI applications being miniaturized, purely injection-current pumped, room-temperature driven, directional and technologically mature. Furthermore, the successful proof-of-concept of UBB-GI using a stand-alone SLD opens the door for a totally new class of GI light sources, namely opto-electronic emitters with a large optical bandwidth as well as large-area emission. Vertical cavity surface emitting laser (VCSEL) with large oxide apertures, broad-area laser diode arrays, random lasers and even high-power LEDs are potential candidates, also in view of enabling two-dimensional UBB-GI with compact opto-electronic emitters.

---

## 6. Summary

---

In conventional imaging systems, the emitted light from a source interacts with an object and the intensity of the transmitted or reflected light is captured by a spatially resolving detector. In this thesis, a fundamentally different imaging principle has been studied, known as *ghost imaging* (GI). In contrast to conventional imaging, GI exploits the intensity correlations of light to form an image of an object. A ghost image is obtained by measuring the total intensity of the transmitted or reflected light of an illuminated object and the spatially resolved intensity of a highly-correlated reference beam which itself has never interacted with the object. The information of both intensities alone is not enough to form an image of the object. However, image reconstruction can be achieved by correlating the two intensities. Intriguingly, the spatial resolution of the ghost image is provided by the non-interacting reference beam.

The work presented in this thesis joins into the continuous strive for making GI applicable to real-world sensing and imaging fields. The title: *Classical ghost imaging with opto-electronic emitters*, reflects one of the approaches to this objective. The second approach is what rather sets this thesis apart from other ongoing work on GI. Instead of utilizing state-of-the-art detection systems, novel GI configurations are developed.

### 6.1. Key findings

Prior to the GI developments, this thesis deals with fundamental coherence studies on light emitted by quantum dot superluminescent diodes (QD SLDs). These spectrally broadband emitting semiconductor light sources generate photons by amplified spontaneous emission (ASE). This mixture of spontaneous and stimulated light generation processes inside a quantized zero-dimensional gain medium together with a high number of modes, forms a particularly interesting state of light. The latter expresses itself within unique temporal second-order correlations which are experimentally determined by exploiting two-photon-absorption (TPA) interferometry for resolving the prevailing ultra-short correlation timescales. With this method, the following two main experimental results have been enabled:

- The simultaneous tailoring of first- and second-order coherence properties of light emitted by a QD SLD applying well-controlled, broadband optical feedback.
- The realization of the *mixed-light* phenomenon on ultra-short correlation timescales by superimposing spectrally broadband ASE from a QD SLD with coherent light from a laser diode.

Supported by a theoretical model, the temporal second-order correlations in both experiments show a full transition from an incoherent to a coherent behavior. In particular, the direct comparison of experimental data with theoretical counterparts identifies a dependency of the second-order correlation function on first-order coherence properties, similar to the Siegert-relation for ideal thermal light [24]. These comprehensive experimental studies put in relation to a quantum optical state of light, provide new insights into the physics of light generation in QD SLDs at the edge of ASE to stimulated emission.

In the central part of the thesis, novel GI concepts are proposed together with the development of GI light sources based on opto-electronic emitters. Specifically, two classical GI detection schemes are developed, which are entitled

- I. Photon statistics-based ghost imaging (PS-GI) based on one single-photon-counting detector.
- II. Ultra-broadband ghost imaging (UBB-GI) using TPA interferometry.

---

Both differ completely from state-of-the-art GI detection methods such as the original, spatial HBT-based scheme with two detectors as well as the computational GI approach using artificially randomized light generated by a spatial light modulator and single-pixel detection. Whereas PS-GI exploits the possibility to evaluate correlation signals by determining complete photon probability distributions, UBB-GI is based on nonlinear absorption enabling intensity correlation signals to be measured at ultra-short correlation timescales. In order to demonstrate their functionality, three proof-of-principle GI experiments are realized utilizing the following opto-electronic emitter-based GI light sources:

- I. a high-quality pseudo-thermal (PT) light source using a semiconductor laser diode in combination with a rotating diffuser
- II. a hybrid PT-SLD light source based on a narrow-stripe QD SLD combined with a rotating diffuser
- III. a broad-area SLD (BA-SLD)

The UBB-GI scheme utilizing the BA-SLD represents, to the best of one's knowledge, the most incoherent GI experiment respecting high temporal incoherence in first- and second-order as well as spatial incoherence with prevailing ultra-short spatio-temporal correlation timescales. In addition, the most compact GI light source is introduced to the field. The here developed GI concepts can be seen as complements to already existing GI technologies enabling a broader platform for applications in future work.

In the following, last section, a detailed summary of the thesis is given together with a discussion of open questions and future perspectives.

## 6.2. Summary, conclusions and outlook

The results of this thesis have been divided into two main chapters. Whereas Chapter 4 was devoted to the fundamental investigations on the coherence of light emitted by QD SLDs, the GI achievements were set out in Chapter 5. The applied measurement techniques for determining higher-order correlations of light, have been presented in Chapter 3.

Specifically, a single-photon-counting system exploiting the time-resolved photon count traces of one single detector has been implemented to determine the photon statistics of a light field. Although the evaluation of the statistics of photon counts is quite common for TCSPC systems, e.g. in the context of fluorescence lifetime imaging, this analysis method has been applied here to extract the probability distribution of photon numbers  $P(n)$  of a light field. One major advantage is the possibility to compute higher-order correlations of light by extracting higher statistical moments. The primarily utilized method however, is the TPA interferometry technique for determining the second-order auto-correlations of light  $g^{(2)}(\tau)$ , which was pioneered by Boitier et al. in 2009. A Michelson-type interferometer has been set up with a semiconductor-based photomultiplier achieving an intensity-intensity correlation time resolution of  $\sim 0.3$ fs.

Motivated by the peculiar hybrid photon generation process of ASE, Chapter 4 has presented studies on the simultaneous tailoring of first- and second-order temporal coherence properties of light emitted by QD SLDs. These spectrally broadband light sources have been chosen with regard to recent observations of a hybrid coherent state of light suggesting a considerably enhanced ratio of stimulated to spontaneous emission processes. Furthermore, the QD-based gain media in SLD structures introduce a non-negligible quantum aspect for the zero-dimensional carrier systems.

Two different experiments achieving a full second-order coherence transition, or in other words a change from thermal-like to coherent photon generation have been presented, thereby exploring fundamental

---

physics at the edge of ASE to stimulated emission. To support the experimentally obtained results, direct comparison to a theoretical model were carried out. A postulated quantum optical state of light, termed *multimode phase-randomized Gaussian (PRAG) state*<sup>33</sup>, captures the complex NIR spectral distributions of QD SLD emission assuming uncorrelated longitudinal modes. This enabled, for the first time, to consider QD SLD light states. The derived analytical expressions for first- and second-order correlations were put into an experimental context. An essential aspect of novelty is the presence of a very high number of longitudinal modes or ultra-broadband light ( $\Delta\nu > 1\text{THz}$ ) which correlation timescales could only be experimentally resolved by TPA interferometry. Both experimental approaches, applying broadband optical feedback (OFB) onto a QD SLD as well as superimposing QD SLD light with highly coherent laser light from a laser diode, have shown a good agreement with the simple PRAG state ansatz for QD SLD ASE. Relevant parameters to changes of  $g^{(2)}(\tau)$  such as the number of modes  $N$  and the statistical properties of their spectral distribution were identified. The validity of an additional constant reduction term to the Siegert-relation for thermal light has been approved for a relatively small number of modes. It is emphasized that the second experiment represents the first demonstration of the *mixed-light* phenomenon at ultra-short correlation timescales, here amounting to sub-100fs.

These observations on second-order coherence changes supported by a quantum optical light state have only been a starting point for further studies on the photon generation process in QD SLDs. Microscopic modeling is indispensable for identifying possible quantum optical mechanisms such as inter-mode correlations and squeezing [257], QD interactions [258], also comprising temperature dependencies and charge carrier distributions among the QDs [259]. More experiments are necessary for substantiating the first-order coherence dependency of the photon statistics. Narrowband spectral filtering could allow studying selected ASE mode subsets of ultra-broad QD SLD emission. Also, experimental investigations on ASE mode cross-correlations could give insight into possible inter-mode correlations. Furthermore, the development of an enhanced  $g^{(2)}(0)$ -precision of the TPA interferometer, currently limited to a relative deviation of 2%, is necessary for verifying the predicted mode number dependency in pure ultra-broadband emission regimes. Finally, low temperature coherence investigations of different QD SLD devices should be carried out in order to find out the limits of validity of the PRAG state model when hybrid states of light appear.

The performed studies of Chapter 4 have shown that pure ultra-broadband ASE from QD SLDs operated at room-temperature, provides a considerably robust temporal second-order incoherence. Both experimental approaches, whether intrinsic or extrinsic, had to intervene strongly in the optical properties of QD SLDs to induce a reduction of  $g^{(2)}$ . Besides having gained new insights into the coherence behavior of QD SLD light, Chapter 4 served as a preliminary characterization of the light source exploited in a large part of Chapter 5. More precisely, the examined QD SLDs match the temporal second-order incoherence condition as a GI source and moreover do provide first-order incoherence in view of the final objective: developing highly incoherent GI concepts.

Following the thesis guideline, Section 5.1 dealt with the development of a novel classical GI concept which was termed *photon statistics-based ghost imaging (PS-GI)*. Based on the complementarity of intensity auto- and cross-correlations of light, the key idea for the scheme was that instead of detecting the bucket signal and the reference signal by two different detectors such as in conventional GI systems, the reference and the object light selected in the respective imaging planes are optically superimposed. The joint photon number probability distribution of this mixed-light is then determined by the implemented photon statistics measurement method using a single detector. Assuming pseudo-thermal statistics, provided experimentally by a laser diode-based PT light source, a simple model has been developed. Therein, the ghost image formation was found to be dictated by the joint intensity auto-correlation behavior of a varying amount of multiple speckle cells contributing to the detected mixed-light signal. The visibility behavior and the image quality have been addressed revealing the mixed-light

---

<sup>33</sup> As already mentioned in Chapter 4, the theoretical model has been developed by M. Sc. Franziska Friedrich in a collaborative work (see page 44).

---

characteristic of the scheme explaining also the fundamental differences with respect to conventional GI. A unique feature of the PS-GI scheme consists in the higher-order functionality using one detector only, which has been confirmed by the mixed-light GI model. Photon number distribution measurements as well as position-position correspondence experiments have substantiated the model predictions within simplest GI scenarios. Finally, a proof-of-principle GI demonstration has been achieved by recording a cross-section of a double-pinhole mask.

Regarding the potential extension of the model, full spatial correlation functions should be addressed by comprising e.g. optical imaging system transfer functions and polarization effects in order to simulate more accurately the ghost images of complex objects. In future developments, single-photon-counting arrays (1D or 2D) and sophisticated TCSPC modules shall be employed for realizing a fast PS-GI camera towards a practical imaging system. Alongside, the feasibility of *non*-single-photon resolving detection should be studied. Instead of measuring the photon statistics  $P(n)$  for computing the statistical moments, one could measure the mean intensity  $\bar{I}$  and the intensity fluctuations  $\Delta^2 I$  for determining the intensity-correlation signals of a ghost image. This would enable a simplified signal acquisition and a low-cost setup.

Within Section 5.2, a second, novel GI experiment was presented based on the combination of temporally incoherent light and TPA interferometry, entitled *ultra-broadband ghost imaging* (UBB-GI). The Michelson-type TPA interferometer was modified into a Mach-Zehnder configuration to enable spatial correlation measurements. Its functionality has been proven by verifying a point-to-point correspondence as well as by recording a proof-of-principle one-dimensional ghost image of a double-pinhole mask. For the first time, a GI experiment with signals exhibiting sub-100fs correlation timescales has been realized. Interestingly, the implemented hybrid PT-SLD light source consisting of a narrow-stripe QD SLD and a rotating ground glass, provided the required spatial incoherence by *slow* speckle pattern generation and simultaneously maintained the ultra-short temporal correlations.

In the final Section 5.3, a completely new light source has been exploited for GI: a miniaturized emitter based on opto-electronic ASE, here in terms of a quantum dot broad-area superluminescent diode (BA-SLD). The intrinsic incoherence of the utilized BA-SLD has been quantified comprehensively regarding the temporal domain as well as the spatial domain. Ideal thermal intensity correlations have been identified with prevailing ultra-short correlation timescales ( $\tau_c < 300$ fs), an ideal thermal photon-bunching degree ( $g^{(2)} = 2$ ) as well as 11 uncorrelated transverse modes. The latter is attributed to sub-picosecond spatio-temporal mode dynamics in the near-field of BA edge emitters [255]. A proof-of-principle GI experiment reconstructing the cross-section of a double-slit transmission mask was realized. Hence, from a fundamental point-of-view, it can be stated that, for the first time, the GI phenomenon has been shown with an *intrinsically completely incoherent light source* meaning that a high level of incoherence is achieved both in the temporal as well as in the spatial domain with prevailing ultrashort spatio-temporal correlation timescales. Indeed, Chapter 5 concluded with fulfilling the thesis guideline of a *highly incoherent GI concept*.

In the context of the scientific history of GI, one could claim that an evolution from quantum to classical, and with this work, to highly incoherent GI has taken place [260]. It is also emphasized that the BA-SLD represents the most compact light source in the field with respect to state-of-the art GI light sources.

This completely novel type of light source is promising in view of potential GI applications yielding miniaturization, directionality and customizable spatial coherence properties. Furthermore, the UBB-GI concept opens the door for a totally new class of GI light sources, namely opto-electronic emitters with a large optical bandwidth as well as large-area emission such as BA lasers and BA VCSELs, which are already established devices in remote sensing applications. Those two types of emitters provide enhanced optical power density compared to BA-SLDs due to their laser structure, which is favorable to the intensity-dependent TPA detection. Whereas a BA laser can have similar facet dimensions to BA-SLDs, BA VCSELs and BA surface-emitting, high-power LEDs could enable two-dimensional UBB-GI. The

---

feasibility of a two-dimensional GI experiment with BA-SLD stacks is investigated in Appendix 8.1 mimicking a SLD array by a scanning procedure showing promising first results. Regarding potential laser diode sources, careful selection of devices must be taken for sufficiently broadband spectral properties for practical TPA interferometry. It is fair to mention that these compact sources are introduced to GI at the cost of a more complex detection technique in terms of nonlinear interferometry. Hence, the justification of UBB-GI as a real alternative to state-of-the-art GI schemes goes with the development of a beneficial application. The provided coherence times as well as the spatial correlation timescales are orders of magnitudes shorter than in state-of-the-art GI light. In combination with the TPA method, this novel classical GI concept provides the image signal as a directly measurable detector current, which principally holds no more limitation for high temporal resolution towards high-speed GI in future work. Moreover, the spectrally broadband light should be advantageous for imaging in turbulent media, representing one of the most promising application fields of GI. Ultrashort spatio-temporal correlation timescales should lower the influence of scattering on the second-order correlation signals and thus enable larger penetration depths into scattering samples in analogy to low-coherence imaging technologies. Finally, the short coherence lengths could be exploited to provide a sharp depth of field for future high-resolution three-dimensional GI systems where the ultra-large spectral bandwidths of QD SLDs could be advantageous.

It can be stated with some certainty that the success or failure of GI depends upon a breakthrough application in the short term, still not demonstrated yet. The increase in complexity for measuring intensity correlations instead of pure intensity comprising multiple beam paths or at least multiple signals for computing cross-correlations, must be justified with a real-world application in which the unique features of GI outplay conventional and established imaging systems. The here developed GI detection concepts, photon statistics-based GI and the ultra-broadband GI expanding also the portfolio of GI light sources, can be seen as complements to already existing GI technologies enabling a broader platform for applications, thus fostering the entrance into practical GI metrology in future work.

---

## 7. Zusammenfassung

---

Bei konventioneller Bildgebung wird die Intensität des Lichtes, welches zunächst von einer Lichtquelle ausgesendet, dann auf das abzubildende Objekt trifft, räumlich aufgelöst detektiert. Ein einfaches Beispiel stellt die Aufnahme durch eine Digitalkamera mit integriertem CCD-Sensor dar. In dieser Arbeit wird ein fundamental anderes Bildgebungsverfahren untersucht, welches unter dem Namen *Ghost Imaging* (GI) bekannt ist<sup>34</sup>. Im Gegensatz zur konventionellen Bildgebung, nutzt GI Intensitätskorrelationen von Licht aus, um ein Bild eines Objektes zu erzeugen [260]. Ein *Ghost Image* entsteht durch die Messung der gesamt-transmittierten oder -reflektierten Intensität des Lichtes, welches mit dem Objekt interagiert und der Intensität eines weiteren hochkorrelierten Referenzstrahls, welcher selbst *nicht* mit dem Objekt interagiert. Die Information beider einzelnen Intensitäten reicht nicht aus um ein Bild zu erzeugen. Durch die Korrelation beider Intensitäten miteinander wird es jedoch möglich, ein Bild zu rekonstruieren. In verblüffender Weise wird die räumliche Auflösung des Bildes durch den Referenzstrahl, der das Objekt nicht *sieht*, gewährleistet.

Die vorliegende Arbeit reiht sich in aktuelle Entwicklungen ein, GI praktikabel für Anwendungsgebiete der Bildgebung und Sensorik zu machen. Der Titel der Dissertation: *Klassisches Ghost Imaging mit opto-elektronischen Lichtquellen* spiegelt eine Herangehensweise wider. Der zweite Ansatz setzt sich von anderen Arbeiten insofern ab, als nicht herkömmliche GI Detektionsverfahren zum Einsatz kommen, sondern neue Detektionsverfahren und -konfigurationen entwickelt werden.

### 7.1. Schlüsselergebnisse

Zunächst werden in dieser Arbeit fundamentale Kohärenzuntersuchungen zur Emission von Quantenpunkt Superlumineszenzdioden (QP SLDs) durchgeführt. Diese spektral breitbandig emittierenden opto-elektronischen Lichtquellen erzeugen Photonen mittels verstärkt spontaner Emission (engl. amplified spontaneous emission (ASE)), welche einen hybriden Lichterzeugungsprozess bestehend aus spontanen und stimulierten Photonen, darstellt [189, 23]. In einem niederdimensionalen, quantisierten Verstärkungsmedium erzeugt und mit einer hohen Anzahl an longitudinalen Moden versehen, liegt ein interessanter Lichtzustand vor. Letzterer spiegelt sich in einzigartigen Korrelationen zweiter Ordnung wider, welche ultrakurze Korrelationszeitskalen aufweisen und durch Zwei-Photonen-Absorptionsinterferometrie (engl. Two-photon-absorption (TPA) interferometry) erst gemessen werden können. Mithilfe dieser Methode, sind die folgenden Hauptergebnisse ermöglicht worden:

- Das simultane Maßscheidern der Kohärenzeigenschaften erster und zweiter Ordnung der Emission von QP SLDs durch kontrollierte, breitbandige optische Rückkopplung [156].
- Die Realisierung des *Mixed-light* Phänomens auf ultrakurzen Korrelationszeitskalen durch das Überlagern von spektral breitbandiger ASE einer QP SLD mit kohärentem Laserlicht einer Laserdiode [157].

Unterstützt durch ein theoretisches Modell, zeigen beide Experimente einen vollständigen Übergang der zeitlichen Korrelationsfunktion zweiter Ordnung von einem inkohärentem zu einem vollständig kohärenten Verhalten. Insbesondere wird durch den direkten Vergleich von experimentellen Daten mit den Modellwerten, eine Abhängigkeit der Intensitätskorrelationen von Korrelationseigenschaften erster Ordnung, ähnlich wie die Siegert-Relation für thermisches Licht [24], festgestellt. Die umfangreichen experimentellen Untersuchungen im Zusammenhang mit einem postulierten quanten-optischen

---

<sup>34</sup> *Ghost Imaging* kann zu *Photonenkorrelations-Abbildungsverfahren* ins Deutsche übersetzt werden. Aufgrund dieses recht unhandlichen Begriffes, wird hier der englische Begriff beibehalten.

---

Lichtzustand, hat demnach zu neuen Erkenntnissen der Lichterzeugung von QP SLDs an der Grenze zwischen verstärkt-spontaner und stimulierter Emission geführt.

Zentraler Bestandteil dieser Arbeit sind neue GI Konzepte in Kombination mit der Entwicklung von GI Lichtquellen auf Basis von opto-elektronischen Emittoren. Insbesondere sind zwei klassische GI Detektionskonzepte entwickelt worden, welche folgendermaßen bezeichnet wurden:

- I. Photonenstatistik-basiertes Ghost Imaging (PS-GI) mit einem einzigen Einzel-Photonen-Zähl Detektor [235, 234]
- II. Ultra-Breitband Ghost Imaging (UBB-GI) basierend auf TPA Interferometrie [236]

Beide Methoden unterscheiden sich grundsätzlich von bestehenden GI Detektionsverfahren, wie die ursprüngliche, HBT basierte Konfiguration mit zwei Detektoren sowie das computational GI, welches auf räumlichen Lichtmodulatoren und Einzel-Pixel Detektion basiert. Während PS-GI die Möglichkeit Korrelationssignale aus vollständig bestimmbar Photonverteilungen ausschöpft, werden beim UBB-GI, Intensitätskorrelationssignale mittels TPA Interferometrie auf ultrakurzen Korrelationszeitskalen gemessen. Um die Funktionalität der Systeme zu demonstrieren, sind drei GI Experimente realisiert worden, wobei die folgenden Lichtquellen implementiert wurden:

- I. Eine pseudo-thermische (PT) Lichtquelle basierend auf einer Laserdiode und einem rotierenden Diffusor
- II. Eine hybrid PT-SLD Quelle bestehend aus einer Schmalstreifen-QP SLD und einem rotierenden Diffusor
- III. Eine Breitstreifen SLD (engl. Broad-area SLD (BA-SLD))

Das UBB-GI Konzept in Kombination mit der BA-SLD stellt, nach bestem Wissen, das inkohärenteste GI Experiment dar, wobei sowohl zeitliche als auch räumliche *Inkohärenz* auf ultrakurzen Korrelationszeitskalen, vorliegen [237]. Zusätzlich ist damit die kompakteste GI Lichtquelle vorgestellt worden. Die hier entwickelten Konzepte können als Erweiterungen bereits bestehender Methoden angesehen werden um eine vielfältigere Plattform für zukünftige GI Anwendungen bereitzustellen.

Im folgenden letzten Abschnitt wird die Arbeit detaillierter zusammengefasst und offene Fragestellungen sowie künftige Entwicklungsmöglichkeiten diskutiert.

## 7.2. Zusammenfassung, Schlussfolgerungen und Ausblick

Die erzielten Ergebnisse sind in zwei Hauptkapiteln dargelegt. Während Kapitel 4 fundamentale Untersuchungen zur Kohärenz des emittierten Lichts aus QP SLDs präsentiert, umfasst Kapitel 5 alle GI Ergebnisse. Die dabei eingesetzten experimentellen Messverfahren zur Bestimmung von Korrelationen höherer Ordnung werden vorausgehend ausführlich in Kapitel 3 beschrieben.

Insbesondere wird ein Einzel-Photon-Zähl-System (engl. single-photon-counting system) implementiert, um mittels zeitaufgelöster Photonenzereihen eines einzigen Detektors, die Photonenstatistik von Lichtfeldern zu ermitteln. Diese Methode ist von zeitaufgelösten single-photon-counting (engl. time-correlated single-photon-counting (TCSPC)) Systemen übernommen [44], welche beispielsweise für die Fluoreszenz-Korrelationsspektroskopie eingesetzt werden. In dieser Arbeit wird die Methode für die Bestimmung von Wahrscheinlichkeitsverteilungen von Photonenzahlen  $P(n)$  des elektromagnetischen Feldes angepasst [37]. Der Vorteil liegt darin, dass dadurch Korrelationen höherer Ordnung aus ein und derselben Messung eines einzigen Detektors berechnet werden können. Die hauptsächlich zum Tragen kommende experimentelle Methode stellt jedoch die Zwei-Photonen-Absorptions-Interferometrie (engl.

---

two-photon-absorption (TPA) interferometry) zur Bestimmung der Korrelationsfunktion zweiten Grades  $g^{(2)}(\tau)$  dar. Nach Vorbild der wegweisenden Arbeiten von Boitier im Jahr 2009 [9, 133], wird hier ein Interferometer in Michelson Konfiguration mit halbleiterbasiertem Photomultiplier implementiert. Die damit erzielte Korrelations-Zeitauflösung beträgt etwa  $\Delta\tau = 0.3fs$ .

Motiviert durch den faszinierenden hybriden Photonen-Erzeugungsprozess der verstärkt-spontanen Emission (ASE), präsentiert Kapitel 4 fundamentale Untersuchungen zum simultanen Maßschneidern von Kohärenzeigenschaften erster und zweiter Ordnung von Licht aus QP SLDs. Diese spektral breitbandigen Lichtquellen wurden aufgrund neuester Beobachtungen von *hybrid kohärenten Lichtzuständen* ausgewählt [23, 48], die auf ein beträchtlich erhöhtes Verhältnis von stimulierten zu spontanen Photonen-Erzeugungsprozessen hinweisen. Des Weiteren bergen Quantenpunkt-basierte Verstärkungsmedien einen interessanten, nicht zu vernachlässigenden Quantenaspekt durch niederdimensionale Ladungsträger-Systeme innerhalb der lichtemittierenden Diode [169].

In zwei unterschiedlichen Experimenten konnte ein vollständiger Kohärenzübergang in zweiter Korrelationsordnung induziert werden, was die Erforschung grundlegender physikalischer Eigenschaften an der Schwelle von verstärkt-spontaner zu stimulierter Emission erlaubt. Die experimentellen Ergebnisse wurden dabei unmittelbar mit einem theoretischen Modell verglichen. Insbesondere wurde ein quantenoptischer Lichtzustand postuliert, der als *multimodaler phasen-gemittelter Gauss'scher-Zustand* (engl. multimode phase-randomized Gaussian (PRAG) state) bezeichnet wurde<sup>35</sup>. Die Parametrisierung dieses Zustandes erlaubt es, eine beliebige spektrale Verteilung wiederzugeben und beinhaltet die Annahme, dass longitudinale Moden untereinander unkorreliert sind. Dies repräsentiert den erstmaligen Versuch, einen quantenoptischen Zustand für QP SLD Licht zu formulieren. Die aus dem PRAG Zustand abgeleiteten analytischen Ausdrücke für Korrelationsfunktionen erster und zweiter Ordnung sind im Experiment überprüft worden. Ein neuer Aspekt besteht in der Berücksichtigung einer hohen Anzahl an Moden des ultra-breitbandigen optischen Spektrums ( $\Delta\nu > 1\text{THz}$ ), deren Korrelationszeitskalen nur mithilfe der TPA Interferometrie aufzulösen sind. Beide Experimente, sowohl die Anwendung von breitbandiger optischer Rückkopplung als auch die Überlagerung mit kohärentem Licht, haben eine gute Übereinstimmung mit den theoretischen Werten des multimoden PRAG Zustands für QP SLD ASE ergeben. Relevante Parameter, wie die Anzahl der emittierten Moden  $N$  als auch statistische Kumulanten und deren spektrale Verteilung konnten identifiziert werden. Ein zusätzlicher, konstanter Term zur wohlbekannten Siegert-Relation für ideal thermisches Licht konnte für den Bereich kleiner Modenzahlen bestätigt werden. Außerdem sei darauf hingewiesen, dass das zweite Experiment die erste experimentelle Realisierung des *mixed-light* Phänomens auf ultrakurzen Korrelations-Zeitskalen ( $<100fs$ ) darstellt [218, 221].

Diese Beobachtungen zur Reduktion des Kohärenzgrades zweiter Ordnung an der Schwelle von verstärkt-spontaner Emission zu stimulierter Emission können nur als Ausgangspunkt weiterer Untersuchungen zum Photonen-Erzeugungsprozess in QP SLDs dienen. Eine mikroskopische Modellierung ist zwingend notwendig um mögliche quantenoptische Mechanismen zu identifizieren, wie beispielsweise intermodale Korrelationen und Squeezing [257], QP Interaktionen [258] und auch um mögliche Temperaturabhängigkeiten und den Einfluss der damit verbundenen Ladungsträgerverteilungen zu beschreiben [259]. Durch den Einsatz schmalbandiger spektraler Filter können sowohl einzelne ASE Moden individuell als auch mögliche intermodale Korrelationen durch Kreuzkorrelationsexperimente untersucht werden. Weiterhin sollte die Präzision des implementierten TPA Interferometers verbessert werden, welche aktuell bei  $\Delta^2 g^{(2)}(0)/g^{(2)}(0) \approx 2\%$  liegt, um die postulierte Abhängigkeit der Photonenstatistik auf Korrelationen erster Ordnung im Bereich hoch-multimodiger Emission experimentell zu überprüfen. Schließlich würden Tieftemperaturexperimente die Möglichkeit bieten, den Gültigkeitsbereich des PRAG Modells auszuloten, welcher durch hybrid kohärente Lichtzustände beschränkt sein könnte.

---

<sup>35</sup> Wie bereits in Kapitel 4 erwähnt, wurde die Theorie von Frau M. Sc. Franziska Friedrich im Rahmen einer Zusammenarbeit mit der Arbeitsgruppe von Prof. Walser (AG Theoretische Quantendynamik, Institut für Angewandte Physik, TU Darmstadt) entwickelt.

---

Kapitel 4 hat unter anderem einen robusten hohen zeitlichen Kohärenzgrad in zweiter Ordnung für Raumtemperatur-betriebene QP SLDs festgestellt. Beide Experimente mussten stark in die optischen Eigenschaften der QP SLDs eingreifen, um eine Reduktion in  $g^{(2)}$  herbeizuführen. Damit dient Kapitel 4 als ausführliche Charakterisierung derjenigen Halbleiteremitter, welche in Kapitel 5 zum Einsatz kommen. Insbesondere erfüllen QP SLDs die zeitliche Korrelationsbedingung zweiter Ordnung als GI Lichtquelle. Außerdem stellen sie geeignete Kohärenzeigenschaften erster Ordnung zur Verfügung, um letztendlich das Ziel *hoch inkohärenter GI Konzepte* umzusetzen.

Gemäß der physikalischen Leitlinie der Dissertation - *neue und hoch inkohärente klassische GI Konzepte* - wird in Abschnitt 5.1 zunächst ein *neuartiges klassisches* GI Detektionsprinzip vorgestellt: das *Photonenstatistik-basierte Ghost Imaging* (engl. photon statistics-based ghost imaging (PS-GI)). Die Schlüsselidee basiert auf der Komplementarität von Intensitätsauto- und Intensitätskreuzkorrelationen. Während bei gewöhnlicher GI Detektion, das räumlich integrierte Objektsignal und das räumlich aufgelöste Referenzsignal durch jeweils einen Detektor separat registriert werden, werden hier die Lichtstrahlen hinter der Objekt- und Referenzebene optisch überlagert. Die Photonenzähl-Statistik dieses überlagerten Lichtsignals wird mit der direkten Messmethode durch einen einzigen Photonzähl-Detektor (Abschnitt 3.1) bestimmt. Basierend auf PT Licht - hier durch eine Laserdiode und einem rotierenden Diffusor realisiert - wurde ein einfaches Modell entwickelt. Die Funktionalität der GI Prinzips konnte durch dieses Modell gezeigt werden. Die Intensitäts-Autokorrelationen einer variierenden Anzahl von multiplen Speckle-Zellen, die zum überlagerten Licht (engl. mixed-light) beitragen, stellen das GI Signal dar. Der Kontrast und die Bildqualität werden durch die *mixed-light* Charakteristik beeinflusst und die Unterschiede zur konventionellen GI Detektion konnten damit erörtert werden. Die einzigartige Möglichkeit der Bestimmung höherer Korrelationsordnungen mit der Messung nur eines einzigen Detektors ist ebenfalls durch das Modell bestätigt. Messungen von Photonverteilungen und von räumlichen Korrelationen in einfachen GI Szenarien stimmen gut mit den Berechnungen des Modells überein. Schließlich konnte ein GI Konzeptnachweis mit der Aufnahme eines Querschnittes einer Doppellochblende erbracht werden.

Als anknüpfende Weiterentwicklung ist eine Erweiterung des Modells auf komplette räumliche Korrelationsfunktionen zu empfehlen, welche optische Transferfunktionen und mögliche Polarisierungseffekte mit komplexen Objekten einbezieht. Außerdem sollte ein Interferenzterm in den Ansatz einfließen, welcher hier der Einfachheit halber vernachlässigt wurde. In zukünftigen experimentellen Arbeiten sollten single-photon-counting Zeilen- oder Flächensensoren zusammen mit TCSPC-Modulen eine schnelle PS-GI Kamera ermöglichen. Zudem sollte die Machbarkeit eines PS-GI Experimentes ohne single-photon-counting Detektor studiert werden. Prinzipiell sind Intensitätskorrelationen mithilfe von mittlerer Intensität  $\bar{I}$  und Intensitätsfluktuationen  $\Delta^2 I$  aus dem Photostrom einer Photodiode bestimmbar, was eine kostengünstige und vereinfachte PS-GI Signalaufnahme erlauben würde.

Die Kombination aus zeitlich inkohärenter Lichtquelle und TPA Interferometrie erlaubt die Einführung eines weiteren, neuen GI Konzeptes in Abschnitt 5.2. Das hier als *Ultra-Breitband Ghost Imaging* (UBB-GI) bezeichnete Detektionskonzept ist durch die Implementierung einer Mach-Zehnder Konfiguration ermöglicht worden um räumliche Korrelationsmessungen durchzuführen. Die Funktionalität dieses GI Konzeptes konnte durch einfache eindimensionale GI Szenarien bewiesen werden. Zum ersten Mal, wurde ein GI Experiment mit spektral breitbandiger Lichtquelle realisiert, wobei die Bildsignale Korrelationszeitskalen unterhalb von 100fs aufwiesen. Die entwickelte hybrid PT-SLD Quelle, bestehend aus einer Schmalstreifen-QP SLD und einem rotierenden Diffusor, liefert die benötigte räumliche Inkohärenz durch *langsame speckle-pattern* Erzeugung und behält interessanterweise die ultrakurzen zeitlichen Korrelationszeitskalen bei.

Im letzten Ergebnisteil (Abschnitt 5.3) wird eine vollständig neue GI Lichtquelle vorgestellt, nämlich ein kompakter Emitter basierend auf opto-elektronischer ASE: die Breitstreifen-QP SLD (engl. broad-area SLD (BA-SLD)). Die intrinsische Inkohärenz der eingesetzten BA-SLD wurde bezüglich der zeitlichen als

---

auch der räumlichen Domäne umfangreich quantifiziert. Ideal thermische Intensitätskorrelationen mit ultrakurzen Korrelationszeitskalen ( $\tau_c < 300\text{fs}$ ), einem Kohärenzgrad zweiter Ordnung von  $g^{(2)} = 2$  und 11 unkorrelierten transversalen Moden wurden festgestellt. Letztere sind auf die Sub-Pikosekunden Modendynamik des Nahfelds von Breitstreifen-Kantenemittern zurückzuführen [255]. Mit dieser BA-SLD wurde ein GI Demonstrationsexperiment realisiert, wobei ein Querschnitt eines Doppelspaltes abgebildet werden konnte. Dieses Experiment stellt den erstmaligen Nachweis des GI Phänomens mit einer intrinsisch *vollständig* inkohärenten Lichtquelle dar. Dabei bezieht sich die Vollständigkeit auf das Vorliegen eines hohen Maßes an Inkohärenz auf ultrakurzen Zeitskalen sowohl in der räumlichen als auch in der zeitlichen Domäne. Somit schließt Kapitel 5 mit dem Erreichen der Zielsetzung, ein hoch inkohärentes GI Konzept umzusetzen. Zusätzlich stellt die BA-SLD die kompakteste GI Lichtquelle dar.

Dieser neue Lichtquellentyp bietet Miniaturisierung, gerichtete Emission und maßschneidbare räumliche Kohärenzeigenschaften. Somit ist er vielversprechend in Blick auf potentielle GI Anwendung. Darüber hinaus öffnet das UBB-GI Konzept die Tür für eine ganze Reihe an neuen GI Lichtquellen, welche sowohl spektral breitbandig als auch großflächig emittieren. Breitstreifenlaser und VCSEL mit großer Oxidapertur (BA-VCSEL) bieten hohe Leistungsdichten für den optimalen Einsatz der Intensitätsabhängigen TPA Interferometrie und sind bereits etablierte Laserquellen für Remote Sensing Anwendungen. Um zweidimensionales UBB-GI zu realisieren, sind zum einen BA-SLD- und BA-Laser-Stapelstruktur denkbar. Zum anderen können BA-VCSEL, oberflächenemittierende Hochleistungs-LEDs und sogar *random Laser* intrinsisch für zweidimensionale räumliche Inkohärenz sorgen. Ein erster Machbarkeitsnachweis für ein zweidimensionales GI Experiment in einer Reflexionsanordnung wird im Anhang (Appendix 8.1) diskutiert. Es sollte ehrlicherweise erwähnt werden, dass die Einführung kompakter, spektral breitbandiger Lichtquellen nur auf Kosten eines komplexeren Messverfahrens möglich ist. Die Rechtfertigung der aufwendigen TPA Interferometrie für das UBB-GI System muss noch in einer nützlichen Anwendung erbracht werden. Dazu sei auf die kurzen Kohärenzzeiten in der räumlichen und der zeitlichen Domäne hingewiesen, welche um mehrere Größenordnungen geringer sind als bei etablierten GI Lichtquellen. Im TPA Detektor sind Korrelationssignale in messbaren Strömen enthalten, sodass prinzipiell hohe zeitliche Auflösungen möglich sind. Schlechte Zeitaufösungen stellen eine der grundlegenden Limitierungen von GI bezüglich dessen Anwendbarkeit dar. Des Weiteren könnte die große spektrale Bandbreite vorteilhaft für GI in turbulenten Medien sein. Die ultrakurzen Korrelationszeitskalen sollten den Einfluss von Streuung auf den Kohärenzgrad zweiter Ordnung mindern und somit für größere Eindringtiefen und robustere Signalqualität sorgen. Schließlich könnten die kurzen Kohärenzlängen für eine scharf definierte Bildebene genutzt werden, um in Zukunft hoch aufgelöstes 3D GI zu ermöglichen.

Es kann mit einiger Sicherheit gesagt werden, dass der Erfolg des GI Verfahrens von einer immer noch fehlenden klaren Anwendung abhängig ist. Die erhöhte technische Komplexität zur Messung von Intensitätskorrelationssignalen mit multiplen optischen Wegen muss durch ein Anwendungsfeld begründet werden, in dem die einzigartigen Eigenschaften von GI gegenüber konventionellen und etablierten Bildgebungsverfahren, welche durch hochentwickelte digitale Bildverarbeitungsmethoden immer weiter optimiert werden, zum Tragen kommen. Die in dieser Arbeit entwickelten Detektionskonzepte - das Photonenstatistik-basierte GI und das ultrabreitband GI - inklusive der Ausweitung des Lichtquellen-Portfolios können als Erweiterung der etablierten GI Methoden betrachtet werden, um in Zukunft GI in einem praktischen Anwendungsfeld wiederzufinden.

## 8. Appendix

### 8.1. Towards ultra-broadband GI in 2D

This short paragraph shall illustrate one conceivable way of developing a two-dimensional UBB-GI system. As discussed within Chapter 6, a perspective solution to the one-dimensional restriction due to edge-emission of the BA-SLD (11x1 transverse modes) could be array structures where multiple BA-SLDs are aligned next to each other as well as stacked on top of each other, analogous to BA laser diode stacks. In order to test the feasibility of such a source concept, a preliminary experiment has been conducted by projecting a horizontal section of the BA-SLD beam profile (see Figure 56) onto the imaging planes. For this purpose, a slit-aperture was placed within the collimated beam (see Figure 58) producing a beam profile height of approximately  $500\mu\text{m}$ . For the purpose of demonstrating a more realistic imaging situation, an object of slightly enhanced complexity, compared to the simple masks in Chapter 5, has been prepared. The letter  $T$  has been written with acrylic color onto a low-quality metallic surface (Figure 59, left). The object is incorporated within the UBB-GI scheme (see Figure 54) at the object plane. However, this GI scenario constitutes a reflective configuration with an inverse mask. Consequently, the scheme is slightly modified for the light-coupling at the object plane (Figure 58). Otherwise, the same experimental settings as in Section 5.3 apply. For recording a two-dimensional ghost image of the object, cross-sections of  $2.2\text{mm}$  width ( $x_{ref}$ -axis) are recorded while the object is scanned vertically within a total range of  $5\text{mm}$  ( $y_{obj}$ -axis).

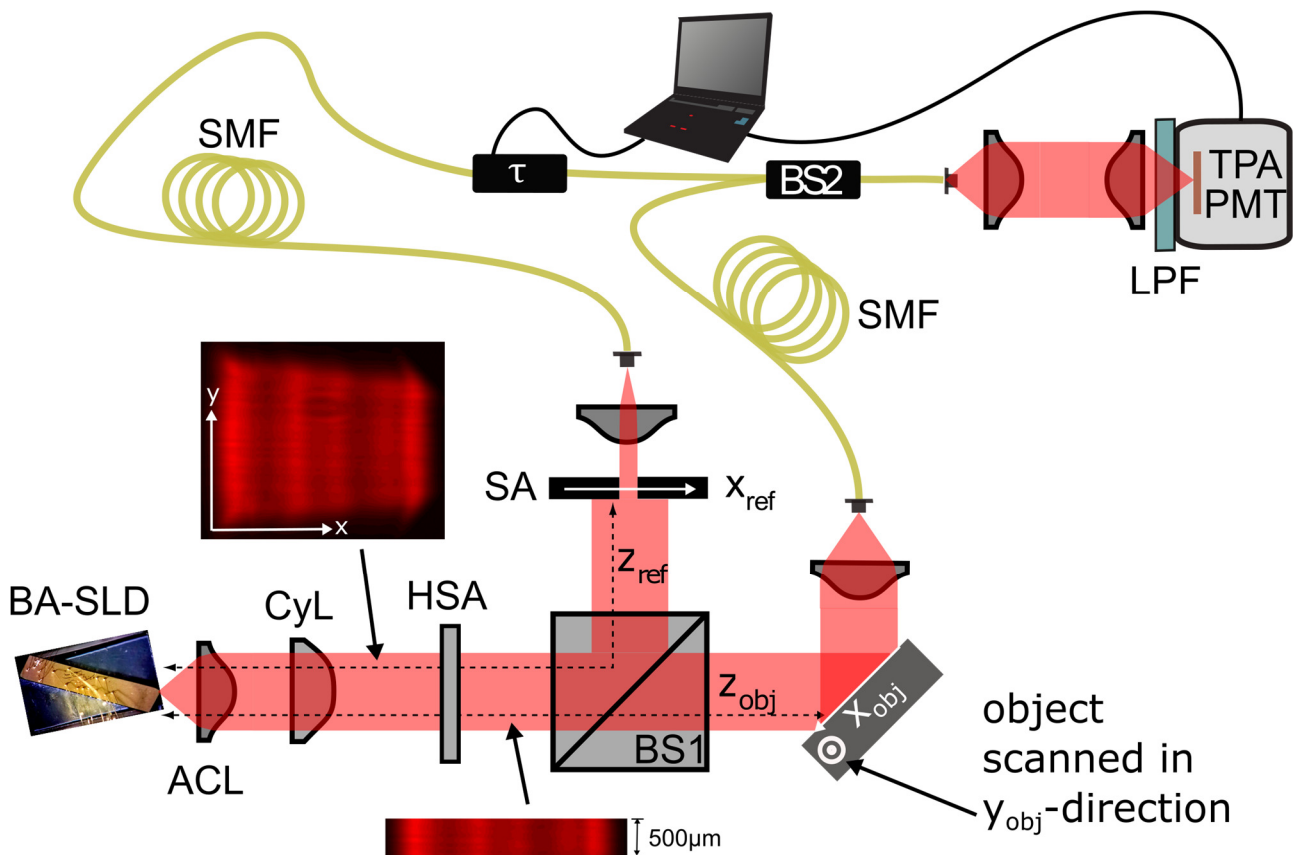


Figure 58. Schematic diagram of the experimental setup for a 2D ultra-broadband GI demonstration of a reflective object, comprising collimation optics (ACL and CyL), a horizontal slit aperture (HSA), 50:50 broadband beamsplitters (BS1 and BS2), a spatially resolving aperture (SA), single-mode fibers (SMF), a long-pass filter (LPF), the TPA detector (TPA PMT). Additionally, two spatial profiles are depicted for illustrating the vertical spatial filtering for achieving spatial resolution in the  $y$ -axis.

Figure 59 (right) shows the reconstructed two-dimensional ghost image from 19 horizontal ( $x_{ref}$ -) cross-sections. The obtained signals,  $g^{(2)}(\tau = 0, x_{ref}, y_{ref})$  with  $y_{ref}$  being mimicked by the displacement of the object in  $y_{obj}$ -direction, are represented as a gray scale. One notices overall reduced  $g^{(2)}$ -values in comparison to the one-dimensional ghost image in Section 5.3.4, due to the contribution of more transverse modes for imaging the inverse mask (compare with Figure 49 and Figure 57). However, a clear signature of the letter  $T$  is apparent in the ghost image. Enhanced  $g^{(2)}$ -values are observed for spatial coordinates corresponding to the periphery of the opaque object and low values of  $g^{(2)} \approx 1$  are measured at positions matching the lettering. Additionally, the irregular shape of the edges of the self-made object seems to be reflected by the ghost image with respect to the object contours depicted in Figure 59 (right), to scale, as well. It should be noticed that the correlation signals show a decreasing tendency at the image borders, to the very left-hand side ( $x_{ref} < 12.5\text{mm}$ ) and to the very right-hand side ( $x_{ref} > 13.8\text{mm}$ ). This loss of image quality is attributed to the lower coupling efficiency into the SM fibers of transverse modes located at the edges of the beam profile, which could be solved by MM fibers or free-space configurations in future work.

This proof-of-principle experiment shows not only a two-dimensional ghost image using an inverse object of higher complexity, but it demonstrates also the potential for UBB-GI in a reflective imaging scenario, which is encouraging for future developments. For more details about perspectives on the development and applications of the UBB-GI scheme, the reader is referred to the outlook discussion in Chapter 6.

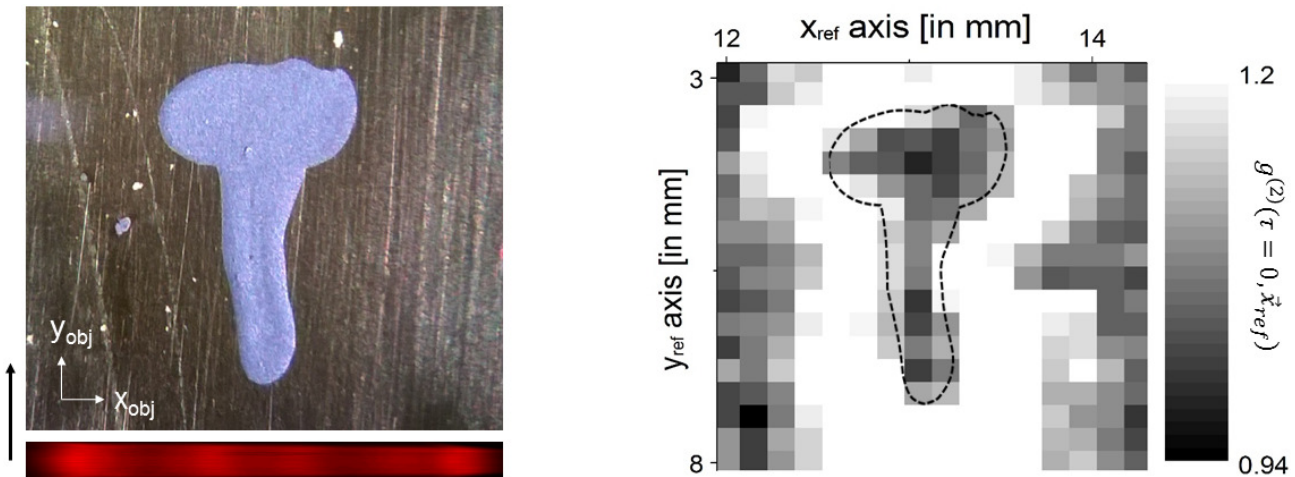


Figure 59. **Reflective scanning ultra-broadband ghost imaging of an inverse mask.** Left: Microscope image of the letter “T” made of acrylic paint onto a low-quality metallic surface. Right: Ghost image of the inverse mask reconstructed from the scanning procedure (see Figure 58). Note that the dashed line indicates the margin of the object, equal in scale.

---

## Bibliography

---

- [1] E. Verdet, "Etude sur la constitution de la lumière non polarisée et de la lumière partiellement polarisée," *Ann. Scient. de L'É.N.S.*, vol. 2, pp. 291-316, 1865.
- [2] A. A. Michelson, "I. On the application of interference methods to astronomical measurements," *Phil. Mag.*, vol. 30, no. 182, pp. 1-21, 1890.
- [3] L. Mandel and E. Wolf, *Optical Coherence and Quantum Optics*, Cambridge: Cambridge Univ. Press, 1995.
- [4] R. Hanbury Brown and R. Twiss, "Correlation between photons in two coherent beams of light," *Nature*, vol. 4497, pp. 27-29, 7 January 1956.
- [5] R. Glauber, *Quantum Theory of Optical Coherence - Selected Papers and Lectures*, Weinheim: Wiley-VCH Verlag GmbH & Co. KGaA, 2007.
- [6] F. T. Arecchi, A. Berné and P. Bulamacchi, "High-Order Fluctuations in a Single-Mode Laser Field," *Phys. Rev. Lett.*, vol. 16, no. 1, pp. 32-35, 1966.
- [7] M. Aßmann, T. Veit, M. Bayer, M. van der Poel and J. Hvam, "Higher-Order Photon Bunching in a Semiconductor Microcavity.," *Science*, vol. 325, no. 5938, pp. 297-300, 2009.
- [8] I. C. Benea-Chelms, C. Bonzon, G. S. C. Maissen, M. Beck and J. Faist, "Subcycle measurement of intensity correlations in the terahertz frequency range," *Phys. Rev. A*, vol. 93, p. 043812, 2016.
- [9] F. Boitier, A. Godard, E. Rosencher and C. Fabre, "Measuring photon bunching at ultrashort timescale by two-photon absorption in semiconductors," *Nat. Phys.*, vol. 5, pp. 267-270, 2009.
- [10] M. Aßmann, T. Berstermann, J. Wiersig, C. Gies, F. Jahnke, C. Kistner, S. Reitzenstein, A. Forchel and M. Bayer, "Ultrafast intensity correlation measurements of quantum dot microcavity lasers," *Phys. Stat. Sol. (c)*, vol. 6, no. 2, pp. 399-402, 2009.
- [11] K. Wakui, Y. Eto, H. Benichi, S. Izumi, T. Yanagida, K. Ema, T. Numata, D. Fukuda, M. Takeoka and M. Sasaki, "Ultrabroadband direct detection of nonclassical photon statistics at telecom wavelength," *Sci. Rep.*, vol. 4, p. 4535, 2014.
- [12] R. Hanbury Brown and R. Q. Twiss, "Interferometry of the Intensity Fluctuations in Light. III. Applications to Astronomy," *Proc. Roy. Soc. A*, vol. 248, no. 1253, pp. 199-221, 1958.
- [13] B. J. Berne and R. Pecora, *Dynamic light scattering*, Mineola: Dover Publications, 2000.
- [14] PicoQuant, "Applications -> Life Science: Fluorescence Correlation Spectroscopy," [Online]. Available: <https://www.picoquant.com/applications/category/life-science/fluorescence-correlation-spectroscopy-fcs>. [Accessed 29 12 2016].
- [15] T. B. Pittmann, Y. H. Shih, D. V. Strekalov and A. V. Sergienko, "Optical imaging by means of two-photon quantum entanglement," *Phys. Rev. A*, vol. 52, p. R3429(R), 1995.
- [16] R. S. Bennink, S. J. Bentley and R. W. Boyd, "'Two-Photon' Coincidence Imaging with a Classical Source," *Phys. Rev. Lett.*, vol. 89, no. 11, p. 113601, 2002.
- [17] A. Gatti, E. Brambilla, M. Bache and L. A. Lugiato, "Ghost Imaging with Thermal Light: Comparing Entanglement and Classical Correlation," *Phys. Rev. Lett.*, vol. 93, no. 9, p. 093602, 2004.
- [18] G. Scarcelli, A. Valencia and Y. Shih, *Phys. Rev. A*, vol. 70, p. 051802(R), 2004.
- [19] B. I. Erkmen, "Computational Ghost Imaging for Remote Sensing Applications," *IPN Progress Report*, vol. 42, no. 185, pp. 1-23, 15th May 2011.
- [20] L. Lugiato, "Ghost imaging": fundamental and applicative aspects," *Istituto Lombardo (Rend. Scienze)*, vol. 148, pp. 139-148, 2013.
- [21] B. Sun, *Three dimensional computational imaging with single-pixel detectors*, PhD Thesis, University of Glasgow, Scotland: Glasgow Theses Service, 2015.

- [22] P. Clemente, V. Durán, V. Torres-Company, E. Tajahuerce and J. Lancis, "Optical encryption based on computational ghost imaging," *Opt. Lett.*, vol. 35, no. 14, pp. 2391-2393, 2010.
- [23] M. Blazek and W. Elsässer, "Coherent and thermal light: Tunable hybrid states with second-order coherence without first-order coherence," *Phys. Rev. A*, vol. 84, no. 6, 2011.
- [24] R. Loudon, *The Quantum Theory of Light*, Oxford: Oxford Univ. Press, 2000.
- [25] W. Schleich, *Quantum Optics in Phase Space*, Berlin: Wiley, 2001.
- [26] P. H. van Cittert, "Die Wahrscheinliche Schwingungsverteilung in Einer von Einer Lichtquelle Direkt Oder Mittels Einer Linse Beleuchteten Ebene," *Physica (Utrecht)*, pp. 201-210, 1934.
- [27] F. Zernike, "The concept of degree of coherence and its application to optical problems," *Physica (Utrecht)*, vol. 5, no. 8, pp. 785-795, 1938.
- [28] G. Verschaffelt, G. Craggs, M. L. F. Peeters, S. K. Mandre, H. Thienpont and I. Fischer, "Spatially Resolved Characterization of the Coherence Area in the Incoherent Emission Regime of a Broad-Area Vertical-Cavity Surface-Emitting Laser," *IEEE J. Quantum Electron.*, vol. 3, pp. 249-255, 2009.
- [29] A. Gatti, M. Bache, D. Magatti, E. Brambilla, F. Ferri and L. Lugiato, "Coherent imaging with pseudo-thermal incoherent light," *J. Mod. Opt.*, vol. 53, p. 739, 2006.
- [30] P. R. Griffiths, J. A. De Haseth and J. D. Winefordner, *Fourier Transform Infrared Spectrometry*, 2nd ed., Wiley, 2007.
- [31] P. Hariharan, "White-Light Interference Microscopy," in *Basics of Interferometry*, 2nd ed., Academic Press, 2010, pp. 105-110.
- [32] W. Drexler and J. Fujimoto, *Optical Coherence Tomography: Technology and Applications*, 2nd ed., Springer Science & Business Media, 2008.
- [33] M. Mansuripur, "Second-order coherence and the Hanbury Brown–Twiss experiment," in *Classical Optics and Its Applications*, 2nd ed., Cambridge, Cambridge University Press, pp. 113-127.
- [34] R. J. Glauber, "The quantum theory of optical coherence," *Phys. Rev.*, vol. 130, no. 6, 1963.
- [35] H.-A. Bachor and T. Ralph, *A Guide to Experiments in Quantum Optics*, 2nd ed., Weinheim: Wiley-CVH Verlag GmbH Co. KGaA, 2004.
- [36] B. L. Morgan and L. Mandel, "Measurement of Photon Bunching in a Thermal Light Beam," *Phys. Rev. Lett.*, vol. 16, no. 22, pp. 1012-1015, 1966.
- [37] M. Fox, "5. Photon statistics," in *Quantum Optics An Introduction*, Oxford, Oxford University Press, 2006, p. 73.
- [38] F. Boitier, N. D. P. D. A. Godard and C. F. & E. Rosencher, "Photon extrabunching in ultrabright twin beams measured by two-photon counting in a semiconductor," *Nature Comm.*, vol. 2, p. 425, 2011.
- [39] P. Hong, J. Liu and G. Zhang, "Two-photon superbunching of thermal light via multiple two-photon path interference," *Phys. Rev. A*, vol. 86, no. 1, p. 013807, 2012.
- [40] M. Beck, "Comparing measurements of  $g(2)(0)$  performed with different coincidence detection techniques," *J. Opt. Soc. Am. B*, vol. 24, no. 10, pp. 2972-2978, Dec 2007.
- [41] U. Fano, "Ionization Yield of Radiations. II. The Fluctuations of the Number of Ions," *Phys. Rev.*, vol. 72, no. 26, pp. 26-29, 1947.
- [42] L. Mandel, "Sub-Poissonian photon statistics in resonance fluorescence," *Opt. Lett.*, vol. 4, p. 205, 1979.
- [43] R. Hanbury Brown and R. Twiss, "A new type of interferometer for use in radio astronomy," *The London, Edinburgh, and Dublin Philosophical Magazine and Journal of Science*, vol. 45, no. 366, pp. 663-682, 1954.
- [44] P. Kapusta, M. Wahl and R. Erdmann, *Advanced Photon Counting*, 1st ed., vol. 15, Springer International Publishing, 2014.

- [45] R. Pecora, *Dynamic Light Scattering: Applications of Photon Correlation Spectroscopy*, New York and London: Springer Science & Business Media, 2013.
- [46] D. J. Pine, D. A. Weitz, P. M. Chaikin and E. Herbolzheimer, "Diffusing wave spectroscopy," *Phys. Rev. Lett.*, vol. 60, no. 12, pp. 1134-1137, Mar 1988.
- [47] LSinstruments, "LSinstruments Technology," LSinstruments, 2016. [Online]. Available: <http://www.lsinstruments.ch/technology/>. [Accessed 30 12 2016].
- [48] M. Blazek, *Thermisch und kohärent: Erzeugung neuartiger Lichtzustände mittels Quantenpunkt-Superlumineszenzdiolen*, PhD Thesis, TU Darmstadt, 2012.
- [49] G. T. Foster, S. L. Mielke and L. A. Orozco, "Intensity correlations of a noise-driven diode laser," *J. Opt. Soc. Am. B*, vol. 15, no. 11, pp. 2646-2653, 1998.
- [50] A. Nevet, T. Michaeli and M. Orenstein, "Second-order optical coherence tomography: deeper and turbulence-free imaging," *J. Opt. Soc. Am. B*, vol. 30, no. 2, pp. 258-265, 2013.
- [51] H. Gross, *Fundamentals of Technical Optics (Radiometry, Handbook of Optical Systems)*, vol. 1, Weinheim: Wiley, 2005.
- [52] R. J. Glauber, "Coherent and incoherent states of the radiation field," *Phys. Rev.*, vol. 131, no. 6, pp. 2766-2788, 1963.
- [53] K. W. C. Chan, M. N. O'Sullivan and R. W. Boyd, "High-order thermal ghost imaging," *Opt. Lett.*, vol. 34, p. 3343, 2009.
- [54] M. Stevens, B. Baeck, E. Dauler, A. Kerman, R. Molnar, S. Hamilton, K. Berggren, R. Mirin and S. Nam, "High-order temporal coherences of chaotic and laser light," *Opt. Exp.*, vol. 18, no. 2, pp. 1430-1437, Jan 2010.
- [55] R. S. Bennink, S. J. Bentley, R. W. Boyd and J. C. Howell, "Quantum and Classical Coincidence Imaging," *Phys. Rev. Lett.*, vol. 92, p. 069901, 2004.
- [56] F. Ferri, D. Magatti, A. Gatti, M. Bache, E. Brambilla and L. A. Lugiato, "High-Resolution Ghost Image and Ghost Diffraction Experiments with Thermal Light," *Phys. Rev. Lett.*, vol. 94, p. 183602, 2005.
- [57] A. Valencia, G. Scarcelli, M. D'Angelo and Y. Shih, "Two-Photon Imaging with Thermal Light," *Phys. Rev. Lett.*, vol. 94, p. 063601, 2005.
- [58] D. Zhang, Y. H. Zhai, L. A. Wu and X. H. Chen, "Correlated two photon imaging with true thermal light," *Opt. Lett.*, vol. 30, no. 18, p. 2354, 2005.
- [59] Y.-H. Zhai, X.-H. Chen, D. Zhang and L.-A. Wu, "Two-photon interference with true thermal light," *Phys. Rev. A*, vol. 72, p. 043805, 2005.
- [60] G. Scarcelli, V. Berardi and Y. Shih, "Can Two-Photon Correlation of Chaotic Light Be Considered as Correlation of Intensity Fluctuations?," *Phys. Rev. Lett.*, vol. 96, p. 063602, 2006.
- [61] A. Gatti, M. Bondani, L. A. Lugiato, M. G. A. Paris and C. Fabre, "Comment on 'Can Two-Photon Correlation of Chaotic Light Be Considered as Correlation of Intensity Fluctuations?'," *Phys. Rev. Lett.*, vol. 98, p. 039301, 2007.
- [62] Y. H. Shih, "The physics of ghost imaging," *Quantum Inf. Process.*, vol. 11, p. 995, 2012.
- [63] M. D'Angelo, A. Valencia, M. H. Rubin and Y. Shih, "Resolution of quantum and classical ghost imaging," *Phys. Rev. A*, vol. 72, p. 013810, 2005.
- [64] J. H. Shapiro and R. W. Boyd, "The physics of ghost imaging," *Quan. Inf. Process.*, vol. 11, p. 1003, 2012.
- [65] S. Ragy and G. Adesso, "The nature of light in ghost imaging," *Sci. Rep.*, vol. 2, p. 651, 2012.
- [66] J. H. Shapiro, D. Venkatraman and F. N. C. Wong, "Ghost Imaging without Discord," *Sci. Rep.*, vol. 3, p. 1849, 2013.
- [67] L. G. Wang, S. Qamar, S. Y. Zhu and M. S. Zubairy, "Hanbury Brown-Twiss effect and thermal light ghost imaging: A unified approach," *Phys. Rev. A*, vol. 79, p. 033835, 2009.

- 
- [68] T. Peng, J. Simon, H. Chen, R. French and Y. Shih, "Popper's experiment with randomly paired photons in thermal state," *Europhys. Lett.*, vol. 109, p. 14003, 2015.
- [69] F. Ferri, D. Magatti, V. G. Sala and A. Gatti, "Longitudinal coherence in thermal ghost imaging," *Appl. Phys. Lett.*, vol. 92, p. 261109, 2008.
- [70] N. S. Bisht, E. K. Sharma and H. C. Kandpal, "The influence of source and object characteristics on coincidence imaging," *J. Opt.*, vol. 12, p. 045701, 2010.
- [71] H. C. Liu and J. Xiong, "The role of the degree of polarization in Nth-order thermal ghost imaging," *J. Phys. B: At. Mol. Opt. Phys.*, vol. 47, p. 145503, 2014.
- [72] I. Vidal, D. P. Caetano, E. J. S. Fonseca and J. M. Hickmann, "Effects of pseudothermal light source's transverse size and coherence width in ghost-interference experiments," *Opt. Lett.*, vol. 34, pp. 1450-1452, 2009.
- [73] Y. Cai and S.-Y. Zhu, "Ghost interference with partially coherent radiation," *Opt. Lett.*, vol. 29, no. 23, p. 2716, 2004.
- [74] G. Scarcelli, A. Valencia and Y. Shih, "Two-photon interference with thermal light," *Europhys. Lett.*, vol. 68, no. 5, pp. 618-624, 2004.
- [75] W. Martienssen and E. Spiller, "Coherence and Fluctuations in Light Beams," *Am. J. Phys.*, vol. 32, no. 12, pp. 919-926, 1964.
- [76] L. E. Estes, L. M. Narducci and R. A. Tuft, "Scattering of Light from a Rotating Ground Glass," *J. Opt. Soc. Am. A*, vol. 61, no. 10, pp. 1301-1306, 1971.
- [77] A. Gatti, D. Magatti and F. Ferri, "Three-dimensional coherence of light speckles: theory," *Phys. Rev. A*, vol. 78, p. 063806, 2008.
- [78] J. Cheng, "Transfer functions in lensless ghost-imaging systems," *Phys. Rev. A*, vol. 78, p. 043823, 2008.
- [79] X.-H. Chen, Q. Liu, K.-H. Luo and L.-A. Wu, "Lensless ghost imaging with true thermal light," *Opt. Lett.*, vol. 34, pp. 695-697, 2009.
- [80] L. Gao, X.-l. Liu, Z. Zheng and K. Wang, "Unbalanced lensless ghost imaging with thermal light," *J. Opt. Soc. Am. A*, vol. 31, pp. 886-890, 2014.
- [81] K. W. C. Chan, "Role of photon statistics of light source in ghost imaging," *Opt. Lett.*, vol. 37, pp. 2739-2741, 2012.
- [82] J. Goodman, *Speckle phenomena in optics: theory and applications*, Greenwood Village, USA: Roberts and Company Publishers, 2007.
- [83] P.-A. Lemieux and D. J. Durian, "Investigating non-Gaussian scattering processes by using nth-order intensity correlation functions," *J. Opt. Soc. Am. A*, vol. 16, no. 7, pp. 1651-1664, 1999.
- [84] D.-Z. Cao, J. Xiong and K. Wang, "Geometrical optics in correlated imaging systems," *Phys. Rev. A*, vol. 71, p. 013801, 2005.
- [85] F. Ferri, D. Magatti, L. A. Lugiato and A. Gatti, "Differential Ghost Imaging," *Phys. Rev. Lett.*, vol. 104, p. 253603, 2010.
- [86] D. Shi, S. Hu and Y. Wang, "Polarimetric ghost imaging," *Opt. Lett.*, vol. 39, p. 1231, 2014.
- [87] T. Iskhakov, A. Allevi, A. D. Kalashniko, V. G. Sala, M. Takeuchi, M. Bondani and M. Chekhova, "Intensity correlations of thermal light - Noise reduction measurements and new ghost imaging protocols," *Eur. Phys. J. Special Topics*, vol. 199, pp. 127-138, 2011.
- [88] H. Chen, T. Peng and Y. Shih, "100% correlation of chaotic thermal light," *Phys. Rev. A*, vol. 88, p. 023808, 2013.
- [89] A. Meda, A. Caprile, A. Avella, I. Ruo Berchera, I. P. Degiovanni, A. Magni and M. Genovese, "Magneto-optical imaging technique for hostile environments: The ghost imaging approach," *Appl. Phys. Lett.*, vol. 106, p. 262405, 2015.

- 
- [90] R. E. Meyers, K. S. Deacon and Y. Shih, "Turbulence-free ghost imaging," *Appl. Phys. Lett.*, vol. 98, p. 111115, 2011.
- [91] M. Bina, D. Magatti, M. Molteni, A. Gatti, L. A. Lugiato and F. Ferri, "Backscattering Differential Ghost Imaging in Turbid Media," *Phys. Rev. Lett.*, vol. 110, p. 083901, 2013.
- [92] Y.-K. Xu, W.-T. Liu, E.-F. Zhang, Q. Li, H.-Y. Dai and P.-X. Chen, "Is ghost imaging intrinsically more powerful against scattering?," *Opt. Exp.*, vol. 23, pp. 32993-33000, 2015.
- [93] J. Shapiro, "Computational ghost imaging," *Phys. Rev. A*, vol. 78, p. 061802(R), 2008.
- [94] Y. Bromberg, O. Katz and Y. Silberberg, "Ghost imaging with a single detector," *Phys. Rev. A*, vol. 79, p. 053840, 2009.
- [95] Y. Yang, J. Shi, F. Cao and G. Z. Jinye Peng, "Computational imaging based on time-correlated single-photon-counting technique at low light level," *Appl. Opt.*, vol. 54, pp. 9277-9283, 2015.
- [96] M. G. Capeluto, H. Duisterwinkel, C. T. Schmiegelow, D. Francisco, S. Ledesma and C. Iemmi, "Ghost imaging and ghost diffraction with pseudo-thermal light generated by means of a programmable SLM," *J. Phys.: Conf. Ser.*, vol. 274, p. 012004, 2011.
- [97] Z. Li, J. Suo, X. Hu and Q. Dai, "Content-adaptive ghost imaging of dynamic scenes," *Opt. Exp.*, vol. 24, pp. 7328-7336, 2016.
- [98] B. Sun, M. P. Edgar, R. Bowman, L. E. Vittert, S. Welsh, A. Bowman and M. J. Padgett, "3D Computational Imaging with Single-Pixel Detectors," *Science*, vol. 340, no. 6134, pp. 844-847, 2013.
- [99] P. Sen, "On the Relationship Between Dual Photography and Classical Ghost Imaging," *arXiv:1309.3007v1 [physics.optics]*, 2013.
- [100] W. Gong, C. Zhao, H. Yu, M. Chen, W. Xu and S. Han, "Three-dimensional ghost imaging lidar via sparsity constraint," *Sci. Rep.*, vol. 6, p. 26133, 2016.
- [101] P. Clemente, V. Durán, E. Tajahuerce, V. Torres-Company and J. Lancis, "Single-pixel digital ghost holography," *Phys. Rev. A*, vol. 86, p. 041803(R), 2012.
- [102] W.-K. Yu, X.-R. Yao, X.-F. Liu, L.-Z. Li, L.-A. Wu and G.-J. Zhai, "Single-pixel ghost microscopy based on compressed sensing and complementary modulation," *arXiv:1501.06002 [physics.optics]*, 2015.
- [103] X. Liu, X. Chen, X. Yao, W. Yu, G. Zhai and L. Wu, "Lensless ghost imaging with sunlight," *Opt. Lett.*, vol. 39, no. 8, pp. 2314-2317, 2014.
- [104] S. Karmakar, *Ghost Imaging with sunlight*, PhD Thesis, Baltimore County: ProQuest Dissertations And Theses, 2012.
- [105] D. Shi., C. Fan, P. Zhang, J. Zhang, H. Shen, C. Qiao and Y. Wang, "Adaptive optical ghost imaging through atmospheric turbulence," *Opt. Exp.*, vol. 20, no. 27, p. 27992, 2012.
- [106] P. Ryczkowski, M. Barbier, A. T. Friberg, J. M. Dudley and G. Genty, "Ghost imaging in the time domain," *Nat. Photonics*, vol. 10, p. 167-170, 2016.
- [107] F. Devaux, P.-A. Moreau, S. Denis and E. Lantz, "Computational temporal ghost imaging," *Optica*, vol. 3, pp. 698-701, 2016.
- [108] Z. Chen, H. Li, Y. Li, J. Shi and G. Zeng, "Temporal ghost imaging with a chaotic laser," *Opt. Eng.*, vol. 52, no. 7, p. 076103, 2013.
- [109] W. Gong and S. Han, "High-resolution far-field ghost imaging via sparsity constraint," *Sci. Rep.*, vol. 5, p. 9280, 2015.
- [110] J. Wu, Z. Xie, Z. Liu, W. Liu, Y. Zhang and S. Liu, "Multiple-image encryption based on computational ghost imaging," *Opt. Comm.*, vol. 359, pp. 38-43, 2016.
- [111] R. Khakimov, B. Henson, D. Shin, S. Hodgman, R. Dall and K. B. & A. Truscott, "Ghost imaging with atoms," *Nature*, vol. 540, pp. 100-103, 2016.

- [112] N. Tian, Q. Guo, A. Wang, D. Xu and L. Fu, "Fluorescence ghost imaging with pseudothermal light," *Opt. Lett.*, vol. 36, pp. 3302-3304, 2011.
- [113] A. Hannonen, A. T. Friberg and T. Setälä, "Classical spectral ghost ellipsometry," *Opt. Lett.*, vol. 41, no. 21, pp. 4943-4946, 2016.
- [114] T. B. Pittman, D. V. Strekalov, D. N. Klyshko, M. H. Rubin, A. V. Sergienko and Y. H. Shih, "Two-photon geometric optics," *Phys. Rev. A*, vol. 53, p. 2804, 1996.
- [115] Friedrich Alexander Universität Erlangen-Nürnberg, „Advances Laboratory Course in Physics: Versuch Nr. B45 Photonenstatistik,“ 27 10 2016. [Online]. Available: [www.fp.fkp.uni-erlangen.de/fortgeschrittenenpraktikum/versuchsangebot-fuer-bsclanf/BSc-Versuchsanleitungen/B45.pdf](http://www.fp.fkp.uni-erlangen.de/fortgeschrittenenpraktikum/versuchsangebot-fuer-bsclanf/BSc-Versuchsanleitungen/B45.pdf). [Zugriff am 22 5 2017].
- [116] S. Kuhn, *Ghost Imaging mittels eines einzigen Photon-Counting Detektors*, M. Sc. Thesis, TU Darmstadt, 2016.
- [117] M. L. M. Ricci, J. Mazzaferri, A. V. Gragas and O. E. Martínez, "Photon counting statistics using a digital oscilloscope," *Am. J. Phys.*, vol. 75, p. 707, 2007.
- [118] P. Koczyk, P. Wiewiór and C. Radzewics, "Photon counting statistics—Undergraduate experiment," *Am. J. Phys.*, vol. 64, p. 240, 1996.
- [119] A. Einstein, "Über einen die Erzeugung und Verwandlung des Lichtes betreffenden heuristischen Gesichtspunkt," *Ann. Phys.*, vol. 17, p. 132, 1905.
- [120] W. J. Thompson, "Don't subtract the background [signal count analysis method]," *Computing in Science & Engineering*, vol. 1, no. 5, pp. 84-88, 1999.
- [121] L. Ma, M. T. Rakher, M. J. Stevens, O. Slattery, K. Srinivasan and X. Tang, "Temporal correlation of photons following frequency up-conversion," *Opt. Exp.*, vol. 19, pp. 10501-10510, 2011.
- [122] Y. Zhai, F. E. Becerra, B. L. Glebov, J. Wen, A. E. Lita, B. Calkins, T. Gerrits, J. Fan, S. W. Nam and A. Migdall, "Photon-number-resolved detection of photon-subtracted thermal light," *Opt. Lett.*, vol. 13, pp. 2171-2173, 2013.
- [123] H. J. Lee, I.-H. Bae and H. S. Moon, "Continuous manipulation of tunable mixed classical light from coherent light to pseudothermal light," *J. Opt. Soc. Am. A*, vol. 4, pp. 560-565, 2011.
- [124] A. Moussaïd and P. N. Pusey, "Multiple scattering suppression in static light scattering by cross-correlation spectroscopy," *Phys. Rev. E*, vol. 60, no. 5, pp. 5670-5676, 1999.
- [125] T. Führer, *Modeling and application of a novel method providing active control of wavelength and linewidth of an external cavity diode laser*, PhD Thesis, TU Darmstadt, 2012.
- [126] L. V. T. Nguen, "Distributed-feedback (DFB) Laser Coherence and Linewidth Broadening," Chief, Electronic Warfare & Radar Division, Research Report, Edinburgh South Australia, 2003.
- [127] L. Maleki, "Laser Focus World, Novel Lasers: Whispering-gallery-mode resonators create ultranarrow-linewidth semiconductor lasers," 10 7 2014. [Online]. Available: <http://www.laserfocusworld.com/articles/print/volume-50/issue-10/features/novel-lasers-whispering-gallery-mode-resonators-create-ultranarrow-linewidth-semiconductor-lasers.html>. [Accessed 7 11 2016].
- [128] M. Wahl, H.-J. Rahn, I. Gregor, R. Erdmann and J. Enderlein, "Dead-time optimized time-correlated photon counting instrument with synchronized, independent timing channels," *Rev. Sci. Instrum.*, vol. 78, p. 033106, 2007.
- [129] V. Torres-Company, C. R. Fernández-Pousa and J. P. Torres, "In-fiber frequency-domain measurement of ultrashort second-order correlations of incoherent light," *Opt. Lett.*, vol. 35, no. 11, pp. 1850-1852, 2010.
- [130] D. F. McAlister and M. G. Raymer, "Ultrafast photon-number correlations from dual-pulse, phase-averaged homodyne detection," *Phys. Rev. A*, vol. 55, no. 3, pp. R1609-R1612, 1997.
- [131] R. W. Boyd, *Nonlinear Optics*, 3rd ed., Rochester, New York: Academic Press, 2008.

- 
- [132] D. J. Griffiths, P. Education. and D. Kindersley, *Introduction to Electrodynamics*, 3rd ed., University of Michigan: Prentice Hall, 1999.
- [133] F. Boitier, *Absorption à deux photons et effets de corrélation quantique dans les semiconducteurs*, PhD Thesis, Chatillon Cedex: Office National d'Études et de Recherches Aérospatiales, 2011.
- [134] R. Salem, *Characterization of Two-Photon-Absorption detectors for applications in high-speed optical systems*, M. Sc. Thesis, Department of Electrical and Computer Engineering, University of Maryland, 2003.
- [135] S. Hartmann, *Investigations on photon statistics of Quantum Dot - Superluminescent Diodes*, M. Sc. Thesis, TU Darmstadt, 2012.
- [136] A. Jechow, M. Seefeldt, H. Kurzke, A. Heuer and R. Menzel, "Enhanced two-photon excited fluorescence from imaging agents using true thermal light," *Nature Phot.*, vol. 7, no. 12, p. 973, 2013.
- [137] C. des Pallières, *Study of the two-photon absorption in the GaAsP photocathode of a photomultiplier tube as a function of wavelength*, internship report, TU Darmstadt, 2014.
- [138] B. R. Mollow, "Two photon absorption and field correlation functions," *Phys. Rev.*, vol. 175, no. 5, pp. 1555-1563, 1968.
- [139] F. Boitier, A. Godard, A. Ryasnyanskiy, N. Dubreuil, P. Delaye, C. Fabre and E. Rosencher, "Second order coherence of broadband down-converted light on ultrashort time scale determined by two photon absorption in semiconductor," *Opt. Exp.*, vol. 18, no. 19, pp. 20401-20408, 2010.
- [140] F. Boitier, A. Godard, N. Dubreuil, P. Delaye, C. Fabre and E. Rosencher, "Two-photon-counting interferometry," *Phys. Rev. A*, vol. 87, p. 013844, 2013.
- [141] K. N. K. & Y. H. Mogi, "A novel real-time measurement method for ultrashort optical pulses," *Jpn. J. Appl. Phys.*, vol. 27, pp. 2078-2081, 1988.
- [142] G. Scarcelli, "Photon bunching two by two," *Nature Phys.*, vol. 5, pp. 252-253, 2009.
- [143] E. Hecht, *Optics*, 4th ed., San Francisco: Addison Wesley, 2002.
- [144] M. Blazek, S. Hartmann, A. Molitor and W. Elsässer, "Unifying intensity noise and second-order coherence properties of amplified spontaneous emission sources," *Opt. Lett.*, vol. 36, no. 17, pp. 3455-3457, 2011.
- [145] M. Blazek and W. Elsässer, "Emission State Hierarchy Governed Coherence and Intensity Noise Properties of Quantum Dot Superluminescent Diodes," *IEEE J. Quantum Electron.*, vol. 48, no. 12, pp. 1578-1582, 2012.
- [146] A. Nevet, A. Hayat, P. Ginzburg and M. Orenstein, "Indistinguishable Photon Pairs from Independent True Chaotic Sources," *Phys. Rev. Lett.*, vol. 107, no. 25, p. 253601, 2011.
- [147] A. Shevchenko, M. Roussey, A. Friberg and T. Setälä, "Ultrashort coherence times in partially polarized stationary optical beams measured by two-photon absorption," *Opt. Exp.*, vol. 23, no. 24, p. 31274, 2015.
- [148] A. Hayat, A. Nevet and P. G. & M. Orenstein, "Applications of two-photon processes in semiconductor photonic devices: invited review," *Semicond. Sci. Technol.*, vol. 26, p. 083001, 2011.
- [149] J. K. Ranka, A. L. Gaeta, A. Baltuska, M. S. Pshenichnikov and D. A. Wiersma, "Autocorrelation measurement of 6-fs pulses based on the two-photon-induced photocurrent in a GaAsP photodiode," *Opt. Lett.*, vol. 22, pp. 1344-1346, 1997.
- [150] A. Nevet, A. Hayat and M. Orenstein, "Ultrafast pulse compression by semiconductor two-photon gain," *Opt. Lett.*, vol. 35, no. 23, pp. 3877-3879, 2010.
- [151] B. C. Thomsen, L. P. Barry, J. M. Dudley and J. D. Harvey, "Ultrahigh speed all-optical demultiplexing based on two-photon absorption in a laser diode," *Electron. Lett.*, vol. 34, no. 19, p. 1871, 1998.

- [152] Z. Zheng, A. Weiner, J. Marsh and M. Karkhanehchi, "Ultrafast optical thresholding based on two-photon absorption GaAs waveguide photodetectors," *IEEE Photon. Technol. Lett.*, vol. 9, no. 4, pp. 493-495, 1997.
- [153] T. Inui, K. Tamura, K. Mori and T. Morioka, "Bit rate flexible chirp measurement technique using two-photon absorption," *Electron. Lett.*, vol. 38, no. 23, pp. 1459-1460, 2002.
- [154] R. Negres, J. Hales, A. Kobayakov, D. Hagan and E. Stryland, "Experiment and analysis of two-photon absorption spectroscopy using a white-light continuum probe," *IEEE J. Quantum Electron.*, vol. 9, pp. 1205-1216, 2002.
- [155] Y. Tanaka, P. Chua, T. Kurokawa, H. Tsuda, M. Naganuma and M. Takeda, "Reflectometry based on two-photon absorption of a silicon avalanche photodiode," in *Optical Fiber Sensors Conference Technical Digest*, Portland, OR, USA, 2002.
- [156] S. Hartmann, A. Molitor, M. Blazek and W. Elsässer, "Tailored first- and second-order coherence properties of quantum dot superluminescent diodes via optical feedback," *Opt. Lett.*, vol. 38, no. 8, pp. 1334-1336, 2013.
- [157] S. Hartmann, F. Friedrich, A. Molitor, M. Reichert, W. Elsässer and R. Walser, "Tailored quantum statistics from broadband states of light," *New J. Phys.*, vol. 17, p. 043039, 2015.
- [158] T.-P. Lee, C. Burrus and B. Miller, "A stripe-geometry double-heterostructure amplified-spontaneous-emission (superluminescent) diode," *IEEE J. Quantum Electron.*, vol. 9, no. 8, pp. 820-828, 1973.
- [159] C. Shen, T. Ng, J. Leonard, A. Pourhashemi, S. Nakamura, S. DenBaars, J. Speck, A. Alyamani, M. El-desouki and B. Ooi, "High-brightness semipolar (2021<sup>-</sup>) blue InGaN/GaN superluminescent diodes for droop-free solid-state lighting and visible-light communications," *Opt. Lett.*, vol. 41, no. 11, pp. 2608-2611, 2016.
- [160] V. R. Shidlovski, "Superluminescent Diode Light Sources for OCT," in *Optical Coherence Tomography*, Berlin Heidelberg, Springer Berlin Heidelberg, 2008, pp. 281-299.
- [161] D. Zhu, M. Shen, H. Jiang, M. Li, M. Wang, Y. Wang, L. Ge, J. Qu and J. Wang, "Broadband superluminescent diode-based ultrahigh resolution optical coherence tomography for ophthalmic imaging," *J. Biomed. Opt.*, vol. 16, no. 12, p. 126006, 2011.
- [162] N. Krstajic, L. Smith, S. Matcher, D. Childs, M. Bonesi, P. Greenwood, M. Hugues, K. Kennedy, M. Hopkinson, K. Groom, S. MacNeil, R. Hogg and R. Smallwood, "Quantum Dot Superluminescent Diodes for Optical Coherence Tomography: Skin Imaging," *IEEE J. Sel. Topics in Quantum Electron.*, vol. 16, no. 4, pp. 748-754, 2010.
- [163] INPHENIX, "INPHENIX Resource Library Publications, Application Instruction 003: Applications of the Superluminescent," 28 11 2011. [Online]. Available: [http://inphenix.com/pdfdoc/Applications\\_of\\_the\\_Superluminescent\\_Diode\\_SLD\\_11.28.11.pdf](http://inphenix.com/pdfdoc/Applications_of_the_Superluminescent_Diode_SLD_11.28.11.pdf). [Accessed 4 1 2017].
- [164] P. Typpo and L. Chase, "Air bearing supported optical distance measuring device for use in e.g. paper industry, has determining device structured and arranged to determine distance to object based on signals from detector system". Patent EP1855083-A1, 14 11 2007.
- [165] O. Celikel and S. E. San, "Design details and characterization of all digital closed-loop interferometric fiber optic gyroscope with superluminescent light emitting diode," *Opt. Rev.*, vol. 16, no. 1, pp. 35-42, 2009.
- [166] L. D. Cecilia, S. Cattini, F. Giovanardi and L. Rovati, "Single-arm Self-mixing Superluminescent Diode Interferometer for Flow Measurements," *Journal of Lightwave Technology*, vol. PP, no. 99, pp. 1-1, 2016.
- [167] G. A. Alphonse und D. B. Gilbert, „Super-luminescent diode“. US Patent US4821277 A, 1989.
- [168] Z. Y. Zhang, R. A. Hogg, X. Q. Lv and Z. G. Wang, "Self-assembled quantum-dot superluminescent light-emitting diodes," *Adv. Opt. Photon.*, vol. 2, pp. 201-228, 2010.

- 
- [169] M. Grundmann, Nano-optoelectronics Concepts, Physics and Devices, Berlin: Springer-Verlag Berlin Heidelberg, 2002.
- [170] V. M., J. Hwang, C. Yang, A. Leenstra, B. de Ronde, J. M. J. Dehollain, F. Hudson, K. Itoh, A. Morello and A. Dzurak, "An addressable quantum dot qubit with fault-tolerant control-fidelity," *Nature Nanotech.*, vol. 9, pp. 981-985, 2014.
- [171] A. Shields, "Semiconductor quantum light sources," *Nature Photon.*, vol. 1, pp. 215-223, 2007.
- [172] M. Bruchez and C. Hotz, Quantum Dots Application in Biology, Totowa, New Jersey: Humana Press Inc., 2007.
- [173] J.-W. Lee, D.-Y. Son, T.-K. Ahn, H.-W. Shin, I. Kim, S.-J. Hwang, M. J. Ko, S. Sul, H. Han and N.-G. Park, "Quantum-Dot-Sensitized Solar Cell with Unprecedentedly High Photocurrent," *Sci. Rep.*, vol. 3, p. 1050, 2013.
- [174] J. Chen, V. Hardev and J. Yurek, "Quantum-Dot Displays: Giving LCDs a Competitive Edge through Color," *Information Display*, vol. 29, no. 1, pp. 12-17, 2013.
- [175] V. Ustinov, A. Egorov, A. Zhukov, N. Ledentsov, M. Maksimov, A. Tsatsul'nikov, N. Bert, A. Kosogov, P. Kop'ev, D. Bimberg and Z. Alferov, "Formation of Stacked Self-Assembled InAs Quantum Dots in GaAs Matrix for Laser Applications," *MRS Proceedings*, vol. 417, p. 141, 1995.
- [176] D. L. Huffaker, G. Park, Z. Zou, O. B. Shchekin and D. G. Deppe, "1.3  $\mu\text{m}$  room-temperature GaAs-based quantum-dot laser," *Appl. Phys. Lett.*, vol. 73, no. 18, pp. 2564-2566, 1998.
- [177] P. Bhattacharya, D. Klotzkin, O. Qasaimah, W. Zhou, S. Krishna and D. Zhu, "High-speed modulation and switching characteristics of In(Ga)As-Al(Ga)As self-organized quantum-dot lasers," *IEEE J. Sel. Topics Quantum Electron.*, vol. 6, pp. 426-438, 2000.
- [178] M. Sugawara, N. Hatori, T. Akiyama, Y. Nakata and H. Ishikawa, "Quantum-dot semiconductor optical amplifiers for high bit-rate signal processing over 40 Gbit/s," in *Proc. Lasers and Electro-Optics*, 2001.
- [179] E. U. Rafailov, M. A. Cataluna and W. Sibbett, "Mode-locked quantum-dot lasers," *Nat. Photon.*, vol. 1, pp. 395-401, 2007.
- [180] X. Huang, A. Stintz, H. Li, L. F. Lester, J. Cheng and K. J. Malloy, "Passive mode-locking in 1.3  $\mu\text{m}$  two-section InAs quantum dot lasers," *Appl. Phys. Lett.*, vol. 78, no. 19, pp. 2825-2827, 2001.
- [181] Z.-Z. Sun, D. Ding, Q. Gong, W. Zhou, B. Xu and Z.-G. Wang, "Quantum-dot superluminescent diode: A proposal for an ultra-wide output spectrum," *Opt. and Quant. Electron.*, vol. 31, no. 12, pp. 1235-1246, 1999.
- [182] Z. Y. Zhang, X. Q. Meng, P. Jin, C. Li, S. Qu, B. Xu, X. Ye and Z. Wang, "A novel application to quantum dot materials to the active region," *J. Cryst. Growth*, vol. 243, pp. 25-29, 2002.
- [183] Z. Y. Zhang, R. A. Hogg, X. Q. Lv and Z. G. Wang, "Self-assembled quantum-dot superluminescent light-emitting diodes," *Adv. in Opt. and Photon.*, vol. 2, pp. 203-219, 2010.
- [184] Y.-C. Xin, A. Martinez, T. Saiz, A. J. Moscho, Y. Li, T. A. Nilsen, A. L. Gray and L. F. Lester, *IEEE Photon. Tech. Lett.*, vol. 19, no. 7, pp. 501-504, 2007.
- [185] R. Yao, N. Weir, C. S. Lee and W. Guo, "Broadband Chirped InAs Quantum-Dot Superluminescent Light-Emitting Diodes With InxAl1-xAs Strain-Reducing Layers," *IEEE Photon. Journal*, vol. 8, no. 3, pp. 1-7, 2016.
- [186] A. W. Smith and J. A. Armstrong, "Laser Photon Counting Distributions Near Threshold," *Phys. Rev. Lett.*, vol. 16, no. 25, pp. 1169-1172, 1966.
- [187] J. C. Chung, J. C. Huang and N. B. Abraham, "Intensity fluctuations and spatial coherence of a single polarized component of a saturating amplified-spontaneous-emission source," *Phys. Rev. A*, vol. 22, no. 3, pp. 1018-1021, 1980.
- [188] S. Balle, F. De Pasquale and M. San Miguel, "Intensity statistics and spatial correlation functions in a noise-driven unidirectional laser amplifier," *Opt. Comm.*, vol. 85, pp. 104-116, 1991.

- [189] L. Allen and G. Peters, "Superradiance, coherence brightening and amplified spontaneous emission," *Phys. Lett. A*, vol. 31, no. 3, pp. 95-96, 1970.
- [190] G. I. Peters and L. Allen, "Amplified spontaneous emission I. The threshold condition," *J. Phys. A: Gen. Phys.*, vol. 4, no. 2, p. 238, 1971.
- [191] L. Allen and G. Peters, "Amplified spontaneous emission II. The connection with laser theory," *J. Phys. A: Gen. Phys.*, vol. 4, no. 3, p. 377, 1971.
- [192] L. Allen and G. Peters, "Amplified spontaneous emission III. Intensity and saturation," *J. Phys. A: Gen. Phys.*, vol. 4, no. 4, p. 564, 1971.
- [193] G. Peters and L. Allen, "Amplified spontaneous emission IV. Beam divergence and spatial coherence," *J. Phys. A: Gen. Phys.*, vol. 5, no. 4, p. 546, 1972.
- [194] X. Wu and H. Cao, "Statistical studies of random-lasing modes and amplified spontaneous-emission spikes in weakly scattering systems," *Phys. Rev. A*, vol. 77, no. 1, p. 013832, 2008.
- [195] Y. Ye, Z. J. Wong, X. Lu, X. Ni, H. Zhu, X. Chen, Y. Wang and X. Zhang, "Monolayer excitonic laser," *Nat. Photon.*, vol. 9, pp. 733-737, 2015.
- [196] S. M. Pietralunga, P. Martinelli and M. Martinelli, "Photon statistics of amplified spontaneous emission in a dense wavelength-division multiplexing regime," *Opt. Lett.*, vol. 28, no. 3, pp. 152-154, 2003.
- [197] V. J. Srinivasan, H. Radhakrishnan, J. Y. Jiang and S. Barry, "OCT methods for capillary velocimetry," *Biomed. Opt. Exp.*, vol. 3, no. 3, p. 158450, Mar 2012.
- [198] N. Ozaki, D. T. D. Childs, J. Sarma, T. S. Roberts, T. Yasuda, H. Shibata, H. Ohsato, E. Watanabe, N. Ikeda, Y. Sugimoto and R. A. Hogg, "Superluminescent diode with a broadband gain based on self-assembled InAs quantum dots and segmented contacts for an optical coherence tomography light source," *J. Appl. Phys.*, vol. 119, no. 8, p. 083107, 2016.
- [199] H. Shibata, N. Ozaki, T. Yasuda, S. Ohkouchi, N. Ikeda, H. Ohsato, E. Watanabe, Y. Sugimoto, K. Furuki and R. A. Hogg, "Imaging of spectral-domain optical coherence tomography using a superluminescent diode based on InAs quantum dots emitting broadband spectrum with Gaussian-like shape," *Jap. J. Appl. Phys.*, vol. 54, no. 4S, p. 04DG07, 2015.
- [200] M. Jedrzejewska-Szczerska, "Shaping coherence function of sources used in low-coherent measurement techniques," *Eur. Phys. J. Special Topics*, vol. 144, pp. 203-208, 2007.
- [201] A. C. Akcay, J. P. Rolland and J. M. Eichenholz, "Spectral shaping to improve the point spread function in optical coherence tomography," *Opt. Lett.*, vol. 28, no. 20, pp. 1921-1923, 2003.
- [202] M. Blazek, W. Elsässer, M. Hopkinson, M. K. P. Resneau, M. Rossetti, P. Bardella, M. Gioannini and I. Montrosset, "Coherence function control of Quantum Dot Superluminescent Light Emitting Diodes by frequency selective optical feedback," *Opt. Exp.*, vol. 17, no. 16, pp. 13365-13372, 2009.
- [203] P. D. L. Greenwood, D. T. D. Childs, K. Kennedy, K. M. Groom, M. Hugues, M. Hopkinson, R. A. Hogg, N. Krstajić, L. E. Smith, S. J. Matcher, M. Bonesi, S. MacNeil and R. Smallwood, "Quantum Dot Superluminescent Diodes for Optical Coherence Tomography: Device Engineering," *IEEE J. Sel. Topics in Quantum Electron.*, vol. 16, no. 4, pp. 1015-1022, 2010.
- [204] S. Shin, U. Sharma, H. Tu, W. Jung and S. A. Boppart, "Characterization and Analysis of Relative Intensity Noise in Broadband Optical Sources for Optical Coherence Tomography," *IEEE Phot. Tech. Lett.*, vol. 22, no. 14, pp. 1057-1059, 2010.
- [205] M. Blazek, *Intensitätsrauschen von Quantenpunkt-Superlumineszenz lichtemittierenden Diode*, Diplomarbeit, TU Darmstadt, 2006.
- [206] M. Blazek, S. Breuer, T. Gensty, W. E. Elsässer, M. Hopkinson, K. M. Groom, M. Calligaro, P. Resneau and M. Krakowski, "Intensity noise of ultrabroadband Quantum Dot Light Emitting Diodes and Lasers at 1.3  $\mu\text{m}$ ," in *Proc. SPIE 6603, Noise and Fluctuations in Photonics, Quantum Optics, and Communications, 66031Y*, Florence, Italy, 2007.

- [207] R. Müller, Rauschen, Zweite, überarbeitete und erweiterte Auflage Hrsg., Springer-Verlag Berlin Heidelberg, 1990.
- [208] K. Komori, S. Arai and Y. Suematsu, "Noise in semiconductor laser amplifiers with quantum box structure," *IEEE Phot. Tech. Lett.*, vol. 3, no. 1, pp. 39-41, 1991.
- [209] L. Drzewietzki, *Mode-locked quantum-dot lasers and amplifiers: Ultra-short pulse generation, amplification and stabilization*, PhD Thesis, TU Darmstadt, 2015.
- [210] M. Rossetti, L. H. Li, A. Markus, A. Fiore, L. Occhi, C. Velez, S. Mikhrin, I. Krestnikov and A. Kovsh, "Characterization and modeling of broad spectrum InAs-GaAs quantum-dot superluminescent diodes emitting at 1.2–1.3  $\mu\text{m}$ ," *IEEE J. Quantum Electron.*, vol. 43, pp. 676-686, 2007.
- [211] P. Bardella, M. Rossetti and I. Montrosset, "Modeling of Broadband Chirped Quantum-Dot Super-Luminescent Diodes," *IEEE J. Sel. Top. Quantum Electron.*, vol. 15, no. 3, pp. 785-791, 2009.
- [212] T. L. Choi, S. K. Ray, Z. Zhang, D. Childs, K. M. Groom, B. J. Stevens, H. Liu, M. Hopkinson and R. A. Hogg, "Quantum Dot Superluminescent Diodes - Bandwidth Engineering and Epitaxy for High Powers," in *19th International Conference on Indium Phosphide and Related Materials*, Matsue, Japan, 2007.
- [213] O. Qasaimeh, "Optical Gain and Saturation Characteristics of Quantum-Dot Semiconductor Optical Amplifiers," *IEEE J. Quantum Electron.*, vol. 39, no. 6, pp. 793-798, 2003.
- [214] T. Heil, I. Fischer, W. Elsässer, B. Krauskopf, K. Green and A. Gavrielides, "Delay dynamics of semiconductor lasers with short external cavities: Bifurcation scenarios and mechanisms," *Phys. Rev. E*, vol. 67, no. 6, p. 066214, 2003.
- [215] F. Schulze, B. Lingnau, S. M. Hein, A. Carmele, E. Schöll, K. Lüdge and A. Knorr, "Feedback-induced steady-state light bunching above the lasing threshold," *Phys. Rev. A*, vol. 89, no. 4, p. 041801, 2014.
- [216] V. Torres-Company, J. P. Torres and A. T. Friberg, "Shaping the Ultrafast Temporal Correlations of Thermal-Like Photons," *Phys. Rev. Lett.*, vol. 109, no. 24, p. 243905, 2012.
- [217] F. T. Arecchi, "Measurement of the Statistical Distribution of Gaussian and Laser Sources," *Phys. Rev. Lett.*, vol. 15, no. 24, pp. 912-916, 1965.
- [218] F. Arecchi, A. Berne, A. Sona and P. Burlamacchi, "1A4 - Photocount distributions and field statistics," *IEEE J. Quan. Electron.*, vol. 2, no. 9, pp. 341-350, 1966.
- [219] C. DeWitt, A. Blandin and C. Cohen-Tannoudji, "Quantum Optics and Electronics, Lectures delivered at Les Houches during the 1964 session of the Summer School of Theoretical Physics at University of Grenoble," p. 621, Les Houches 1964, 1965.
- [220] G. Present and D. B. Scarf, "Two-Photon Correlations in a Mixture of Gaussian and Laser Light," *Appl. Opt.*, vol. 11, no. 1, pp. 120-124, 1972.
- [221] G. Lachs, "Theoretical Aspects of Mixtures of Thermal and Coherent Radiation," *Phys. Rev.*, vol. 138, no. 4B, pp. B1012-B1016, 1965.
- [222] J. Perina and R. Horak, "On the quantum statistics of the superposition of coherent and chaotic fields," *J. Phys. A (Gen. Phys.)*, vol. 2, pp. 702-712, 1969.
- [223] J. Liu, Y. Zhou, W. Wang, F.-l. Li and Z. Xu, "Experimental study of the second-order coherence of partially polarized thermal light," *Opt. Comm.*, vol. 317, pp. 18-23, 2014.
- [224] M. Padgett, "Ghost imaging with entangled photons and orbital angular momentum," in *APS March Meeting 2016, abstract #Y1.001*, Baltimore, US, 2016.
- [225] R. S. Aspden, N. R. Gemmell, P. A. Morris, D. S. Tasca, L. Mertens, M. G. Tanner, R. A. Kirkwood, A. Ruggeri, A. Tosi, R. W. Boyd, G. S. Buller, R. H. Hadfield and M. J. Padgett, "Photon-sparse microscopy: visible light imaging using infrared illumination," *Optica*, vol. 2, no. 12, pp. 1049-1052, 2015.

- [226] Z. Zhang, X. Ma and J. Zhong, "Single-pixel imaging by means of Fourier spectrum acquisition," *Nat. Commun.*, vol. 6, p. 6225, 2015.
- [227] M. Aßmann and M. Bayer, "Compressive adaptive computational ghost imaging," *Sci. Rep.*, vol. 3, p. 1545, 2013.
- [228] B. Sun, S. S. Welsh, M. P. Edgar, J. H. Shapiro and M. J. Padgett, "Normalized ghost imaging," *Opt. Exp.*, vol. 20, no. 15, pp. 16892-16901, 2012.
- [229] W. Wang, Y. P. Wang, J. Li, X. Yang and Y. Wu, "Iterative ghost imaging," *Opt. Lett.*, vol. 39, no. 17, pp. 5150-5153, 2014.
- [230] R. E. Meyers, K. S. Deacon and Y. Shih, "Positive-negative turbulence-free ghost imaging," *Appl. Phys. Lett.*, vol. 100, no. 13, p. 131114, 2012.
- [231] W. Chen and X. Chen, "Marked ghost imaging," *Appl. Phys. Lett.*, vol. 104, no. 25, p. 251109, 2014.
- [232] P. Zerom, Z. Shi, M. N. O'Sullivan, K. W. C. Chan, M. Krogstad, J. Shapiro and R. Boyd, "Thermal ghost imaging with averaged speckle patterns," *Phys. Rev. A*, vol. 86 063817, 2012.
- [233] W. Gong, "High-resolution pseudo-inverse ghost imaging," *Photon. Research*, vol. 3, no. 5, pp. 234-237, 2015.
- [234] S. Kuhn, S. Hartmann and W. Elsässer, "Photon-statistics-based classical ghost imaging with one single detector," *Opt. Lett.*, vol. 42, no. 12, pp. 2863-2866, 2016.
- [235] S. Hartmann, S. Kuhn and W. Elsässer, "Characteristic properties of the spatial correlations and visibility in mixed light ghost imaging," *Appl. Opt.*, vol. 55, no. 28, pp. 7972-7979, 2016.
- [236] S. Hartmann, A. Molitor and W. Elsässer, "Ultra-broadband Ghost Imaging using opto-electronic Amplified Spontaneous Emission," *Opt. Lett.*, vol. 40, no. 24, pp. 5770-5773, 2015.
- [237] S. Hartmann and W. Elsässer, "A novel, fully incoherent amplified spontaneous emission light source for ghost imaging," *Sci. Rep.*, vol. 7, p. 41866, 2017.
- [238] X.-H. Chen, I. N. Agafonov, K.-H. Luo, Q. Liu, R. Xian, M. V. Chekhova and L.-A. Wu, "High-visibility, high-order lensless ghost imaging with thermal light," *Opt. Lett.*, vol. 35, no. 8, pp. 1166-1168, 2010.
- [239] R. V. Hogg, A. Craig and J. W. McKean, *Introduction to Mathematical Statistics*, 7th ed., New Jersey: American Mathematical Society, 2013.
- [240] C. M. Grinstead and J. L. Snell, "Chap. 7.1. Sums of Discrete Random Variables," in *Introduction to Probability*, P.O. Box 6248, Providence, Rhode Island, American Mathematical Society, 1998.
- [241] D.-Z. Cao, J. Xiong, S.-H. Zhang, L.-F. Lin, L. Gao and K. Wang, "Enhancing visibility an resolution in nth-order intensity correlation of thermal light," *Appl. Phys. Lett.*, vol. 92, no. 20, p. 201102, 2005.
- [242] K. W. C. Chan, M. N. O'Sullivan and R. W. Boyd, "Optimization of thermal ghost imaging: high-order correlations vs. background subtraction," *Opt. Exp.*, vol. 18, no. 6, pp. 5562-5573, 2010.
- [243] H.-C. Liu and J. Xiong, "Properties of high-order ghost imaging with natural light," *J. Opt. Soc. Am. A*, vol. 30, no. 5, pp. 956-961, 2013.
- [244] Y. Ding, A. Alhazime, D. Nikitichev, K. Fedorova, M. Ruiz, M. Tran, Y. Robert, A. Kapsalis, H. Simos, C. Mesaritakis, T. Xu, P. Bardella, M. Rossetti, I. Krestnikov, D. Livshits, I. Montrosset, D. Syvridis, M. A. Cataluna, M. Krakowski and E. Rafailov, "Tunable Master-Oscillator Power-Amplifier Based on Chirped Quantum-Dot Structures," *IEEE J. Quantum Electron.*, vol. 24, no. 20, pp. 1841-1844, 2012.
- [245] L. Basano and P. Ottonello, "Experiment in lensless ghost imaging with thermal light," *Appl. Phys. Lett.*, vol. 89, no. 9, p. 091109, 2006.
- [246] Z. Liu, S. Tan, J. Wu, E. Li, X. Shen and S. Han, "Spectral Camera based on Ghost Imaging via Sparsity Constraints," *Sci. Rep.*, vol. 6, p. 25718, 2016.

- 
- [247] D. B. Phillips, R. He, Q. Chen, G. M. Gibson and M. J. Padgett, "Non-diffractive computational ghost imaging," *Opt. Exp.*, vol. 24, no. 13, pp. 14172-14182, 2016.
- [248] M. P. Edgar, G. M. Gibson, R. W. Bowman, B. Sun, N. Radwell, K. J. Mitchell, S. S. Welsh and M. J. Padgett, "Simultaneous real-time visible and infrared video with single-pixel detectors," *Sci. Rep.*, vol. 5, p. 10669, 2015.
- [249] N. Huynh, E. Zhang, M. Betcke, S. Arridge, P. Beard and B. Cox, "Single-pixel optical camera for video rate ultrasonic imaging," *Optica*, vol. 3, no. 1, pp. 26-29, 2016.
- [250] C. Mesaritis, A. Kapsalis, H. Simos, C. Simos, M. Krakowski, I. Krestnikov and D. Syvridis, "Tapered InAs/InGaAs quantum dot semiconductor optical amplifier design for enhanced gain and beam quality," *Opt. Lett.*, vol. 38, no. 14, pp. 2404-2406, 2013.
- [251] H. G. Berry, G. Gabrielse and A. E. Livingston, "Measurement of the Stokes parameters of light," *Appl. Opt.*, vol. 16, no. 12, pp. 3200-3205, 1977.
- [252] L. Mandel and E. Wolf, "Chapter 3.1. The complex analytical signal," in *Optical Coherence and Quantum Optics*, Cambridge University Press, 1995, pp. 92-108.
- [253] H. Partanen, J. Tervo and J. Turunen, "Spatial coherence of broad-area laser diodes," *Appl. Opt.*, vol. 52, no. 14, pp. 3221-3228, 2013.
- [254] H. Braun, S. Rogosky, U. Schwarz, S. Brüningshoff, A. Lell, S. Lutgen and U. Strauß, "Supermodes in Broad Ridge (Al,In)GaN Laser Diodes," *IEEE J. Quantum Electron.*, vol. 45, no. 9, pp. 1074-1083, 2009.
- [255] I. Fischer, O. Hess, W. Elsässer and E. Göbel, "Complex spatio-temporal dynamics in the near-field of a broad-area semiconductor laser," *Europhys. Lett.*, vol. 35, no. 8, pp. 579-584, 1996.
- [256] C. K. Hitznerberger, M. Danner, W. Drexler and A. F. Fercher, "Measurement of the spatial coherence of superluminescent diodes," *J. Mod. Opt.*, vol. 46, no. 12, pp. 1763-1774, 1999.
- [257] F. Marin, A. Bramati and E. Giacobino, "Squeezing and Intermode Correlations in Laser Diodes," *Phys. Rev. Lett.*, vol. 75, no. 25, pp. 4606-4609, 1995.
- [258] J. Krzywda and K. Roszak, "Phonon-mediated generation of quantum correlations between quantum dot qubits," *Sci. Rep.*, vol. 6, p. 23753, 2016.
- [259] H. Huang and D. G. Deppe, "Rate equation model for nonequilibrium operating conditions in a self-organized quantum-dot laser," *IEEE J. Quant. Electron.*, vol. 37, no. 5, pp. 691-698, 2001.
- [260] B. I. Erkmen and J. H. Shapiro, "Ghost imaging: from quantum to classical to computational," *Adv. Opt. Photon.*, vol. 2, no. 4, pp. 405-450, 2010.
- [261] L. Mandel, "Quantum Electronics," in *Proceedings of the Third International Congress*, 1964.
- [262] H. K. Tsang, R. V. Penty, I. H. White, R. S. Grant, W. Sibbett, J. B. D. Soole, H. P. LeBlanc, N. C. Andreadakis, R. Bhat and M. A. Koza, "Two-photon absorption and self-phase modulation in InGaAsP/InP multi-quantum-well waveguides," *J. Appl. Phys.*, vol. 70, no. 7, pp. 3992-3994, 1991.
- [263] D. Reid, W. Sibbett, J. Dudley, L. Barry, B. Thomsen and J. Harvey, "Commercial Semiconductor Devices for Two Photon Absorption Autocorrelation of Ultrashort Light Pulses," *Appl. Opt.*, vol. 37, no. 34, pp. 8142-8144, 1998.
- [264] Hamamatsu-Photonics, "www.hamamatsu.com, Photon counting head H7421 series," [Online]. Available: <http://www.hamamatsu.com/resources/pdf/etd/m-h7421e.pdf>. [Accessed 10 12 2016].
- [265] E. Wolf, in *Proceeding of the Symposium on Optical Masers*, 1963.
- [266] D. Pelliccia, A. Rack, M. Scheel, V. Cantelli and D. M. Paganin, "Experimental X-Ray Ghost Imaging," *Phys. Rev. Lett.*, vol. 117, p. 113902, 2016.
- [267] R. Holyst, A. Poniewierski and X. Zhang, "Analytical form of the autocorrelation function for the fluorescence correlation spectroscopy," *Soft Matter*, vol. 13, pp. 1267-1275, 2017.

- 
- 
- [268] F. Friedrich, “Hybrid coherent light: modeling quantum dot superluminescent diodes,” M. Sc. Thesis, TU Darmstadt, 2013.
- [269] C. Gies, J. Wiersig, M. Lorke and F. Jahnke, “Semiconductor model for quantum-dot-based microcavity lasers,” *Phys. Rev. A*, vol. 75, p. 013803, 2007.

---



---

## List of figures

---

Figure 1. Illustration of second-order temporal correlations. Left: Illustrative intensity auto-correlation functions originating from coherent light (blue), from thermal light (red), from non-classical light (dash-dotted) and from light showing extra-bunching (dotted). Right: Visualization of photon streams for the four different levels of photon-bunching. ....	10
Figure 2. Exemplary photon number probability distributions $P(n)$ : a Bose-Einstein distribution (red) and a Poissonian distribution (blue) with a mean photon number of $n = 8$ . ....	10
Figure 3. Schematic drawing of a coincidence measurement based on the HBT configuration for determining the second-order correlation function $g_2\tau$ . Here, the time delay $\tau$ is introduced by varying the optical path delay $s$ by $s + \Delta s$ between the two detectors $D_1$ and $D_2$ connected to a correlator C. ....	11
Figure 4. Detection schemes for determining higher order temporal correlations. Left: $j$ detectors connected to a correlator unit for measuring the $j$ -th order correlation function with $j - 1$ time delays. Right: Two detectors connected to a time-tagging unit acquiring individually and synchronously the photon count time-traces. The $j$ -th order correlation function with one time delay are evaluated by calculation. ....	13
Figure 5. Typical schematics of a classical GI experiment using a pseudo-thermal light (PTL) source and a spatial HBT configuration with a beamsplitter (BS), the object arm (OA) comprising the object and the bucket detector (BD), the reference arm (RA) comprising the spatially resolving detector (SRD) and finally the correlator (C). ....	16
Figure 6. Schematic of the pseudo-thermal light source. Here, a He-Ne laser is depicted illuminating a rotating ground glass (RGG) which leads to the generation of speckle patterns in a specific far-field plane. ....	16
Figure 7. Illustration of the speckle pattern transmission in the object arm. Three possible speckle patterns generated at times $t_i$ are impinging with an intensity distribution $I_{obj}(t_i, x_{obj})$ onto a transmission mask with the field-transmission function $t(x_{obj})$ . Behind the mask, different levels of intensity are recorded by the spatially integrating bucket detection $I_b(t_i)$ . Further propagation effects between the object and the bucket detector are neglected such that Eq. (28) holds strictly. ....	16
Figure 8. Schematics of a computational ghost imaging scheme. A light source illuminates here a digital micro-mirror device (DMD) which produces random light spot patterns guided onto an object. Correlations between the pre-computed random patterns and the single-pixel bucket detector signal are computed to form a ghost image. ....	20
Figure 9. Diagrammatic scheme of the single-photon-counting detection. A single-photon-counting detector (Hamamatsu H10330A-45, $V_{PMT} = 700V$ ) is connected to an oscilloscope (TEK 3032, 300MHz (2.5 GS/s)) to acquire single-photon-count time traces (A). A 2mV threshold has a discrimination functionality to minimize the data acquisition by LabView control, which subsequently counts photon counts within a time-binning window $T$ adjusted to be smaller than the coherence time of the investigated light (B). A magnified picture of the oscilloscope shows a single-photon-count of $\sim 7mV$ amplitude and 2ns width. The oscilloscope voltage scale is 5mV (C) [116]. ....	24
Figure 10. Dark count analysis. Left: Voltage distribution when laser light illuminates the PMT (black data) and when the PMT shutter is closed (red data). Right: Dark count probability distribution determined from a closed PMT shutter measurement adjusting $T_{bin} = 250ns$ resulting in $n_{dark} = 0.43$ [116]. ....	26
Figure 11. Exemplary measurements of (left row, A-C) laser light (discrete mode (DM) diode laser) and (right row, D-F) pseudo-thermal (PT) light. A, B and D, E show measured probability distributions (black data) together with theoretical distributions (red data) of Poisson and Bose-Einstein, respectively. C and F depict the calculated coherence degrees (black data) according to Eq. (47) together with the theoretical values for ideally coherent and ideally thermal light (red data). ....	28

Figure 12. Schematic representation of two-photon-absorption (TPA) inside a semiconductor material. The energy band diagram as a function of wave vector $k$ (conduction band (CB), valence band (VB)) is shown for the direct band gap ( $Eg$ ) case with two exemplary TPA events of different photon energy combinations $h\nu_1$ und $h\nu_2$ .....	31
Figure 13. Two-photon-absorption in a semiconductor-based photomultiplier. Left: Energy band diagram of the VIS sensitive PMT photocathode (Hamamatsu H7421-40) illuminated by NIR photons. Right: TPA photon count rate as a function of incoming optical power recorded by the counting box (Hamamatsu C8855-01) of the PMT. ....	33
Figure 14. Schematic of the implemented TPA Michelson interferometer. The light source is fiber-coupled into a single-mode optical fiber (SMF). The mean intensities of the individual interferometer arms are denoted by $I_1$ and $I_2$ . Further components: Non-polarizing beamsplitter (BS), high-precision linear stage ( $\tau$ ), achromatic lenses (ACL), long-pass filter blocking visible light (LPF) to suppress fundamental absorption. ....	34
Figure 15. Representative TPA interferogram of light emitted by a broadband ASE source. Left: Full interferogram in terms of TPA Counts/s (right axis) and normalized TPA count rate (Eq. (57), left axis) as a function of optical path delay (bottom abscissa) as well as the corresponding time delay $\tau$ (top abscissa). Right: Zoom-in of the left graph showing highly resolved TPA interference fringes. ....	35
Figure 16. Fourier transformation (FFT) of the TPA interferogram from Figure 15 (double logarithmic scale). Left: Full FFT spectrum with indications of the three frequency components of Eq. (57): (i) low-frequency range ( $\propto G_2(\tau)$ ), (ii) optical frequency range, (iii) frequency-doubled component as well as additional frequency contributions (*) due to interferometric artifacts. The vertical dashed line (red) denotes the low-pass cut-off frequency utilized for the extraction of $G_2(\tau)$ . Right: Zoom into (ii) with comparison to an optical spectrum measured by a commercial optical spectrum analyzer (linear scale).....	36
Figure 17. Retrieved fast oscillating contributions of the TPA interferogram from Figure 15. Left: First-order frequency components (ii) using an IFFT of the bandpass window: 223-237THz. Right: Frequency-doubled oscillation components (iii) using an IFFT of the bandpass from 450 to 467THz.....	37
Figure 18. Second-order correlation extraction from the TPA interferogram. Left: Data extracted from the TPA interferogram of Figure 15. Right: Statistics of the extracted second-order coherence degree taken from a set of 90 TPA interferograms. A Gaussian fit (blue line) yields a mean value of $g_2^0 = 2.01$ and a variance of $\Delta_2 g_2^0 = 0.04$ . ....	38
Figure 19. The superluminescent diode. Digital camera image of a mounted SLD (left) and schematic diagram of the diode structure with indications of some typical characteristics and emission region (right). The three-dimensional schematic has been adapted from Ref. [167].....	41
Figure 20. Quantum dot gain material. Left: Energy band diagram in the space domain of a single quantum dot. The solid arrows indicate possible electron relaxations from the conduction band (CB) of the bulk material into the QD wetting layer (WL) and the radiative energy levels (SES, ES, GS) to finally recombine with electron holes located in the valence band (VB). Right: Schematic cross-section of 10 inhomogeneously broadened QD layers within a possible epitaxial structure comprising GaAs space layers (turquoise), cladding layers (darker blue) and electrical contacts (light blue). ....	43
Figure 21. Opto-electronic characteristics of a quantum dot SLD. Left: P-I curve showing the optical power $P_{opt}$ behavior as a function of injection current $I_{pump}$ . Right: Representative optical spectra at different injection current levels revealing ground state (GS), first excited state (ES) and even second excited state emission (SES) of inhomogeneously broadened QD layers. ....	43
Figure 22. Phase space diagram of a single phase-randomized Gaussian state. This state is prepared in a thermal state displaced by $\gamma_j = \gamma_j \exp(i\phi_j)$ with randomized phase angles according to Eq. (63). [Courtesy of Franziska Friedrich taken from [157]] .....	45
Figure 23. Central second-order coherence degree of a MM PRAG state as a function of the number of contributing modes $N$ . Exemplary trajectories for four different values of $\Delta_2 p p_2$ are depicted for a	

range of $0 < N < 1650$ (left) and an enlarged section for higher number of modes $300 < N < 1600$ revealing the trajectories on a small $g(2)$ -scale (right). .....	48
Figure 24. Microscopic picture of the SLD. The SLD was epitaxially grown by the University of Sheffield and processed by Thales III-V Lab (Palaiseau, Paris) within the European project Nano UB-Sources (device number: VN590). .....	48
Figure 25. Schematic diagram of the optical feedback experiment. The free-space emitting SLD is split by a non-polarizing 50:50 beamsplitter (BS). The broadband feedback arm comprises a variable attenuator (attn) and an optional interference filter (filter) yielding $\Delta\lambda_{FWHM} = 10\text{nm}$ . The second BS output is guided through an optical isolator (iso) to prevent further optical feedback effects and finally the light is sent to $g2\tau$ -analysis. ....	49
Figure 26. Central second-order coherence degree under broadband optical feedback as a function of the spectral width. The indications (a), (b) and (c) are exemplary data points for which the optical spectra (over wavelength) are depicted on the right-hand side. ....	50
Figure 27. Central second-order coherence degree under optical feedback as a function of the number of modes. The indications (a), (b) and (c) are exemplary data points for which the optical spectra (over optical frequency) are depicted on the right-hand side, together with indications of the extracted modes (darker red data) on the basis of the 13dB threshold (horizontal solid line). ....	50
Figure 28. Schematic diagram of the mixed-light experiment. The power ratio between laser light (SM laser) and SLD light (QD SLD) is controlled by variable attenuators (attn). Optical isolators (iso) prevent back-reflections into the emitters. A fiber combiner (fiber BS) enables a simple implementation of the two light fields, which is then guided into the TPA interferometer and to a commercial OSA (ADVANTEST Q8384). Note, the TPA detector from Section 4.2 (Hamamatsu R928) has been exchanged by a semiconductor-based head-on PMT (Hamamatsu H7421-40) with enhanced sensitivity [135]. ....	54
Figure 29. SLD in operation. Left: Microscopic picture from top. Right: Chip schematics showing the bended waveguide structure, the sub-mount dimensions and the AR coating specifications. ....	54
Figure 30. Representative optical spectrum of the superimposed light measured by a commercial OSA. The optical frequencies have been translated from a measured wavelength abscissa. The indications on the spectral width is assumed according to the manufacturer specification (SM laser) and determined by the Suessmann measure (QD SLD). Here, a power ratio of 1:1 between laser and SLD light has been adjusted. ....	54
Figure 31. Individual second-order correlations of (left) SLD light and (right) laser light. Bottom: Measured TPA interferogram. Top: Extracted second-order correlations functions (red) and calculated functions (blue) according to Eq. (73) on the basis of measured optical spectra (Figure 30). ....	57
Figure 32. Exemplary second-order correlations of a mixed-light scenario with a power-ratio of $\zeta = 0.6$ . Bottom: TPA interferogram. Top: Extracted second-order correlations functions (red) and calculated functions (blue) according to Eq. (82) on the basis of a measured optical spectrum (comparable to Figure 30). ....	57
Figure 33. Ultra-broadband mixed-light: experimental data and model values of the central second-order coherence degree. The theoretical limits of ideal thermal and coherent light values are indicated by horizontal lines as a guide-to-the-eye. Model values are calculated according to Eq. (82) at $\tau = 0$ on the basis of measured optical spectra (Figure 30). ....	58
Figure 34. Schematic diagram of the photon statistics-based ghost imaging experiment with the PT light source, a collimation lens (L), the beamsplitter (BS) and the imaging planes $x$ and $y$ located at $z_{ref}$ and $z_{obj}$ , respectively. The right part of the figure shows the superposition (e.g. by optical fibers and a fiber combiner) of the reference and the object beam ( $\Sigma$ ) with subsequent detection (single-photon-counting (SPC) detector) and data acquisition (oscilloscope with LabView-based read-out and evaluation). Additionally, a measured, static speckle pattern (negative image) originating from the PT source is depicted within the beam paths to illustrate the speckle pattern propagation within the lensless GI configuration. ....	64
Figure 35. The implemented pseudo-thermal light source. Left: Schematic drawing comprising the packaged discrete mode laser (single-mode laser (SM laser)), the collimation and focussing lenses	

for the speckle size control (L1, L2 and L3) and the rotating diffusor (RGG). Right: Representative speckle-pattern in the imaging plane of the PS-GI setup measured with a CCD camera (Apogee AP1). .....	64
Figure 36. Representative probability distributions of photons originating from a single speckle cell exclusively in the reference plane $x$ (A) and exclusively in the object plane $y$ (B) as well as for superimposed speckle cells at correspondingly equal, $x = y_0$ (C), and unequal positions, $x = y_0 + 1.5\text{mm}$ (D). Additionally, the central second-order coherence degree as well as the fidelity factor are given in each graph. In (D), the fidelity is explicitly denoted by $FBE$ for reasons of comparison with the next section (Figure 38). .....	67
Figure 37. Measured position-position correlations $g(2)(\tau = 0, x)$ in terms of a transverse displacement $x$ in the reference plane having fixed the position in the object plane at $y_0 = 0$ for two selected, different speckle diameters [116]: 0.68mm (left) and 1.01mm (right). $x = 0$ corresponds to the equal positioning of object and reference aperture. Errors bars represent the statistical variance of a set of 3 measurements. The fitted functions (red line) are based on assuming a Gaussian respecting error bar weights.....	67
Figure 38. Photon distributions of two different superimposed speckle-cells. Experimental data and BE distribution taken from Figure 36 (D) and calculated convolution of two BE distributions reconstructing the experimentally obtained photon statistics. Experimentally, the SM fiber in the reference plane has been displaced by $\Delta x = 1.5\text{mm}$ with respect to $x = y_0$ (equal positions within the speckle pattern at each planes) in order to ensure the superposition of two different speckle cells (compare with Figure 37). .....	71
Figure 39. Visibility of the higher-order position-position correlations in mixed-light GI for the orders 2, 3 and 4 as a function of $\zeta = I_{111} + I_2$ . .....	72
Figure 40. Visibility of an object with multiple speckle transmission for the correlation orders 2 (red), 3 (blue) and 4 (green) as a function of the relative intensity ratio $\zeta = I_{ref}/I_{ref} + I_{obj}$ . The arrows illustrate the shift of maximum visibility from $N_{obj} = 2$ to $N_{obj} = 20$ of a given correlation order. To get a better idea of possible imaging scenarios: $N_{obj} = 2$ could image a maximum of two features, i.e. a double pinhole mask, whereas a total number of $N_{obj} = 20$ - coupled into the object arm - would resolve a maximum of 20 different object features. ....	74
Figure 41. Experimentally determined spatial higher-order correlations ( $\zeta=0.5$ ). The fitted Gaussians (solid lines) take the error bar weights into account originating from the statistical variance of set of 3 measurements. The dashed lines denote the calculated minimum and maximum values by the model, also listed in Table 6. Note that this solely serves as an indication and not as a spatial trend description. ....	76
Figure 42. Visibility of the spatial second-order correlations in PS-GI as a function of the adjusted power ratio $\zeta$ between both imaging planes. ....	78
Figure 43. Ghost image cross-section of a double-pinhole mask. Left: Experimentally obtained higher-order ghost image cross-sections. Right: Legends of graphs (top), microscopic picture of the transmission mask (middle) made of an aluminium plate together with a schematic drawing of the object with dimensioning indications (bottom). ....	80
Figure 44. Visibility as a function of object complexity in terms of number of coherence areas fitting into an object transmission mask ( $A_{obj}/A_c$ ). Coloured and black trajectories correspond to the PS-GI model and conventional higher-order calculations, respectively. Inset: Illustration of the coherence area $A_c$ and the object area $A_{obj}$ for an exemplary binary object of the letter "T".....	83
Figure 45. Calculated higher-order PS-GI images (maximum and minimum values) of a two-dimensional transmission mask (A) depicting the acronym of the Technische Universität Darmstadt (TUD). The expected PS-GI signal amplitudes for the correlation order 2 (B), 3 (C) and 4 (D), assuming optimal visibility conditions (see Section 5.1.2), are visualized as a contour-plot with an adjusted equal scaling of 0.2 for illustrating the visibility enhancement with increasing correlation order.....	83
Figure 46. First- and second-order coherence of the QD SLD light: Left: Optical power spectrum (measured by an OSA, ADVANTEST Q8384) as a function of wavelength with various indicated measures: the central wavelength/frequency (green) as well as the spectral widths in terms of	

- wavelength/frequency according to the FWHM (orange) and to the Suessmann measure (blue). Right: Representative TPA interferogram (black line) of a single measurement and extracted second-order correlation function (red line). .....85
- Figure 47. Schematic diagram of the experimental setup for ultra-broadband ghost imaging using the hybrid pseudo-thermal-SLD light: free-space emitting superluminescent diode (narrow-stripe QD SLD), achromatic lenses (ACL), optical isolator (ISO), rotating ground glass plate (RGG), broadband 50:50 beam splitters (BS), long pass filter (LPF) blocking fundamental absorptions ( $\lambda < 1000\text{nm}$ , SCHOTT RG1000), variable attenuator (attn) for optimizing the intensity distribution between both interferometer arms, motorized (Newport LTA-Series) linear translation stage ( $\tau$ , Newport M-443) and the photomultiplier in TPA mode (TPA PMT). .....86
- Figure 48. Representative point-to-point correspondence of ultra-broadband GI using the hybrid PT-SLD light. Top: TPA signals corresponding to the intensities of the single arms (reference pinhole and fixed pinhole) as well as the combined intensities taken from the interferogram at time delays far from coherence. Bottom: Central second-order coherence degree as a function of the relative transverse displacement of the two split beams. A Gaussian fit is depicted as a guide-to-the-eye. The error bars correspond to the statistical variance of a set of 3 subsequent measurements. Inset: Schematic illustration (not to scale) of the speckle-pattern size and the fixed pinhole in the object plane ( $x_{obj}$ ) which cross-section is also indicates in the graph (red dashed line). .....87
- Figure 49. Ultra-broadband GI with a double-pinhole object: Top: TPA signals corresponding to the intensities of the single arms (reference pinhole and fixed double-pinhole object) as well as the combined intensities taken from the interferogram at time delays far from coherence  $\tau \gg \tau_c$ . Bottom: Ghost image cross-section (central second-order coherence degree as a function of the relative transverse displacement between reference and object beam) with error bars corresponding to the statistical variance of a set of 3 subsequent measurements. A double Gaussian fit (black solid line) is depicted as a guide-to-the-eye. Inset: Schematic drawing of the object and the beam size (not to scale) with object details given: the individual pinhole diameter  $d = 500\mu\text{m}$  and the pinhole separation  $s = 1000\mu\text{m}$ , which are depicted as a cross-section (red dashed line) in the bottom graph. ....89
- Figure 50. Measured (black line) and low-pass filtered (red line) TPA interferograms of single measurements corresponding to the ghost image (Figure 49, bottom) at  $x_{ref} = 1000\mu\text{m}$  (left) and at  $x_{ref} = 600\mu\text{m}$  (right). .....90
- Figure 51. The broad-area superluminescent diode. Left: Schematic of the BA-SLD structure. Note that this drawing does not represent the actual proportions. The GaAs (100) substrate (n-doped) of the device with about  $200\mu\text{m}$  thickness is more than 100 times larger than the diode transition. The broad-area facet coordinates are denoted as  $x_{fac}$  and  $y_{fac}$ , perpendicular and along the epitaxial growth direction, respectively. Right: Optical spectrum measured with a commercial OSA (ADVANTEST Q8384) with indications of the spectral distribution center and the FWHM both in terms of frequency and wavelength. The corresponding Suessmann measure amounts to  $\Delta\nu_S = 4.29\text{THz}$ . .....92
- Figure 52. First-order temporal correlations of the BA-SLD light. Left: Experimentally determined  $Re[g_1(\tau)]$  function (black) and thermal light model with Gaussian-distributed optical frequencies calculated with the experimentally determined coherence time  $\tau_c = 233\text{fs}$  (red line); inset: zoom-in showing highly resolved interference fringes; Right: optical spectrum obtained by three different methods: an OSA trace (black line), experimental FFT data (black squares) from the left graph and the Gaussian distribution with  $\tau_c = 233\text{fs}$  (red line). .....93
- Figure 53. Second-order temporal correlations of the BA-SLD light. Extracted correlation function (black) from a measured TPA interferogram and theoretically expected second-order correlation function for thermal light with Gaussian distributed frequencies calculated with the experimentally determined coherence time  $\tau_c = 233\text{fs}$  (red line). .....94
- Figure 54. Diagrammatic drawing of the fiber-based ultra-broadband GI setup: Free-space emitting BA-SLD as the GI light source, collimation lens (CL), cylindrical lens (CyL), two broadband 50:50 beam splitters (BS1, fiber-based BS2), single-mode fibers (SMF), long pass filter (LPF) blocking

fundamental absorptions ( $\lambda < 1000\text{nm}$ , SCHOTT RG1000), and the photomultiplier in TPA mode (TPA-PMT). .....	96
Figure 55. Spatial correlations of the BA-SLD light at the imaging planes. Experimentally determined spatial intensity auto-correlations (left) along the horizontal $x_{ref}$ -axis with different slit widths (the deduced mode expansion $\sigma c \approx 2\sigma G$ is illustrated by the arrow) and (right) along the vertical $y_{ref}$ -axis. A slope of a linear fit (dashed line) amounts to 0 with a constant function of 1.58. ....	96
Figure 56. Light spot profile at the imaging planes. The two white lines denote the selected cross-sections depicted as additional graphs at the top and on the right-hand side of the contour plot. In the top graph, the histogram bars illustrate the dominant spatial modes yielding the experimentally determined mode expansion of $\sigma c = 256\mu\text{m}$ . .....	97
Figure 57. Ghost image cross-section of a double-slit object. Left: Experimental data (black squares) with error bars corresponding to the statistical variance of a set of three measurements, fitted double Gaussian function (red line) respecting the error bar weights and indications of the object dimensions (dashed line). Right: Digital camera record of the object through a microscope, which cross-section is depicted in the graph (blue dashed line). .....	98
Figure 58. Schematic diagram of the experimental setup for a 2D ultra-broadband GI demonstration of a reflective object, comprising collimation optics (ACL and CyL), a horizontal slit aperture (HSA), 50:50 broadband beamsplitters (BS1 and BS2), a spatially resolving aperture (SA), single-mode fibers (SMF), a long-pass filter (LPF), the TPA detector (TPA PMT). Additionally, two spatial profiles are depicted for illustrating the vertical spatial filtering for achieving spatial resolution in the y-axis. ....	111
Figure 59. Reflective scanning ultra-broadband ghost imaging of an inverse mask. Left: Microscope image of the letter "T" made of acrylic paint onto a low-quality metallic surface. Right: Ghost image of the inverse mask reconstructed from the scanning procedure (see Figure 58). Note that the dashed line indicates the margin of the object, equal in scale. ....	112

---

## Acknowledgement

---

I would first of all like to acknowledge the kind provision of excellent discrete mode semiconductor laser devices by R. Phelan (Eblana Photonics) for the implementation of the pseudo-thermal light source. Also, I gratefully acknowledge the fabrication and the processing of the superluminescent diode devices from I. Krestnikov (Innolume GmbH), M. Hopkinson (University of Sheffield) and M. Krakowski (III-V Lab) within the framework of the past European projects Nano UB-Sources and FAST-DOT.

The work of this thesis was partly supported by the Deutsche Forschungsgemeinschaft (DFG) grant EL 105/21.

At this point, I want to say *Thank You* to those who supported me during my PhD time and beyond, contributed to where I am today. To express my sincere gratitude in an appropriate manner I switch language to German.

- Herrn Prof. Dr. Wolfgang Elsässer danke ich für die Chance an einem aktuellen Forschungsgebiet promoviert haben zu dürfen, für die Betreuung meiner Doktorarbeit sowie für die große Unterstützung bei den vielen ehrgeizigen Zielen.
- Herrn Prof. Dr. Reinhold Walser danke ich für das Übernehmen des Zweitgutachtens und für die gute Kooperation.
- Dr. Martin Blazek bin ich dankbar für die Betreuung meiner Abschlussarbeiten während meines Studiums und für die Motivationsfähigkeit, ohne die ich sicherlich nicht so weit gekommen wäre.
- Dr. Andreas Molitor danke ich für die konstruktive, kollegiale Zusammenarbeit während der Zeit, in der wir uns ein Büro teilten. Darüber hinaus danke ich ihm für die geteilte Sportbegeisterung, die zahlreichen Gespräche, die wir miteinander geführt haben und für die entstandene Freundschaft.
- Till Mohr danke ich für den unkomplizierten fachlichen Austausch sowie für seine experimentellen Ideen im Labor. Darüber hinaus bin ich für die gemeinsame Lernzeit während des Studiums sehr dankbar.
- Franziska Friedrich danke ich für die gute Zusammenarbeit zwischen Theorie und Experiment, für die Beantwortung von vielen Theoriefragen und für die wertvolle Korrekturhilfe.
- Ich bedanke mich bei Robert Pawlus für die angenehme Büroatmosphäre und die zahlreichen sportlichen Aktivitäten.
- Bei Andreas Herdt bedanke ich mich herzlich für die häufig angebotene Hilfe jeglicher Korrekturarbeiten, die ich immer dankend angenommen habe.
- Der Arbeitsgruppe Halbleiteroptik danke ich für das angenehme Arbeitsklima, die große Hilfsbereitschaft und Frau Maria Musso für ihre organisatorische Unterstützung.
- Mein Dank gilt auch all denjenigen Studenten, die zu meinem Promotionsthema beigetragen haben: Moritz Reichert (Mixed-light), Simone Kuhn (PS-GI), Christophe des Pallières (TPA Interferometer Charakterisierung) und den beiden Masterstudenten Lydia Fischer und Patrick Janassek für die Weiterführung der Ghost Imaging Projekte.
- Besonderer Dank geht natürlich an meine gesamte Familie, insbesondere an meine Eltern, Catherine und Hans, die mich stets unterstützt haben. Mein größter Dank gilt meiner Frau Tessa für die bedingungslose Unterstützung in den letzten Jahren, für den täglichen Zuspruch und für die liebevolle Umsorgung und ihr Verständnis in der Zeit der Fertigstellung der Dissertation.

---

---

## Curriculum Vitae

---

- 2005           Abitur ARG Heusenstamm
- 2005-2006     Freiwilliges Soziales Jahr (Landessportbund Hessen)
- 2006-2012     physics studies at TU Darmstadt
- Bachelor of Science (June 2010)  
thesis: *Investigations of Quantum Dot Superluminescent Diodes at lowest light emission levels*
  - Master of Science (November 2012)  
thesis: *Investigations on the photon statistics of Quantum Dot Superluminescent Diodes*, with distinction.
  - Gerhard-Herzberg master research price 2013 (TU Darmstadt)
- 2013-2017     PhD student and scientific assistant within the group of Prof. Elsässer (Semiconductor Optics Group)

**Journal papers**

1. M. Blazek, S. Hartmann, A. Molitor and W. Elsässer, “Unifying intensity noise and second-order coherence properties of amplified spontaneous emission sources”, *Opt. Lett.* **36** (17), 3455 (2011)
2. A. Molitor, S. Hartmann, W. Elsässer, "Stokes vector characterization of the polarization behavior of vertical-cavity surface-emitting lasers", *Opt. Lett.* **37** (22), 4799, (2012)
3. **S. Hartmann, A. Molitor, M. Blazek, W. Elsässer, "Tailored first and second order coherence properties of QD SLD via optical feedback", *Opt. Lett.* **38** (8), pp. 1334-1336, (2013)**
4. A. Molitor, P. Debernardi, S. Hartmann, W. Elsässer, "Spatially resolved Stokes parameters of small-area vertical-cavity surface-emitting lasers: experiment and simulation", *Opt. Lett.* **38** (22), 4777 (2013)
5. A. Molitor, S. Hartmann, and W. Elsässer, “Investigations on spatio-spectrally resolved Stokes polarization parameters of oxide-confined vertical-cavity surface-emitting lasers”, *Opt. Lett.* **40** (13), 3121 (2015)
6. **S. Hartmann, F. Friedrich, A. Molitor, M. Reichert, W. Elsässer and R. Walser, “Tailored quantum statistics from broadband states of light”, *New J. Phys.* **17**, 043039 (2015)**
7. **S. Hartmann, A. Molitor and W. Elsässer, “Ultra-broadband Ghost Imaging using opto-electronic Amplified Spontaneous Emission”, *Opt. Lett.* **40** (24), 5770 (2015)**
8. A. Molitor, T. Mohr, S. Hartmann and W. Elsässer, “Investigations on spectro-temporally resolved Stokes polarization parameters of transverse multi-mode Vertical-Cavity Surface-Emitting Lasers”, *IEEE J. Quant. Electron.* **52** (2), 2400109 (2016)
9. P. Janassek, S. Hartmann, A. Molitor, F. Michel, and W. Elsässer, “Investigations of the polarization behavior of quantum cascade lasers by Stokes parameters”, *Opt. Lett.* **41** (2), 305 (2016)
10. S. Kuhn, S. Hartmann, and W. Elsässer, “Photon statistics based ghost imaging with a single detector”, *Opt. Lett.* **41** (12), 2863-2866 (June, 2016)
11. **S. Hartmann, S. Kuhn, and W. Elsässer, "Characteristic properties of the spatial correlations and visibility in mixed light ghost imaging," *Appl. Opt.* **55**, 7972-7979 (2016)**
12. **S. Hartmann and W. Elsässer, “A novel semiconductor-based, amplified spontaneous emission light source for ghost imaging”, *Sci. Rep.* **7**, 41866; doi: 10.1038/srep41866 (2017)**

---

## Conference proceedings

1. S. Hartmann, M. Blazek and W. Elsässer, "Photon statistics at the transition of amplified spontaneous emission to stimulated emission", DPG Frühjahrstagung 2012, Stuttgart, Germany, Q 9.8 (talk)
2. A. Molitor, S. Hartmann, W. Elsässer, " Stokes vector characterization of the polarization behavior of Vertical-Cavity Surface-Emitting Lasers", in European Semiconductor Laser Workshop, Brussels, Belgium 2012 (talk)
3. A. Molitor, S. Hartmann, W. Elsässer, "Tailoring wave chaos in VCSEL via polarization control", in Wave Chaos from the Micro- to the Macroscale, Dresden, Germany 2012 (poster)
4. S. Hartmann, A. Molitor, M. Blazek, W. Elsässer, "Investigations on photon statistics of Quantum-Dot-Superluminescent Diodes via Two-Photon-Absorption in semiconductors", in CFN Summer School 2012 on Nano-Photonics (Karlsruhe Institute of Technology – DFG-center for Functional Nanostructures), Bad Herrenalb, Germany 2012 (poster)
5. A. Molitor, S. Hartmann, P. Debernardi, W. Elsässer, " Spatially resolved Stokes parameters of small area oxide-confined Vertical-Cavity Surface-Emitting Lasers", in Conference on Lasers and Electro-Optics/Europe - European Quantum Electronics Conference, CB-P.4, Munich, Germany 2013 (poster)
6. S. Hartmann, A. Molitor, M. Blazek, W. Elsässer, "Photon Statistics of Quantum Dot Superluminescent Diodes at the Transition from Amplified Spontaneous Emission to Stimulated Emission", in Conference on Lasers and Electro-Optics/Europe - European Quantum Electronics Conference, CB-5.6, Munich, Germany 2013 (talk)
7. A. Molitor, S. Hartmann, P. Debernardi, W. Elsässer, " Spatio-spectrally resolved Stokes parameters of Vertical-Cavity Surface-Emitting Lasers", in Conference on Lasers and Electro-Optics, San Jose, California, USA 2013 (talk)
8. A. Molitor, S. Hartmann, R. Michalzik, W. Elsässer, " Spatially resolved Stokes parameters of Vertical-Cavity Surface-Emitting Lasers", in European Semiconductor Laser Workshop, Bristol, UK 2013 (talk)
9. A. Molitor, P. Debernardi, S. Hartmann, W. Elsässer, " Spatially resolved Stokes parameters of small area VCSEL: experiment and simulation", in DPG-Frühjahrstagung, Q30.43, Berlin, Germany 2014 (poster)
10. S. Hartmann, F. Friedrich, A. Molitor, M. Reichert, R. Walser and W. Elsässer, "Tunable photon statistics: a new approach for mixed light consisting of semiconductor-based ultra-broadband amplified spontaneous emission and coherent laser light", Quantum Optics VII, Mar del Plata, Argentina 2014 (poster)
11. S. Hartmann, F. Friedrich, A. Molitor, M. Reichert, R. Walser and W. Elsässer, "Experiments on the quantum statistics of broadband light states emitted by quantum dot superluminescent diodes", CLEO Europe 2015 Munich, Germany - EA-P.17 – (Poster)
12. F. Friedrich, S. Hartmann, W. Elsässer, and R. Walser, "Coherence studies of broadband light states from quantum-dot superluminescent diodes", CLEO Europe 2015 Munich, Germany - EA-P.16 – (Poster)
13. MARIANGELA GIOANNINI, ROBERT PAWLUS, LUKAS DRZEWIETZKI, SÉBASTIEN HARTMANN, WOLFGANG ELSÄßER, and STEFAN BREUER, „Relative intensity noise reduction of a quantum dot laser subject to optical feedback“, DPG Frühjahrstagung Heidelberg 2015, Germany (Poster)

- 
14. F. Friedrich, S. Hartmann, W. Elsässer and R. Walser, “Coherence studies of light emitting quantum-dot superluminescent diodes”, DPG Frühjahrstagung Heidelberg 2015, Germany (talk)
  15. S. Kuhn, S. Hartmann and W. Elsässer, “Experimental investigations on photon statistics of a pseudo-thermal light source at 1300nm”, DPG Frühjahrstagung Heidelberg 2015, Germany – Q8.5 - (talk)
  16. ROBERT PAWLUS, MARIANGELA GIOANNINI, LUKAS DRZEWIETZKI, SÉBASTIEN HARTMANN, WOLFGANG ELSÄßER, and STEFAN BREUER, „Amplitude stability of a continuous-wave emitting two-state InAs/InGaAs quantum-dot laser: experiment and simulation“ , DPG Frühjahrstagung Heidelberg 2015, Germany (poster)
  17. S. Kuhn, S. Hartmann and W. Elsässer, “Investigations of 2<sup>nd</sup> order coherence of a pseudothermal light source at 1300nm”, 8<sup>th</sup> International Summer School “New Frontiers in Optical Technologies”, Tampere 2015, Finland (poster)
  18. S. Hartmann, A. Molitor and W. Elsässer, “Ultra-broadband Ghost Imaging using semiconductor-based opto-electronic Amplified Spontaneous Emission”, 600. Wilhelm und Else Heraeus-Seminar “Frontiers of Quantum Optics”, Bad Honnef, Germany 2015 (poster)
  19. S. Hartmann and W. Elsässer, “1D and 2D Ghost Imaging with LEDs”, Photon16, Leeds, England 2016 (talk)
  20. S. Hartmann, S. Kuhn, and W. Elsässer, “Photon statistics based Ghost Imaging with a single detector”, Photon16, Leeds, England 2016 (talk)
  21. S. Hartmann, and W. Elsässer, “Ghost Imaging with superluminescent diodes”, Lindau Nobel Laureate Meeting 2016, Germany 2016 (Poster)
  22. P. Janassek, S. Blumenstein, and W. Elsässer, „Spectral intensity correlations of broadband amplified spontaneous emission from superluminescent diodes“, DPG Frühjahrstagung Mainz 2017, Q26.1, Germany (talk)
  23. L. Fischer, S. Kuhn, S. Blumenstein, and W. Elsässer, „Photon-statistics-based ghost imaging with one single detector“, DPG Frühjahrstagung Mainz 2017, Q44.5, Germany (talk)
  24. D. Laukhardt, T. Mohr, S. Blumenstein, and W. Elsässer, „Single pixel” imaging and its application to beam profile analysis“, DPG Frühjahrstagung Mainz 2017, Q43.2, Germany (talk)

---

## Supervised theses

---

- Patrick Janassek, “Anwendung von ultrabreitband Ghost Imaging in der Frequenzdomäne” (TU Darmstadt, M.Sc. 2017).
- Lydia Fischer, “Realisierung eines Photonenstatistik-basierten 2D Ghost Imaging Systems” (TU Darmstadt, M.Sc. Jun. 2017).
- Daniel Laukhardt, “Untersuchungen zum “Single-pixel” Hadamard Imaging Verfahren und dessen Anwendung für die Strahlprofilanalyse” (TU Darmstadt, B.Sc. 2016).
- Simone Kuhn, “Ghost Imaging mittels eines einzigen Photon-Counting Detektors“ (TU Darmstadt, M.Sc., Jan. 2016).
- Patrick Janassek, „Untersuchung der Polarisation von Quantenkaskadenlasern mittels Stokes-Parametern“, (TU Darmstadt, B.Sc., Okt. 2015).
- Christophe des Pallières, „Investigation on TPA and photon statistics of NIR ASE sources“, (TU Darmstadt, Ecole Centrale de Lyon, Praktikum, Oct. 2015).
- Andreas Massinger, “Untersuchungen zur Effizienz der Frequenzverdopplung eines Lithiumjodat Kristalls mit verschiedenen Lichtquellen“ (TU Darmstadt, B.Sc., Aug. 2015).
- Simone Kuhn, „Realisierung eines Photon-Counting-Experimentes zur Untersuchung der Photonenstatistik einer pseudothermischen Lichtquelle bei 1300nm“ (TU Darmstadt, B.Sc. Jul. 2014).
- Moritz Reichert, “Realisierung einer Halbleiter-basierten Lichtquelle mit abstimmbarer Photonenstatistik“ (TU Darmstadt, B.Sc., März 2014).
- Kerstin Lux, “Spektral hochaufgelöste Untersuchungen des Intensitätsrauschens von Quantenpunkt-Superlumineszenzdiolen” (TU Darmstadt, B.Sc. Jun. 2013).

---

---

## Erklärungen

---

### Selbstständigkeitserklärung

Hiermit erkläre ich, dass ich die vorliegende Arbeit „Classical ghost imaging with opto-electronic light sources: novel and highly incoherent concepts“ selbstständig verfasst und keine anderen als die angegebenen Quellen und Hilfsmittel verwendet habe.

Erzhausen, 7. Februar 2017

Sébastien Blumenstein

### Erklärung über frühere Promotionsversuche

Hiermit erkläre ich, dass von mir keine früheren Promotionsversuche mit dieser oder einer anderen Dissertation erfolgt sind. Die vorliegende Arbeit wurde bisher weder im In- noch im Ausland in gleicher oder ähnlicher Form einer anderen Prüfungsbehörde vorgelegt.

Erzhausen, 7. Februar 2017

Sébastien Blumenstein